INAUGURAL – DISSERTATION

zur
Erlangung der Doktorwürde
der
Naturwissenschaftlich-Mathematischen
Gesamtfakultät
der
Ruprecht-Karls-Universität
Heidelberg

Vorgelegt von
M.Sc. Kim Alix Jakob
aus Nidda

2017

Tag der mündlichen Prüfung: 02.05.2017

Late Pliocene to early Pleistocene millennial-scale climate fluctuations and sea-level variability: A view from the tropical Pacific and the North Atlantic

Gutachter:

Prof. Dr. Oliver Friedrich
Prof. Dr. Jörg Pross

TABLE OF CONTENTS

ACKNOWLEDGMENTS

First of all, my sincere thanks are given to my supervisors **Oliver Friedrich and Jörg Pross**, who offered me the possibility of a PhD position at Ruprecht-Karls University Heidelberg, which provided an excellent chance for me. I really appreciated the way we were collaborating and discussing during the past three years, and I am very grateful for the time you spent on reading and correcting endless manuscript and proposal versions. I would like to use this opportunity to address special thanks to both of you for invaluable assistance and support, enthusiastic encouragement, and useful critiques during my PhD work.

Further, I would like to thank:

Clara, Paul and Richard – During my PhD project, I got the opportunity to work together with you as leading scientists in the field of paleoceanography. In this context, I would like to emphasize the close cooperation with Paul A. Wilson (National Oceanography Centre Southampton, UK) and Clara T. Bolton (CEREGE, France). Thanks to both of you for reading all my manuscript versions and for improving their quality. In this regard, special thanks belong to Paul, who invited me for a research stay at the National Oceanography Centre Southampton – many thanks for being so welcoming. Many thanks also to Richard D. Norris (Scripps Institution of Oceanography, University of California, San Diego, USA) for invaluable help in foraminiferal taxonomy.

André and Andreas, Julia and Kenji – The ideas developed during my PhD work have benefited from many discussions with members of the research groups "Sedimentology and marine paleoenvironmental dynamics" and "Palynology and paleoenvironmental dynamics" at Heidelberg University. I am grateful to all the people from our groups including my office mates Julia Hoffmann and Kenji Hatsukano. In this context, I would also like to express special thanks to André Bahr for helpful scientific discussions, advice with regard to Mg/Ca sample processing, help (and patience) with spectral analysis, and for being a member of my examination panel. Many thanks also to Andreas Koutsodendris for his support with AnalySeries.

Mario – Thanks to Mario Trieloff for being a member of my examination panel.

Jens and Sven – I am really grateful for technical assistance from Jens Fiebig and Sven Hofmann during uncountable stable-isotope analyses at Goethe University Frankfurt.

Silvia, Christian and Stefan – Many thanks to Silvia Rheinberger, Stefan Rheinberger and Christian Scholz for invaluable support during Mg/Ca measurements and general laboratory assistance at Heidelberg University.

Matt and Andy, Anya and Diederik – I am grateful to Matthew Cooper and J. Andy Milton for laboratory assistance during my research stay at the National Oceanography Centre Southampton (UK). In this regard, I would also like to thank Anya Crocker and Diederik Liebrand for being so welcoming and offering me a place to stay during my two-week stay in Southampton.

Jens and Bärbel, Hans-Peter and Alexander – I gratefully acknowledge SEM assistance from Jens O. Herrle and Bärbel Schminke (Goethe University Frankfurt) as well as Hans-Peter Mayer and Alexander Varychev (Heidelberg University).

Jasmin, Patrick and Norbert – Thanks to Jasmin Link, Patrick Blaser and Norbert Frank for helping me with neodymium-isotope analysis at the Institute of Environmental Physics (Heidelberg University).

Barbara, Jakob, Jani, Karsten, Lisa, Tobias and Verena – Many thanks to Barbara Hennrich, Jakob Gänzler, Jani Biber, Karsten Kähler, Lisa Pees, Tobias Syla and Verena Braun. You did a great job helping me with sample processing!

Phil – Thanks to Phil Rumford and his team at the Gulf Coast Repository (College Station, Texas) for support during the sampling process.

Elfriede, Torsten and Francisco – I gratefully acknowledge administrative assistance from Elfriede Grohmann and Torsten Hoffmann. Further I would like to thank Francisco J. Cueto for computer assistance and moral support.

Lastly, I would like to thank my **family and friends** for helping me to keep my PhD work in perspective and being endlessly encouraging.

Funding for this thesis was provided by the German Research Foundation (grants FR2544/2 and FR2544/6 to O.F. and PR651/15 to J.P.). This research used samples provided by the Ocean Drilling Program (ODP) and the Integrated Ocean Drilling Program (IODP). The European Consortium for Ocean Research Drilling (ECORD) is gratefully acknowledged for selecting me for an ECORD Scholarship as well as an ECORD Research Grant holder.

ABSTRACT

In light of the need for high-fidelity, quantitative projections of future climate change, it is mandatory to understand climate variability at timescales that do justice to the tempo of anthropogenic climate change (i.e., sub-millennial). At the same time, information on the lower-frequency (i.e., orbital-scale) baseline characteristics of climate change underlying the short-term variability is required for a full mechanistic understanding. Such information can be obtained from time intervals of Earth's history that comprise climatic boundary conditions as they are to be encountered in the near future.

In this context, this thesis aims to contribute toward accurately deciphering past climate fluctuations and sea-level variability on glacial-interglacial (G-IG) to (sub-)millennial timescales during past times of "near-modern" paleogeography and warmer-than-present climatic boundary conditions – the late Pliocene to early Pleistocene (~2.75–2.4 million years ago [Ma], Marine Isotope Stages [MIS] G6–95). This time period falls within the transition from a warmer Pliocene climate without larger-scale Northern Hemisphere ice sheets to a progressively cooler Pleistocene climate dominated by a stronger response of the climate/cryosphere system to orbital forcing, widely being termed "intensification of Northern Hemisphere Glaciation" (iNHG). The target interval includes MIS 100 through 96, three large-amplitude G-IG cycles (~1‰ in benthic $\delta^{18}O$) that represent the culmination of iNHG.

The first part of this thesis focuses on identifying the mechanisms that regulated G-IG primary productivity changes in the Eastern Equatorial Pacific (EEP) upwelling system, which constitutes an important component of the Earth's atmospheric and marine carbon budget. For this purpose, high-resolution carbon isotopes from benthic and planktic foraminiferal calcite, and sand-accumulation rates have been investigated for the time interval between ~2.65 and 2.4 Ma (MIS G1–95) at Ocean Drilling Program (ODP) Site 849, which is located in the heart of the EEP upwelling regime. The presented records show increasing productivity levels for glacials from MIS 100 onward, with an onset during full glacial conditions and a maximum during glacial terminations. This productivity pattern is explained with enhanced nutrient delivery from the high southern latitudes during full glacial conditions in combination with superimposed intensified regional upwelling toward glacial terminations.

The second part of this thesis focuses on changes in equatorial Pacific surface-water structure across iNHG to elucidate whether these are related to El Niño- and La Niña-like climate dynamics. The strong inter-annual variability between El Niño and La Niña events in the modern tropical Pacific plays a major role in the global climate system. During the Pliocene, the Pacific warm pool was greatly expanded relative to today, implying a surface-ocean temperature field akin to modern El Niño events. The iNHG marks the transition from this warm Pliocene state toward modern conditions with strong upwelling in the EEP and stronger zonal temperature and primary productivity gradients. In this thesis, this transition is examined based on new, high-resolution planktic foraminiferal Mg/Ca- and $\delta^{18}O$-derived sea-surface temperature and salinity data for ODP Site 849 in the EEP for ~2.75–2.4 Ma (MIS G6–95). To investigate zonal gradients that are indicative for El Niño- and La Niña-like climate dynamics, these records are compared to similar records from the Western Equatorial Pacific. While no G-IG pattern is seen in the temperature gradient, obliquity-paced oscillations are documented in the salinity gradient. These oscillations originate from a response to a glacial southward and interglacial northward migration of the Intertropical Convergence Zone over the EEP rather than to fluctuations between El Niño- and La Niña-like climate states.

The final study of this thesis reconstructs high-resolution sea-level records for ODP Site 849 in the EEP and Integrated Ocean Drilling Program (IODP) Site U1313 in the North Atlantic covering ~2.65–2.4 Ma (MIS G1–95) based on benthic foraminiferal $\delta^{18}O$ and Mg/Ca data. New sea-level lowstand estimates for MIS 100–96 show substantially lower values for Site 849 than for Site U1313 (peak values of ~55–85 m *versus* ~110–130 m below present), while interglacial highstand estimates are consistent (~0–30 m above present). In comparison to previous estimates, values for Site U1313 appear to be overestimated, most likely due to uncertainties induced by changing deep-water masses at that site. Nevertheless, the sea-level evolution for MIS 100 and 96 emerges as strikingly reminiscent of late Pleistocene glacials (asymmetric "sawtooth" structure, rapid termination, final sea-level drop before the termination). This suggests that similar mechanisms controlled early and late Pleistocene G-IG cycles. Remarkably, the generated data from EEP Site 849 and North Atlantic Site U1313 imply a ~50–100 m sea-level rise into early Pleistocene interglacials. This would require complete melting of Greenland and West Antarctic Ice Sheets and a partial retreat of the "stable" East Antarctic Ice Sheet, hinting at its future vulnerability.

KURZFASSUNG

Um künftige Klimaveränderungen zuverlässig prognostizieren zu können, ist es zwingend erforderlich, kurzfristige Klimaschwankungen, die dem Tempo des anthropogenen Klimawandels entsprechen, im Detail zu verstehen. Ebenso wichtig ist es, die grundlegenden Mechanismen hinter den niedrigerfrequenten Klimaschwankungen zu verstehen, welche den kurzfristigen Schwankungen unterliegen. Derartige Informationen können aus Intervallen der Erdgeschichte gewonnen werden, die der nahen Zukunft vergleichbare klimatische Rahmenbedingungen aufweisen.

Vor diesem Hintergrund befasst sich diese Arbeit mit der Rekonstruktion von Klimaschwankungen unter paläoklimatischen und paläogeographischen Rahmenbedingungen, die mit der heutigen Situation vergleichbar sind. Dabei werden sowohl kurzfristige als auch langfristige (Glazial-Interglazial [G-IG]) Klimaschwankungen betrachtet. Der Untersuchungszeitraum umfasst das späte Pliozän und frühe Pleistozän (~2.75–2.4 Millionen Jahre, Marine Isotopenstadien [MIS] G6–95). Dieser Zeitabschnitt repräsentiert den Übergang vom relativ warmen Klima des Pliozäns ohne substantielle Vereisungen auf der Nordhemisphäre hin zum kühleren Pleistozän, welches durch ausgeprägte G-IG-Schwankungen geprägt ist. Dieser Übergang wird häufig als „Intensivierung der Nordhemisphärenvereisung“ (INHV) bezeichnet. Der betrachtete Untersuchungszeitraum umfasst unter anderem MIS 100–96, drei stark ausgeprägte G-IG-Zyklen, welche die finale Phase der INHV repräsentieren.

Der erste Teil dieser Arbeit beschäftigt sich mit der Identifikation der grundlegenden Mechanismen, die Änderungen der Primärproduktivität im äquatorialen Upwelling-Gebiet des östlichen Pazifiks hervorrufen und daher einen beachtlichen Einfluss auf den globalen Kohlenstoffhaushalt haben. Hierzu wurden Proben von Ocean Drilling Program (ODP) Site 849 untersucht, welcher sich im Zentrum des äquatorialen Upwelling-Gebiets des östlichen Pazifiks befindet. Es wurden zeitlich hochauflösende Datensätze basierend auf Kohlenstoff-Isotopen benthischer und planktischer Foraminiferen und Sand-Akkumulationsraten für das Zeitintervall ~2.65–2.4 Millionen Jahre (MIS G1–95) generiert. Die erzeugten Daten deuten auf eine steigende Primärproduktion insbesondere während der Glaziale MIS 100, 98 und 96

hin, wobei die maximale Produktivität während der Terminationen erreicht wurde. Dies ist zum einen auf einen erhöhten Nährstoffgehalt im Oberflächenwasser während des Maximums eines Glazials zurückzuführen, zum anderen auf verstärktes Upwelling während der Termination.

Der zweite Teil dieser Arbeit befasst sich mit Änderungen in der Oberflächenwasser-Struktur des äquatorialen Pazifiks während der INHV und ob diese gegebenenfalls mit El Niño- und La Niña-ähnlichen Klimaveränderungen zusammenhängen. Im heutigen Pazifik spielt die Variabilität zwischen El Niño- und La Niña-Ereignissen eine entscheidende Rolle für das globale Klima. Während des Pliozäns war der pazifische „Warmpool“ im Vergleich zu heute wesentlich stärker ausgeprägt, was auf eine Oberflächenwasser-Struktur im äquatorialen Pazifik hinweist, wie sie unter heutigen El Niño-Ereignissen herrscht. Die INHV stellte eine Übergangsphase dar, welche die Entwicklung des wärmeren pliozänen Klimas hin zur heutigen Situation mit starkem Upwelling im östlichen Pazifik und ausgeprägten Ost-West-Gradienten in Oberflächenwasser-Temperatur und Produktivität darstellt. In dieser Arbeit erfolgt eine genauere Betrachtung dieser Übergangsphase. Dazu wurden zeitlich hochaufgelöste Mg/Ca- und $\delta^{18}O$-Datensätze an planktischen Foraminiferen von ODP Site 849 für das Zeitintervall ~2.75–2.4 Millionen Jahre erzeugt. Diese erlauben es, Rückschlüsse auf Oberflächenwasser-Temperaturen und -Salinitäten zu ziehen. Die Daten wurden mit vergleichbaren Datensätzen aus dem westlichen äquatorialen Pazifik verglichen. Ost-West-Temperatur- und Salinitätsgradienten erlauben es, Aussagen über eine mögliche Dynamik zwischen El Niño- und La Niña-ähnlichen Klimazuständen zu treffen. Während der rekonstruierte Temperaturgradient keinen G-IG-Zyklus aufweist, ist ein solcher im Salinitätsgradienten nachweisbar. Diese Schwankungen weisen jedoch nicht auf El Niño- und La Niña-ähnliche Klimaveränderungen hin, sondern resultieren vielmehr aus einer Verschiebung der Innertropischen Konvergenzzone über dem östlichen Pazifik (Richtung Norden während Interglazialen und Richtung Süden während Glazialen).

Der dritte Teil dieser Arbeit fokussiert auf die Rekonstruktion zeitlich hochaufgelöster, Mg/Ca- und $\delta^{18}O$-basierter Meeresspiegelschwankungen. Hierzu wurden Proben benthischer Foraminiferen aus dem östlichen äquatorialen Pazifik (ODP Site 849) und dem Nord-Atlantik (Integrated Ocean Drilling Program [IODP] Site U1313) für das Zeitintervall ~2.65–2.4 Millionen Jahre (MIS G1–95) untersucht. Die generierten Werte (relativ zum heutigen Meeresspiegel) variieren zwischen -55 und -85 m (Site 849) und -110 und -130 m (Site U1313) für die Glaziale MIS 100–96 und zwischen 0 und +30 m (beide Sites) für die entsprechenden Interglaziale. Im Vergleich zu vorherigen Untersuchungen erscheinen die

Werte von Site U1313 als zu hoch, was auf Unsicherheiten zurückzuführen ist, die mit einer erforderlichen Wassermassenkorrektur für diesen Site zusammenhängen. Unabhängig davon erinnert die Struktur, die für die Glaziale MIS 100 und 96 rekonstruiert wurde, an diejenige spätpleistozäner Glaziale (asymmetrische, sägezahnförmige Struktur, schnelle Termination, finaler Meeresspiegel-Rückgang vor der Termination). Diese Gemeinsamkeiten lassen vermuten, dass ähnliche – wenn nicht sogar identische – Mechanismen die früh- und spätpleistozänen G-IG-Zyklen gesteuert haben. Der rekonstruierte Meeresspiegel-Anstieg von ~50–100 m in frühpleistozäne Interglaziale impliziert ein komplettes Abschmelzen des Grönländischen und des Westantarktischen Eisschildes sowie ein Teilabschmelzen des vermeintlich „stabilen“ Ostantarktischen Eisschildes. Die daraus abzuleitende Vulnerabilität des Ostantarktischen Eisschildes unter wärmeren klimatischen Rahmenbedingungen als heute ist hinsichtlich des zukünftigen Klimawandels von elementarer Bedeutung.

CHAPTER 1

OBJECTIVES AND OUTLINE

1.1 Objectives

The current debate on anthropogenically induced present-day global warming as a consequence of enhanced greenhouse-gas emission highlights the increasing manifestation of anthropogenic forcing on Earth's climate (e.g., Miller et al., 2005; IPCC, 2014). In light of the need for high-fidelity, quantitative projections of future climate change, it is important to understand climate variability at timescales that do justice to the tempo of anthropogenic climate change (i.e., sub-millennial). At the same time, information on the lower-frequency (i.e., orbital-scale) baseline characteristics of climate change underlying the short-term variability is required in order to obtain a full mechanistic understanding.

In this context, the variability documented in early Pleistocene and late Pliocene climate archives can provide insight into the processes and mechanisms connected to climatic changes on long-term (million years [Myr]), glacial-interglacial (100–41 kiloyears [kyr]) and (sub-) millennial (<1,000 years [yr]) timescales without the influence of human activity. Results derived from paleoclimate studies of this time interval therefore (i) allow to assess the contribution of human *versus* natural factors to global warming, (ii) facilitate the understanding of the Earth's climate system, and (iii) allow to reliably model and predict future climate change.

Because oceans cover ~70% of the Earth's surface, they are arguably the most important factor influencing the global climate system. For instance, changes in physical parameters in the global oceans, most notably temperature and salinity, are closely coupled to climate fluctuations by controlling ocean circulation and global ice volume/sea level through complex feedback mechanisms (e.g., Broecker, 1991; Rahmstorf, 1997). At the same time, global ocean primary production as an important component of the Earth's carbon cycle is a pivotal factor for global climate evolution (e.g., Schlitzer, 2004; Takahashi et al., 2009).

The overall objective of this thesis is to provide insight into the processes and mechanisms that controlled glacial-interglacial (G-IG) to (sub-)millennial-scale climate fluctuations and

sea-level variability during times of "near-modern" paleogeography and warmer-than-present climatic boundary conditions. Understanding the climatic evolution under such conditions is directly relevant for our understanding of future climate warming and sea-level change.

1.2 Outline

In light of the above considerations, the selected target interval for this thesis is the late Pliocene to early Pleistocene (~2.75 to 2.4 million years ago [Ma], Marine Isotope Stages [MIS] G6 to 95). This time period – portrayed in detail in **Chapter 2 –** falls within the transition from a warmer Pliocene climate without larger-scale Northern Hemisphere ice sheets to a progressively cooler Pleistocene climate dominated by a stronger response of the climate/cryosphere system to orbital forcing (Lisiecki and Raymo, 2005). The time interval comprising these changes is typically considered to span from ~3.6 to 2.4 Ma (Mudelsee and Raymo, 2005) and is widely termed "Northern Hemisphere Glaciation". The target interval of this thesis (~2.75–2.4 Ma, MIS G6–95) includes (i) glacial MIS G6 (~2.7 Ma), which is often considered to mark the onset of large-scale glaciations in the Northern Hemisphere because it is characterized by the first ice-rafting events in the North Atlantic and the occurrence of high-amplitude climate fluctuations (Bartoli et al., 2006; Bailey et al., 2013), and (ii) MIS 100–96 (~2.5 Ma), the first three large-amplitude G-IG cycles (with an amplitude of ~1‰ in globally representative benthic foraminiferal oxygen isotopes [Lisiecki and Raymo, 2005]) known as the "intensification of Northern Hemisphere Glaciation" (iNHG).

In this thesis, benthic and planktic foraminifer-based proxy records for ocean temperature, surface-water salinity, primary productivity and sea level (**Chapter 2**) are examined for iNHG (~2.75 to 2.4 Ma, MIS G6 to 95). Records have been generated on deep-sea sediment cores that were drilled within the framework of (i) Ocean Drilling Program Leg 138 in the Eastern Equatorial Pacific (Site 849) and (ii) Integrated Ocean Drilling Program Expedition 306 in the North Atlantic (Site U1313) (**Chapter 3**).

The Eastern Equatorial Pacific Ocean (EEP) is the main focus of **Chapters 4 to 5**. Due to its sheer size, this region plays a major role in the global climate system and thus is important for understanding and predicting global climate variations. For instance, the EEP supports >10% of the present-day global ocean primary production (Pennington et al., 2006). Organic-matter export and CO_2 removal from the surface ocean make this region an important component in Earth's atmospheric and marine carbon budget (e.g., Schlitzer, 2004; Takahashi et al., 2009).

Traditionally, it has been argued that since iNHG changes in EEP productivity have predominantly depended on trade wind strength-controlled upwelling intensity (e.g., Cleaveland and Herbert, 2007; Etourneau et al., 2010). An alternative hypothesis suggests that EEP productivity is primarily controlled by changes in the nutrient content of the upwelled water masses (Lawrence et al., 2006; Etourneau et al., 2013). To test these competing hypotheses as they have been proposed to explain G-IG productivity change, **Chapter 4** provides new high-resolution (~780 yr) carbon-isotope data from benthic and planktic foraminiferal calcite, and sand-accumulation rates for the time interval between ~2.65 and 2.4 Ma (MIS G1 to 95) from EEP Site 849. This site is ideally suited to study primary productivity changes because it is located within the equatorial divergence system in the heart of the highly productive upwelling regime (Mix et al., 1995).

The strong inter-annual variability between El Niño and La Niña climate states as they are parts of the El Niño-Southern Oscillation dynamics in the tropical Pacific Ocean also plays a major role in the modern global climate system (McPhaden et al., 2006). On a timescale of two to seven years, the climate in the modern EEP varies between anomalously warm (El Niño) and cold (La Niña) conditions. The question whether and yes, to what extent these dynamics were a feature of the geological past is a matter of lively debate. Numerical model experiments suggest El Niño-like and La Niña-like states (i.e., a surface-ocean structure akin to modern El Niño or La Niña conditions) in the tropical Pacific to be associated with interglacial and glacial periods, respectively (Philander and Fedorov, 2003; Fedorov et al., 2006). Other studies, however, are incompatible with G-IG changes in surface-water structure in the tropical Pacific during the early Pleistocene and thus with fluctuations between El Niño-like and La Niña-like climate states (Lee and Poulsen, 2005; Bolton et al., 2010a). **Chapter 5** offers new insight into this debate based on new high-resolution planktic foraminiferal Mg/Ca- and oxygen-isotope-derived sea-surface temperature and salinity data. Specifically, it presents the reconstruction of gradients between EEP Site 849 (this thesis) and Site 806 in the West Pacific Warm Pool (Medina-Elizalde and Lea, 2010) between ~2.75 and 2.4 Ma (MIS G6–95). These gradients allow to critically assess if changes in equatorial Pacific surface-water structure are related to El Niño- and La Niña-like climate dynamics.

Considering the anthropogenic forcing on Earth's climate (e.g., Miller et al., 2005; IPCC, 2014), there is also a need for refined information on the potential response of ice volume/sea level in the context of global warming. The need for reliable predictions of future sea-level rise is highlighted by the fact that with a sea-level increase of merely 40 cm – a value likely to be reached by the end of the 21st century (IPCC, 2014) – as many as 270 million people

presently living in near-coastal lowlands will lose their habitats (Mimura, 2013). To allow for accurate future sea-level projections, continuous, highly resolved and well-quantified records of paleo-sea-level evolution are required that reflect past climate fluctuations under warmer-than-modern background conditions as they prevailed prior to 0.5 Ma. While several highly resolved sea-level reconstructions exist for the past 0.5 Myr (e.g., Siddall et al., 2003; Rohling et al., 2009), our knowledge on high-resolution sea-level and deep-sea temperature fluctuations during older periods of Earth's history is yet limited. Such temporally highly resolved information is, however, essential in order to obtain a detailed picture of natural sea-level dynamics under warmer-than-modern climatic conditions.

This thesis addresses this knowledge gap by presenting and evaluating new, highly resolved ([sub-]millennial-scale) sea-level and deep-sea temperature records from ~2.65 to 2.4 Ma (MIS G1 to 95) for two ocean basins (**Chapter 6**). The presented records are based on a combined approach using benthic foraminiferal oxygen isotopes and Mg/Ca from Site 849 in the EEP and Site U1313 in the North Atlantic. In comparison to already available lower-resolved data for that time period (Bintanja and Van de Wal, 2008; de Boer et al., 2014), the presented new high-resolution records from the East Pacific and North Atlantic show critical details for assessing global sea-level/ice-volume dynamics under warmer-than-modern climatic boundary conditions that are relevant for an accurate projection of future sea-level rise.

CHAPTER 2

INTRODUCTION

2.1 Plio-Pleistocene climates

The Pliocene (5.3–2.6 Ma) and Pleistocene (2.6–0.01 Ma) epochs constitute the uppermost and lowermost divisions of the Neogene (23.0–2.6 Ma) and Quaternary (past 2.6 Myr) periods, respectively (Gradstein and Ogg [2012]; Figure 2.1a). Climatic changes over the past 5 Myr ultimately culminated in today's world characterized by bipolar glaciation (Figure 2.1b), a scenario that is unique within the entire Cenozoic (past 66.0 Myr) (Zachos et al., 2001; DeConto et al., 2008; Zachos et al., 2008).

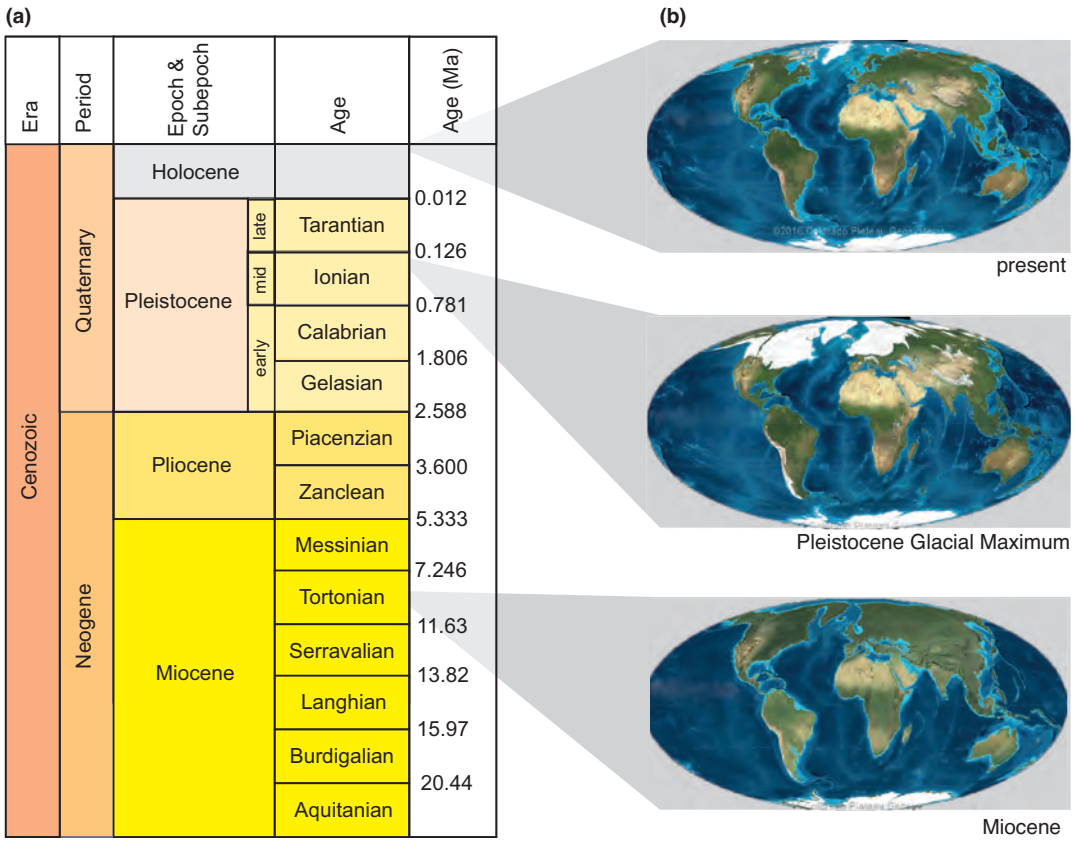

Figure 2.1. The Plio-Pleistocene time period in a wider temporal context. **(a)** Timescale for the Neogene and Quaternary after Gradstein and Ogg (2012)*. **(b)** Paleogeographic maps of selected time intervals highlighting the evolution of global ice volume. Maps from Global Paleogeography and Tectonics in Deep Time series by Ron Blakey (© Colorado Plateau Geosystems Inc.).

Note that the Pliocene/Pleistocene boundary has recently been redefined from the base of the Calabrian (1.806 Ma) to the base of the Gelasian (2.588 Ma) (Gibbard et al., 2010). Therefore, the early Pleistocene is referred to as late Pliocene in older (pre-2010) studies.

In short, the past 5 Myr of Earth's climate history can be subdivided into three major intervals: First, the early Pliocene global warm period without large-scale glaciations in the Northern Hemisphere; second, the transition from Northern Hemisphere ice-free conditions of the early Pliocene to the first strong obliquity-controlled glacial-interglacial (G-IG) cycles with significant waxing and waning of Northern Hemisphere ice sheets during the late Pliocene/early Pleistocene – a period known as the "Northern Hemisphere Glaciation" (NHG [Mudelsee and Raymo, 2005]); and third, the late Pleistocene dominated by high-amplitude climate fluctuations and strong, eccentricity-paced ice ages. In the following, the overall climate evolution (Chapter 2.1.1) and the reasons that may have led to NHG (Chapter 2.1.2) are discussed in detail.

2.1.1 General characteristics of Plio-Pleistocene climates

Climate evolution

The early Pliocene warm period (~5.3–3.6 Ma) is characterized by a reduced meridional sea-surface temperature (SST) gradient compared to the present-day situation (Dowsett et al., 2009). Relative to modern values, mean SSTs were up to ~7°C warmer in high-latitude (e.g., Cronin et al., 1993; Lawrence et al., 2009) and ~3–4°C warmer in low- and mid-latitude oceans (e.g., Lawrence et al., 2006; Dekens et al., 2007). Atmospheric carbon dioxide concentrations (pCO_2) for the Pliocene warmth were on the order of 350–450 ppmv (e.g., Raymo et al., 1996; Pagani et al., 2010; Seki et al., 2010), significantly higher than the pre-industrial pCO_2 level of 280 ppmv (Luthi et al., 2008) and akin to modern "Anthropocene-like" values (Figure 2.2b). Sea-level highstand estimates for the Pliocene warm period are 10–30 m higher than modern values (Miller et al., 2012), with small-scale (<10 m) amplitudes only (de Boer et al., 2014) (Figure 2.2b). The former observation suggests a reduced ice-sheet volume compared to the present-day situation. Indeed, model simulations indicate that Greenland Ice Sheets did not exist such that perennial ice-free conditions likely prevailed in the Arctic Ocean (DeConto et al., 2008; Dolan et al., 2011).

The climate of the early Pliocene epoch as described above shares similarities with the climate projected for the end of the 21st century, such as temperatures that globally were on average 2–3°C warmer than today or pCO_2 concentrations in the range of today's values. At the same time, it is characterized by a "near-modern" paleogeography. Representing boundary conditions as they are expected in the context of future climate warming and sea-level change, this time period is widely studied as the most recent geological analogy for predicting the effects of near-future warming (e.g., Robinson et al., 2008; Dowsett et al., 2013).

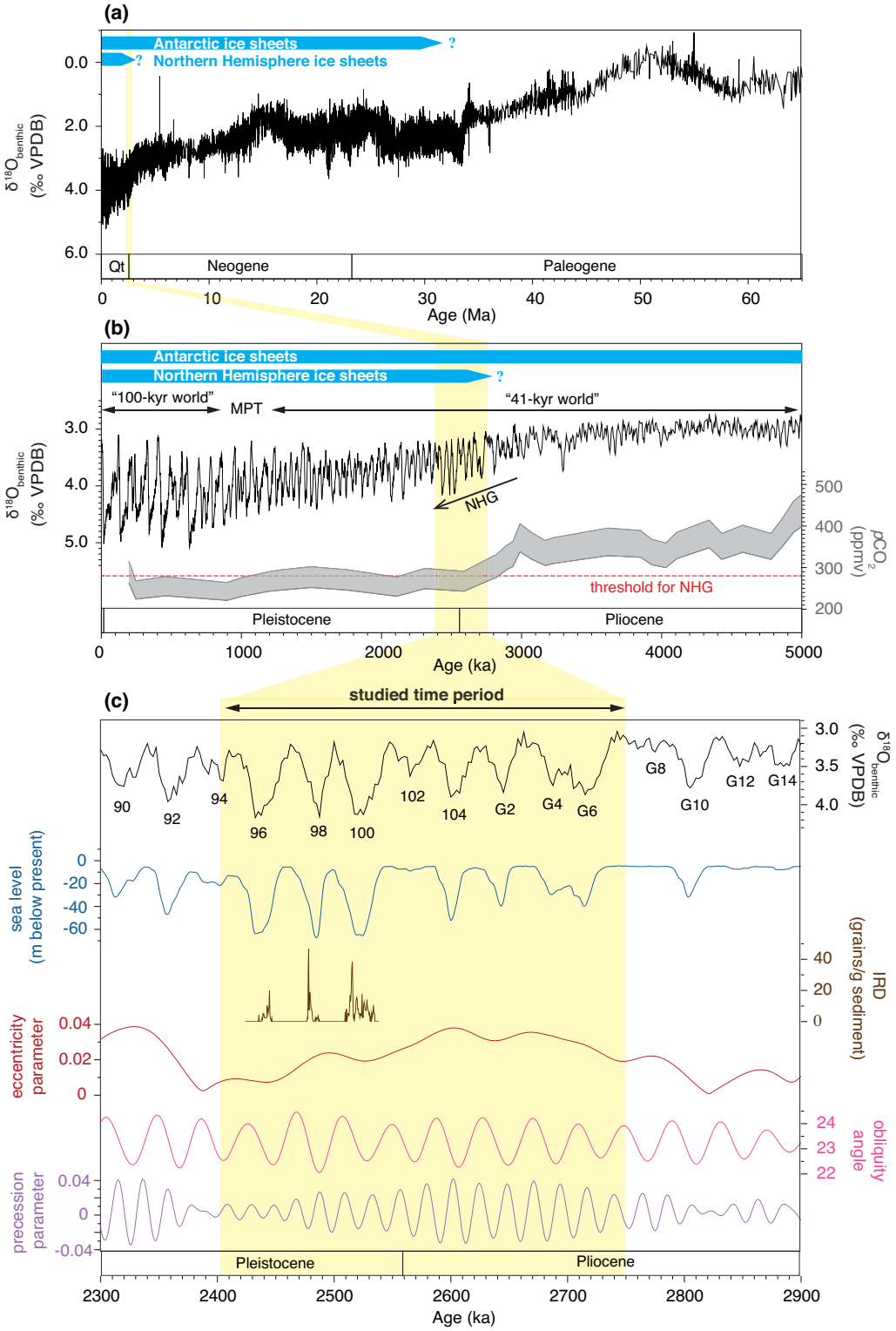

Figure 2.2. Overview of climatic records for **(a)** the past 65 Myr, **(b)** the past 5 Myr, and **(c)** the Plio-Pleistocene transition. Yellow shading indicates the study interval of this thesis (~2.75–2.4 Ma, MIS G6–95). Black: Benthic foraminiferal $\delta^{18}O$ after Zachos et al. (2008) in (a) and after Lisiecki and Raymo (2005) in (b) and (c); grey: Atmospheric pCO_2 range estimates (Seki et al., 2010) with a hypothesized threshold value for Northern Hemisphere ice buildup (red line) (DeConto et al., 2008); blue: Modeled global sea level relative to present (Bintanja and Van de Wal, 2008); brown: Ice-rafted debris (IRD) record from Site U1313 (Bolton et al., 2010c), which is located at the extreme southern limit of the IRD belt (Ruddiman, 1977a, b); red, pink and purple: Orbital parameters (eccentricity, obliquity and precession) (Laskar et al., 2004). Qt = Quaternary; VPDB = Vienna Pee Dee Belemnite; MPT = Mid-Pleistocene Transition; NHG = Northern Hemisphere Glaciation.

Early Pliocene warm conditions began to deteriorate rapidly with the onset and intensification of Northern Hemisphere Glaciation, typically considered to span from ~3.6 to 2.4 Ma (Mudelsee and Raymo, 2005) (Figure 2.2b). An increase in benthic foraminiferal $\delta^{18}O$ of ~0.4‰ from Marine Isotope Stage (MIS) G16 to G10 (~2.92–2.82 Ma) is interpreted to represent the first phase of substantial Northern Hemisphere ice growth (Bartoli et al., 2005, and references therein). Marine Isotope Stage G6 (~2.7 Ma) is often described to mark the actual onset of NHG as it is characterized by the first ice-rafting events in the North Atlantic and the occurrence of high-amplitude climate fluctuations (Bartoli et al., 2006; Bailey et al., 2013). The following period, known as the "intensification of Northern Hemisphere Glaciation" (iNHG), is associated with a stronger response of the climate/cryosphere system to orbital forcing. This is indicated by increasing amplitudes in obliquity-paced (~41 kyr) G-IG cycles in benthic foraminiferal $\delta^{18}O$ from MIS G6 onward. This development culminated during MIS 100 to 96 in the first three large-amplitude (~1‰ in benthic $\delta^{18}O$) G-IG cycles that indicate significant waxing and waning of Northern Hemisphere ice sheets (Lisiecki and Raymo, 2005) (Figure 2.2c). Of particular significance during iNHG is MIS 100 (~2.5 Ma), which is considered as the earliest glacial during which ice rafting became widespread across the North Atlantic Ocean (e.g., Shackleton et al., 1984a; Naafs et al., 2013) (Figure 2.2c); the provenance of its ice-rafted debris in the subpolar North Atlantic is comparable to that of the Last Glacial Maximum (Bailey et al., 2013). This indicates that glaciers or ice sheets extended on the sea from circum-North Atlantic terranes (Balco and Rovey, 2010; Bailey et al., 2012; Lang et al., 2014). At that time, a permanent bipolar glaciation had been established, although smaller-scale glaciers that extended to the sea have occurred in high northern latitudes as early as during the middle Eocene (Eldrett et al., 2007).

Sea-level estimates for the early Pleistocene as they are yet available cover a wide spectrum (see below), which makes it difficult to reliably constrain the dynamics of the early Pleistocene climate/cryosphere system. A brief overview on available sea-level lowstand estimates (relative to present) for prominent iNHG glacials MIS 100–96 along with the technique applied to is given in the following (for more details see Chapter 6): Sea-level lowstands on the order of -55 to -90 m are inferred from benthic foraminiferal $\delta^{18}O$ (Miller et al., 2011) and paired benthic Mg/Ca and $\delta^{18}O$ data (Dwyer et al., 1995; Sosdian and Rosenthal, 2009). Considerably higher estimates (-80 to -110 m) are inferred from sequence stratigraphy applied to continental margins in New Zealand (Naish, 1997). Inverse forward modeling based on globally representative $\delta^{18}O$ (LR04; Lisiecki and Raymo, 2005) also covers a wide range, estimating lowstands of -65 to -75 m (Bintanja and Van de Wal, 2008;

Lourens et al., 2010) (Figure 2.2c) to more modest values of -35 to -45 m (de Boer et al., 2014). Siddall et al. (2010) used a non-linear transfer function between benthic foraminiferal $\delta^{18}O$ and sea level and estimated values of -20 to -40 m. The yet most modest sea-level lowstand values of +10 to -15 m have recently become available through planktic foraminiferal oxygen-isotope analyses in the eastern Mediterranean Sea (Rohling et al., 2014). Notwithstanding the wide spectrum of these ranges, the estimates consistently document a shift to larger-amplitude sea-level fluctuations, i.e., stronger glacials, at ~2.7 Ma (MIS G6) and ~2.5 Ma (MIS 100–96) contemporaneous with the first occurrence of ice-rafted debris in North Atlantic sediments (e.g., Shackleton et al., 1984a; Bailey et al., 2013; Naafs et al., 2013).

Over the course of the Pleistocene, the amplitude of obliquity-driven waxing and waning of Northern Hemisphere ice sheets became progressively stronger (Figure 2.2b). Over the Mid-Pleistocene Transition (~1.2–0.7 Ma; Clark et al. [2006]), the climatic cyclicity shifted from an obliquity-dominated "41-kyr world" of the late Pliocene and early Pleistocene to an eccentricity-dominated "100-kyr world" characteristic for the late Pleistocene (Berger and Jansen, 1994; Lisiecki and Raymo, 2005). As evidenced in benthic foraminiferal $\delta^{18}O$ (Lisiecki and Raymo, 2005), the shape of G-IG cycles also changed across the Mid-Pleistocene Transition: While shorter, small-amplitude, symmetric cycles prevailed throughout the "41-kyr world", longer, large-amplitude, asymmetric ("sawtooth-shaped") cycles are characteristic for the late Pleistocene "100-kyr world" (Figure 2.2b).

2.1.2 The intensification of Northern Hemisphere Glaciation

Several hypotheses have been proposed to explain the initiation and expansion of Northern Hemisphere ice sheets during the latest Pliocene and earliest Pleistocene. The most generally accepted mechanism is the reduction of atmospheric pCO_2 below a critical threshold value (for details see below) (e.g., DeConto et al., 2008; Lunt et al., 2008a; Seki et al., 2010). Other hypotheses include a decrease in incoming solar radiation (e.g., Kennett et al., 1977; Maslin et al., 1998), changes in oceanic gateway configuration (e.g., Keigwin, 1982; Haug and Tiedemann, 1998; Cane and Molnar, 2001), changes in stratification and moisture supply in the North Pacific Ocean (e.g., Sigman et al., 2004; Haug et al., 2005), and the termination of "permanent El Niño-like conditions" (Philander and Fedorov, 2003; Barreiro et al., 2005). These hypotheses are discussed in the following.

Decrease in incoming solar radiation

Several studies suggest that the increasing glaciation of Greenland may have been driven by a decrease in incoming solar radiation, either directly through variations in orbital parameters (i.e., precession, obliquity and eccentricity [Milankovitch, 1941]) or indirectly through variations in atmospheric aerosol concentration or volcanic dust (e.g., Haug and Tiedemann, 1998; Maslin et al., 1998; Prueher and Rea, 1998).

Volcanic activity. The rapidity of the onset of glacial conditions in Greenland (i.e., 1000–2000 yr [Prueher and Rea, 1998]) casts doubt on the idea of this process being a direct response to orbital forcing or tectonic processes. Therefore, some studies consider climate forcing mechanisms on decadal to millennial timescales – such as volcanic activity – to have triggered Greenland ice-sheet expansion (Kennett and Thunnell, 1975; Kennett et al., 1977; Prueher and Rea, 1998). Data from Ocean Drilling Program Leg 145 indeed document an increase in massive explosive volcanism in North Pacific volcanic arcs at a time identical with iNHG (~2.67 Ma) (Prueher and Rea, 1998). An increase in volcanic dust concentration in the atmosphere and the resulting dimming of incoming solar insolation may thus have contributed to Northern Hemisphere cooling (Prueher and Rea, 1998).

Orbital forcing. Long-term variations in Earth's orbit and rotation are widely accepted as fundamental causes for Pleistocene ice ages, with changes in latitudinal and seasonal insolation being key factors for the global climate system (Milankovitch, 1941). For a glaciation to develop, Milankovitch's astronomical theory requires low summer insolation to prevent winter snow accumulations from melting – a scenario given in times of high-amplitude obliquity (Milankovitch, 1941). Accordingly, the increase in the amplitude of obliquity cycles as documented for ~3–2.5 Ma (Figure 2.2c) is hypothesized to have initiated the onset of substantial NHG (Maslin et al., 1995; Haug and Tiedemann, 1998; Maslin et al., 1998). In addition, a sharp rise in the amplitude of precession, closely matching insolation at 60°N, at ~2.8–2.55 Ma (Figure 2.2c) may have forced rapid ice-sheet buildup in the Northern Hemisphere (Maslin et al., 1998).

However, it has been hypothesized that orbital forcing alone cannot have been the primary cause for iNHG: Instead, a combination of below-mentioned preconditions in concert with a favorable orbital configuration may have initiated the onset of strong glaciations in the Northern Hemisphere (Raymo, 1994; Maslin et al., 1998). Recently published modeling data (Willeit et al., 2015) support this hypothesis, indicating that the abrupt intensification of Northern Hemisphere Glaciation ~2.7 Ma ago may have been due to a threshold behavior of

ice sheets in response to both orbital forcing and a gradual pCO_2 decrease (see below for details).

Changes in the configuration of oceanic gateways

The opening and closing of oceanic gateways exerts strong influence on oceanic and atmospheric circulation patterns and thus on Earth's climate (e.g., Keigwin, 1982; Maier-Reimer et al., 1990; Groeneveld et al., 2014). For many years, the tectonically driven closure of the Central American Seaway (CAS) and the restriction of the Indonesian Seaway have been discussed as triggers for the onset and expansion of Greenland glaciation (Keigwin, 1982; Haug and Tiedemann, 1998).

Central American Seaway. A key factor for building up and maintaining ice sheets is an adequate moisture source. Several studies suggest that CAS closure might have strengthened the Atlantic Meridional Overturning Circulation and increased North Atlantic temperatures and evaporation, thereby providing an adequate moisture source for the high northern latitudes (e.g. Stokes, 1955; Keigwin, 1982; Haug and Tiedemann, 1998; Lunt et al., 2008b). These feedback mechanisms require the CAS to be effectively closed with respect to its influence on deep-ocean circulation. However, the cutoff of deep-water connections between the east Pacific and the Caribbean Sea occurred in the mid-Miocene (Sepulchre et al., 2014) to early Pliocene (Frank et al., 1999); this significantly pre-dates iNHG, which by extension argues against CAS closure having been responsible for Greenland glaciation. Regardless of the timing, results from a coupled ocean-atmosphere general circulation model experiment indicate only a minor Greenland ice-volume response to CAS closure that is equivalent to a ~5 cm sea-level difference in the "closed" *versus* "open" CAS scenario (Lunt et al., 2008b).

Indonesian Seaway. The restriction of the Indonesian Seaway together with a northward drift of New Guinea ~4–3 Ma ago has repeatedly been considered a possible precondition (albeit not an ultimate cause) for the onset of NHG (Cane and Molnar, 2001; Karas et al., 2009). The closure of the Indonesian Seaway may have altered atmospheric and oceanic circulation pattern over the Pacific Ocean (Cane and Molnar, 2001; Karas et al., 2009). Specifically, the closure of the Indonesian Seaway may have caused a cooling and shoaling of the thermocline in the tropical Indian Ocean, and contributed to the global thermocline shoaling recorded for the Pliocene (Philander and Fedorov, 2003; Wara et al., 2005; Steph et al., 2006). This led to the development of the east Pacific "cold tongue" and enhanced the tropical Pacific sea-surface temperature gradient (see Chapters 3 and 5 for details). It has been further speculated

that this change in equatorial Pacific surface-water structure may have strengthened the tropical Pacific Walker Circulation and reduced poleward heat transport, thereby favoring high-latitude cooling and the buildup of extensive Northern Hemisphere ice sheets (Cane and Molnar, 2001).

North Pacific Ocean stratification and moisture supply

An abrupt productivity crash in the subarctic North Pacific Ocean at ~2.7 Ma as evidenced by a decrease in opal accumulation has been interpreted to result from an increase in water-column stratification, possibly caused by autumn surface-ocean warming (e.g., Haug et al., 1999; Haug et al., 2005). The associated evaporation increase over the North Pacific Ocean provided an adequate moisture source for the accumulation of snow over Greenland (Haug et al., 2005). Furthermore, suppressed upwelling in a well-stratified North Pacific water column isolated CO_2-rich deep-waters from ocean-atmosphere CO_2 exchange processes, thereby decreasing pCO_2 by 30–40 ppmv, which favored global cooling (Haug et al., 1999; Sigman et al., 2004).

Termination of "permanent El Niño-like conditions"

In the Pliocene the Pacific warm pool was greatly expanded relative to today, giving rise to a surface-ocean temperature field akin to modern El Niño conditions (therefore often referred to a "permanent El Niño-like state" [e.g., Wara et al., 2005; Fedorov et al., 2015]). The iNHG marks the transition from this warm Pliocene climate state to a climate state that approximates modern conditions with strong upwelling in the east of the basin and more developed zonal temperature and primary productivity gradients (e.g., Ravelo et al., 2004; Wara et al., 2005; Bolton et al., 2010a) (for details see Chapter 5). A "permanent El Niño-like state" prior to ~3 Ma could have prevented ice-sheet growth in the high northern latitudes: Latent heat released in the tropical Pacific during such climatic conditions produced, through atmospheric teleconnections, warming over North America, which may have helped to maintain this region ice-free (Barreiro et al., 2005). Accordingly, the termination of "permanent El Niño-like conditions" would have provided increasingly favorable conditions for ice buildup in the Northern Hemisphere (Philander and Fedorov, 2003; Barreiro et al., 2005).

Reduction of atmospheric CO_2

The most generally accepted cause for iNHG is a drawdown of atmospheric CO_2 (DeConto et al., 2008; Lunt et al., 2008a; Willeit et al., 2015). Model simulations indicate that glaciations

occur in the Northern Hemisphere when pCO_2 drops below a threshold value (~280 ppmv [DeConto et al., 2008]); a value much lower than that required for Antarctica glaciations (~750 ppmv [DeConto et al., 2008]). This hypothesis is supported by alkenone- and boron-based pCO_2 estimates that demonstrate a gradual decrease from pCO_2 levels on the order of 350–450 ppmv during the early Pliocene to concentrations similar to pre-industrial times (250–300 ppmv) at about ~2.4 Ma (e.g., Seki et al., 2010; Martinez-Boti et al., 2015) (Figure 2.2b). A reduction in pCO_2 could have caused global cooling and thus increasingly favorable conditions for the expansion of ice sheets in the Northern Hemisphere.

Modeling efforts indicate that climatic shifts solely associated with changes in oceanic gateway configuration or the termination of "permanent El Niño-like conditions" as discussed above were not sufficient to significantly contribute to Northern Hemisphere ice-sheet expansion, while cooler summer temperatures under low pCO_2 conditions may have driven increasing Greenland glaciation (Lunt et al., 2008a). Under favorable orbital configuration, a decline in pCO_2 from high early Pliocene values to lower values of the Quaternary therefore appears as the most likely factor responsible for the onset of extensive NHG (DeConto et al., 2008; Lunt et al., 2008a; Willeit et al., 2015).

The process behind the hypothesized CO_2 removal from the atmosphere in the late Pliocene is, however, still debated. Possible mechanisms include (i) enhanced chemical weathering during the uplift of the Tibetan-Himalayan Plateau (e.g., Raymo et al., 1988; Raymo and Ruddiman, 1992), although the elevation of the Tibetan-Himalayan Plateau may have remained unchanged at least since 8–15 Ma (Harrison et al., 1992; Spicer et al., 2003), and (ii) reduced upwelling in a well-stratified North Pacific Ocean at ~2.7 Ma (Haug et al., 1999; Sigman et al., 2004) (see above).

2.2 Foraminifera as paleoclimatic and paleoceanographic proxies

Paleoclimatic and paleoceanographic proxies are measurable parameters for unobservable environmental variables of the past. The isotopic and elemental composition of calcareous shells of microfossils, for example, delivers such valuable paleoceanographic information (Fisher and Wefer, 1999).

Over the recent past, benthic and planktic foraminifera have become one of the most important biotic proxy carriers for paleoenvironmental reconstruction (e.g., Rohling and Cooke, 1999; Ravelo and Hillaire-Marcel, 2007) (Chapter 2.2.1). For example, the chemical

composition of foraminiferal tests (e.g., stable oxygen [$\delta^{18}O$] and carbon [$\delta^{13}C$] isotopes, Mg/Ca ratios) is commonly used to reconstruct past water-mass characteristics such as temperature and salinity, to estimate ice volume/sea level and/or to identify different water masses (e.g., Emiliani, 1955; Nürnberg et al., 1996; Rohling and Cooke, 1999; Bolton et al., 2010c; Friedrich et al., 2013) (Chapter 2.2.2). The species composition of planktic foraminiferal assemblages is often used to reconstruct surface-water conditions such as temperature, salinity or primary productivity (e.g., Hemleben et al., 1989; Kucera et al., 2005; Friedrich et al., 2008b), while benthic foraminiferal assemblages are used to estimate bottom-water oxygen concentration or prevailing water masses (e.g., Jorissen et al., 1995; Friedrich and Hemleben, 2007). This wide array of possible applications highlights why foraminifera are frequently used as a micropaleontological and geochemical tool in paleoceanographic, paleoecologic and paleoclimatic studies.

2.2.1 Ecology of benthic and planktic foraminifera

Foraminifera are unicellular, sand-sized protists with calcitic or agglutinated shells (so-called "tests") that are commonly composed of 10–20 chambers in the adult stage (Sen Gupta, 1999a; Schiebel and Hemleben, 2005). Foraminifera are highly diverse – to date, the number of extant foraminiferal species is estimated to be about 10,000 (Vickermann, 1992). The majority of modern foraminifera are benthic, and only 40–50 planktic species exist (Vickermann, 1992). Foraminifera occur in large numbers across a wide range of marine environments from the tropics to the poles (Bé, 1977) and from the sea surface to the deep seafloor (Arnold and Parker, 1999; Culver and Buzas, 1999). Therefore, above the carbonate compensation depth a vast area of the ocean's seafloor is composed of foraminiferal tests. The widespread spatiotemporal abundance from the Cambrian onward (Sen Gupta, 1999b) makes foraminifera uniquely useful for paleoceanographic and biostratigraphic studies of modern and past marine environments. In addition, the biology and ecology of modern foraminifera is well understood (for details see below). Therefore, foraminifer-based empirical calibrations (i.e., measuring chemical parameters of a recent foraminiferal species while simultaneously observing ambient environmental variables associated with its habitat [Kucera, 2007]) allow to reliably reconstruct past climates.

Benthic foraminifera

Benthic foraminifera are the most important component of the marine meiofauna (size between 45 µm and 1 mm) as they make up to 80% of the meiofaunal biomass (Snider et al.,

1984). They are heterotrophic organisms that inhabit all marine ecosystems from the intertidal zone to the deep ocean. Benthic foraminifers are most common at the sediment-water interface (epifaunal) or in the uppermost centimeters of the sediment column (shallow infaunal). There are also species that penetrate into 10 cm (up to 30 cm) sediment depth (deep infaunal) (Murray, 1991).

The distribution of benthic foraminifera in past and modern oceans is mainly regulated by the oxygen concentration of bottom waters and the nutrient availability, while bottom-water temperature and salinity are of minor importance (van der Zwaan, 1999). The connection between food availability, oxygen content and benthic foraminiferal abundance pattern is summarized in the so-called TROX ("TRophic OXygen") model (Jorissen et al., 1995) (Figure 2.3). Thereafter the limiting factor for benthic foraminiferal distribution is oxygen in eutrophic ecosystems, and is food supply (i.e., the flux of particulate organic matter from the upper ocean to the seafloor) in oligotrophic ecosystems.

In principle, benthic foraminifera are characterized by (i) a widespread abundance in space and time (at least since the late Precambrian ~635 Ma ago [Pawlowski et al., 2003; Bosak et al., 2011]), (ii) a high morphological diversity (recently ~10,000 species [Vickermann, 1992]), (iii) a narrow ecological tolerance of single species and (iv) good preservation

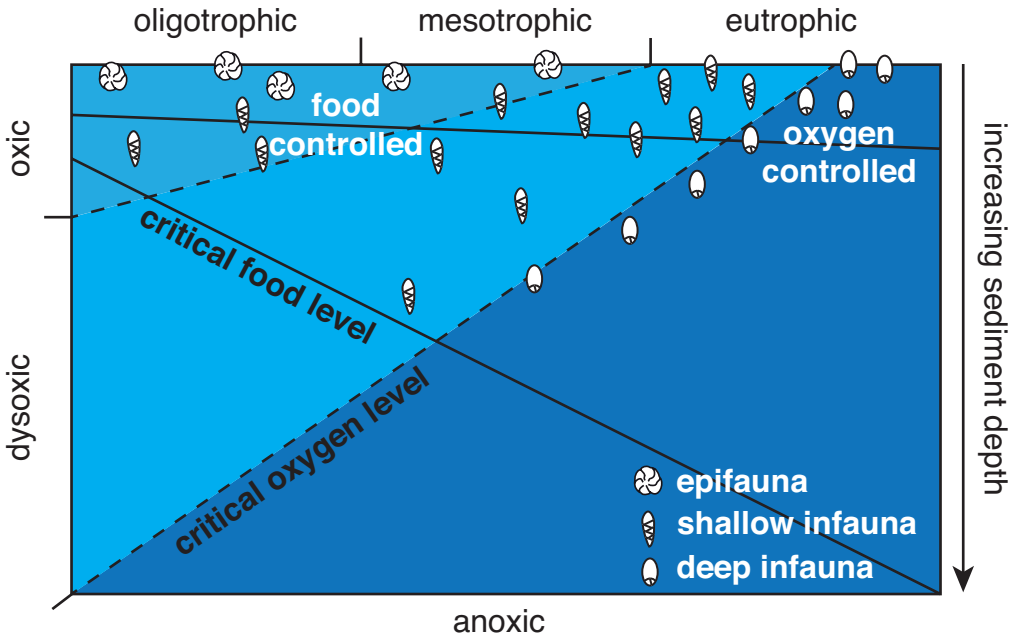

Figure 2.3. TROX (TRophic OXygen) model after Jorissen et al. (1995), explaining a benthic foraminiferal microhabitat by oxygenation and food availability: The penetration depth of benthic foraminiferal species in eutrophic ecosystems is limited by oxygen, while, vice versa, food availability is the controlling factor for the microhabitat of benthic foraminifera in dysoxic to anoxic environments.

potential (see Chapter 2.2.2 for details). These characteristics underscore why benthic foraminiferal proxy data are commonly used for paleoceanographic and paleoenvironmental studies (e.g., Friedrich et al., 2008a; Sosdian and Rosenthal, 2009; Lear et al., 2015).

Planktic foraminifera

Although planktic foraminifera constitute only a minor percentage of the total living marine zooplankton (Vickermann, 1992), the constant deposition of empty shells on the seafloor – in principle in regions of high productivity – contributes substantially to the formation of deep-sea biogenic carbonates (Hemleben et al., 1989). However, as a consequence of dissolution in the water column and at the sediment-water interface only ~25% of the initially produced planktic foraminiferal tests settle on the seafloor (Schiebel, 2002). Nevertheless, the contribution of planktic foraminifers to the global deep-marine carbon budget is substantially higher (32%–80%) than the contribution of coccolithophores (~12%), pteropods (~10%) or calcareous dinoflagellates (~3.5%) (Schiebel, 2002, and references therein) (Figure 2.4). This highlights why planktic foraminifera are the most common source of paleoceanographic proxies (Kucera, 2007).

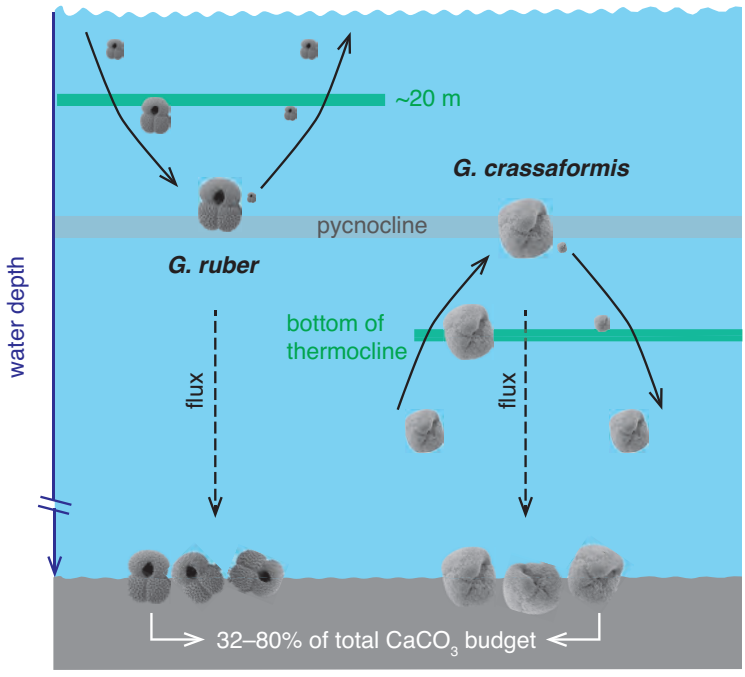

Figure 2.4. Schematic illustration of life cycles of surface-dwelling (e.g., *Globigerinoides ruber*) and deep-dwelling (e.g., *Globorotalia crassaformis*) planktic foraminifers in an open marine environment after Schiebel and Hemleben (2005). Green bars highlight the assumed average depth habitats of *G. ruber* and *G. crassaformis*. Reproduction (i.e., the release of 200,000 to 400,000 gametes) likely occurs close to the pycnocline (grey bar) where food availability is high. Shallow-dwelling species reproduce once to twice per month triggered by the lunar cycle (Bijma et al., 1990a). Deep-dwelling species reproduce less often, but at least once per year (Hemleben et al., 1989). After reproduction, empty adult tests sink to the seafloor, contributing by 32–80% to the global $CaCO_3$ budget (Schiebel, 2002).

Modern species of planktic foraminifera can be grouped into five main assemblages that define tropical, subtropical, temperate, subpolar and polar provinces (Bé and Tolderlund, 1971; Hemleben et al., 1989). The distribution depends on surface-water properties, physiological requirements, and food preferences, but sea-surface temperature appears to be the most important factor (Bé and Tolderlund, 1971; Bijma et al., 1990b). Although planktic foraminifera tolerate a large temperature range, their highest abundances are usually restricted to a narrow (i.e., optimum) temperature zone (Kucera et al., 2005; Kucera, 2007). The abundance of recent planktic foraminiferal species can be empirically calibrated to environmental variables such as temperature, which is why fossil planktic foraminiferal assemblages can be statistically analyzed and used, for example, for paleotemperature reconstructions (Kucera et al., 2005; Kucera, 2007).

The chemical composition of planktic foraminiferal tests strongly depends on temperature (and other water-mass characteristics) of the ambient seawater. Therefore, this group has been widely used in paleoceanographic and paleoclimatic studies. It is, however, essentially important to take species-specific depth habitats (Figure 2.4) and seasonal abundances into account when interpreting planktic foraminifer-based proxy records, as briefly outlined in the following.

Studies on shell fluxes of modern planktic foraminifera indicate that particularly temperate to cold-water species in mid to high latitudes show a distinct seasonal flux pattern (Fraile et al., 2009; Jonkers and Kučera, 2015). The abundance of planktic foraminifers generally follows the overall primary productivity pattern (Schiebel and Hemleben, 2005, and references therein). In polar regions, for example, foraminifera are most abundant during summer when light and temperature conditions allow for high primary productivity rates. For temperature reconstructions, this can lead to offsets from actual mean annual conditions by several degrees (Fraile et al., 2009). In contrast, in low-latitude settings, seasonality is low due to high year-round temperature and light intensity; here the amount of planktic foraminifera rather depends on regional conditions such as upwelling intensity that controls primary productivity rates (see Chapter 4 for details).

Moreover, it is well known that planktic foraminiferal species are adapted to different depth habitats depending on species-specific preferences such as water temperature, oxygen concentration, food availability or light intensity (e.g., Wilke et al., 2009; Pados and Spielhagen, 2014). Whenever the vertical habitat-depth preference of a species is known, this provides the opportunity to reconstruct the biochemical state and hydrography of the water

column by using multiple species from different depths. However, heterogeneities in the chemical composition (e.g., Mg/Ca and $\delta^{18}O$) of tests of a single species related to its size have been observed. These heterogeneties result from depth migrations as a function of ontogeny (Eggins et al., 2003; Friedrich et al., 2012; Steinhardt et al., 2015). For instance, surface-dwelling species migrate for reproduction to greater depth levels compared to the water depth they usually inhabit. In contrast, deep dwellers reproduce in lower depths compared to their average habitat depth (Schiebel and Hemleben, 2005). Hence, the geochemical signature of a complete test reflects an integrated signal of different water depths experienced across the entire ontogenetic cycle of a specimen (Hemleben and Bijma, 1994) (Figure 2.4).

2.2.2 Foraminifer-derived geochemical proxies in paleoceanography

The stable-isotope composition of foraminiferal tests is an important proxy for the reconstruction of paleoclimatic and paleoceanographic changes, and for global stratigraphic correlation. For instance, the carbon-isotope composition of foraminiferal calcite allows to track shifts in ocean circulation and paleoproductivity (Zahn et al., 1986; Mackensen and Bickert, 1999). Planktic and benthic foraminiferal oxygen-isotope records are commonly used as a global correlation and dating tool (Lisiecki and Raymo, 2005; Wang et al., 2010). While benthic foraminiferal oxygen-isotope records approximate sea-level variations that are primarily controlled by ice-volume (Lisiecki and Raymo, 2005), paired benthic foraminiferal Mg/Ca and oxygen-isotope analysis enables quantitative reconstruction of past deep-ocean temperature and sea-level variability (Sosdian and Rosenthal, 2009). Applying the same approach to planktic foraminiferal calcite allows to quantitatively reconstruct surface-ocean temperatures and to estimate relative surface-ocean salinity variability (Friedrich et al., 2013; Groeneveld et al., 2014).

The utilization of foraminiferal calcite for accurate paleoceanographic reconstructions, however, requires that tests are precipitated in equilibrium with the ambient seawater and that the initial geochemical signature has not been affected by diagenetic processes (compare Rohling and Cooke, 1999; Ravelo and Hillaire-Marcel, 2007). In the following, the fundamental controls on foraminiferal $\delta^{18}O$, $\delta^{13}C$ and Mg/Ca, and their implications for paleoceanographic interpretations are summarized.

Foraminiferal oxygen isotopes as paleoceanographic proxy

The application of stable oxygen isotopes in marine carbonates plays an invaluable role in paleoclimatologic and paleoceanographic research. This dates back to the work of Urey (1947) and the idea of using oxygen isotopes of a calcitic shell to determine its calcification temperature. In the 1950's, foraminiferal oxygen isotopes were first used for paleotemperature reconstructions (Emiliani, 1955). Soon it became clear, however, that the oxygen-isotope composition of marine carbonates (including benthic or planktic foraminifera) is not only controlled by seawater temperature, but also – as outlined in the following – by the oxygen-isotope composition of seawater ($\delta^{18}O_{sw}$), itself in turn a function of global ice volume and salinity (compare Ravelo and Hillaire-Marcel, 2007) (Figure 2.5).

The oxygen-isotope composition of seawater is strongly controlled by local and global fractionation processes within the hydrological cycle, mainly evaporation, atmospheric vapor transport, precipitation, and freshwater runoff (compare Rohling and Cooke, 1999; Ravelo and Hillaire-Marcel, 2007). During evaporation, water molecules composed of lighter isotopes ($H_2{}^{16}O$) preferentially turn into gas phase, while heavier molecules ($H_2{}^{18}O$) remain in seawater, causing a local enrichment of $\delta^{18}O$ in the ambient surface water. Salinity increases during evaporation – a change of 0.5‰ in mean global surface-water $\delta^{18}O$ is commonly interpreted to represent a 1.0 psu (practical salinity unit) change in average global seawater salinity (Ravelo and Hillaire-Marcel, 2007; Rohling, 2007). This relationship demonstrates the potential of oxygen isotopes for the reconstruction of paleosalinity (see Craig and Gordon, 1965; Benway et al., 2006), which, however, largely differs locally (an adjustment developed by Zachos et al. [1994] allows to account for latitudinal variations in seawater $\delta^{18}O$).

Fractionation processes during precipitation are principally the same as during evaporation, but work in the opposite direction (compare Rohling and Cooke, 1999). When water droplets are formed from atmospheric vapor, isotopically heavier molecules ($H_2{}^{18}O$) are removed and the remaining vapor becomes enriched in lighter molecules ($H_2{}^{16}O$). Thus, at or near the source region, the isotopic composition of condensed water droplets is similar to that of the original seawater. With increasing latitude, that is a longer pathway from the source area, the isotopic composition of the atmospheric vapor becomes progressively more depleted through ongoing precipitation, culminating in $\delta^{18}O$-depleted rain or snow in high latitudes compared to the tropics ("Rayleigh distillation process").

In light of the above, the waxing and waning of ice sheets must have an affect on seawater $\delta^{18}O$: Growing ice sheets are isotopically depleted with respect to $\delta^{18}O$, while the ocean

becomes isotopically enriched. For instance, modern ice sheets yield values of -34 to -36‰ (Greenland) to more extreme values of -40 to -50‰ (Antarctica) (Duplessy et al., 2002; Lhomme and Clarke, 2005). Present-day seawater has a $\delta^{18}O$ value of 0‰ by definition (Craig, 1961), while during the Last Glacial Maximum ~21 ka ago, for example, mean global $\delta^{18}O_{sw}$ was ~1‰ higher compared to modern values (Adkins et al., 2002; Duplessy et al., 2002). Since changes in global ice volume are directly linked to global sea level, $\delta^{18}O_{sw}$ can be used to estimate past sea-level changes: An increase of 0.11‰ in $\delta^{18}O_{sw}$ approximates a 10 m sea-level drop during the Pleistocene period (Fairbanks and Matthews, 1978).

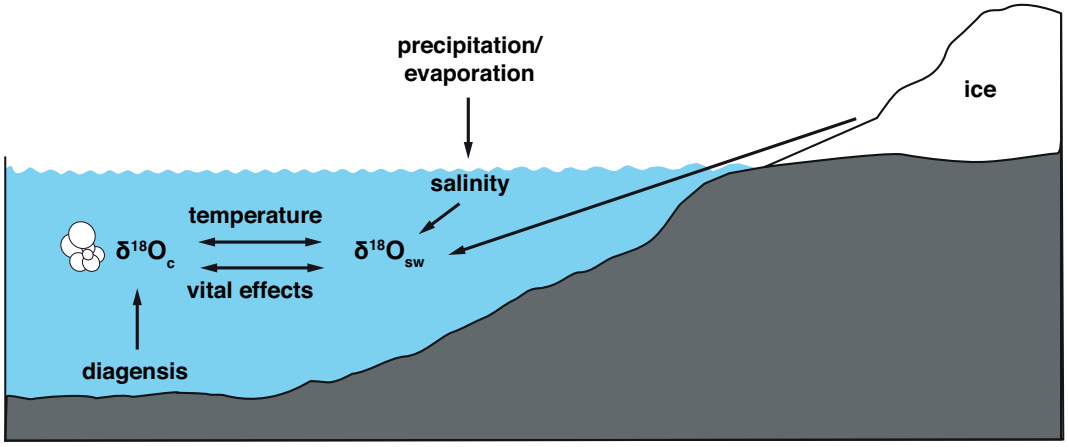

Figure 2.5. Main factors influencing the oxygen-isotope composition of foraminiferal carbonate ($\delta^{18}O_c$) (see text for references). Vital effects include the symbiont photosynthesis effect, the gametogenic calcite effect, the ontogenetic effect, and the carbonate-ion effect.

The early idea of using foraminiferal calcite as a proxy for ocean temperature is based on the assumption that tests are precipitated in isotopic equilibrium with ambient seawater, and that the fractionation of oxygen isotopes between water and foraminiferal carbonate strongly depends on the surrounding temperature. A ~0.21–0.23‰ decrease in foraminiferal $\delta^{18}O$ is commonly interpreted to represent a 1°C temperature increase (compare Ravelo and Hillaire-Marcel, 2007). Hence, whenever $\delta^{18}O_{sw}$ is known, foraminiferal $\delta^{18}O$ can be used as a "isotopic paleothermometer" (Bemis et al., 1998 and references therein). Vice versa, the oxygen-isotope composition of seawater and thus sea level can be reconstructed when the seawater temperature is known, i.e., using a multi-proxy approach including, for instance, benthic $\delta^{18}O$ and Mg/Ca (e.g., Sosdian and Rosenthal, 2009; see also Chapter 6).

Foraminiferal oxygen isotopes are widely used in paleoceanographic studies, although there is evidence that a great variety of planktic and some benthic foraminiferal species do not calcify in thermodynamic equilibrium with ambient seawater notably because of "vital effects" (Duplessy et al., 1970). The amount of deviation from isotopic equilibrium varies between

species (Duplessy et al., 1970). For some species this value is known such that measured $\delta^{18}O$ (and $\delta^{13}C$) can be corrected (Table 2.1). The most important vital effects that have the potential to alter foraminiferal $\delta^{18}O$ are briefly discussed in the following.

Ontogenetic effect. A critical aspect when analyzing the oxygen-isotope composition of foraminiferal tests is the species-specific test-size-$\delta^{18}O$-relationship. For planktic foraminifera, both a progressive increase in $\delta^{18}O$ (e.g., for *Globorotalia crassaformis*) (e.g., Spero and Lea, 1996; Elderfield et al., 2002) as well as a $\delta^{18}O$ decrease (e.g., for *Globigerinoides ruber*) (Friedrich et al., 2012) with increasing test size have been observed. To avoid such ontogenetic effects, only a narrow size fraction should be used for planktic foraminiferal $\delta^{18}O$ analysis (e.g., Friedrich et al., 2012). Instead, the $\delta^{18}O$ composition of epibenthic foraminiferal tests (such as the species *Oridorsalis umbonatus* and *Cibicidoides wuellerstorfi*) appears to be less sensitive to ontogeny (Corliss et al., 2002; Franco-Fraguas et al., 2011).

Symbiont photosynthesis effect. Although less than 10% of ~150 families of foraminifera bear algal endosymbionts, these families provide ~20% of the present-day global carbonate production and are therefore an intensively studied group (Hallock, 1999, and references therein). Common symbionts are dinoflagellates and chrysophycophytes, influencing the $\delta^{18}O$ of its foraminiferal host as follows: Increased CO_2 consumption by symbionts for photosynthesis most probably favors rapid skeletogenesis and a depletion in foraminiferal $\delta^{18}O$ relative to the ambient seawater (e.g., Spero and Lea, 1993). Furthermore, an increased symbiont-density (that is enhanced photosynthesis) with test size has been documented to additionally deplete respective foraminiferal $\delta^{18}O$ during advanced ontogenetic states (e.g., Spero and Parker, 1985).

Gametogenic calcite effect. Specific planktic foraminiferal species mantle their complete test surface with gametogenic calcite before gamete release at the end of their life cycle (e.g., Spero and Lea, 1993; Bemis et al., 1998). Since the usually strongly $\delta^{18}O$-enriched gametogenic calcite forms up to one fourth of the shell mass (e.g., Bé, 1980; Bouvier-Soumagnac and Duplessy, 1985), it has a major impact on the total $\delta^{18}O$ signature of a test. Gametogenic calcite can be easily identified by scanning electron microscopy as it, for example, covers pores in the case of perforate foraminifers.

Carbonate-ion effect. The carbonate-ion concentration of seawater [CO_3^{2-}], thus seawater pH, most probably affects the $\delta^{18}O$ signature of foraminiferal tests. Culturing experiments on planktic foraminiferal species demonstrate decreasing $\delta^{18}O$ values of tests during times of

increased [CO_3^{2-}] and pH (Spero et al., 1997), such as during glacials (Saynal et al., 1995). The magnitude of this relationship is species-specific (Spero et al., 1997).

Table 2.1. Deviation from oxygen and carbon isotopic equilibrium between foraminiferal tests and ambient seawater for selected species.

Species	$\delta^{18}O$ correction	$\delta^{13}C$ correction
O. umbonatus	close to equilibrium (Graham et al., 1981; Shackleton et al., 1984b)	close to equilibrium (Wendler et al., 2013)
C. wuellerstorfi	+0.64‰ (Shackleton et al., 1984b)	close to equilibrium (Zahn et al., 1986; Mackensen et al., 1993)
G. crassaformis	lack of laboratory investigations	
G. ruber (white)	close to equilibrium (Koutavas and Lynch-Stieglitz, 2003)	+0.94‰ (Spero et al., 2003)

Foraminiferal oxygen isotopes as stratigraphic proxy

Time series of foraminiferal $\delta^{18}O$ provide important information on climate change. Owing to the observed similarity of most marine $\delta^{18}O$ records during the past 5 Myr and the global ice-volume signal, $\delta^{18}O$ time series are an important stratigraphic tool by providing the opportunity to place marine climate records on a common timescale (Lisiecki and Raymo, 2005). For this purpose, so-called "stacks" are used, which are averages of single foraminiferal $\delta^{18}O$ records from multiple site locations (Lisiecki and Raymo, 2005; Wang et al., 2010). The most widely used stack is the so-called "LR04 stack" (Lisiecki and Raymo, 2005) (Figure 2.2b). This stack contains benthic foraminiferal $\delta^{18}O$ measurements of *Uvigerina peregrina* and *Cibicidoides wuellerstorfi* from 57 globally distributed sites at orbital-scale resolution (2.5 kyr) spanning the past 5.3 Myr. The LR04 stack is commonly applied for age control in Plio-Pleistocene studies (e.g., Lawrence et al., 2006; Bailey et al., 2010; Bolton et al., 2010c) (see also Chapters 4 and 5).

Foraminiferal carbon isotopes as paleoceanographic proxy

Among the application of oxygen isotopes as a paleoceanographic and paleoclimatic proxy, carbon isotopes of foraminiferal tests have also become a major and widely used tool in paleoceanographic research. The carbon-isotope signature of tests precipitated by foraminifera depends on the isotopic composition of dissolved inorganic carbon in seawater at the point of calcification, which can be used to track shifts in ocean circulation and paleoproductivity (Duplessy et al., 1984) (see also Chapter 4). As outlined in the following,

the carbon-isotope composition of dissolved inorganic carbon in seawater is controlled by several (global and regional) factors of the carbon cycle, including the balance between photosynthesis and respiration (thus the rate of biological production), the amount of organic matter remineralization (deep-water "age"), the atmospheric $\delta^{13}C$ composition, and the amount of carbon stored in geologic reservoirs (compare Rohling and Cooke, 1999; Ravelo and Hillaire-Marcel, 2007) (Figure 2.6).

In general, several fractionation processes during photosynthesis favor the preferential uptake of lighter $^{12}CO_2$ molecules by phytoplankton in sea-surface waters and likewise by vegetation on continents (e.g., Park and Epstein, 1960). With regard to the marine environment, organic matter formed during photosynthesis is strongly depleted in $\delta^{13}C$, whereas ambient surface waters become strongly enriched. Carbonates formed in this water mass, such as planktic foraminifera, reflect this $\delta^{13}C$-enriched signature and are therefore often used as a proxy for local surface-ocean primary productivity (e.g., Zahn et al., 1986; Sarnthein et al., 1988; Mackensen and Bickert, 1999). Whenever organic matter formed in surface waters sinks toward the seafloor, it releases the previously incorporated depleted $\delta^{13}C$ signature during remineralization. This will be recorded by calcifying organisms living in the deep sea such as benthic foraminifera. Thereafter, the benthic-planktic $\delta^{13}C$ difference can be used to measure the strength of the so-called "biological pump" (e.g., Zahn et al., 1986; Sarnthein et al., 1988; Mackensen and Bickert, 1999). During times with a strong biological pump or enhanced (export) productivity, the local surface-to-deep sea $\delta^{13}C$ gradient increases.

The $\delta^{13}C$ signature reported by benthic foraminifera, however, is also influenced by the $\delta^{13}C$ composition of the prevailing deep-water mass. Deep-water masses are commonly sourced in high latitudes where surface water cools and sinks. On the pathway to lower latitudes, the water mass ages and becomes progressively depleted compared to its initial $\delta^{13}C$ signature due to ongoing remineralization. Accordingly, the $\delta^{13}C$ signature reported by benthic foraminifera can be also used to identify different water masses and to reconstruct oceanic circulation pattern and water-mass pathways (Duplessy et al., 1984; Mackensen et al., 2001; Curry and Oppo, 2005).

Through equilibration between sea-surface water and atmosphere, temporal variability in the atmospheric $\delta^{13}C$ composition is another controlling factor for seawater $\delta^{13}C$. Temporal variations in atmospheric $\delta^{13}C$ occur on different timescales such as seasonal or G-IG, or respond to a single event, such as the anthropogenic combustion of fossil fuels. With regard on G-IG cycles, the size of the terrestrial biosphere increases during interglacials so that a

larger amount of ^{12}C is stored on land compared to glacials (see above), thus resulting in enriched atmospheric and, through equilibration, seawater $\delta^{13}C$ (Berger and Vincent, 1986). The same mechanism holds true for seasonal fluctuations, only with smaller amplitudes between winter and summer $\delta^{13}C$.

Since marine organic material is commonly concentrated in shelf areas and basin margins (Pelet, 1987), it has been suggested that a change in sea-level also has an influence on the $\delta^{13}C$ composition of seawater (Voigt and Hilbrecht, 1997; Jarvis et al., 2006). During sea-level fall, marine erosion of previously deposited sediments and exposure of basin margins led to reduced organic-carbon burial in marine reservoirs and oxidation of previously deposited organic matter, which causes seawater $\delta^{13}C$ values to fall (Jarvis et al., 2006).

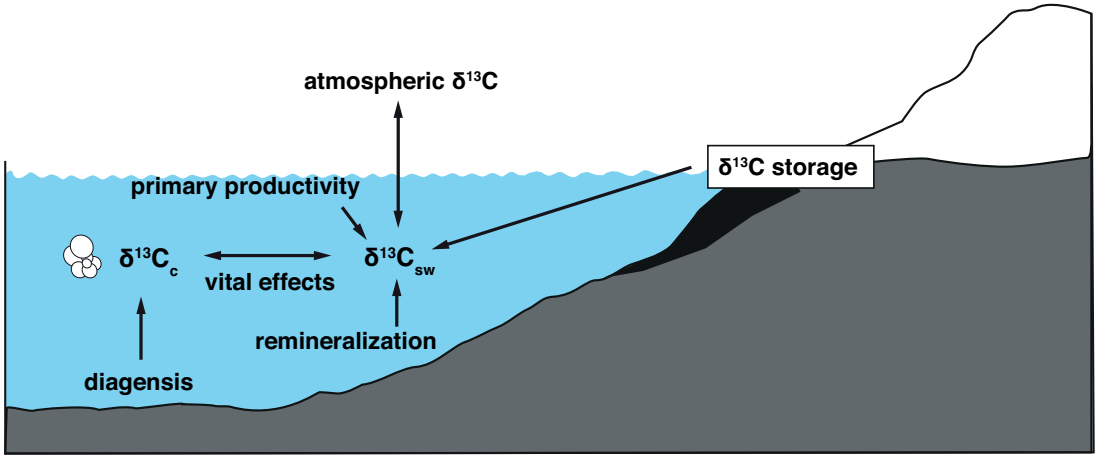

Figure 2.6. The carbon-isotope composition of foraminiferal carbonate ($\delta^{13}C_c$) (see text for references). Vital effects are related to metabolic CO_2, symbiont photosynthesis, ecology, and the carbonate-ion concentration.

Apart from the $\delta^{13}C$ value of seawater that is influenced by several factors and controls the $\delta^{13}C$ signature of a foraminiferal test, other factors influence the foraminiferal $\delta^{13}C$ signal during calcification. Multiple kinetic fractionation processes cause an offset between $\delta^{13}C$ of the "internal foraminiferal carbon pool" and actual seawater $\delta^{13}C$ as follows (compare Rohling and Cooke, 1999; Ravelo and Hillaire-Marcel, 2007) (see also Table 2.1):

Metabolic CO_2. The utilization of isotopically light metabolic CO_2 during shell formation seems to contribute to deviations from equilibrium between foraminiferal calcite and ambient seawater $\delta^{13}C$. The amount of established disequilibrium largely depends on the metabolic rate. During early life stages, high metabolic rates cause $\delta^{13}C$-depleted shell signatures, whereas during later growth stages lower metabolic rates favor a precipitation closer to equilibrium (e.g., Bouvier-Soumagnac and Duplessy, 1985).

Symbiont photosynthesis. Symbionts in planktic foraminifera preferentially take use of isotopically lighter $^{12}CO_2$ molecules for photosynthesis. Therefore, the microenvironment in which a symbiont-bearing organism calcifies is $\delta^{13}C$-enriched compared to the microenvironment of its non-symbiont-bearing counterpart (Spero and Williams, 1988; McConnaughey, 1989). Thus, calcite of a symbiont-bearing foraminifer typically yields higher $\delta^{13}C$ values than a test of a non-symbiont-bearing species.

Ecology. In symbiont-bearing species, the symbiont density has been observed to increase with test size (Spero and Parker, 1985) such that each new chamber is calcified under progressively higher $\delta^{13}C$ values (see above). The size-related photosynthesis effect is, however, weakened due to the suggested migration of growing symbiont-bearing foraminiferal species to progressively deeper habitats with in general lower $\delta^{13}C$ values related to the biological pump (Ravelo and Fairbanks, 1995) (see also Figure 2.4).

Carbonate-ion concentration or seawater pH. Similar to $\delta^{18}O$ (see above), the carbonate-ion concentration of seawater, thus seawater pH, affects the foraminiferal carbon-isotope composition. Laboratory experiments demonstrate that foraminiferal $\delta^{13}C$ decreases with increasing $[CO_3^{2-}]$ and that the magnitude of this relationship is species-specific (Spero et al., 1997).

Foraminiferal Mg/Ca ratio as paleoceanographic proxy

First evidence for a relationship between Mg/Ca ratios of foraminiferal tests and seawater temperature has been documented in the 1970's (Savin and Douglas, 1973; Bender et al., 1975). During the 1990's, several empirical and culture studies on marine carbonates like ostracodes (Dwyer et al., 1995), corals (Mitsuguchi et al., 1996) or foraminifera (e.g., Nürnberg et al., 1996; Lea et al., 1999; Mashiotta et al., 1999) showed the potential of Mg/Ca as a paleothermometer. Since that time, planktic foraminiferal Mg/Ca has emerged as a valuable and widely applied paleotemperature proxy for surface waters (e.g., Friedrich et al., 2013; Groeneveld et al., 2014). In addition, the more recent development of paired $\delta^{18}O$ and Mg/Ca measurements on the same biotic carrier has enabled to separate the temperature and seawater $\delta^{18}O$ components of foraminiferal $\delta^{18}O$ records, allowing for improved reconstructions of global ice volume and local salinity variability (e.g. Elderfield and Ganssen, 2000; Lear et al., 2000; Sosdian and Rosenthal, 2009) (Chapters 5 and 6).

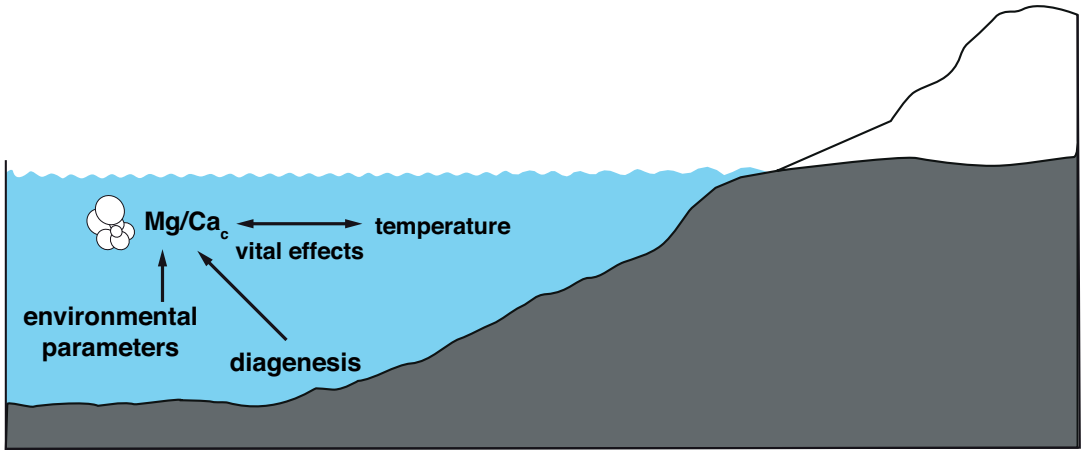

Figure 2.7. Main factors influencing the Mg/Ca ratio of foraminifers (Mg/Ca$_c$) (see text for references). Vital effects include ontogenetic and ecological effects; environmental parameters include seawater salinity, seawater pH and seawater Mg/Ca.

Numerous calibration studies based on planktic foraminifera demonstrate that Mg/Ca increases exponentially by 6–10% per 1°C in most species (Elderfield and Ganssen, 2000; Anand et al., 2003; McConnell and Thunell, 2005). Benthic foraminiferal Mg/Ca applications have been more limited and the relationship between Mg/Ca and bottom-water temperature, i.e., linear *versus* exponential, remains a matter of ongoing debate (Lea et al., 2000; Marchitto et al., 2007; Sosdian and Rosenthal, 2009; Lear et al., 2015). Notwithstanding, the substitution of Mg^{2+} into marine calcite is thermodynamically favored at higher temperatures (Mucci, 1987; Oomori et al., 1987). The observed temperature response in foraminiferal calcite as described above (6–10% per 1°C), however, is larger than predicted by theory (1–3% per 1°C) (Hönisch et al., 2013; and references therein). In addition, Mg/Ca ratios in many foraminifera are about 1–2 orders of magnitude lower (Lea et al., 1999) than expected for inorganically precipitated calcite (Mucci, 1987; Burton and Walter, 1991). The discrepancy between theory and observation implies that the empirical Mg/Ca-temperature relationship is influenced by additional environmental parameters and/or species-specific biological fractionation processes (Hönisch et al., 2013) (Figure 2.7), and, perhaps, explains why some benthic foraminiferal Mg/Ca-temperature relationships appear not to be exponential. Factors other than temperature that have the potential to influence test calcite Mg/Ca include the following:

Ontogeny. Species-specific fractionation processes are thought to be related to ontogeny since it has been found that Mg/Ca ratios even vary within a single specimen. Because ontogenetically younger foraminifera have higher calcification rates compared to older individuals of the same species, their Mg/Ca ratio is lower (e.g. Elderfield et al., 2002;

Friedrich et al., 2012). To avoid this effect, Mg/Ca analyses should be restricted to a very narrow size range of fully-grown individuals (Friedrich et al., 2012).

Ecology. Species-specific differences in Mg/Ca can also be a result of differences in calcification temperature, which in turn is related to the seasonal appearance of a species (Boltovskoy, 1964; Darling et al., 2003) or its habitat depth (Sadekov et al., 2008; Friedrich et al., 2012). Especially infaunal benthic and deeper-dwelling planktic foraminifera can actively migrate during their life cycle in order to reach their preferred microhabitat (Hemleben et al., 1989) (Figure 2.4). As temperatures vary with respect to water/sediment depth the specimen inhabits, the Mg/Ca ratio of the whole test reflects an average value of all temperatures experienced during life cycle.

Seawater salinity. While laboratory culture experiments only demonstrate a 3–8% increase in Mg/Ca per salinity unit (Kısakürek et al., 2008; Hönisch et al., 2013), coretop studies suggest that the Mg/Ca sensitivity to salinity is much greater (up to 59% increase in Mg/Ca per salinity unit) (Ferguson et al., 2008; Mathien-Blard and Bassinot, 2009; Arbuszewski et al., 2010). Thus, the actual influence of seawater salinity on test calcite Mg/Ca remains a matter of ongoing debate.

Carbonate-ion concentration or seawater pH. A growing number of studies demonstrate relationships between various geochemical parameters recorded in calcium carbonate and changes in the carbonate-ion concentration in seawater [CO_3^{2-}] or pH (Lea et al., 1999; Russell et al., 2004; Rathmann and Kuhnert, 2008). It has been shown that below present-day seawater pH (pH = 8.2), foraminiferal Mg/Ca decreased by up to 16% per 0.1 unit increase in pH, while changes above modern pH were insignificant (Russell et al., 2004). The sensitivity of test Mg/Ca to seawater pH is species-specific and even appears to be not existent for some species, such as the benthic foraminifer *O. umbonatus* (Rathmann and Kuhnert, 2008).

Seawater Mg/Ca. A variation in seawater Mg/Ca through time related to changes in weathering input, hydrothermal activity, dolomitization or carbonate production (Drever et al., 1988; Fantle and DePaolo, 2006) possibly influences foraminiferal Mg/Ca ratios on timescales longer than the residence time of these elements, i.e., >1 Myr (e.g., Fantle and DePaolo, 2005, 2006). An adjustment for Mg/Ca-based temperature estimates compensating past changes in seawater Mg/Ca has been recently developed (Medina-Elizalde et al., 2008). This correction requires seawater Mg/Ca values for the relevant time period, which, however, are often only poorly constrained (Fantle and DePaolo, 2006; Rausch et al., 2013).

Influence of diagenesis on foraminifer-derived geochemical proxies

The use of foraminiferal calcite for accurate paleoceanographic reconstructions relies on the assumption that the primary geochemical signature is not altered by diagenesis. In general, diagenetic alteration of foraminiferal calcite is less problematic in benthic than in planktic foraminifers. Studies demonstrate that even extensive recrystallization of benthic foraminiferal calcite results only in minimal shifts from primary $\delta^{18}O$ and $\delta^{13}C$ values (Pearson et al., 2001; Edgar et al., 2013). This is because (i) benthic foraminifera are less susceptible to dissolution than their planktic counterparts due to more heavily calcified tests, (ii) recrystallization of benthic foraminiferal calcite typically occurs within the same water mass that the test was initially formed in (Edgar et al., 2013; and references therein), and (iii), with respect to Mg/Ca, calcite generally formed in colder waters (with lower Mg/Ca) tends to be less susceptible to dissolution (Marchitto et al., 2007).

However, numerous studies suggest a significant influence of early-stage diagenesis on the geochemical signature of planktic foraminifera. With regard on Mg/Ca, this occurs either through partial dissolution of the test or microcrystalline overgrowth. On the one site, progressive calcite dissolution in deeper and less calcite-supersaturated to -undersaturated bottom waters causes initial Mg/Ca ratios to decrease (e.g., Brown and Elderfield, 1996; Lea et al., 2000; Regenberg et al., 2014), pretending colder temperatures. On the other site, the addition of inorganic calcite from sediment pore fluids onto foraminiferal tests (overgrowths) with a larger Mg/Ca signature than its biogenic counterpart (Regenberg et al., 2007) causes initial test Mg/Ca to increase, thereby overestimating calcification temperatures. Recrystallization of planktic foraminifera during early-stage diagenesis is also expected to shift initial test $\delta^{18}O$ to higher values, biasing any resulting paleoreconstruction (e.g., Pearson et al., 2001; Sexton et al., 2006). This is because recrystallization occurs in bottom waters that are significantly cooler compared to surface waters in which the test was initially precipitated.

Altogether, these findings highlight the need to carefully consider the possibility of diagenetic alteration when interpreting foraminifer-derived geochemical proxy records. Preservation of foraminiferal tests can be evaluated by (i) taking micrographs of specimens to check for fine features such as the original wall structure, pore channels or secondary calcite (see Chapters 4 and 6), or by (ii) generating a foraminiferal fragmentation index (Le et al., 1995) (see Chapters 4 and 5).

CHAPTER 3

STUDY AREA AND SAMPLE MATERIAL

Data presented in this thesis have been generated based on deep-sea sediment cores drilled within the framework of Ocean Drilling Program (ODP) Leg 138 in the Eastern Equatorial Pacific (Chapter 3.1) and Integrated Ocean Drilling Program (IODP) Expedition 306 in the North Atlantic (Chapter 3.2) (Figure 3.1). The generated geochemical datasets are derived from the benthic foraminifers *Cibicidoides wuellerstorfi* and *Oridorsalis umbonatus* and the planktic foraminifers *Globigerinoides ruber* and *Globorotalia crassaformis* (Chapter 3.3).

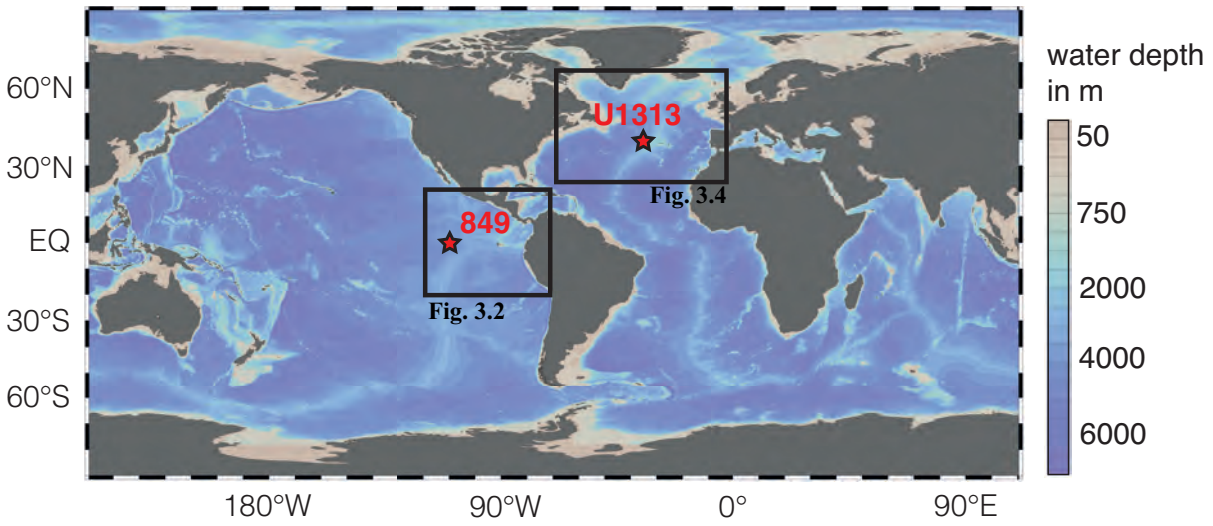

Figure 3.1. Bathymetric map showing the location of sites investigated in this thesis. Close-up views for Sites 849 in the Eastern Equatorial Pacific and U1313 in the North Atlantic are provided in Figures 3.2 and 3.4, respectively. Water depth (m) after World Ocean Atlas (Boyer et al., 2013).

3.1 Study area 1: the Eastern Equatorial Pacific

As study area for this thesis, the Eastern Equatorial Pacific (EEP) (Figure 3.2) has been selected due to its key role in the global climate system. It is an important factor for the Earth's atmospheric and marine carbon budget (e.g., Toggweiler and Sarmiento, 1985; Takahashi et al., 2002; Takahashi et al., 2009), and at the same time exerts strong control on the ocean-atmosphere circulation (Fedorov and Philander, 2000; Pennington et al., 2006).

3.1.1 Geographic, oceanographic and climatic boundary conditions

Geographic setting

The northern (~25°N) and southern (~25°S) boundaries of the EEP are defined by the North and South Pacific tropical gyres (Wyrtki, 1966; Kessler, 2006). To the west, the EEP reaches up to ~140°W; to the east, the modern EEP is confined by the American continent (Wyrtki, 1966; Kessler, 2006). The eastern geographic boundary of the EEP has, however, changed over the course of Earth's history: An open Central American Seaway allowed for a deep-water connection between the east Pacific and the Caribbean Sea until the mid-Miocene (e.g., Sepulchre et al., 2014), and for surface-water exchange processes until the late Pliocene (Steph et al., 2010; Groeneveld et al., 2014) (see Chapters 4 and 5 for a detailed discussion). The modern east Pacific basin is characterized by narrow continental shelves along the American continent and a steep continental slope (Wyrtki, 1966). Average water depths are on the order of 3500–4500 m (Wyrtki, 1966) (Figure 3.2).

From a tectonic perspective, the EEP region covers the Cocos Plate in the northeast, the Nazca Plate in the southeast, and the Pacific Plate in the west. The boundary between the Cocos and Nazca Plates in the east to the Pacific Plate in the west constitutes a north-south-stretching oceanic ridge near 110°W (Figure 3.2). This ridge, termed East Pacific Rise, is the most striking geographical feature within the east Pacific and divides the EEP into a western and an eastern basin. The latter is subdivided into a series of smaller basins separated by secondary, more or less transversely-running ridges. While water masses in the open Pacific Ocean west of the East Pacific Rise approximate a global-ocean signal (Mix et al., 1995), the more isolated water masses east of the ridge potentially bear a regional oceanographic signature within each basin that may be also prone to terrestrial influence from the American continent (Messié and Chavez, 2011; Messié and Chavez, 2012).

Sediments of each basin in the east Pacific have a distinct calcium-carbonate content. This content depends on the depth of the carbonate compensation depth, which is a function of (i) $CaCO_3$ flux from the surface water to the deep ocean and (ii) the dissolution rate of $CaCO_3$ coupled to the saturation state of bottom waters and the degradation of C_{org} (Lyle et al., 1995; Lyle et al., 2002). East of the East Pacific Rise, the carbonate compensation depth is generally 500–1000 m shallower than west of the East Pacific Rise (4500–4700 m [Lyle et al., 1995; Pälike et al., 2012]). Thus, the amount of carbonate burial in the eastern EEP is relatively low despite high carbonate production in the surface water by plankton (Lyle et al., 1995; and references therein; Lyle et al., 2002).

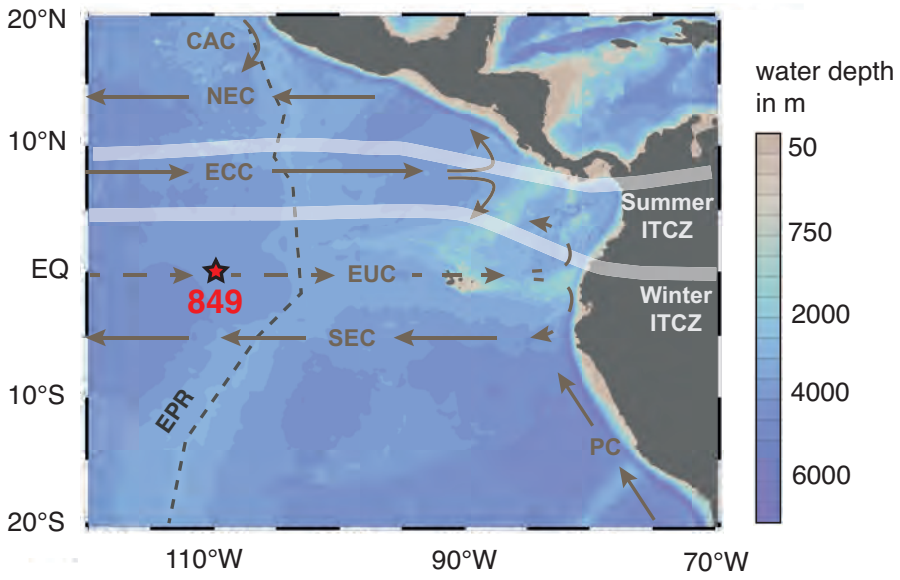

Figure 3.2. Bathymetric map showing the location of Site 849 in the EEP. Dark grey dashed line marks the position of the East Pacific Rise (EPR). Grey arrows indicate the modern general circulation of major surface (solid) and subsurface (dashed) currents (NEC = North Equatorial Current, ECC = Equatorial Countercurrent, EUC = Equatorial Undercurrent, SEC = South Equatorial Current, CAC = California Current, PC = Peru Current) (Pisias et al., 1995). White lines show the modern northernmost and southernmost positions of the Intertropical Convergence Zone (ITCZ). Modern ITCZ positions were determined using 55-yr (1958–2013) satellite observations of monthly rainfall in the tropical Pacific provided by the NASA Tropical Rainfall Measuring Mission (http://trmm.gsfc.nasa.gov). Water depth (m) after World Ocean Atlas (Boyer et al., 2013).

Oceanographic and climatic background conditions

In the modern tropical Pacific Ocean, the zonal atmospheric Walker circulation causes a strong asymmetry in east-to-west surface-air pressure, sea-surface temperatures and thermocline depth along the equator (Figure 3.3a). This circulation comprises easterly and westerly winds at the lower and upper troposphere, and rising motion and subsidence over the western and eastern tropical Pacific, respectively (Bjerknes, 1969; McPhaden et al., 2006). The westward-blowing trade winds drive surface-water divergence along the equator and force warm waters to pile up in the west and cold waters to upwell in the east. This results in a deep thermocline (~150 m) and a thick, warm (~29°C) mixed layer in the "West Pacific Warm Pool"; at the same time, it yields a shallow thermocline (~50 m) and a thin, relatively cold (~23°C) mixed layer in the east Pacific "cold tongue" (Wang et al., 2000; Locarnini et al., 2013) (Figure 3.3a). The equatorial upwelling regime in the east Pacific is fed by relatively cold, highly saline and nutrient-enriched waters of the Equatorial Undercurrent, which, as such, yields high primary productivity rates (Lukas, 1986; Pennington et al., 2006).

The modern Walker circulation in the equatorial Pacific is associated with the inter-annual phenomenon of the El Niño-Southern Oscillation (ENSO) (see McPhaden et al., 2006, for a

review). On a timescale of two to seven years, the climate characterizing the modern EEP varies between anomalously warm (El Niño) and cold (La Niña) conditions. Under La Niña conditions, stronger trade winds, i.e., a stronger atmospheric Walker circulation, favor upwelling of cold waters of the Equatorial Undercurrent in the east Pacific. This intensifies the tilt of the thermocline and the "normal" sea-surface temperature gradient along the equator. During El Niño events, trade winds weaken along the equator as atmospheric pressure rises in the west Pacific and falls in the east Pacific. This weakening of the atmospheric Walker circulation is accompanied by a shoaling of the thermocline toward the west Pacific and a deepening of the thermocline over much of the EEP where upwelling and thus primary productivity become reduced (Fiedler, 2002). Through exerting control on ocean–atmosphere circulation, biological productivity and ecosystem structure, ENSO

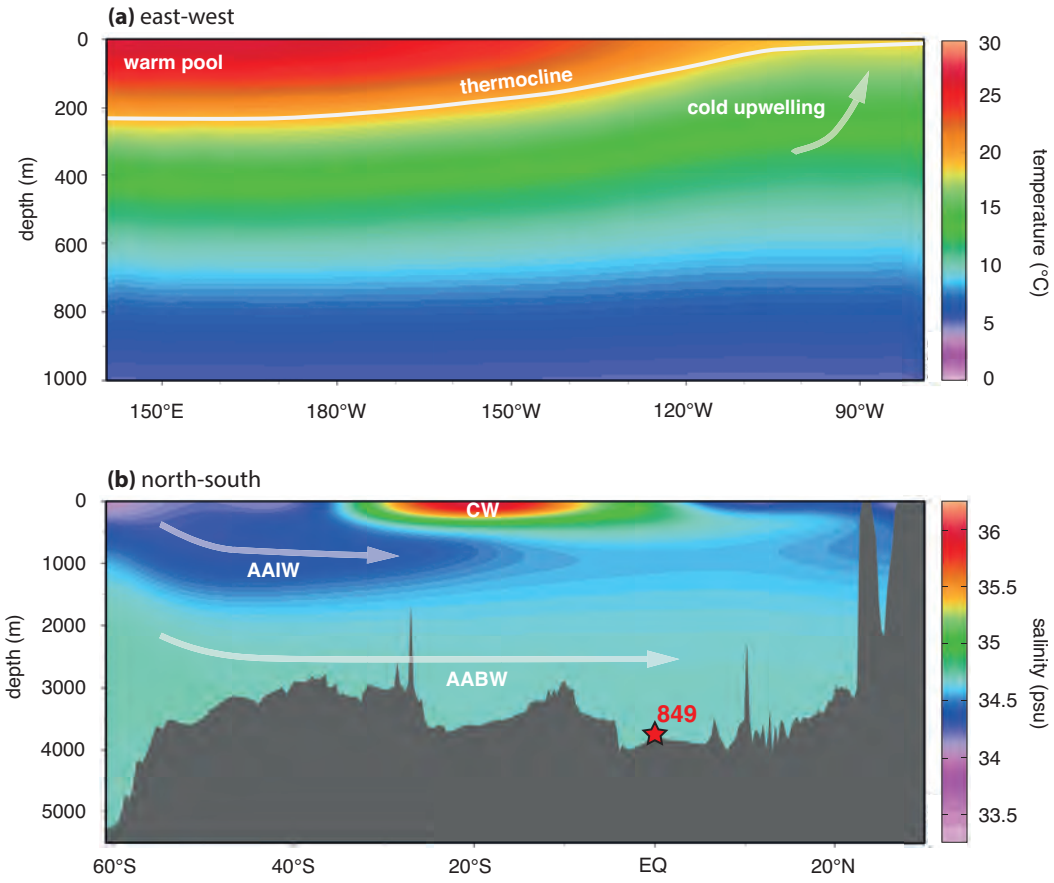

Figure 3.3. (a) Modern east-west (140°E to 80°W) temperature (°C) cross section for the uppermost 1000 m of the equatorial Pacific Ocean. The thermocline (white line) is defined by the 20°C isotherm (Wang et al., 2000; Kessler, 2006). The temperature profile highlights the strong asymmetry in east-to-west temperature and thermocline depth along the equator in the Pacific Ocean with a thick, warm mixed layer in the "West Pacific Warm Pool" and a cold, nutrient-rich mixed layer in the east Pacific "cold tongue". **(b)** Modern north-south (60°S to 30°N) salinity (psu) profile for the Pacific Ocean along 110°W. Arrows indicate the pathway of Antarctic Intermediate Waters (AAIW) and Antarctic Bottom Waters (AABW). Water masses are defined after Emery (2003): Salinity values of 34.4–36.4 psu, 33.8–34.5 psu, and 34.6–34.7 psu are characteristic for the Eastern South Pacific Central Water (CW), AAIW, and AABW, respectively. Red star marks location of Site 849 in the EEP. Cross sections after World Ocean Atlas (Boyer et al., 2013).

dynamics constitute a key component of the tropical and, through atmospheric and oceanographic teleconnections, the global climate system (Fedorov and Philander, 2000; Pennington et al., 2006).

The modern climate state (Figure 3.3a) and present-day ENSO dynamics in the tropical Pacific, however, have not been a permanent feature during Earth's history. The warm Pliocene equatorial Pacific Ocean was characterized by a greatly expanded West Pacific Warm Pool relative to today, giving rise to a surface-ocean temperature field akin to modern El Niño conditions (e.g., Wara et al., 2005; Fedorov et al., 2006) (therefore often referred to a "permanent El Niño-like" climate state [Molnar and Cane, 2002])[*]. The intensification of Northern Hemisphere Glaciation (see Chapter 2) marks the transition from an El Niño-like climate state to a more modern one with strong upwelling in the EEP and thus stronger zonal temperature gradients (e.g., Wara et al., 2005; Zhang et al., 2014). The onset of modern ENSO dynamics did not occur prior to ~5.5 ka (Ehlert et al., 2013, and references therein). The existence of fluctuations between El Niño-like and La Niña-like climate states on glacial-interglacial timescales during the Plio-Pleistocene, however, is still a matter of debate (Philander and Fedorov, 2003; Fedorov et al., 2006; Bolton et al., 2010a) (see Chapter 5 for details).

In addition to the Walker Circulation in a zonal vertical plane over the equatorial Pacific, a meridional circulation cell exists in tropical to subtropical regions. This so-called Hadley circulation (Hadley, 1735) comprises rising of heated air in the tropics, which flows in the upper troposphere toward the subtropical region. There it cools, sinks, and flows back toward the equator, where it converges into the tropical rain belt known as the Intertropical Convergence Zone (ITCZ) to complete the circulation. In the present-day climate system, the position of the ITCZ is always north of the equator over the EEP and exhibits a distinct annual cycle in its strength and latitudinal position. In particular, the modern ITCZ migrates seasonally between its northernmost position at ~9°N in boreal summer and its southernmost position at ~2°N in boreal winter in the EEP (Figure 3.2). The migration of the ITCZ is related to seasonal changes in trade-wind intensity, which are influenced by the strength and position of the subtropical high-pressure system that in turn responds to changes in the pole-to-equator temperature gradient, in the seasonal monsoonal heating of continents, and in the west Pacific sea-level pressure (Rind, 1998; Dekens et al., 2007). The direction of ITCZ

[*]*It is important to note that the terms "El Niño-like" and "La Niña-like" climate states characterize a mean state and do not consider higher-frequency climate variability such as modern seasonal ENSO dynamics. In order to clearly differentiate a, for instance Pliocene, "El Niño-like mean state" from a single El Niño event of the modern, the term "El Padre" has been suggested for the former (Ravelo et al., 2014).*

movement is typically toward a hemisphere that warms more relative to the other caused by changes in insolation, but with exceptions, such as during El Niño events, where ITCZ migration is primarily driven by tropical changes in atmospheric energy input (see Schneider et al., 2014, for a review; see also Chapter 5).

As part of the Hadley circulation, trade winds further north and south of the equator have a stronger north-south component compared to the east-west component close to the equator (Cannariato and Ravelo, 1997). Shore-parallel, equatorward trade winds and offshore Ekman pumping results in offshore transport of surface waters along the northeast and southeast Pacific, which is balanced by coastal upwelling of cold, nutrient-rich waters from below the thermocline. Both equatorial and coastal upwelling contribute to the formation of the EEP "cold tongue", and support more than 10% of the global biological production in the present-day oceans (Pennington et al., 2006).

3.1.2 ODP Site 849

Site 849 was drilled during ODP Leg 138 in 1991. A nearly complete sequence of late Miocene to Holocene sediments has been recovered (Mayer et al., 1992). The purpose of this expedition was to shed new light onto climatic and oceanographic changes during the late Cenozoic period (Mayer et al., 1992).

Site 849 is located in the EEP, ~860 km west of the East Pacific Rise (0.11°N, 110.31°W; Figure 3.2); thus, it records an open-ocean signal (Mix et al., 1995). Exhibiting a present-day water depth of 3851 m (Mix et al., 1995), Site 849 is primarily bathed by deep waters derived from the Southern Ocean (Figure 3.3b). The water depth at Site 849 is close to the modern lysocline (3200–3400 m [Adelseck and Anderson, 1978; Berger et al., 1982]), but well above the carbonate compensation depth that is deeper than 4500 m (Pälike et al., 2012). Site 849 is positioned in the present-day equatorial divergence zone within the so-called "cold tongue" (Wyrtki, 1981) where convergent trade winds from the Northern and Southern Hemispheres induce the year-round upwelling of cold, nutrient-rich waters of the Equatorial Undercurrent from below the thermocline to the surface (see above for more details). Sedimentation rates at Site 849 are on the order of 2.5–3.0 cm kyr^{-1} for the past 5 Myr (Mayer et al., 1985; Mix et al., 1995), which is high enough to acquire highly resolved proxy records.

In this thesis, 380 samples were investigated on 2-cm intervals along the primary shipboard splice (Mayer et al., 1992) from cores 849C-7H-1-80 cm to 849C-7H-2-21 cm and 849D-6H-5-102 cm to 849D-7H-5-57 cm (77.02 to 67.78 m composite depth [mcd]), representing

~2.75–2.4 Ma (Marine Isotope Stages [MIS] G6–95) according to the age model of Mix et al. (1995). Investigated sediments consist of white to light grey diatom nannofossil ooze, interbedded with slightly darker diatom-rich intervals. Foraminifera are common within the upper 100 m of Site 849 sediments (Mayer et al., 1992). Because the resolution (~4 kyr) of the already available benthic foraminiferal oxygen-isotope stratigraphy for Site 849 that covers the past 5 Myr (Mix et al., 1995) is too low for the purpose of this thesis, a new, higher-resolved oxygen-isotope stratigraphy has been developed for this site covering 2.75 to 2.4 Ma (see Chapters 4 and 5).

3.2 Study area 2: the North Atlantic

As a second study area for this thesis, the North Atlantic (Figure 3.4) has been selected because of its proximity to the large, dynamic Northern Hemisphere ice sheets and its fundamental role in deep-water formation. Both these characteristics make the North Atlantic one of the climatically most sensitive region on Earth.

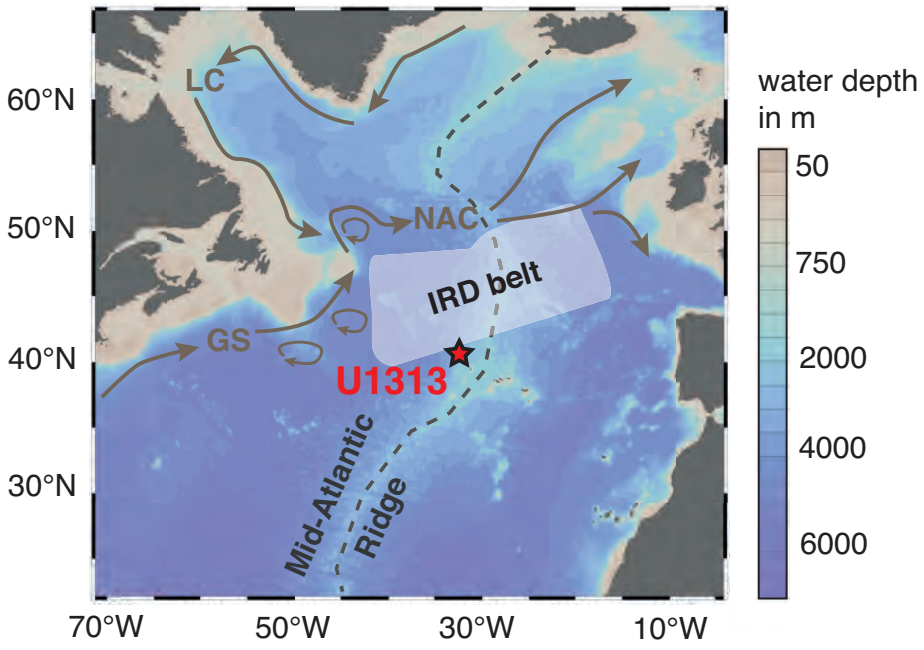

Figure 3.4. Bathymetric map showing the location of Site U1313 in the North Atlantic. Grey arrows demonstrate the modern general circulation of major surface currents (GS = Gulf Stream, LC = Labrador Current, NAC = North Atlantic Current) (Fratantoni, 2001). White shaded area highlights approximate position of the Central North Atlantic "Ice-rafted debris (IRD) belt" during the last glacial (Ruddiman, 1977a, b). Water depth (m) after World Ocean Atlas (Boyer et al., 2013).

3.2.1 Geographic, oceanographic and climatic boundary conditions

Geographic setting

The North Atlantic Ocean is bounded by North America in the west, Europe in the east, and the Equatorial Counter Current at about 8°N in the south. Through the Arctic Ocean in the north, the North Atlantic is linked to the Pacific Ocean. The most important first-order geographical feature within the North Atlantic Ocean is the north-south-stretching North Atlantic Ridge (Figure 3.4), which exerts a major influence on the circulation of near-bottom-water masses (Levin and Gooday, 2003). It constitutes the northern extension of the Mid-Atlantic Ridge, together extending from Iceland in the north to approximately 60°S in the lower bathyal zone at water depths of 800–3500 m. The North Atlantic Ridge, as such formed by a divergent tectonic plate boundary between the Eurasian Plate and the North American Plate, divides the North Atlantic Ocean longitudinally into two halves, each with a series of major basins delimited by secondary, more or less transversely-running ridges (Levin and Gooday, 2003).

In general, Atlantic sediments have a higher calcium-carbonate content than Pacific sediments, because the carbonate compensation depth is much deeper in the Atlantic (>5000 m [Levin and Gooday, 2003, and references therein]) compared to the Pacific (~4200 m [Berger et al., 1976]) – exception is the equatorial Pacific were the carbonate compensation depth is between 4700–4900 m (e.g., Berger et al., 1976; Lyle et al., 1995; Pälike et al., 2012). As a result, carbonate oozes are the dominant sediment type in the Atlantic, while red clays, from which the carbonate has been removed through dissolution, are restricted to relatively deep, small areas in the Atlantic, but cover vast tracts of the deep Pacific.

Oceanographic and climatic background conditions

A prominent feature in the North Atlantic Ocean is the so-called “Ice-rafted debris (IRD) belt” at ~40–55°N (Figure 3.4). The IRD belt originally describes the southwest-northeast-trending band of maximum iceberg melting and hence IRD deposition (as defined by mineral grains >62 μm) in open-marine sediments during the last glacial (Ruddiman, 1977a, b). Within the IRD belt in the midlatitude North Atlantic, abrupt changes occurred in IRD input during the last glaciation, while in higher latitudes such as the Labrador or Nordic Seas the deposition of IRD was more continuous.

Another important feature in the modern North Atlantic region is the Atlantic Meridional Overturning Circulation, which is a complex current system that constitutes a part of the global ocean conveyor belt (Broecker, 1991). The present-day large-scale hydrography of the North Atlantic Ocean is dominated by the overall near-surface, northward movement of warm, oligotroph waters through the Gulf Stream and its northeastern extension, the North Atlantic Current (Figure 3.4). As the ocean loses heat to the atmosphere at higher latitudes in the North Atlantic – which gives northwest Europe its mild climate – northward-flowing surface waters become denser (Broecker, 1991; Srokosz and Bryden, 2015, and references therein). In the icy Labrador and Greenland Seas, the water sinks as it becomes colder through intense winter cooling to produce the North Atlantic Deep Water (NADW) that spreads southward to complete the overturning circulation. Heat transport and its potential to decline and perhaps even switch off highlights the importance of the Atlantic Meridional Overturning Circulation for the global climate system (Broecker, 1991; Srokosz and Bryden, 2015, and references therein).

Despite the NADW being part of the Atlantic Meridional Overturning Circulation, other deep-water masses also exist in the North Atlantic, including Antarctic Bottom Waters (AABW) in deep (>4500 m) basins off Northwest Africa and high-saline Mediterranean Outflow Waters at depths of 500–1500 m entering the North Atlantic through the Strait of Gibraltar and flowing around the Northwest European continental margin (Emery, 2003; Levin and Gooday, 2003; Bahr et al., 2015) (Figure 3.5). While NADW is formed north of Iceland in the Labrador Sea, AABW forms on continental shelves in the Southern Ocean. The cold, fresh AABW underlies the comparatively warm and salty NADW because of its higher density (Figure 3.5). The modern distribution of deep-water masses in the Atlantic Ocean as shown in Figure 3.5 was, however, not a permanent feature throughout Earth's history. Changing deep-water masses from high northern and southern latitudes alternately influenced the seafloor in the deep North Atlantic on glacial-interglacial timescales (Boyle and Keigwin, 1985; Dwyer and Chandler, 2008; Lang et al., 2016) (see Chapters 3.2.2 and 6).

Being part of the Atlantic Meridional Overturning Circulation, the North Atlantic Current represents a noteworthy hydrographic feature in the midlatitude North Atlantic. It serves as a transitional zone between warm, oligotrophic surface waters connected to the subtropical gyre at mid- to low-latitudes and cold, more productive waters connected to the subpolar gyre at higher latitudes. Glacial-interglacial changes in its strength or position influence the amount of heat transport to the (sub)polar North Atlantic, which has important consequences for the growth of high northern latitude ice sheets and climate (e.g., Stein et al., 2009; Naafs et al.,

2010; Friedrich et al., 2013; Hennissen et al., 2014). During late Pleistocene glacials, for example, surface-ocean circulation was significantly different compared to the modern situation as arctic waters extended into the midlatitudes, producing a southward shift of the North Atlantic Current (Pflaumann et al., 2003; Stein et al., 2009; Voelker et al., 2010; Emanuele et al., 2015) with icebergs episodically filling the North Atlantic basin north of 40°N (Ruddiman, 1977a). A weaker/more southward position of the North Atlantic Current occurred also during prominent glacials of the intensification of Northern Hemisphere Glaciation, a process that was perhaps important for Plio-Pleistocene Northern Hemisphere ice-sheet growth (Naafs et al., 2010; Hennissen et al., 2014). This is, however, controversy debated, because other studies rather imply a position of the North Atlantic Current further north during prominent glacials of the intensification of Northern Hemisphere Glaciation compared to late Pleistocene glacials (Friedrich et al., 2013).

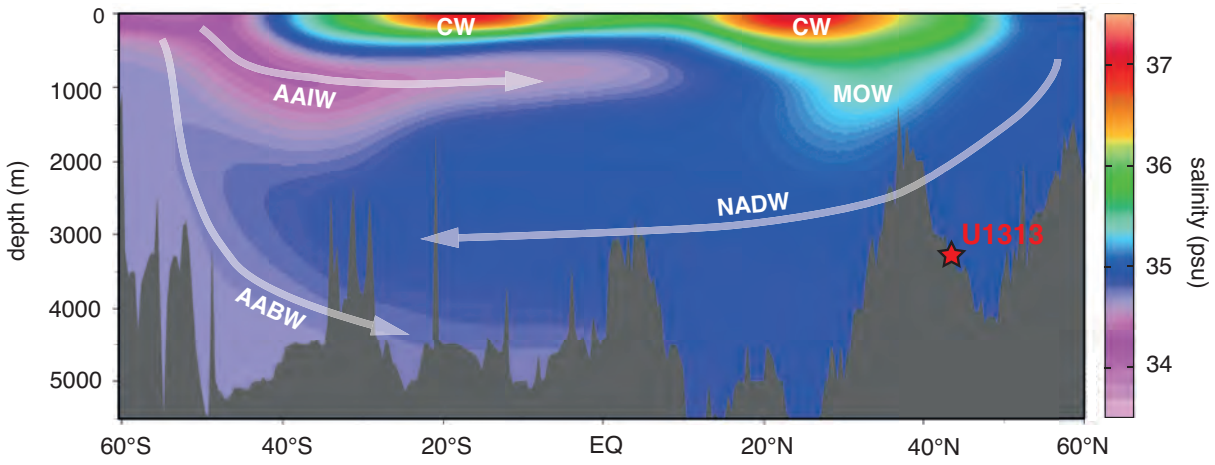

Figure 3.5. Modern north-south (60°S to 60°N) salinity (psu) profile for the Atlantic Ocean along 32°W after World Ocean Atlas (Boyer et al., 2013). Arrows indicate the pathway of Antarctic Intermediate Waters (AAIW), Antarctic Bottom Waters (AABW), and North Atlantic Deep Waters (NADW). Water masses are defined after (Emery, 2003): Salinity values of 34.8–35 psu, 33.8–34.8 psu, and 34.6–34.7 psu are characteristic for NADW, AAIW, and AABW, respectively. Mediterranean Outflow Waters (MOW), Eastern North Atlantic Central Waters and South Atlantic Central Waters (CW) are defined by a salinity range of 35.0–36.2 psu, 35.2–36.7 psu and 34.3–35.8 psu, respectively. Red star marks location of Site U1313 in the North Atlantic.

3.2.2 IODP Site U1313

Site U1313 was drilled within the framework of IODP Expedition 306 in 2005 (Expedition 306 Scientists, 2006). It is a reoccupation of Deep Sea Drilling Program Site 607 drilled during Leg 94 in 1983. Site 607 constitutes a benchmark mid-depth site monitoring subpolar North Atlantic climate evolution and has provided key insights into Pleistocene paleoceanography (e.g., Raymo et al., 1989; Raymo et al., 1992). The cores from reoccupied

Site U1313 offer distinct advantages over those from Site 607 because they exhibit very few coring caps or sediment fabric disturbances (e.g., Raymo et al., 1989; Raymo et al., 1992).

Site U1313 is located in the subpolar North Atlantic ~400 km northwest of the Azores (41°N, 32.5°W) at the base of the upper western flank of the Mid-Atlantic Ridge at the southernmost end of the IRD belt (Figure 3.4) (Expedition 306 Scientists, 2006). In a water depth of 3426 m (Expedition 306 Scientists, 2006) Site U1313 is presently under the direct influence of NADW (Figure 3.5). During late Pliocene to Pleistocene periods of glacial cooling, the influence of NADW became restricted at this site relative to deep waters (AABW) derived from the high southern latitudes (Boyle and Keigwin, 1985; Dwyer and Chandler, 2008; Lang et al., 2016). With respect to surface waters, drifter trajectories indicate that Site U1313 is predominantly influenced by surface waters originating from the North Atlantic Current, although this site is located slightly south of the modern core pathway of that current (Figure 3.4) (Fratantoni, 2001; Reverdin et al., 2003).

Consistently high sedimentation rates on the order of 4–5 cm kyr^{-1} at Site U1313 for the Plio-Pleistocene (Expedition 306 Scientists, 2006) provide the opportunity to work at high resolution and on the basis of maximum stratigraphic precision. For this thesis, 248 samples were examined on 8-cm intervals (temporal resolution: ~1550 yr according to the age model of Bolton et al. [2010c]), with a higher 4-cm (~775 yr) spacing during glacial terminations, and a 2-cm (~388 yr) spacing for MIS 100. Samples were investigated along the primary shipboard splice from 125.25 to 114.12 mcd, representing 2.64 to 2.41 Ma (MIS G1–95) (cores U1313B-12H-2-118 cm to U1313B-12H-6-120 cm, U1313B-13H-1-74 cm to U1313B-13H-1-127 cm, U1313C-12H-3-112 cm to U1313C-12H-5-52 cm, and U1313C-13H-3-2 cm to U1313C-13H-4-22 cm). A robust age model for Site U1313 is already available for the time interval focused upon in this thesis and is based on a high-quality benthic foraminiferal oxygen-isotope stratigraphy (Bolton et al., 2010c) tuned to the LR04 stack (Lisiecki and Raymo, 2005).

3.3 Investigated foraminiferal species

In this thesis, geochemical records of foraminiferal tests from Sites 849 and U1313 (see above) were generated for the time interval ~2.75 to 2.4 Ma. The benthic foraminiferal species *Cibicidoides wuellerstorfi* (Figure 3.6a–b) and *Oridorsalis umbonatus* (Figure 3.6c–d) were used for stratigraphy and to reconstruct bottom-water characteristics, respectively.

Reasons for involving another benthic species (*O. umbonatus*) as a recorder for bottom-water characteristics than used for stratigraphy (*C. wuellerstorfi*) are: (i) *O. umbonatus* has fewer/larger chambers compared to the numerous/small chambers of *C. wuellerstorfi*, which makes cleaning for Mg/Ca analyses much easier (see Chapter 6 for details), and (ii) *O. umbonatus* is less prone to the carbonate-ion effect than *C. wuellerstorfi* (Rathmann and Kuhnert, 2008), making this species a more reliable Mg/Ca recorder. Furthermore, the planktic species *Globigerinoides ruber* (Figure 3.6e–f) as an indicator for surface-water conditions and *Globorotalia crassaformis* (Figure 3.6g–h) as a proxy for sub-thermocline conditions have been involved (see also Figure 2.4). A brief overview on these species is given in the following.

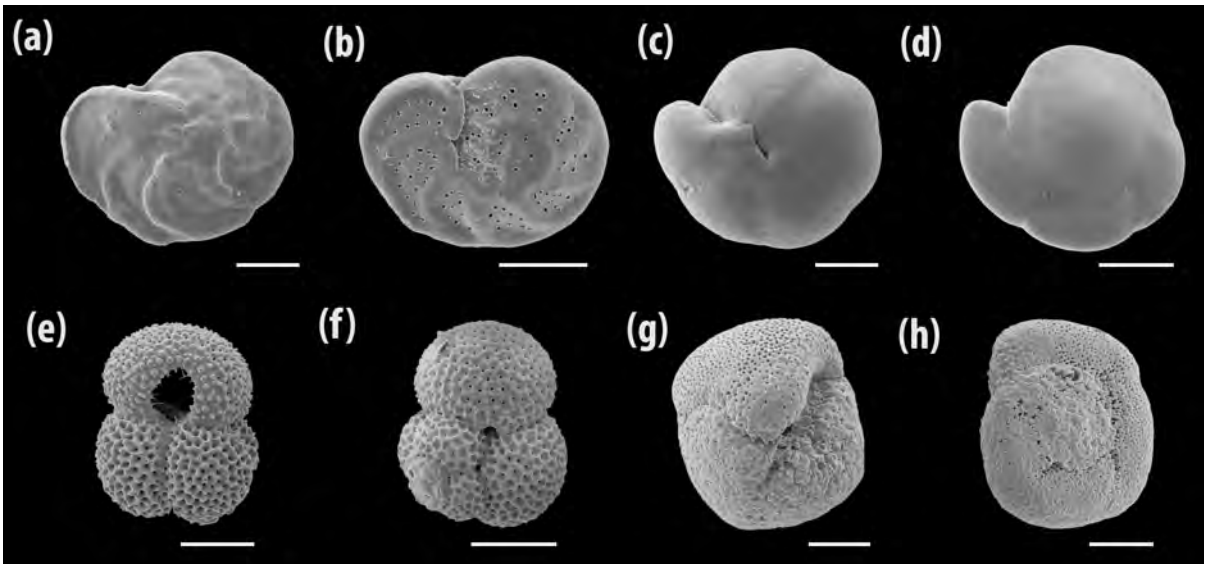

Figure 3.6. Scanning electron microscope images of benthic (a–d) and planktic (e–h) foraminiferal species from EEP Site 849 investigated in this thesis. White bars represent 100 µm. **(a)** Umbilical side of *Cibicidoides wuellerstorfi* (sample 849D-7H-2-41 cm to 849D-7H-2-43 cm). **(b)** Spiral side of *Cibicidoides wuellerstorfi* (sample 849D-7H-2-41 cm to 849D-7H-2-43 cm). **(c)** Umbilical side of *Oridorsalis umbonatus* (sample 849D-7H-2-41 cm to 849D-7H-2-43 cm). **(d)** Spiral side of *Oridorsalis umbonatus* (sample 849D-7H-2-41 cm to 849D-7H-2-43 cm). **(e)** Umbilical side of *Globigerinoides ruber* (white, s.s.) (sample 849D-6H-6-6 cm to 849D-6H-6-8 cm). **(f)** Spiral side of *Globigerinoides ruber* (white, s.s.) (sample 849D-6H-6-6 cm to 849D-6H-6-8 cm). **(g)** Umbilical side of *Globorotalia crassaformis* (sinistral) (sample 849C-7H-2-1 cm to 849C-7H-2-3cm). **(h)** Spiral side of *Globorotalia crassaformis* (sinistral) (sample 849C-7H-2-1 cm to 849C-7H-2-3cm).

3.3.1 *Cibicidoides wuellerstorfi*

Cibicidoides wuellerstorfi (synonym *Planulina wuellerstorfi;* Figure 3.6a–b) is one of the most commonly used benthic foraminiferal species to reconstruct bottom-water $\delta^{18}O$ and $\delta^{13}C$ (e.g., Lisiecki and Raymo, 2005; Bolton et al., 2010c). This species has a worldwide distribution with an epifaunal life mode commonly in bathyal regimes.

Calcareous tests of *C. wuellerstorfi* are slightly trochospiral with a coarsely perforate, flattened, evolute spiral side and a finely perforate, slightly convex umbilical side. In studies of this thesis, the $\delta^{18}O$ record of *C. wuellerstorfi* is used for stratigraphy by correlating to the LR04 stack (Lisiecki and Raymo, 2005) (see Chapters 4 and 5 for details).

3.3.2 *Oridorsalis umbonatus*

Another benthic foraminiferal species that is often used in paleoceanographic studies is *Oridorsalis umbonatus* (e.g., Lear et al., 2004; Friedrich et al., 2013) (Figure 3.6c–d). *Oridorsalis umbonatus* is a slightly infaunal species that inhabits lower-neritic to abyssal settings under oligotrophic and well-oxygenated conditions. Because of its geographic (worldwide) and stratigraphic (late Cretaceous to present [Kaiho, 1998]) appearance, *O. umbonatus* has been used in numerous paleoceanographic studies (e.g., Lear et al., 2004; Friedrich et al., 2013).

Morphologically, the calcareous shell of *O. umbonatus* is slightly trochospiral with an evolute, convex spiral side, and an involute, less convex umbilical side. The final whorl consists of five to six chambers.

3.3.3 *Globigerinoides ruber*

An important recorder of surface-water conditions is the planktic foraminiferal species *Globigerinoides ruber* (Figure 3.6e–f), one of the shallowest-dwelling species among modern planktic foraminifera (Dekens et al., 2002; Rippert et al., 2016). *Globigerinoides ruber* inhabits the mixed layer and is most common in (sub)tropical surface waters. In the tropics, where seasonal climate variability is low, this species is a suitable recorder for mean annual surface-water conditions (e.g., Deuser et al., 1981; Lin et al., 1997; Tedesco and Thunell, 2003), while in extratropical regions *G. ruber* most likely represents summer surface-water conditions (e.g., Schiebel and Hemleben, 2000; Schiebel et al., 2002). *Globigerinoides ruber* is symbiont-(dinoflagellate-)bearing and therefore restricted to the euphotic zone during the entire life cycle (Hemleben et al., 1989). However, for reproduction *G. ruber* migrates to greater water depths (Figure 2.4).

Morphologically, the trochospiral, highly perforate shell consists of three chambers in the final whorl with a wide-opened aperture on the umbilical site and two small apertures on the spiral site. Two morphotypes of *G. ruber* can be distinguished by shell color. The first morphotyp is a pink form that inhabits warmer waters (compared to the second morphotyp) in

the Atlantic Ocean and the Mediterranean Sea. The pink variety became extinct in the Indo-Pacific realm in the late Pleistocene (~120.000 yr) (Thompson et al., 1979). The second morphotyp has white tests and occurs globally. For the white variety of *G. ruber* two different genotypes (*G. ruber* sensu stricto [s.s.] and *G. ruber* sensu lato [s.l.]) are existent (Kuroyanagi et al., 2008; Aurahs et al., 2011). Since morpho- and genotypes of *G. ruber* have different preferences with regard on ecological requirements and seasonal abundance (e.g., Tolderlund and Bé, 1971), they should be handled separately in paleoceanographic studies. Any mixture of *G. ruber* genotypes, for instance, biases generated proxy records, because *G. ruber* (s.s.) thrives in shallower water depths in the upper mixed layer compared to *G. ruber* (s.l.) (e.g., Wang, 2000; Steinke et al., 2005).

3.3.4 *Globorotalia crassaformis*

Another important planktic foraminiferal species is *Globorotalia crassaformis* (Figure 3.6g–h), which is a sub-thermocline-dwelling species in low- to midlatitudes. *Globorotalia crassaformis* occurs year-round (Tedesco and Thunell, 2003) and is most common when the thermocline is shallow and upwelling intensive (Ravelo and Andreasen, 1999). This species is often used in paleoceanographic studies to monitor changes in thermocline depth.

Morphologically, tests of *G. crassaformis* are characterized by four chambers in the final whorl and a slit-like aperture. As in many planktic foraminiferal species, sinistral and dextral coiling forms exist (compare Chapter 4). However, the controlling parameters for the coiling direction of *G. crassaformis* have not yet been identified.

CHAPTER 4

PLIO-PLEISTOCENE GLACIAL-INTERGLACIAL PRODUCTIVITY CHANGES IN THE EASTERN EQUATORIAL PACIFIC UPWELLING SYSTEM*†

4.1 Introduction

Oceanic upwelling regions play a key role in controlling Earth's climate (e.g., Toggweiler and Sarmiento, 1985; Watson and Garabato, 2006). High phytoplankton growth rates and standing stocks supported by relatively nutrient-rich waters in upwelling zones promote organic matter export from the surface ocean and removal of CO_2 from the surface ocean-atmosphere system (e.g., Schlitzer, 2004; Takahashi et al., 2009), with a significant influence on both the global carbon and nutrient cycles (e.g., Schlitzer, 2004). An ideal natural laboratory for studying the dynamics of an upwelling system is the Eastern Equatorial Pacific Ocean (EEP). There, both equatorial upwelling and coastal upwelling contribute to conditions that support more than 10% of the global biological production in the present-day oceans (Pennington et al., 2006). Relatively high year-round primary productivity levels are responsible for relatively high sedimentation rates on the order of 2.5 to 3.0 cm kyr^{-1} for the past 5 Myr (Mayer et al., 1985; Mix et al., 1995), allowing the generation of highly temporally resolved proxy records in this region. However, given the supply of upwelled nutrient-rich waters, modern biological production in the EEP is not as high as we might expect because of iron limitation (Coale et al., 1996), characterizing the EEP Ocean as a high-nutrient, low-chlorophyll (HNLC) region.

During the late Pliocene, large ice sheets were established on North America and Eurasia (e.g., Shackleton et al., 1984a; Bailey et al., 2013) probably in response to a slow decline in carbon dioxide levels and therefore global temperature (DeConto et al., 2008; Lunt et al., 2008a). This so-called "intensification of Northern Hemisphere glaciation" (iNHG) resulted in large productivity changes in the oceans on both secular and glacial-interglacial (G-IG) timescales. At the global scale proxy records for export productivity demonstrate high-

* *Published in Jakob et al. (2016), Paleoceanography, 31, 453–470.*

† *Data for this Chapter are provided in Tables A.1.1–A.1.3 (Appendix A.1) and B.1.1. (Appendix B.1).*

latitude productivity shifts (e.g., Hillenbrand and Fütterer, 2001; Bolton et al., 2011) that are broadly coincident with but opposite in sign to (sub)tropical productivity patterns in upwelling regions (e.g., Lawrence et al., 2006, 2013; Bolton et al., 2011). The mechanisms driving these low-latitude productivity fluctuations are a subject of ongoing debate with hypotheses including changes in trade-wind strength/upwelling intensity ("upwelling hypothesis") (see Cleaveland and Herbert, 2007; Etourneau et al., 2010) and/or changes in the nutrient content of the upwelled water masses ("nutrient delivery hypothesis") (see Lawrence et al., 2006, 2013; Bolton et al., 2011; Lyle and Baldauf, 2015).

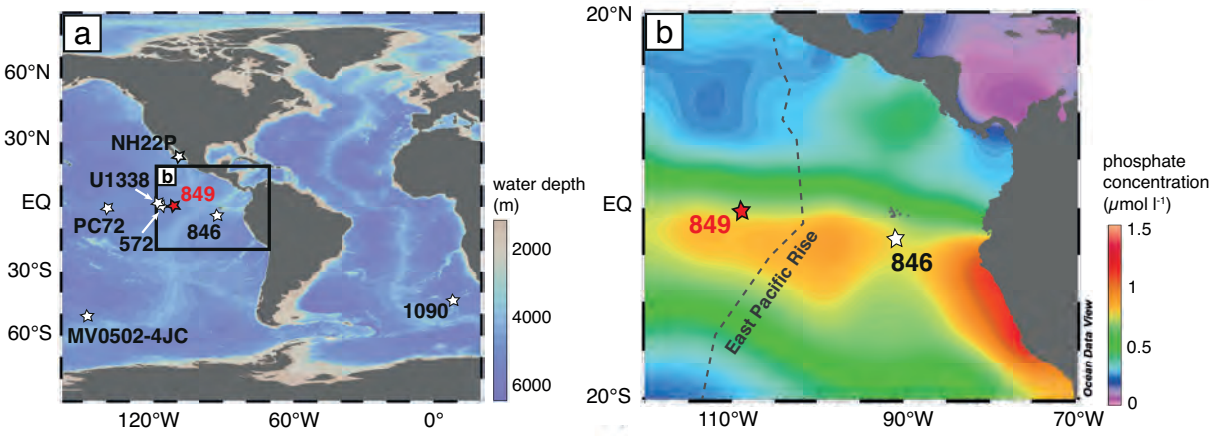

Figure 4.1. **(a)** Bathymetric map showing the location of ODP Site 849 (red; this study) and other sites mentioned in the text (white). Water depth (m) after World Ocean Atlas. **(b)** Location map of ODP Sites 849 (red; this study) and 846 (white). Modern annual sea-surface phosphate concentrations (µmol l^{-1}) after World Ocean Atlas (Garcia et al., 2014).

Here we present new proxy records of suborbital resolution from Ocean Drilling Program (ODP) Site 849 to shed new light on the dynamics and the origin of G-IG productivity changes in the EEP. We analyzed the time interval from 2.65 to 2.4 Ma (Marine Isotope Stage [MIS] G1 to 95, latest Pliocene/early Pleistocene following Gibbard et al. [2010]), including the first three consecutive large-amplitude (~1‰ in benthic $\delta^{18}O$ [Lisiecki and Raymo, 2005]) G-IG cycles (MIS 100 to 96) representing the culmination of late Pliocene iNHG. Marine Isotope Stage 100 has particular significance because it was the first glacial during which (i) the Laurentide Ice Sheet (LIS) advanced into the midlatitudes (Bailey et al., 2010; Balco and Rovey, 2010; Lang et al., 2014) and (ii) ice rafting first became widespread across the North Atlantic Ocean (e.g., Shackleton et al., 1984a; Kleiven et al., 2002; Naafs et al., 2013) with ice-rafted debris flux and provenance in the subpolar North Atlantic comparable to that of the Last Glacial Maximum (LGM) (Bailey et al., 2013). Advance of the LIS into the midlatitudes has important implications for atmospheric circulation and hydroclimate

regionally (Bailey et al., 2010; Hennissen et al., 2014; Lang et al., 2014; Oster et al., 2015) and may also have influenced the behavior and dynamics of upwelling in the EEP. Here we use suborbitally resolved sand-accumulation rates in combination with lower-resolution planktic foraminiferal fragmentation and planktic foraminiferal and radiolarian accumulation rates from Site 849 as a productivity proxy (e.g., Diester-Haass et al., 2002) to compare with an alkenone-based paleoproductivity record from ODP Site 846 (Lawrence et al., 2006) (Figures 4.1). We also generated suborbitally resolved $\delta^{13}C$ records in three foraminiferal species (shallow-dwelling planktic, thermocline-dwelling planktic, and benthic) to investigate the potential influence of different water masses at the study site (e.g., Mackensen et al., 2001; Curry and Oppo, 2005) and to evaluate $\delta^{13}C$ gradients between the sea surface and thermocline, shedding new light on changes in thermocline depth and thus upwelling intensity (e.g., Pierre et al., 2001).

4.2 Modes and drivers of past variability in Eastern Equatorial Pacific productivity during the Plio-Pleistocene

Biological production underwent a progressive decrease in the high-latitude oceans during iNHG while increasing in low- to mid-latitude settings (e.g., Sarnthein and Fenner, 1988; Bolton et al., 2011; Etourneau et al., 2012; Lawrence et al., 2013). Different driving mechanisms have been proposed to explain the secular shift toward a more productive regime in low latitudes during Pliocene iNHG. The (sub)tropical productivity increase is suggested to result (i) from a shoaling of the tropical thermocline/upwelling intensification, predominantly depending on the trade-wind strength and thus the equator-to-pole temperature gradient (Pisias and Mix, 1997, and references therein; Cleaveland and Herbert, 2007; Etourneau et al., 2010), and/or (ii) from a reorganization of the nutrient content in high southern latitude surface waters (Lawrence et al., 2006, 2013; Bolton et al., 2011; Lyle and Baldauf, 2015) that feed low-latitude upwelling regions (Tsuchiya et al., 1989; Toggweiler et al., 1991). Over the early and middle Miocene, a major source for the waters upwelled in the EEP was the deep water formed in the higher-latitude Southern Ocean, as evidenced by small benthic carbon-isotope gradients (Poore et al., 2006; Cramer et al., 2009) and neodymium-isotope records (Holbourn et al., 2013) across the Pacific Ocean basin. Over the course of the Neogene, the export of Southern Ocean deep water to the lower latitude Pacific generally increased (van de Flierdt et al., 2004), ultimately culminating in the present-day situation where upwelled waters in the EEP are primarily sourced from the Southern Ocean with an insignificant

contribution from the North Pacific (Tsuchiya et al., 1989; Toggweiler et al., 1991). Hence, long-term shifts in the rate of primary productivity in the EEP are controlled not only by the strength of upwelling but also by the chemical composition of the source waters. Long-term changes in Southern Ocean source water properties such as increasing nutrient contents may have been regulated by a secular increase in sea-ice coverage (Hillenbrand and Cortese, 2006), stronger water-column stratification (Haug et al., 1999), and/or a long-term equatorward shift in the position of the Southern Ocean westerly winds (Lawrence et al., 2013), inducing a high-latitude productivity crash in step with a subpolar and mid- to low-latitude productivity increase during iNHG at ~2.5 Ma (Lawrence et al., 2013, and references therein).

In addition to the secular productivity increase in (sub)tropical upwelling regimes during iNHG, G-IG productivity fluctuations in low latitudes became more pronounced, strongly paced by Earth's obliquity (41 kyr) (Lawrence et al., 2006). It has been demonstrated that low-latitude productivity was elevated during glacials compared to interglacials (Lawrence et al., 2006; Bolton et al., 2010b) and that the amplitude of these G-IG productivity fluctuations increased across iNHG (Lawrence et al., 2006). To explain the variability in biological production on G-IG timescales, two competing hypotheses have been proposed, invoking either changes in the upwelling intensity (Cleaveland and Herbert, 2007; Etourneau et al., 2010) or changes in the nutrient availability within the upwelled water masses in the low latitudes (Lawrence et al., 2006; Etourneau et al., 2013) or a combination of both factors (Filippelli et al., 2007). Traditionally, it has been argued that observed G-IG changes in EEP primary productivity were linked to variations in upwelling rates in response to modified trade-wind strengths (e.g., Bjerknes, 1969; Etourneau et al., 2010), a process that has been also proposed for late Pleistocene glacials (e.g., Pisias and Mix, 1997, and references therein). In this interpretation, an increased equator-to-pole temperature gradient during glacials acts to trigger a strengthening of the trade winds and therefore upwelling of cold nutrient-rich waters leading to a simultaneous increase in biological production (the upwelling hypothesis). However, more recent studies from EEP upwelling zones suggest that primary productivity and temperature were decoupled from one another during the past 5 Myr, a scenario that is incompatible with upwelling strength being the only driver of productivity changes (Loubere, 2000; Dekens et al., 2007). These observations have led to the suggestion that the productivity increase during Plio-Pleistocene glacials recorded in the EEP may have primarily resulted from an enhanced nutrient content in upwelled waters sourced from the high southern latitudes (Lawrence et al., 2006; Etourneau et al., 2013). In this interpretation, the strength of

the upwelling system plays a subordinate role in modulating EEP G-IG productivity changes. Instead, climate conditions in the higher-latitude Southern Ocean and primary productivity and thus nutrient utilization in that region control the nutrient content of upwelled EEP waters on G-IG timescales (the nutrient delivery hypothesis).

Regardless of which of these two hypotheses holds true, G-IG primary productivity changes may also be influenced by aeolian dust input (e.g., McGee et al., 2007; Winckler et al., 2008; Lang et al., 2014), especially in HNLC ecosystems such as the EEP where nutrient concentrations are high, but biological production is limited by iron availability (Coale et al., 1996). Because dust serves as a natural source of iron and other micronutrients (Winckler et al., 2008), higher glacial than interglacial dust fluxes sourced in northern South America (Nakai et al., 1993; Stancin et al., 2006) may have resulted in an additional increase (decrease) in biological production during glacials (interglacials). Enhanced glacial dust fluxes are suggested to have driven increased productivity for at least the past five G-IG cycles within the EEP (McGee et al., 2007; Winckler et al., 2008). On the other hand, a study of central equatorial Pacific spanning the Miocene to Holocene demonstrated no systematic relationship between iron input or pathway and total biological export production for Pleistocene G-IG cycles (Ziegler et al., 2008).

In this study we test the competing hypotheses for G-IG productivity change in the EEP during the latest Pliocene to earliest Pleistocene.

4.3 Site description

All Plio-Pleistocene EEP productivity records on G-IG timescales used in support of either the upwelling hypothesis or the nutrient delivery hypothesis come from sites located east of the East Pacific Rise (EPR) (Figure 4.1b). To quantify changes in primary productivity within the open-ocean equatorial Pacific, we investigated sediments from Site 849 (0°11′N, 110°31′W) (Figure 4.1), which is located ~860 km west of the EPR; thus, it records a more global-ocean signal (Mix et al., 1995). Site 849 was drilled during ODP Leg 138 in 1991 (Mayer et al., 1992). A nearly complete sequence of late Miocene to Holocene sediments was recovered (Mayer et al., 1992). Site 849 is situated at a present-day water depth of 3851 m (Mix et al., 1995), close to the modern lysocline in the equatorial Pacific (3.2–3.4 km water depth [Adelseck and Anderson, 1978; Berger et al., 1982]) and well above the carbonate compensation depth (estimated deeper than 4.5 km water depth in the equatorial Pacific

during the Plio-Pleistocene transition [Pälike et al., 2012]). Site 849 is positioned in the present-day equatorial divergence zone within the so-called "cold tongue" (Wyrtki, 1981) where convergent trade winds from the Northern and Southern Hemispheres induce the year-round upwelling of cold, nutrient-rich waters from below the thermocline to the surface (for details see Chapter 3).

Changes in the paleoposition of Site 849 were negligible over the past 4 Myr (Pisias et al., 1995), but our geographical (EEP) and stratigraphic (Plio-Pleistocene boundary) focus means that the closure of the Central American Seaway (CAS) has the potential to influence paleoceanographic records from Sites 849 and especially 846 (Figure 4.1). Global climate-ocean ecosystem model experiments suggest that the first-order effect of CAS closure is likely to have promoted increased upwelling rates and surface-water nutrient concentrations in the EEP (Schneider and Schmittner, 2006). The timing of this closure has received considerable recent attention, and it is important to understand what is meant by the terms open *versus* closed. The CAS may maintain a shallow (<50 m) connection between the EEP and the Caribbean Sea but be effectively closed with respect to its influence on ocean circulation, while the migration of mammals between North and South America requires a continuous land bridge (Groeneveld et al., 2014). Some studies place CAS closure (i.e., cutoff of deep-water connection between the EEP and the Caribbean Sea) in the mid-Miocene (e.g., Sepulchre et al., 2014), whereas other investigations point to a surface-water exchange between the EEP and the Caribbean Sea until the late Pliocene (Steph et al., 2010) with temporary glacioeustatic sea-level-led gateway closures with a significant impact on ocean circulation during prominent iNHG glacials (Groeneveld et al., 2014).

4.4 Methods

4.4.1 Sampling

To study our target interval centered on MIS 100 to 96, we sampled cores 849C-7H-1-80 cm to 849C-7H-2-21 cm and 849D-6H-5-102 cm to 849D-7H-3-73 (74.17 to 67.78 m composite depth [mcd]). To generate a record at suborbital resolution (mean ~780 years), 20 cm^3 samples were taken at 2-cm intervals. The sampled core material consists of biogenic sediment without clay components – a white to light grey nannofossil ooze (Mayer et al., 1992). Samples were dried, weighed, and washed over a 63 μm sieve. The coarse residue (sand fraction) primarily consists of $CaCO_3$-producing organisms, namely, planktic and

benthic foraminifera together with siliceous radiolarians (see Figure A.1.1 in Appendix A.1). The fine fraction, in turn, is predominantly composed of calcareous nannoplankton (coccoliths) together with rare siliceous diatoms (Mayer et al., 1992; Flores et al., 1995).

4.4.2 Stable-isotope analysis

A total of 229 samples from ODP Site 849 between 74.16 and 67.78 mcd were analyzed for foraminiferal stable oxygen- and carbon-isotope compositions ($\delta^{18}O$ and $\delta^{13}C$). To develop the benthic $\delta^{18}O$ and $\delta^{13}C$ records, an average of six specimens of the benthic foraminifera *Cibicidoides wuellerstorfi* were picked from the >150 μm dried sediment fraction of all samples. The resulting dataset was supplemented by the dataset of Mix et al. (1995) (35 samples also based on *C. wuellerstorfi*), yielding a total of 264 stable-isotope data points for our $\delta^{18}O$ and $\delta^{13}C$ stratigraphy.

Specimens of the planktic foraminifera *Globigerinoides ruber* (white) were used to characterize the sea-surface $\delta^{13}C$ variability across the study interval. We used the morphotype *G. ruber* sensu stricto (s.s.), which thrives in shallower waters of the upper mixed layer than *G. ruber* sensu lato (s.l.) and thus yields lower $\delta^{18}O$ and higher $\delta^{13}C$ values (e.g., Wang, 2000; Steinke et al., 2005). On average, 11 specimens of *G. ruber* s.s were picked per sample. A narrow size range of 250–315 μm was chosen to avoid ontogenetic effects (Elderfield et al., 2002; Friedrich et al., 2012).

To monitor changes in the thermocline, we followed the approach of Ravelo and Fairbanks (1992) and Kemle von Mücke and Oberhänsli (1999) and generated a $\delta^{13}C$ record of the planktic foraminifera *Globorotalia crassaformis*. To avoid ontogenetic effects, *G. crassaformis* was picked from the 315–400 μm dried sediment fraction (Elderfield et al., 2002). An average of 19 specimens was picked per sample. Many planktic foraminifera, such as *G. crassaformis*, have a dextral and a sinistral coiling form. We preferentially selected the most abundant coiling direction (sinistral). However, the sinistral coiling forms did not occur continuously over the sampling interval. Thus, we also used the dextral coiling tests for some intervals. Comparison between $\delta^{13}C$ measurements of sinistral and dextral coiling forms within the same sample indicates that there is no defined offset in $\delta^{13}C$ between specimens with different coiling directions (see Figure A.1.2 in Appendix A.1). Thus, whenever required, we spliced together records of sinistral and dextral coiling forms of *G. crassaformis* without applying an intertaxon adjustment factor.

Stable isotopes were measured at the Institute of Geosciences, Goethe University Frankfurt (Germany), using a ThermoFinnigan MAT253 gas source mass spectrometer equipped with a Gas Bench II. The results are reported relative to Vienna Pee Dee Belemnite (VPDB) through the analysis of an in-house standard calibrated to NBS-18 and NBS-19. Analytical precision was better than 0.08‰ and 0.06‰ (at 1σ level) for oxygen and carbon isotopes, respectively. Following Shackleton and Hall (1984), $\delta^{18}O$ values of *C. wuellerstorfi* reported herein were adjusted for species-specific offset from equilibrium by the addition of +0.64‰ (see Table 2.1 in Chapter 2). *Cibicidoides wuellerstorfi* precipitates its shell close to $\delta^{13}C$ equilibrium; thus, no adjustment factor is required (e.g., Zahn et al., 1986; Mackensen et al., 1993). $\delta^{13}C$ values of *G. ruber* were adjusted by the addition of +0.94‰ according to the $\delta^{13}C$ normalization of Spero et al. (2003). The lack of laboratory investigations into $\delta^{13}C$ fractionation in *G. crassaformis* dictates that we simply report the $\delta^{13}C$ values measured on this species (no adjustment factor).

4.4.3 Preservation of foraminiferal tests

To assess the preservation of planktic foraminiferal tests used for stable-isotope analysis at Site 849, selected specimens representing both glacial and interglacial intervals were examined using a LEO 440 scanning electron microscope (SEM) at the Institute of Earth Sciences, Heidelberg University. Further, we determined a planktic foraminiferal fragmentation index (FFI) at G-IG resolution following Le and Shackleton (1992) and Le et al. (1995):

$$FFI\ [\%] = (\text{number of fragments}/8) \times (\text{number of fragments}/8 + \text{complete tests})^{-1} \times 100\%$$

The number of fragments (part of a test which is less than two thirds of an original test [Berger et al., 1982]) and of complete planktic foraminiferal tests was counted on at least 300 specimens (using a microsplitter) from aliquots of the >150 μm size fraction. The number of fragments was divided by 8 because a foraminiferal test on average splits into eight fragments (Le and Shackleton [1992] and Saraswat [2015] for a review).

4.4.4 Sand, foraminiferal, and radiolarian accumulation rates

To identify changes in sea-surface productivity in these biogenic sediments, accumulation rates of the sand fraction (SAR; suborbital resolution), of planktic foraminifera (PFAR; G-IG resolution), and of radiolarians (RAR; G-IG resolution) were calculated according to Herguera and Berger (1991):

SAR [g cm^{-2} kyr^{-1}] = DBD x LSR x SF

PFAR [number of specimens cm^{-2} kyr^{-1}] = DBD x LSR x PF

RAR [number of specimens cm^{-2} kyr^{-1}] = DBD x LSR x R

where DBD is the dry bulk density (g cm^{-3}), LSR is the linear sedimentation rate (cm kyr^{-1}), SF is the portion of the >63 μm sand fraction per gram dry sediment, PF is the number of planktic foraminifera per gram dry sediment (>63 μm), and R is the number of radiolarians per gram dry sediment (>63 μm). The number of planktic foraminifera and radiolarians was counted on at least 300 specimens (using a microsplitter) from aliquots of the >63 μm fraction. Because the resolution of available DBD data for the herein investigated time interval at Site 849 is insufficient, DBD was calculated from high-resolution GRAPE density (g cm^{-3}) shipboard measurements (IODP JANUS database [Mayer et al., 1992]) using an equation developed for lithologic homogeneous samples of Hole 849B (Hovan, 2013) as a reference (R^2 = 0.93, p <0.01, number of samples = 158; see Figure A.1.3 in Appendix A.1):

DBD [g cm^{-3}] = 1.58 x GRAPE - 1.61

4.4.5 Cross-spectral analyses

To identify coherencies and to quantify phase lags between records, Blackman-Tukey cross-spectral analyses with 30% overlap were conducted using the AnalySeries software package version 2.0.8 (Paillard et al., 1996). Data for cross-spectral analyses were linearly interpolated, detrended, and prewhitened.

4.5 Results and discussion

4.5.1 Chronology

Our age model for Site 849 (Figure 4.2 and Table A.1.1 in Appendix A.1) was constructed by visual correlation of the benthic oxygen-isotope record (including benthic $\delta^{18}O$ data of Mix et al. [1995]) to the LR04 stack (Lisiecki and Raymo, 2005) using the AnalySeries software package version 2.0.8 (Paillard et al., 1996). To minimize errors during tuning, only one tie point at the midpoint of each G-IG $\delta^{18}O$ transition was used (e.g., Bolton et al., 2010c).

Our high-resolution $\delta^{18}O$ record of *C. wuellerstorfi* shows a clear G-IG cyclicity, with lower values during interglacial stages (mean: 3.52‰; minimum value: 3.02‰) and highest values during glacial stages (mean: 3.89‰; maximum value: 4.31‰; Figures 4.2a and 4.2b). The spike in benthic $\delta^{18}O$ during MIS 102, which represents the lowest values of the entire record,

consists of two independently generated data points (this study and Mix et al. [1995]). Core images taken during core sampling show no sign of local reworking for this core section. Therefore, it appears reasonable to assume that this spike is real, albeit peculiar.

The new chronology for Site 849 results in a mean temporal sample resolution of 780 years and an average linear sedimentation rate of 2.6 cm kyr^{-1} for the time interval between 2.65 and 2.4 Ma (Figure 4.2c). These sedimentation rates are in close agreement with those of other records published for the late Pliocene/early Pleistocene from the EEP region (e.g., Deep Sea Drilling Project Site 572: 2.1 cm kyr^{-1} [Mayer et al., 1985] [Figure 4.1a] and ODP Site 849: 2.5–3.0 cm kyr^{-1} [Mix et al., 1995]).

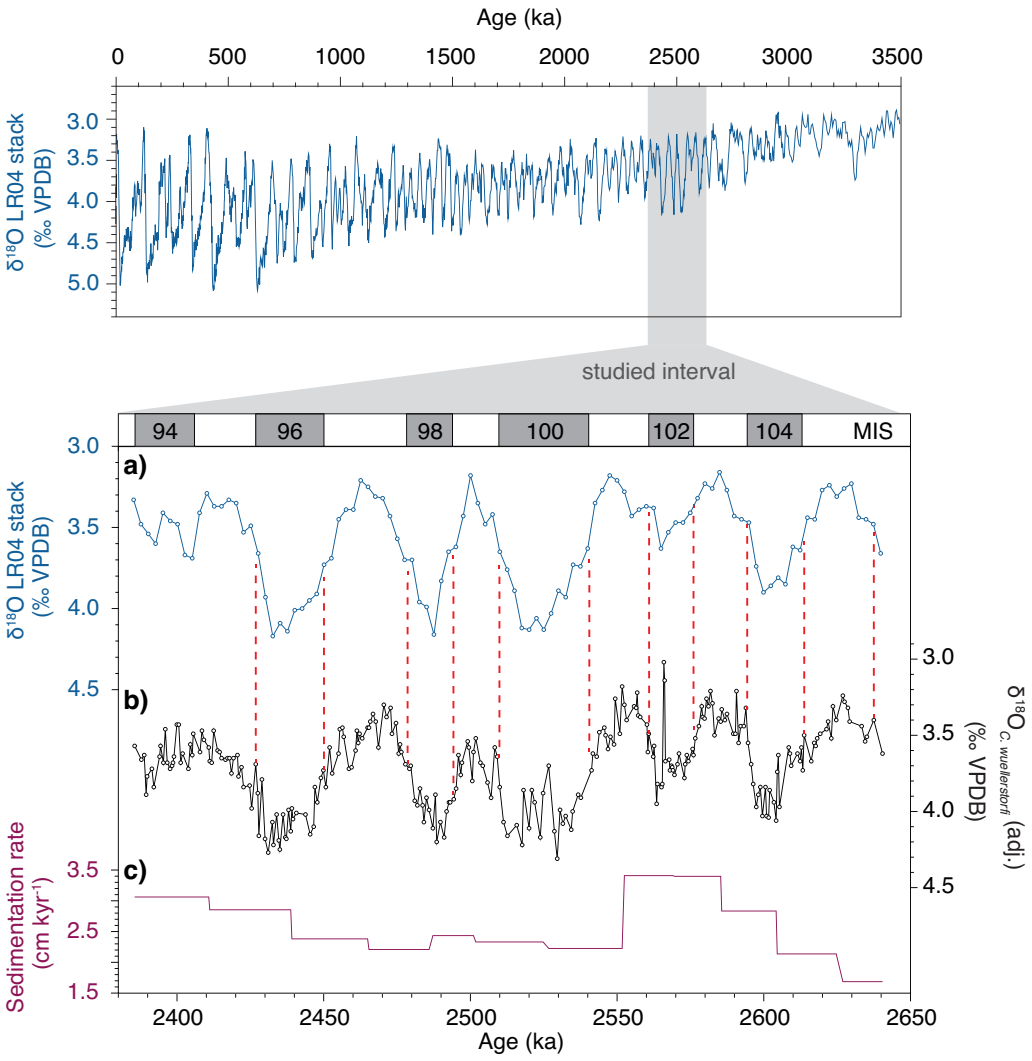

Figure 4.2. (top) Global benthic foraminiferal $\delta^{18}O$ record (Lisiecki and Raymo, 2005) for the last 3.5 Myr (LR04 stack). **(bottom)** Age model from ODP Site 849 for 2640 to 2385 ka, tuned to the LR04 stack (Lisiecki and Raymo, 2005). **(a)** LR04 stack for MIS G1 to 94 (Lisiecki and Raymo, 2005). **(b)** Benthic foraminiferal (*C. wuellerstorfi*) $\delta^{18}O$ record from Site 849; this record contains a combination of our own measurements and data from Mix et al. (1995). **(c)** Average linear sedimentation rates (cm kyr^{-1}). Red dashed lines in Figures 4.2a and 4.2b show the tie points for tuning. Tuning points are provided in Table A.1.1 (Appendix A.1).

We also decided to re-tune the benthic $\delta^{18}O$ record from Site 846 (Shackleton et al., 1995) to the LR04 stack (Lisiecki and Raymo, 2005) over the time interval 2.65 to 2.4 Ma (Figures 4.3a and 4.3b; Table A.1.2 in Appendix A.1) although these benthic $\delta^{18}O$ data are part of the LR04 stack. Reasons for this are threefold: (i) The Site 846 $\delta^{18}O$ record is not an initial alignment target (using original terminology of Lisiecki and Raymo [2005, p. 5]) for the LR04 stack for the time interval investigated in this study, i.e., 23 more $\delta^{18}O$ records besides the $\delta^{18}O$ record from Site 846 feed the LR04 stack between 2.65 and 2.4 Ma (Lisiecki and Raymo, 2005). (ii) Comparison of the $\delta^{18}O$ record from Site 846 (Shackleton et al., 1995) with LR04-tuned benthic $\delta^{18}O$ from Site 849 demonstrates significant discrepancies (Figure 4.3c). This is most likely a consequence of the different tuning techniques. (iii) Therefore, exactly the same tuning procedures have been applied (i.e., using only one tie point at the midpoint of each G-IG $\delta^{18}O$ transition) to allow for the best possible comparison between sites.

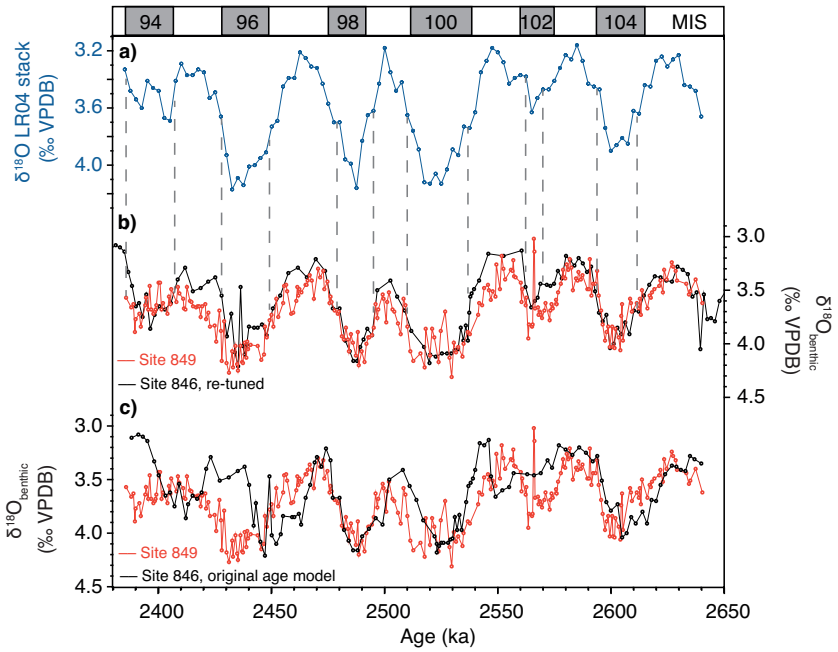

Figure 4.3. Age model from ODP Site 846 for MIS G1 to 94 (2640 to 2385 ka). **(a)** LR04 stack for MIS G1 to 94 (Lisiecki and Raymo, 2005). **(b)** Re-tuned benthic foraminiferal $\delta^{18}O$ record from Site 846 (black) compared to benthic foraminiferal $\delta^{18}O$ from Site 849 (red). **(c)** Benthic foraminiferal $\delta^{18}O$ record from Site 846 (original age model [black] [Shackleton et al., 1995]) and Site 849 (red). Grey dashed lines in Figures 4.3a and 4.3b show the tie points for tuning. Tuning points are provided in Table A.1.2 (Appendix A.1).

4.5.2 Preservation of planktic foraminiferal tests

While low-resolution shipboard investigations on core catchers report poor preservation of planktic foraminiferal tests at Site 849 (Mayer et al., 1992), none of these observations correspond to samples from our study interval. Scanning electron microscope images of both

glacial and interglacial samples from our sample set indicate that the preservation of planktic foraminifers is consistently good enough to acquire high-quality stable-isotope data (see Sexton et al., 2006) throughout the target interval (Figure 4.4). This interpretation is confirmed by relatively low mean FFIs at Site 849 (~5%; Figure 4.5b) compared to previous published FFIs from Site 846 for the last 0.8 Myr (~9% [Le et al., 1995]) and from Site 849 for the last G-IG cycle (~6 to 18% [Marchitto et al., 2005]), indicating that the effect of dissolution on planktic foraminiferal tests was minor throughout our study interval.

Furthermore, in contrast to the late (early) Pleistocene Pacific Ocean carbonate dissolution pattern, in which maximum fragmentation is usually seen during interglacials (glacials) (e.g., Le and Shackleton, 1992; Le et al., 1995; Marchitto et al., 2005; Lalicata and Lea, 2011; Sexton and Barker, 2012), FFIs at Site 849 show no G-IG pattern over the interval of study. This is evidenced by a lack of a statistically significant correlation between FFI and benthic $\delta^{18}O$ at Site 849 throughout the interval of study ($R^2 = 0.004$, $p = 0.74$; see Figure A.1.4 in Appendix A.1).

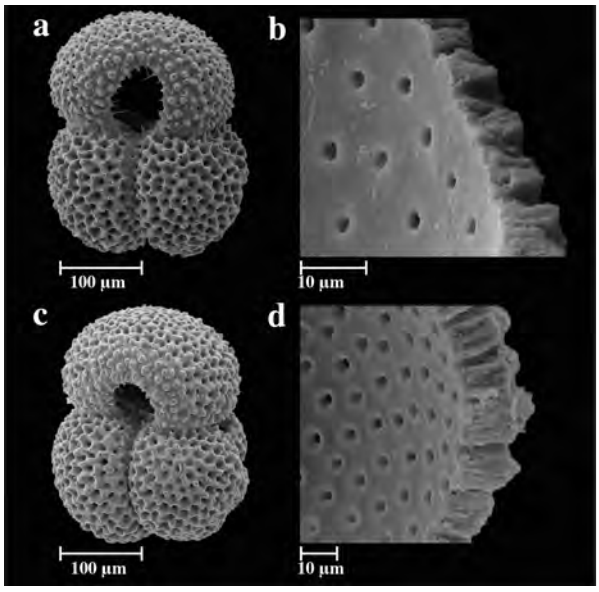

Figure 4.4. Scanning electron micrographs of *Globigerinoides ruber* (s.s.) from EEP Site 849. Both interglacial **(a, b)** (sample 849D-6H-6-6 cm to 849D-6H-6-8 cm) and glacial **(c, d)** (sample 849C-7H-1-146 cm to 849C-7H-1-148 cm) foraminiferal tests are well preserved, allowing for the acquisition of reliable stable-isotope data. Note the preservation of delicate spines in the aperture region.

4.5.3 Glacial-interglacial variations in the sand-accumulation rate as a tracer for paleoproductivity

The SAR record at Site 849 shows a clear G-IG cyclicity from MIS 100 onward, with lowest values toward the end of each interglacial-to-glacial transition (minimum value: 0.04 g cm^{-2} kyr^{-1}) and progressively increasing values starting at peak glacials and culminating at glacial

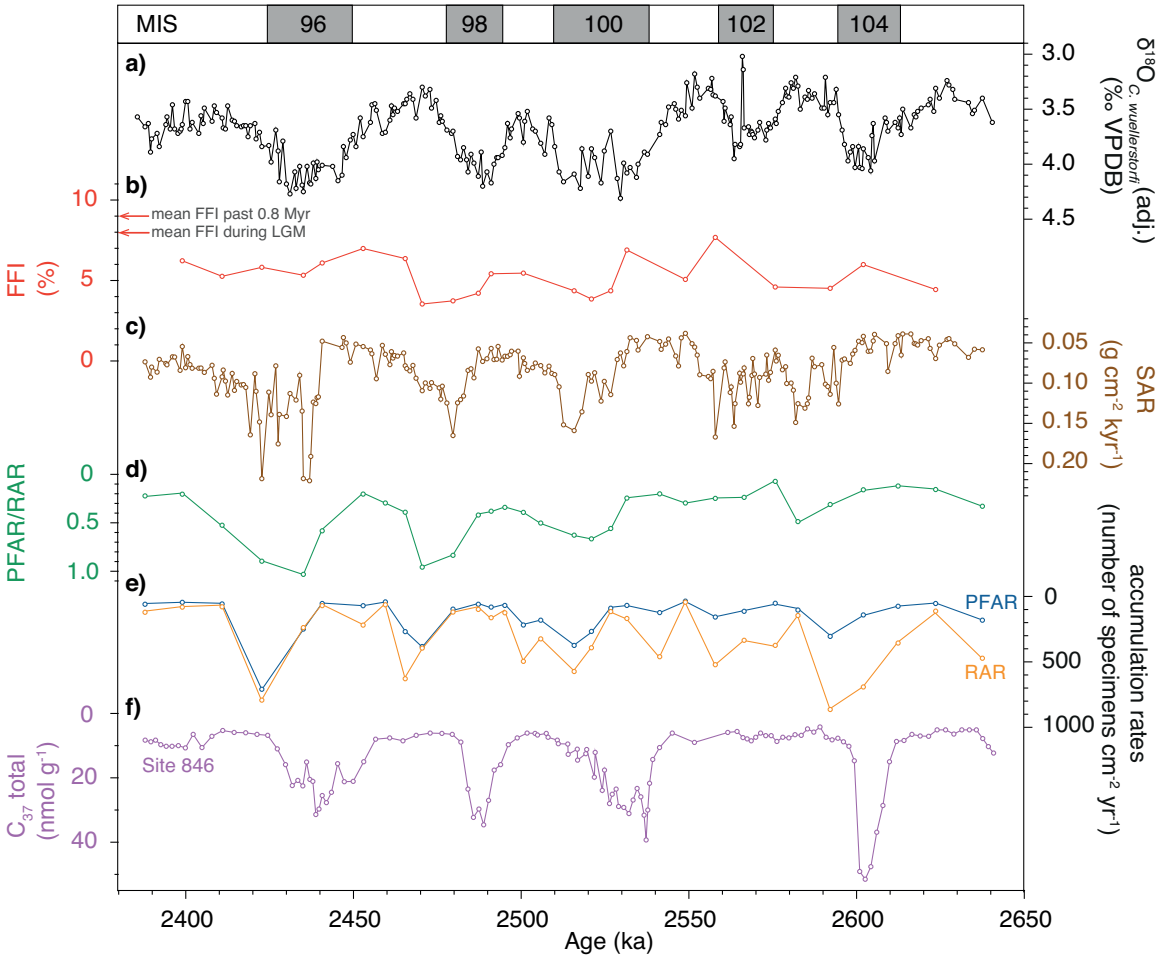

Figure 4.5. Dissolution and productivity proxy records from the EEP upwelling system. **(a)** $\delta^{18}O$ in benthic foraminifera (*C. wuellerstorfi*) from Site 849 (this study). **(b)** Percentage planktic foraminiferal fragmentation from Site 849 (this study). Red arrows depict mean FFIs for the past 0.8 Myr at Site 846 (~9% [Le et al., 1995]) and for the LGM at Site 849 (~8% [Marchitto et al., 2005]). Holocene FFIs reach ~16% at Site 849 (Marchitto et al., 2005) and ~30% (Le et al., 1995) at Site 846. **(c)** Sand-accumulation rates (>63 µm) from Site 849 (this study). **(d)** Ratio between planktic foraminiferal and radiolarian accumulation rates at Site 849 (this study). **(e)** Planktic foraminiferal accumulation rates (blue) and radiolarian accumulation rates (orange) at Site 849 (this study). **(f)** C_{37} alkenone abundances from Site 846 (Lawrence et al., 2006) re-tuned to the LR04 stack.

terminations (maximum value: 0.22 g cm^{-2} kyr^{-1}; Figure 4.5c). Such G-IG variations also seem to appear prior to MIS 100, but that signal is much less distinct. There are at least three processes to consider when interpreting this record. First, SARs in deep-sea sites are often interpreted as an indicator of carbonate dissolution (e.g., Johnson et al., 1977; Wu et al., 1990; Bassinot et al., 1994). A second possibility is that changes in the sand fraction are controlled by changes in export productivity (Diester-Haass et al., 2002), and a third possibility is that SARs are controlled by the strength of bottom-water currents leading to winnowing (Berstad et al., 2003). Although we cannot completely rule out sediment redistribution as a controlling mechanism for SARs at Site 849 (e.g., Pichat et al., 2004), present-day bottom-water current speeds in this region are generally less than ~10 cm s^{-1} (Johnson, 1972), i.e., too sluggish to

redistribute coarser particles (Beaulieu, 2002). Therefore, we suggest that in a deep open-ocean setting such as the deep equatorial Pacific with a relatively flat topography, sand redistribution by the relatively weak deep-sea bottom water currents is unlikely (Paytan et al., 2004). Based on the lack of statistically significant correlation between SAR and FFI ($R^2 = 0.03$, $p = 0.35$; see Figure A.1.4 in Appendix A.1), we also exclude a major influence of carbonate dissolution on SAR (see also Chapter 4.5.2).

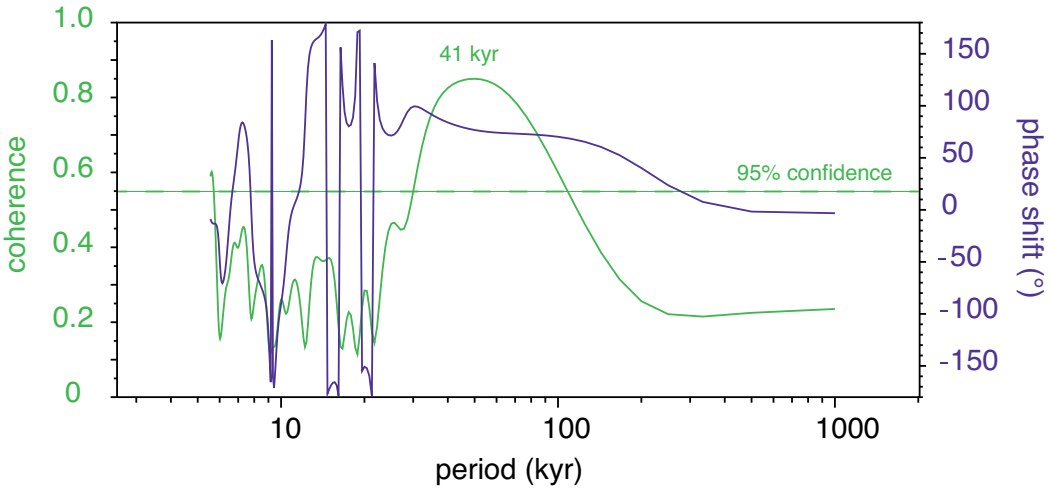

Figure 4.6. Blackman-Tukey cross-spectral analysis for the identification of phase shifts at Site 849 for the time interval from ~2.65 to 2.4 Ma at the 95% confidence level. Coherence (green) and phase (purple) relationship between global ice volume ($\delta^{18}O_b$) and productivity (SAR) from Site 849 are plotted on log scales. Positive values in this phase plot indicate that productivity lags global ice volume, i.e., by 82.2° (equal to -9.5 kyr) for the 41 kyr period.

Contrary to our findings from Site 849, observations from ODP Site 846 (Figure 4.5f) based on C_{37} alkenone accumulation rates (Lawrence et al., 2006), and calcareous nannofossil assemblages and siliceous fragment fluxes (Lawrence et al., 2006; Bolton et al., 2010b) demonstrate that primary productivity was highest during full glacials MIS 104, 100, 98, and 96, nearly in phase with benthic $\delta^{18}O$ (lead of ~2 to 3 kyr [Lawrence et al., 2006]; see also Figure A.1.6 in Appendix A.1). There are at least two processes to consider when interpreting these findings. First, productivity records from Site 849 and 846 are based on different proxies, namely, zooplankton (Site 849) and haptophyte algae (Site 846). Second, the observed lag of ~11 kyr in peak productivity between Site 849 (SAR, termination) and Site 846 (C_{37} alkenone accumulation rates, nearly peak glacial) represents a real time lag that is too large to result from age model discrepancies (Figures 4.3, 4.6; Figure A.1.6 in Appendix A.1), suggesting that biological production at Sites 846 and 849 was regulated by different mechanisms at least during these late Pliocene/early Pleistocene glacials. We note that secular timescale changes in export productivity over the Plio-Pleistocene also appear to be

decoupled between Sites 846 and 849 (Ma et al., 2015), suggesting that different mechanisms or nutrient sources drive productivity in these two distinct regions of the highly heterogeneous EEP (Pennington et al., 2006).

It has been suggested that the Panamanian Gateway was closed during MIS 100 to 98, opened during MIS 97, and closed again toward the end of MIS 96 (Groeneveld et al., 2014). Assuming that CAS closure helps to promote upwelling in the EEP (Schneider and Schmittner, 2006), we might expect these closures to result in increased export production during MIS 100, 99, and 98, low productivity rates during MIS 97, and again enhanced productivity toward the end of MIS 96. However, this is not consistent with our SAR record at least for MIS 100 to 98, which documents significant G-IG changes in export production at Site 849 between MIS 100, 99, and 98 (Figures 4.5c; Figure A.1.7 in Appendix A.1). Thus, we suggest that the influence of temporary full CAS closure on upwelling intensification at Site 849 plays only a minor role in regulating G-IG upwelling changes across the studied succession. Furthermore, we find no evidence to suggest that dust input played a major role in controlling the observed changes in export production at Site 849. The reasons for this interpretation are twofold: (i) In our records maximum productivity occurs during glacial terminations at least during MIS 100, 98, and 96 (Figure 4.5c), while, based on late Pleistocene records, we might expect dust input at Site 849 to have peaked during full glacial conditions (McGee et al., 2007; Winckler et al., 2008), and (ii) low-resolution data on aeolian dust flux from Leg 138 yield no evidence for G-IG changes in dust input to the EEP across the studied time interval (Hovan, 1995). This interpretation is consistent with a study of export production from the central equatorial Pacific covering iNHG, indicating that iron supply is not responsible for changes in export production (Ziegler et al., 2008).

To decipher the importance of wind-driven upwelling *versus* mode water nutrient supply on observed G-IG changes in primary productivity at Site 849, we use the carbon-isotope signature of benthic, thermocline-, and sea surface-dwelling foraminiferal species.

4.5.4 $\delta^{13}C$ values at Site 849 trace glacial-interglacial changes in delivery of macronutrients to the equatorial Pacific from the Southern Ocean

The $\delta^{13}C$ signature of foraminiferal tests is routinely used as a proxy for surface-water primary productivity (e.g., Zahn et al., 1986; Sarnthein et al., 1988; Mackensen and Bickert, 1999). An increase in primary productivity during times with a strong and efficient biological pump increases $\delta^{13}C$ values in the surface water (traceable in surface-dwelling planktic

foraminifera, $\delta^{13}C_s$) and progressively decreases $\delta^{13}C$ values with increasing water depth (recorded in thermocline-dwelling planktic foraminifera, $\delta^{13}C_t$, and benthic foraminifera, $\delta^{13}C_b$). In our dataset, all three $\delta^{13}C$ records show a clear G-IG cyclicity with higher $\delta^{13}C$ values during interglacials and lower $\delta^{13}C$ values during glacials (Figures 4.7a–d). This trend is weak, however, during MIS 102 suggesting that associated environmental change during this modest glacial was too subtle to induce larger-scale changes in the mechanisms that controlled benthic and planktic foraminiferal $\delta^{13}C$. The parallel trends and relatively constant gradients in our $\delta^{13}C_b$ (*C. wuellerstorfi*) and $\delta^{13}C_{s,t}$ (*G. ruber* and *G. crassaformis*) records (Figures 4.7b–d; Figure A.1.8 in Appendix A.1) suggest that the foraminiferal $\delta^{13}C$ at Site 849 does not simply trace in situ changes in the strength of the biological pump during the interval of study, and an alternative explanation for the observed pattern is required.

We must also consider the possibility that our $\delta^{13}C$ records reflect changes in the isotopic signature of source waters (Southern Ocean Water [SOW] and Antarctic Bottom Water [AABW]) that feed the equatorial Pacific upwelling system. For our interval of study, the best available $\delta^{13}C_b$ records for approximating isotopic change in Southern Ocean waters end-member values (Billups et al., 2002; Pusz et al., 2011) are those from South Pacific Site MV0502-4JC (50°20′S, 148°08′W, 4286 m water depth [Waddell et al., 2009]; Figure 4.1a) and from South Atlantic ODP Site 1090 (42°55′S, 8°54′E, 3702 m water depth [Hodell et al., 2003]; Figure 4.1a). These records have similar absolute values and G-IG amplitude to our record from Site 849, suggesting that $\delta^{13}C_b$ values recorded at Site 849 bear a high-latitude Southern Ocean signature (see Figure A.1.9 in Appendix A.1). Crucially, our benthic and planktic foraminiferal $\delta^{13}C$ records from Site 849 show very similar trends to one another, lending support to the idea that our records are controlled by changes in the isotopic composition of the upwelled waters sourced in the high-latitude Southern Ocean from MIS G1 to 95, with minor G-IG fluctuations prior to MIS 100 and larger-scale G-IG changes from MIS 100 onward.

Contrary to the observed pattern of change in our SAR record, visual evaluation of Figures 4.7a–d indicates that carbon-isotope records do not lag $\delta^{18}O$. Hence, we infer that productivity at Site 849 as recorded by our SAR record was stimulated by changes in water-mass properties (i.e., nutrient content) at the beginning of glacials MIS 100, 98, and 96 and further escalated toward terminations.

To conclude, the covariance as well as the constant offset observed between our $\delta^{13}C_{s,t}$ and $\delta^{13}C_b$ records from Site 849 can be explained when interpreting these records as tracers of

Southern Ocean water-mass signatures. This observation lends strong support to the hypothesis that Plio-Pleistocene surface-water properties in the EEP largely result from high-latitude forcing.

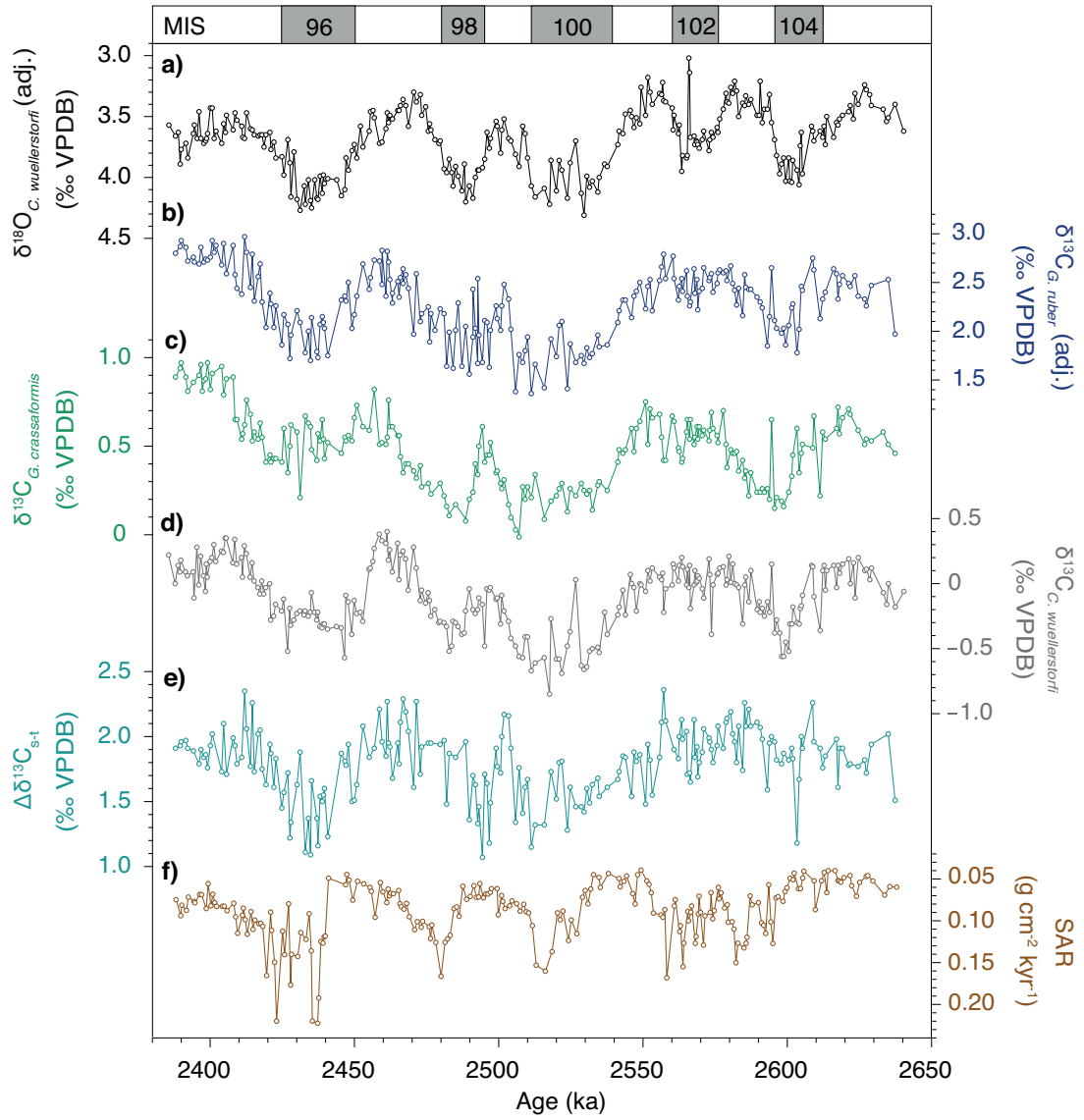

Figure 4.7. High-resolution foraminiferal $\delta^{13}C$ proxy records from Site 849. **(a)** Benthic foraminiferal (*C. wuellerstorfi*) $\delta^{18}O$ record. **(b)** $\delta^{13}C$ record of the sea surface-dwelling planktic foraminifera *G. ruber*. **(c)** $\delta^{13}C$ record of the subthermocline-dwelling planktic foraminifera *G. crassaformis*. **(d)** $\delta^{13}C$ record of the benthic foraminifera *C. wuellerstorfi*. **(e)** $\delta^{13}C$ gradient between *G. ruber* and *G. crassaformis*. **(f)** Sand-accumulation rates (>63 µm).

4.5.5 Evidence for superimposed strengthened trade wind-induced upwelling in the equatorial Pacific during glacial terminations 100 through 96

In light of our SAR record, it seems that productivity at Site 849 starts to increase during full glacial conditions in response to enhanced nutrient delivery from high southern latitudes (as evidenced by our $\delta^{13}C$ records) and culminates, toward glacial terminations, possibly in

response to local intensification in upwelling. To test for the hypothesized influence of upwelling intensification on biological production at Site 849, we make use of vertical $\delta^{13}C$ gradients between sea-surface (*G. ruber*, $\delta^{13}C_s$) and thermocline-dwelling (*G. crassaformis*, $\delta^{13}C_t$) foraminifera ($\Delta\delta^{13}C_{s-t}$). This gradient is a useful proxy to decipher changes in the depth of the thermocline (e.g., Pierre et al., 2001), which in turn is related to upwelling intensity. In the case of increased upwelling strength, the thermocline shoals, resulting in lower $\Delta\delta^{13}C_{s-t}$.

Our $\Delta\delta^{13}C_{s-t}$ record (Figure 4.7e) shows relatively constant values prior to MIS 100, indicating that upwelling intensity was stable from ~2.64 to ~2.56 Ma. For the interval spanning MIS 100 to 96, however, a decrease in the $\Delta\delta^{13}C_{s-t}$ gradient of >1‰ occurred during glacials, reaching its minimum value toward glacial terminations (Figure 4.7e). This suggests a prominent shoaling of the thermocline probably in response to intensified regional upwelling during terminations, a mechanism which was activated from MIS 100 onward at least during the investigated time interval (see Chapter 4.6.2).

4.6 Primary productivity variability in the Eastern Equatorial Pacific: a response to glacial-interglacial ice sheet dynamics?

Our results point to G-IG changes in export productivity in the equatorial Pacific Ocean during the culmination of iNHG, controlled by nutrient supply from the Southern Ocean and superimposed wind-driven upwelling during MIS 100, 98, and 96. Next we explore potential mechanisms for these linkages that involve G-IG waxing and waning of the LIS and sea-ice extent in the Southern Ocean.

The LIS and Southern Ocean sea-ice coverage have the potential to affect the EEP upwelling system in at least two ways. First, G-IG changes in the size of the LIS are a main controlling factor for meridional pressure gradients that regulate trade-wind intensity and equatorial upwelling strength (e.g., Pisias and Mix, 1997, and references therein; Oster et al., 2015). Second, G-IG changes of Antarctic sea-ice coverage control, through light limitation, the rate of biological production and thus the nutrient content in the Southern Ocean surface waters (e.g., Nürnberg et al., 1997; Bonn et al., 1998; Hillenbrand and Cortese, 2006). Because Antarctic and sub-Antarctic surface waters are the major source for the upwelled water in the EEP (e.g., Toggweiler et al., 1991; van de Flierdt et al., 2004; Sarmiento et al., 2004), changes in the composition of this water mass may strongly influence the rate of primary productivity in the EEP upwelling system.

4.6.1 Strong control of primary productivity in the equatorial Pacific upwelling system by sea-ice coverage in the Southern Ocean

One implication of our $\delta^{13}C$-based interpretation of G-IG changes in nutrient supply to the equatorial Pacific is that Southern Ocean biological production was higher during interglacials than during glacials during iNHG (Sigman et al., 2004; Hillenbrand and Cortese, 2006), presumably because of reduced sea-ice coverage (Hillenbrand and Cortese, 2006). This picture is analogous to reconstructions of the late Pleistocene Southern Ocean (e.g., Charles et al., 1991; Mortlock et al., 1991). At Site 849, high interglacial $\delta^{13}C$ signatures are seen in our records in response to the enhanced Southern Ocean biological production (Figure 4.8a). This suggestion gains support from the similarity between the $\delta^{13}C_b$ record from Site 849 and the $\delta^{13}C_b$ record from Site MV0502-4JC (Waddell et al., 2009), which is located within the pathway of AABW water mass advection from their high-latitude source area to the EEP (see Chapter 4.5.4 and Figure A.1.9 in Appendix A.1). Through mixing of the AABW with SOW and upwelling to the sea surface at Site 849, this high interglacial $\delta^{13}C$ signature is also imprinted in planktic thermocline- and sea-surface-dwelling foraminiferal tests as seen in our records (Figures 4.7b–d). Moreover, reduced nutrient supply, resulting from the upwelling of relatively nutrient-depleted water masses sourced in the Southern Ocean, limits the biological production in the EEP during interglacials, as documented in our productivity records and in the paleoproductivity proxy data from Site 846 (Lawrence et al., 2006; Bolton et al., 2010b) (Figure 4.5).

The opposite signal is seen during glacials (Figure 4.8b) when biological production in the Southern Ocean is reduced compared to interglacials, probably because of light limitation in response to increased Antarctic sea-ice cover as argued for late Pleistocene glacials (e.g., Nürnberg et al., 1997; Bonn et al., 1998; Hillenbrand and Cortese, 2006). Reduced glacial primary productivity in the Southern Ocean results in less efficient use of nutrients and a slowdown of the biological pump, an observation that has also been recorded for the LGM (Mortlock et al., 1991). In response to reduced phytoplankton activity, $\delta^{13}C$ in high-latitude sea-surface waters decreases during glacials. The downwelled Southern Ocean surface waters bear this low glacial $\delta^{13}C$ signature and feed the AABW and the SOW and thus ultimately the upwelling system in the EEP (Tsuchiya et al., 1989; Toggweiler et al., 1991). At Site 849, the inherited low glacial $\delta^{13}C$ signatures of the AABW and the SOW are recorded by benthic and planktic sea-surface and thermocline-dwelling foraminifera, respectively (Figures 4.7b–d). Furthermore, the enhanced glacial nutrient content of the source water leads to an increase in

primary productivity within the EEP. This is documented by paleoproductivity records from Sites 849 (this study) and 846 (Lawrence et al., 2006; Bolton et al., 2010b) (Figure 4.5).

Our benthic and planktic foraminiferal $\delta^{13}C$ records indicate that nutrient delivery from high southern latitudes was active during the investigated time interval, but only with minor implications for G-IG primary productivity changes in the EEP prior to MIS 100 compared to the time interval from MIS 100 onward. We suggest that this is a consequence of less significant changes in Antarctic sea-ice extent during the relatively weak glacials MIS 102 and 104.

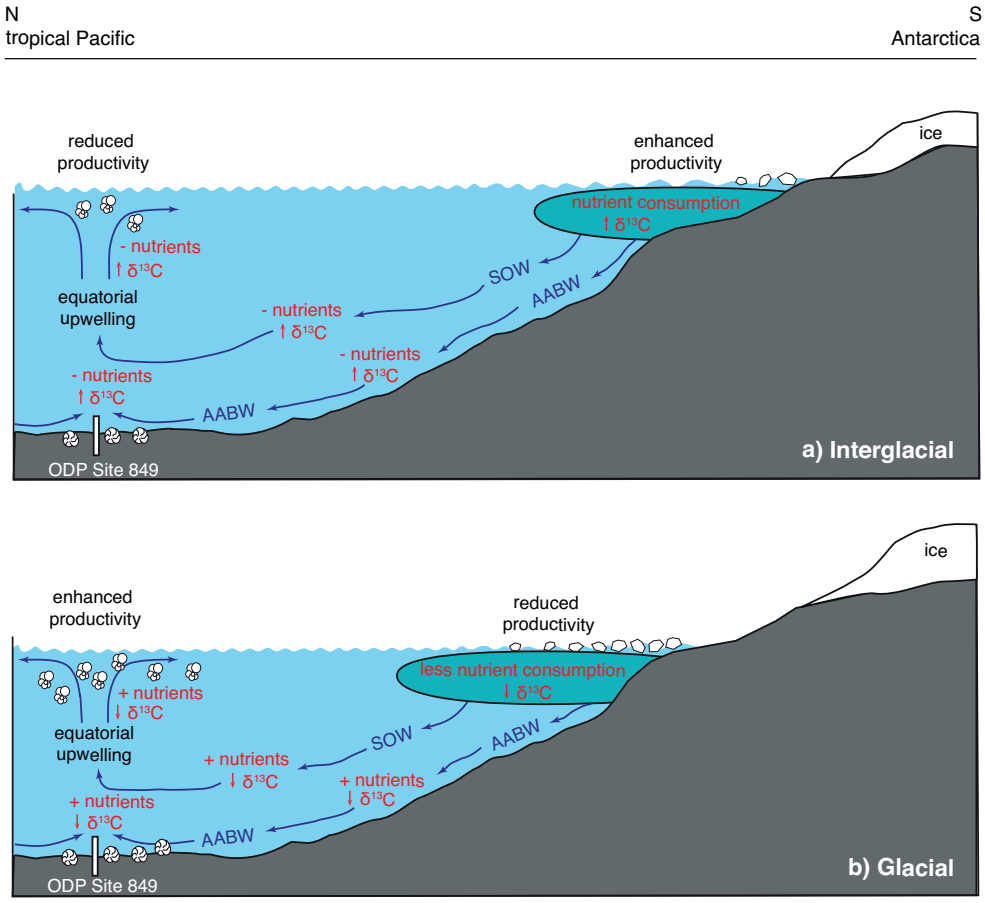

Figure 4.8. Schematic north-south section of the South Pacific Ocean from Antarctica/Southern Ocean to the EEP upwelling system. Primary productivity and resulting nutrient utilization and $\delta^{13}C$ signatures are proposed for early Pleistocene **(a)** interglacial and **(b)** glacial periods. AABW: Antarctic Bottom Water; SOW: Southern Ocean Water.

4.6.2 Superimposed enhanced upwelling during glacial terminations from MIS 100 onward in response to retreat of the Laurentide Ice Sheet?

In addition to the enhanced glacial nutrient delivery from the Southern Ocean to the EEP upwelling regime, we suggest that the rate of wind-induced upwelling of nutrients at Site 849 significantly increased toward glacial terminations MIS 100, 98, and 96. As evidenced by

decreasing $\Delta\delta^{13}C_{s\text{-}t}$ values (compare Chapter 4.5.5 and Figure 4.7e), wind-driven upwelling intensification was active from MIS 100 onward at least during the investigated time interval. The timing of the onset of this behavior is unlikely to be a coincidence. Marine Isotope Stage 100 was the first glacial to result in ice rafting throughout the open North Atlantic Ocean (e.g., Shackleton et al., 1984a). Its significance for the equatorial Pacific Ocean may lie in being the first glacial during which the LIS advanced into the midlatitudes of North America (Naafs et al., 2013), something that perhaps did not occur again until ~1.3 Ma (Balco and Rovey, 2010). Studies of the LGM suggest that a large LIS is associated with major changes in atmospheric circulation well beyond North America (e.g., Oster et al., 2015). The profile of the LIS during MIS 100 must have been lower slung than its late Pleistocene counterparts, probably in response to ready flow on soft nonpreglaciated substrates (Clark and Pollard, 1998; Bailey et al., 2010), but LIS height and extent during iNHG and MIS 100 in particular had a major impact on hydroclimate, both over the ice sheet itself (Bailey et al., 2010) and beyond the ice front in the midlatitudes (Naafs et al., 2012; Hennissen et al., 2014, 2015; Lang et al., 2014) and perhaps into the arid North American southwest (Lang et al., 2014).

Our data suggest enhanced glacial equatorial upwelling strength during our study interval from MIS 100 onward implying strengthened meridional pressure gradients and trade-wind intensity. Export production (SAR), however, lags global ice volume (benthic $\delta^{18}O$) by ~9.5 kyr in our records (Figure 4.6). Similar observations have been made for the past 1 Myr and for the LGM at central equatorial Pacific Sites PC72 (Murray et al., 2000) and U1338 (Lyle and Baldauf, 2015), EEP Site 849 (Ma et al., 2015), and northeast Pacific Site NH22P (Ganeshram et al., 2000; Kienast et al., 2002) (Figure 4.1a). Explanations for this lagged relationship are speculative. Suggestions include (i) upwelling intensification during glacial terminations (Kienast et al., 2002; Hayes et al., 2011) and/or (ii) deglacial nutrient supply from continental shelves either during sea-level rise associated with glacial terminations ("glacial outwash" [Ma et al., 2015]) or during sea-level fall associated with glacials (Flores et al., 2012), assuming a lag between cause (weathering on exposed shelves) and effect (nutrient delivery to the deep ocean) of 10–20 kyr ("shelf sediment offloading" [Filippelli et al., 2007; Markovic et al., 2015]). We do not favor nutrient input from continental shelves attributable to glacial outwash or shelf sediment offloading to explain the lag of productivity with respect to climate (benthic $\delta^{18}O$) in our records. These mechanisms should give rise to a regional response affecting all EEP productivity records covering MIS 100 to 96. Yet productivity does not lag benthic $\delta^{18}O$ at Site 846 (Figure A.1.6 in Appendix A.1) (e.g., Lawrence et al., 2006; Bolton et al., 2010b; Etourneau et al., 2013). Instead, we suggest that

upwelling intensification during glacial terminations can be traced to strengthening of the eastern Pacific subtropical high-pressure system and northeasterly trade winds as the LIS retreated. Climate modeling experiments covering the past 18 kyr show major changes in wind, sea-level pressure, and sea-surface temperature pattern for reduced *versus* maximum North American ice-sheet size (Kutzbach and Ruddiman, 1993; Kutzbach et al., 1993). A strengthening of surface atmospheric circulation (including the eastern Pacific and Bermuda high-pressure systems) associated with ice-sheet retreat is well documented in these atmospheric simulations coinciding with the last deglaciation (e.g., COHMAP Members, 1988; Kutzbach et al., 1993; Bartlein et al., 1998, and references therein). Thus, we conclude that glacial terminations of the lowslung slippery late Pliocene/early Pleistocene LIS (Bailey et al., 2010) influenced regional climate and upwelling in the EEP system in a manner analogous to the late Pleistocene.

4.7 Conclusions

We present new records from ODP Site 849 to test competing hypotheses for G-IG changes in productivity during Plio-Pleistocene iNHG (MIS G1–95, ~2.65–2.4 Ma). The most salient features of this study are as follows.

Primary productivity changes in the low-latitude Pacific Ocean follow the obliquity-dominated G-IG cyclicity but lag peak glacials by ~9.5 kyr at Site 849. Export productivity increased during early Pleistocene glacials and reached maximum values during the glacial terminations of MIS 100, 98, and 96.

Two processes are identified that regulate the observed G-IG variability in primary productivity at Site 849. These processes are (i) nutrient delivery from the Southern Ocean to the EEP, which was a regulating factor from MIS G1 to 95 and was presumably controlled by sea-ice extent in the Southern Ocean, and (ii) the intensity of trade wind-induced upwelling in the EEP, which played a major role in regulating EEP export productivity during MIS 100, 98, and 96 and which we hypothesize to be controlled by strengthening of the eastern Pacific subtropical high-pressure system and northeasterly trade winds in response to retreat of the LIS. We propose that an interplay between intensified upwelling strength and enhanced nutrient delivery from high southern latitudes increased primary productivity rates in the EEP during glacials from MIS 100 to 96.

CHAPTER 5

GLACIAL-INTERGLACIAL CHANGES IN EQUATORIAL PACIFIC SURFACE-WATER STRUCTURE DURING THE PLIO-PLEISTOCENE INTENSIFICATION OF NORTHERN HEMISPHERE GLACIATION*†

5.1 Introduction

A number of influential studies of the long-term evolution of the tropical Pacific mean state have suggested that the warm Pliocene equatorial Pacific Ocean was characterized by a "perennial El Niño-like state" (e.g., Wara et al., 2005; Fedorov et al., 2006) and that the intensification of Northern Hemisphere Glaciation (iNHG) was associated with a gradual increase in west-to-east (zonal) equatorial Pacific sea-surface temperature (SST) gradients (Wara et al., 2005). However, this interpretation is a matter of ongoing debate (Ravelo et al., 2014; Zhang et al., 2014). Also debated is the suggestion that fluctuations took place between El Niño- and La Niña-like climate states on glacial-interglacial (G-IG) timescales across iNHG (e.g., Philander and Fedorov, 2003; Fedorov et al., 2006; Bolton et al., 2010a).

The iNHG, typically considered to span the interval ~3.6 to ~2.4 Ma (Mudelsee and Raymo, 2005), is part of a strong long-term cooling trend following the Mid-Piacenzian warm period. Of particular significance during iNHG is Marine Isotope Stage (MIS) 100 (~2.5 Ma), which is suggested to be the earliest glacial during which the Laurentide Ice Sheet advanced into the midlatitudes (Balco and Rovey, 2010). Advance and retreat of the Laurentide Ice Sheet had important consequences for ice rafting in the North Atlantic (Bailey et al., 2013). It is also hypothesized to have influenced trade-wind strength and thus the strength of upwelling in the Eastern Equatorial Pacific (EEP) during glacial terminations (Chapter 4). These observations highlight the need to improve our understanding of obliquity-controlled surface-water

* *Published in Jakob et al. (2017), Earth and Planetary Science Letters, 463, 69–80.*

† *Data for this Chapter are provided in Tables A.2.2 (Appendix A.2) and B.2.1–B.2.2 (Appendix B.2).*

dynamics including Walker Cell circulation in the tropical Pacific during iNHG. The Pacific Walker Cell circulation comprises easterly and westerly winds at the lower and upper troposphere, and rising motion and subsidence over the western and eastern tropical Pacific, respectively (McPhaden et al., 2006). This circulation is weaker during El Niño states and stronger during La Niña states of the El Niño-Southern Oscillation (ENSO) dynamics (McPhaden et al., 2006). Some studies invoke strong changes in ocean-atmosphere dynamics related to Walker Cell circulation (Philander and Fedorov, 2003; Fedorov et al., 2006; Zhang et al., 2014) to account for G-IG variability in zonal SST gradients in the Plio-Pleistocene Pacific Ocean. Other studies invoke ocean-atmosphere teleconnections to southern high latitudes rather than local fluctuations between El Niño- and La Niña-like climate states as a driver for tropical G-IG climate fluctuations (de Garidel-Thoron et al., 2005; Lee and Poulsen, 2005; Lawrence et al., 2006; Bolton et al., 2010a).

To further investigate whether changes in Walker Cell circulation may have driven large-scale changes in tropical Pacific Ocean conditions, particularly west-east thermocline-tilt-related changes in surface-water characteristics, during the late Pliocene to early Pleistocene iNHG, we present high-resolution planktic foraminiferal Mg/Ca and $\delta^{18}O$ records from EEP Ocean Drilling Program (ODP) Site 849 (Figure 5.1) covering the time interval ~2.75–2.4 Ma (MIS G6–95). These new records complement benthic and planktic foraminiferal $\delta^{13}C$ records and a productivity record for MIS G1–95 from the same site presented in Chapter 4. In the current study, we compare our new Mg/Ca-temperature and $\delta^{18}O$ records with previously published records from ODP Site 846 in the EEP upwelling tongue (Lawrence et al., 2006), ODP Site 1241 in the East Pacific Warm Pool (Groeneveld et al., 2014), and ODP Site 806 in the West Pacific Warm Pool (WPWP) (Medina-Elizalde and Lea, 2010). We calculate zonal equatorial Pacific SST (ΔSST) and ice volume-adjusted $\delta^{18}O$ seawater ($\Delta\delta^{18}O_{ivc\text{-}sw}$), i.e., surface-water salinity (ΔSSS), gradients between Western Equatorial Pacific (WEP) Site 806 (data from Medina-Elizalde and Lea, 2010) and EEP Site 849 (this study). These records are all based on the same substrate (planktic foraminifer *Globigerinoides ruber*), thus allowing us to reliably test for obliquity-controlled surface-water dynamics during this time interval.

In the modern ocean the thermocline is poised at shallow depths in the EEP, so small changes in its depth through east-west tilting can affect surface-water properties by upwelling cold, high-salinity Equatorial Undercurrent waters, while in the WEP the thermocline is too deep for similar-scale depth changes to induce large changes in surface-water properties (for details see Chapter 3). If oscillations between El Niño- and La Niña-like climate states occurred in

the equatorial Pacific on G-IG timescales, 41-kyr-paced variability in both zonal ΔSST and ΔSSS records should be observed with larger-scale G-IG amplitudes in SST and SSS in the eastern compared to the western equatorial Pacific (Philander and Fedorov, 2003).

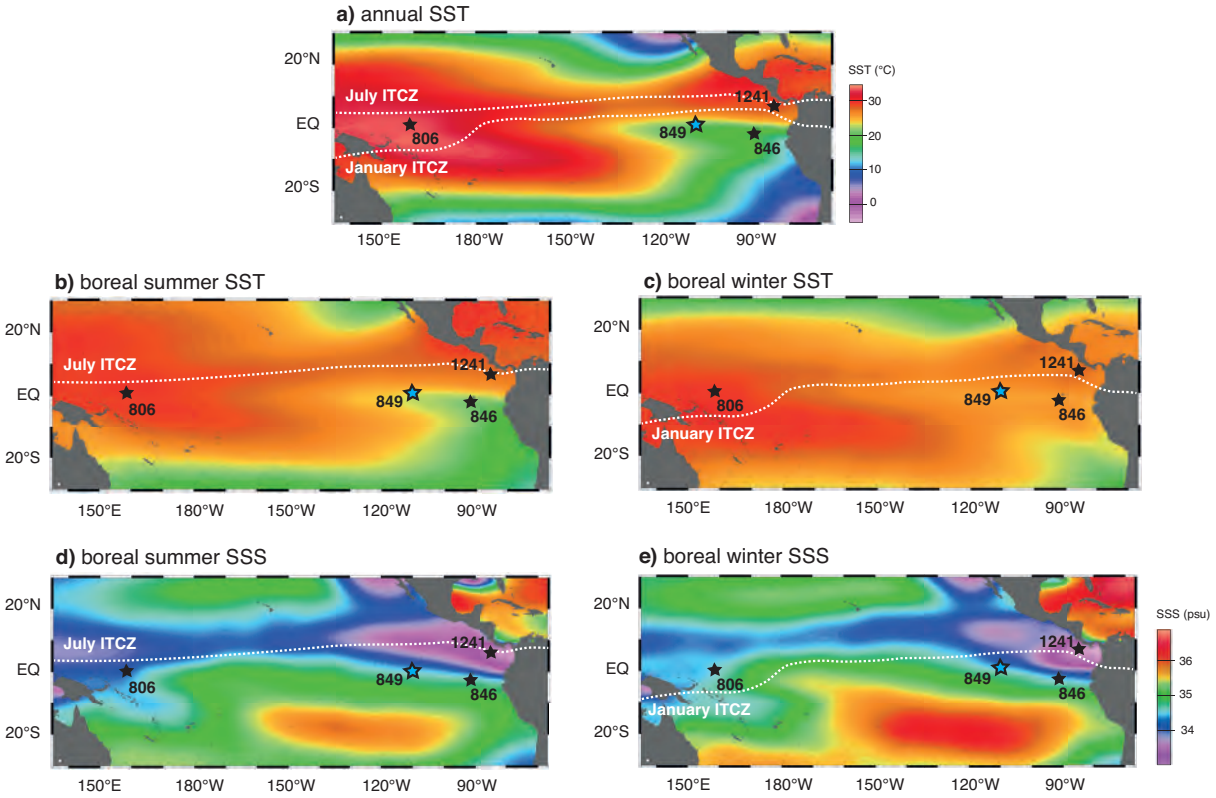

Figure 5.1. Location map of ODP Sites 849 (blue, this study; 0°11'N, 110°31'W, 3851 m [Mayer et al., 1992]), 846 (black, 3°5'N, 90°49'W, 3296 m), 806 (black, 0°19'N, 159°21'E, 2520 m) and 1241 (black, 5°51'N, 86°27'W, 2027 m). Modern mean **(a)** annual, **(b)** boreal summer (Jul–Sep) and **(c)** boreal winter (Jan–Mar) SSTs (°C), and modern mean **(d)** boreal summer (Jul–Sep) and **(e)** boreal winter (Jan–Mar) SSSs (psu) are shown after World Ocean Atlas (Boyer et al., 2013). Summer SSTs approximate modern La Niña conditions, while winter SSTs resemble modern El Niño conditions. White lines show the modern northernmost and southernmost positions of the Intertropical Convergence Zone (ITCZ) in July and January, respectively. Modern ITCZ positions were determined using 55-yr (1958–2013) satelite observations of monthly rainfall in the tropical Pacific provided by the NASA Tropical Rainfall Measuring Mission (http://trmm.gsfc.nasa.gov).

5.2 ENSO dynamics of the equatorial Pacific Ocean

5.2.1 Modern equatorial Pacific Ocean

In the modern tropical Pacific Ocean, zonal atmospheric circulation causes a strong asymmetry in east-to-west surface-air pressure, SST and thermocline depth along the equator (Figure 5.1a–c). Westward-blowing trade winds drive surface-water divergence along the equator and force warm water to pile up in the west. This results in a deep thermocline (~150 m) (Wang et al., 2000) and a thick, warm mixed layer in the WPWP and a shallow

thermocline (~50 m) (Wang et al., 2000) and a thin, relatively cold and nutrient-rich mixed layer in the EEP "cold tongue". Along the equator, modern mean annual SSTs range from ~23°C in the EEP cold tongue to ~29°C in the WPWP (Boyer et al., 2013). This ocean-atmosphere pattern is characterized by a strong inter-annual variability dominated by ENSO (La Niña and El Niño events). Under La Niña conditions, a stronger atmospheric Walker Cell circulation intensifies the zonal SST gradient and tilt of the thermocline in the tropical Pacific while, during El Niño events, a weakened Walker circulation reduces this asymmetry (Figure 5.1b–c), resulting in more uniform temperatures across the tropical Pacific and remote effects including higher global mean temperatures, extratropical heat export and regional hydrological impacts (McPhaden et al., 2006).

5.2.2 Secular evolution of the equatorial Pacific climate state since the early Pliocene

An area of vigorous debate concerns the extent to which east-to-west surface-water temperature gradients along the equatorial Pacific Ocean were a feature of the geological past. A recent study, using organic temperature proxies, suggested that a relatively constant zonal SST gradient of ~3°C persisted across the equatorial Pacific during the warm late Miocene and Pliocene (Zhang et al., 2014). However, Ravelo et al. (2014) posit that these data support, within error, the interpretation derived from several Mg/Ca- and model-based paleoclimate studies that the SST gradient was weak along the equator during the early Pliocene ~5 to 3 Ma ago (e.g., Wara et al., 2005; Fedorov et al., 2006). A reduced zonal SST gradient in the equatorial Pacific Ocean under warm Pliocene conditions is attributed to a weak or non-existent equatorial cold tongue (Wara et al., 2005) resulting from a deep tropical thermocline relative to the modern or upwelling of warmer subsurface mode waters (Fedorov et al., 2006). This hypothesized climate state is approximated by a surface-ocean structure found today in the region during El Niño events (Wara et al., 2005; Fedorov et al., 2006) and is therefore often referred to a "permanent El Niño-like state" (e.g., Wara et al., 2005; Fedorov et al., 2015).

Regardless of whether a strong zonal SST gradient existed in the warm Pliocene equatorial Pacific Ocean (Zhang et al., 2014) or not (e.g., Wara et al., 2005; Fedorov et al., 2006), a gradual ΔSST increase since ~2.5 Ma, i.e., since the three major G-IG cycles of the Pleistocene (MIS 100–96) that represent the culmination of iNHG, is suggested (e.g., Wara et al., 2005; Zhang et al., 2014). This ΔSST increase is hypothesized to result from long-term deep-ocean cooling, a gradual shoaling of the tropical thermocline (Philander and Fedorov,

2003), and cooling of EEP surface-waters, while SSTs in the Western Equatorial Pacific remained relatively stable (Wara et al., 2005; Lawrence et al., 2006; Medina-Elizalde and Lea, 2010). By ~1.6 Ma, a Walker circulation system with a west-to-east ΔSST approximating the modern, 4–6°C, was reached (e.g., Wara et al., 2005; Lawrence et al., 2006).

5.2.3 Orbital-scale variability in equatorial Pacific surface-water structure

The results of some numerical model experiments suggest that obliquity-controlled surface-water dynamics, characterized by a see-sawing of the west-east tropical Pacific thermocline on 41-kyr periods, occurred between 3 and 1 Ma (Philander and Fedorov, 2003; Fedorov et al., 2006). These studies suggest El Niño-like and La Niña-like states associated with interglacials and glacials, respectively. Other model results suggest that the response of tropical Pacific Walker Cell circulation and thermocline tilt was not strongly influenced by changes in axial tilt during the Pleistocene (Lee and Poulsen, 2005). In line with this proposed relative insensitivity of tropical climate response to axial tilt, proxy records from the tropical Pacific are incompatible with obliquity-related changes in thermocline slope and trade-wind intensity during the early Pleistocene. For instance, calcareous nannofossil-based paleoproductivity estimates spanning MIS 101–95 demonstrate similar, almost in-phase obliquity-paced G-IG productivity pattern in the EEP and WPWP that are interpreted to be unrelated to a west-east tilting of the thermocline and thus fluctuations from an El Niño-like to a La Niña-like climate state on G-IG timescales (Bolton et al., 2010a). Alternative explanations for the drivers of changes in tropical Pacific SST and productivity on G-IG (41 kyr) timescales invoke ocean-atmosphere teleconnections to southern high latitudes (Lee and Poulsen, 2005; Lawrence et al., 2006) rather than local G-IG fluctuations between El Niño- and La Niña-like climate states (Philander and Fedorov, 2003; Fedorov et al., 2006).

5.3 Material and methods

5.3.1 Site description

Here we reconstruct late Pliocene to early Pleistocene surface-water conditions in the EEP and compare them with previously published surface-water records from ODP Site 806 in the WPWP (Medina-Elizalde and Lea, 2010). Our data come from ODP Leg 138 Site 849 (0°11'N, 110°31'W; Mayer et al., 1992) (Figure 5.1). This site, where a nearly complete

sequence of late Miocene to Holocene sediments was recovered (Mayer et al., 1992), is situated ~860 km west of the East Pacific Rise and thus records an open-ocean signal (Mix et al., 1995). Site 849 is positioned in the present-day equatorial divergence zone within the so-called "cold tongue". Westward-blowing trade winds induce year-round upwelling of cold, nutrient-rich Equatorial Undercurrent waters, resulting in mean annual SSTs at Site 849 that are up to 3°C colder compared to surface waters outside the cold tongue (Figure 5.1a; Boyer et al., 2013). The present-day water depth at Site 849 is 3851 m (Mix et al., 1995). This is close to the modern lysocline in the equatorial Pacific, but well above the equatorial Pacific carbonate compensation depth (for details see Chapter 3).

5.3.2 Sampling

To study planktic foraminifer-based surface-water Mg/Ca and $\delta^{18}O$ variability across iNHG in the tropical east Pacific, we analyzed 375 samples from cores 849C-7H-1-80 cm to 849C-7H-2-21 cm and 849D-6H-5-102 cm to 849D-7H-5-57 cm (77.02 to 67.78 m composite depth [mcd]). Sediments consists of white to light grey diatom nannofossil ooze, interbedded with slightly darker diatom-rich intervals (Mayer et al., 1992). Foraminifera are common within the upper 100 m (Mayer et al., 1992). For generating a record at suborbital resolution, 20 cm^3 samples were taken at 2-cm intervals. Samples were oven-dried, washed over a 63 μm sieve, and weighed. Preservation of foraminiferal tests in our study interval is good, with fine features such as delicate spines and original wall structure such as pore channels well preserved, and a lack of secondary calcite on test surfaces (see Text A.2.1 and Figure A.2.1 in Appendix A.2).

To develop a high-resolution benthic foraminiferal oxygen-isotope ($\delta^{18}O_b$) stratigraphy, an average of six specimens of the benthic foraminifera *Cibicidoides wuellerstorfi* were picked from the >150 μm dried sediment fraction of 125 samples from 77.02 to 74.19 mcd. The resulting dataset was supplemented by data presented in Chapter 4 covering the interval from 74.16 to 67.78 mcd (229 samples based on *C. wuellerstorfi*) and from Mix et al. (1995) from 76.71 to 67.71 mcd (57 samples, also based on *C. wuellerstorfi*), yielding a total of 411 stable-isotope data points for our $\delta^{18}O_b$ stratigraphy for 77.02 to 67.71 mcd.

The shallow-dwelling foraminifera *Globigerinoides ruber* (white, sensu stricto) was used to measure sea-surface $\delta^{18}O$ and Mg/Ca values across the study interval at Site 849 (77.02 to 67.78 mcd). To avoid ontogenetic effects (Elderfield et al., 2002; Friedrich et al., 2012), a narrow size fraction of 250–315 μm for $\delta^{18}O$ analyses and 200–250 μm for Mg/Ca

measurements was selected. The limited number of individuals per sample within narrow size fractions dictated the use of different size fractions for $\delta^{18}O$ and Mg/Ca measurements. On average, twelve specimens were picked for $\delta^{18}O$ analyses and 40 specimens for Mg/Ca analyses. While the size fraction of *G. ruber* specimens used for $\delta^{18}O$ analyses in our study is almost identical to that used to generate the Site 806 *G. ruber*-based $\delta^{18}O$ and Mg/Ca records (250–350 µm) (Medina-Elizalde and Lea, 2010), the size fraction used for Mg/Ca is smaller in our study (200–250 µm *versus* 250–350 µm). Ontogenetic effects on *G. ruber*-derived Mg/Ca are a controversial issue: while Elderfield et al. (2002) record a ~0.5 mmol/mol increase (~2°C) from the 212–250 µm to the 300–350 µm size fraction, Friedrich et al. (2012) demonstrate no significant differences between these two size fractions.

5.3.3 Geochemical analyses

Mg/Ca analyses

For Mg/Ca measurements, tests of *G. ruber* were cracked to reveal individual chambers. The cracked shell material was carefully cleaned to remove clay minerals, organic material and re-adsorbed contaminants following the protocol of Barker et al. (2003). Cleaned samples were analyzed using the Agilent Inductively Coupled Plasma-Optical Emission Spectrometer (ICP-OES) 720 at the Institute of Earth Sciences, Heidelberg University. To allow inter-laboratory comparison, we normalized Mg/Ca data relative to the ECRM752-1 standard applying the Mg/Ca reference value of 3.762 mmol/mol (Greaves et al., 2008). To ensure instrumental precision of the ICP-OES, the ECRM standard was analyzed at least every 20 samples. Based on replicate measurements of the ECRM reference material, we obtained a standard deviation for Mg/Ca of ±0.02 mmol/mol (equals ±0.1°C). Elemental ratios of Al/Ca, Fe/Ca and Mn/Ca were monitored to identify contamination by clay particles or diagenetic coatings. Results indicate that the Mg/Ca content of the analyzed tests is unaffected by contamination (see Text A.2.2 and Figure A.2.2 in Appendix A.2 for detailed discussion).

Oxygen-isotope analyses

Oxygen-isotope analyses were performed at the Institute of Geosciences, Goethe-University Frankfurt using a ThermoFinnigan MAT253 gas source mass spectrometer equipped with a Gas Bench II. Results are reported relative to the Vienna Pee Dee Belemnite (VPDB) standard through the analysis of an in-house standard calibrated to NBS-18 and NBS-19. Analytical precision is better than 0.08‰ (at 1σ level). The $\delta^{18}O$ values of *C. wuellerstorfi*

reported herein were adjusted for the species-specific offset from equilibrium by the addition of +0.64‰ ($\delta^{18}O_{adj.}$) (Shackleton and Hall, 1984). We assume that *G. ruber* secretes calcite close to $\delta^{18}O$ equilibrium (Koutavas and Lynch-Stieglitz, 2003).

5.3.4 Calculation of sea-surface temperature and $\delta^{18}O_{ivc\text{-}sw}$

We converted *G. ruber* Mg/Ca (mmol/mol) into SSTs (°C) using the species-specific equation of Lea et al. (2000) (see Text A.2.3, Table A.2.1 and Figure A.2.3 in Appendix A.2 for a detailed methodical discussion). Ice volume-adjusted seawater $\delta^{18}O$ ($\delta^{18}O_{ivc\text{-}sw}$ in ‰ Standard Mean Ocean Water, SMOW) was estimated by subtracting an estimation of the global Plio-Pleistocene ice-volume (given by $\delta^{18}O_b$) from the $\delta^{18}O_{sw}$ record, following the approach of Karas et al. (2009) (hereinafter method 1). We also used the eustatic sea-level reconstruction of Rohling et al. (2014) for the same purpose (hereinafter method 2) (see Figure A.2.4 and Text A.2.4 in Appendix A.2 for a detailed methodical discussion). The zonal Pacific $\delta^{18}O_{ivc\text{-}sw}$ gradient was determined for both method 1 and 2, and, because the effect of global ice volume should be identical to both east and west Pacific records, by using the uncorrected $\delta^{18}O_{sw}$ records (hereinafter method 3).

5.3.5 Spectral analyses

Spectral analyses were performed to identify significant orbital frequencies in the data using the program Paleontological Statistics (PAST) version 3.11 (Hammer et al., 2001). To identify cyclicities and coherencies between records, Blackman-Tukey cross-spectral analyses with 30% overlap were conducted using the AnalySeries software package version 2.0.8 (Paillard et al., 1996). Data for cross-spectral analyses were linearly interpolated, detrended, and prewhitened; $\delta^{18}O$ values were inverted.

The relationship between Site 849 proxy records and variance at the 41-kyr period was investigated by superimposing each record on the output of a band-pass Gaussian filter centered on 0.0244 kyr^{-1} with a band width of 0.01 kyr^{-1}. The 41-kyr-filtered data were compared to the astronomical solution for obliquity (Laskar et al., 2004). Before filtering, records were detrended and linearly interpolated. Filtering was performed using AnalySeries.

5.3.6 Chronology

For the time interval ~2.6–2.4 Ma the Site 849 age model presented in Chapter 4 is used. A new chronology for Site 849 is established for the time interval ~2.75–2.6 Ma (Figure 5.2; see

Table A.2.2 in Appendix A.2) by visual correlation of our new $\delta^{18}O_b$ record (supplemented by data from Mix et al. [1995]) to the LR04 stack (Lisiecki and Raymo, 2005) using the AnalySeries software package version 2.0.8 (Paillard et al., 1996). To minimize errors during tuning, tie points at stage transitions were used ("midpoint method"). To facilitate comparison between Site 849 (this study) and Sites 846, 1241 and 806, we also re-tuned the benthic $\delta^{18}O$ data from these sites to the LR04 stack (Lisiecki and Raymo, 2005) across the interval ~2.75–2.4 Ma applying the "midpoint method" (see Figure A.2.5 and Table A.2.2 in Appendix A.2).

Our high-resolution $\delta^{18}O_b$ record of *C. wuellerstorfi* (Figures 5.2a–b, 5.3a) follows the 41-kyr G-IG cyclicity seen in the LR04 stack (Figure 5.4a; see also Figure A.2.6 in Appendix A.2) and allows us to readily identify MIS G6 through 95 in our record. Oxygen-isotope values range from 2.95 to 4.31‰. For iNHG, $\delta^{18}O_b$ shows a modest long-term increase from MIS G6 to MIS 95, which is attributed to higher glacial $\delta^{18}O_b$ values (and thus more pronounced G-IG amplitudes) from MIS 100 onward.

The revised chronology for Site 849 yields a mean temporal sample resolution of ~800 yr and an average linear sedimentation rate of 2.7 cm kyr^{-1} (Figure 5.2c) for the time interval ~2.75–2.4 Ma (MIS G6–95). This is similar to the sedimentation rate of 2.6 cm kyr^{-1} observed in Chapter 4 for Site 849 for the time interval ~2.65–2.4 Ma (MIS G1–95).

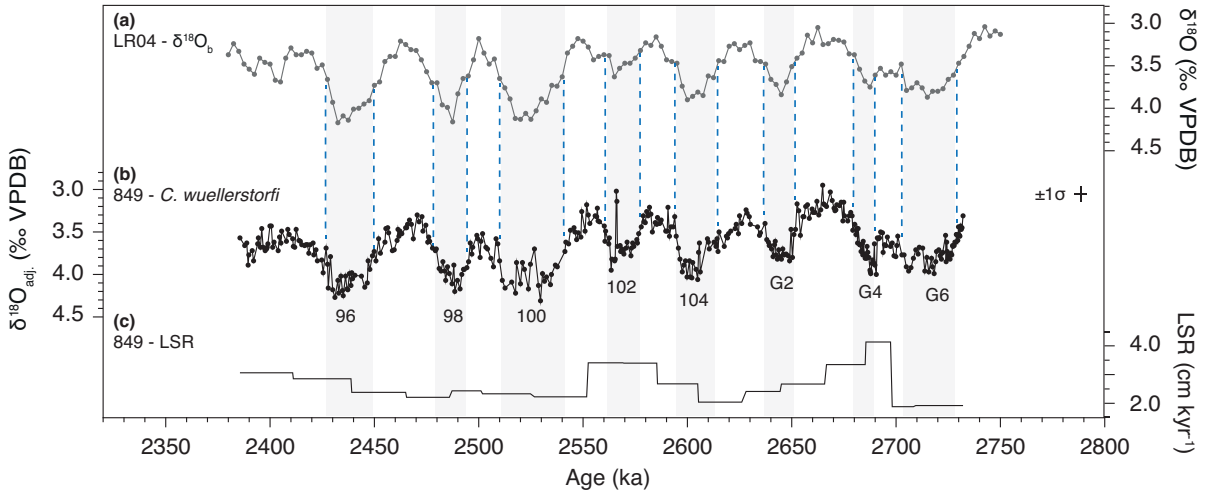

Figure 5.2. Revised age model, tuned to the LR04 stack (Lisiecki and Raymo, 2005), for ODP Site 849 spanning MIS G6–95 (~2.75–2.4 Ma). **(a)** LR04 stack for MIS G6–95 (Lisiecki and Raymo, 2005). **(b)** Benthic foraminiferal (*C. wuellerstorfi*) $\delta^{18}O$ record from Site 849. The record consists of new data supplemented by published data of Mix et al. (1995). Bars indicate the 1σ standard deviation. Blue dashed lines in Figure 5.2a–b show the tie points used for tuning. Tuning points are provided in Table A.2.2 (Appendix A.2). **(c)** Average linear sedimentation rate (LSR) in cm kyr^{-1}. Grey bars highlight glacial periods.

5.4 Results and discussion

5.4.1 Plio-Pleistocene planktic foraminiferal $\delta^{18}O$ variability in the tropical Pacific

The *G. ruber*-based $\delta^{18}O$ record from Site 849 documents eight G-IG oscillations between ~2.75 and 2.4 Ma (MIS G6–95), closely matching variations in Earth's obliquity (Figures 5.3b and 5.4b; see also Figure A.2.6 in Appendix A.2). The lack of precessional power in planktic foraminiferal $\delta^{18}O$ and all other Site 849 records in our study may indicate that surface-water properties at that location are relatively insensitive to precessional forcing compared to G-IG obliquity-controlled climate change and associated feedbacks during the late Pliocene to early Pleistocene (see Figure A.2.6 in Appendix A.2).

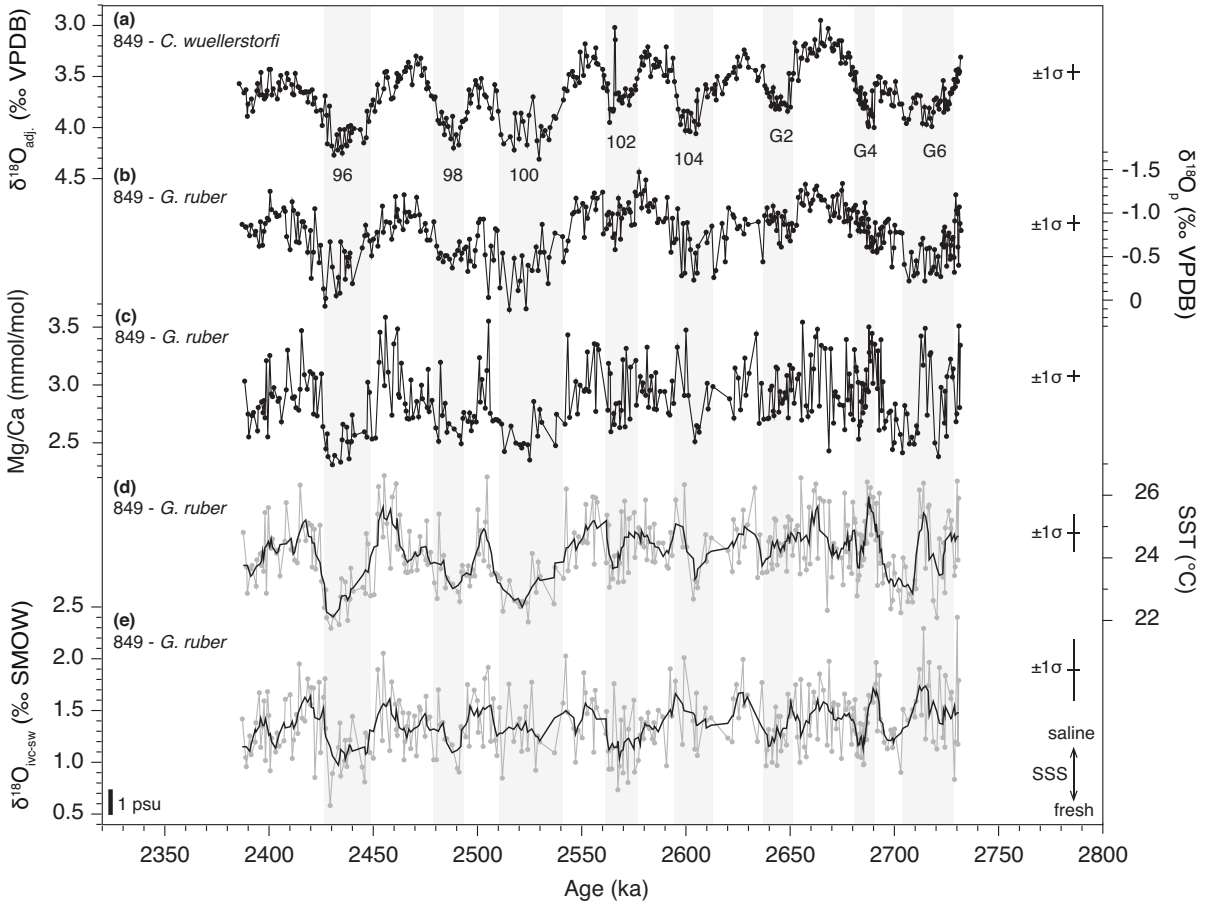

Figure 5.3. Planktic foraminiferal temperature and salinity proxy data based on our revised benthic foraminiferal stratigraphy from ODP Site 849 for MIS G6–95 (~2.75–2.4 Ma). **(a)** Benthic foraminiferal (*C. wuellerstorfi*) $\delta^{18}O$ stratigraphy. **(b)** Planktic foraminiferal (*G. ruber*) $\delta^{18}O$ record ($\delta^{18}O_p$). **(c)** *Globigerinoides ruber* Mg/Ca record adjusted to the ECRM standard (Greaves et al., 2008). **(d)** *Globigerinoides ruber* Mg/Ca-based SST estimates. **(e)** Ice-volume-adjusted $\delta^{18}O_{sw}$ record ($\delta^{18}O_{ivc\text{-}sw}$) as a proxy for SSS. Higher (lower) $\delta^{18}O_{ivc\text{-}sw}$ values are interpreted to indicate saltier (fresher) sea-surface waters at Site 849. Using a regional $\delta^{18}O_{sw}$–SSS relationship, 1 psu corresponds to ~0.2‰ (Schmidt et al., 1999) (see Chapter 5.4.4). Grey points in Figure 5.3d–e depict individual data points, black line illustrates the five-point smoothed average of a record. Horizontal and vertical bars indicate the 1σ standard deviation associated with the age model and the individual proxy records, respectively. Grey bars highlight glacial periods.

Planktic foraminiferal $\delta^{18}O$ values fluctuate between -1.47 and 0.11‰, with higher values associated with glacials and lower values associated with interglacials. Glacial-interglacial $\delta^{18}O$ cycles increase in amplitude from MIS 100 onward (>1‰), with interglacial $\delta^{18}O$ values remaining invariant (around -1‰), whereas glacial $\delta^{18}O$ values shift to higher values from approximately -0.5 to 0‰.

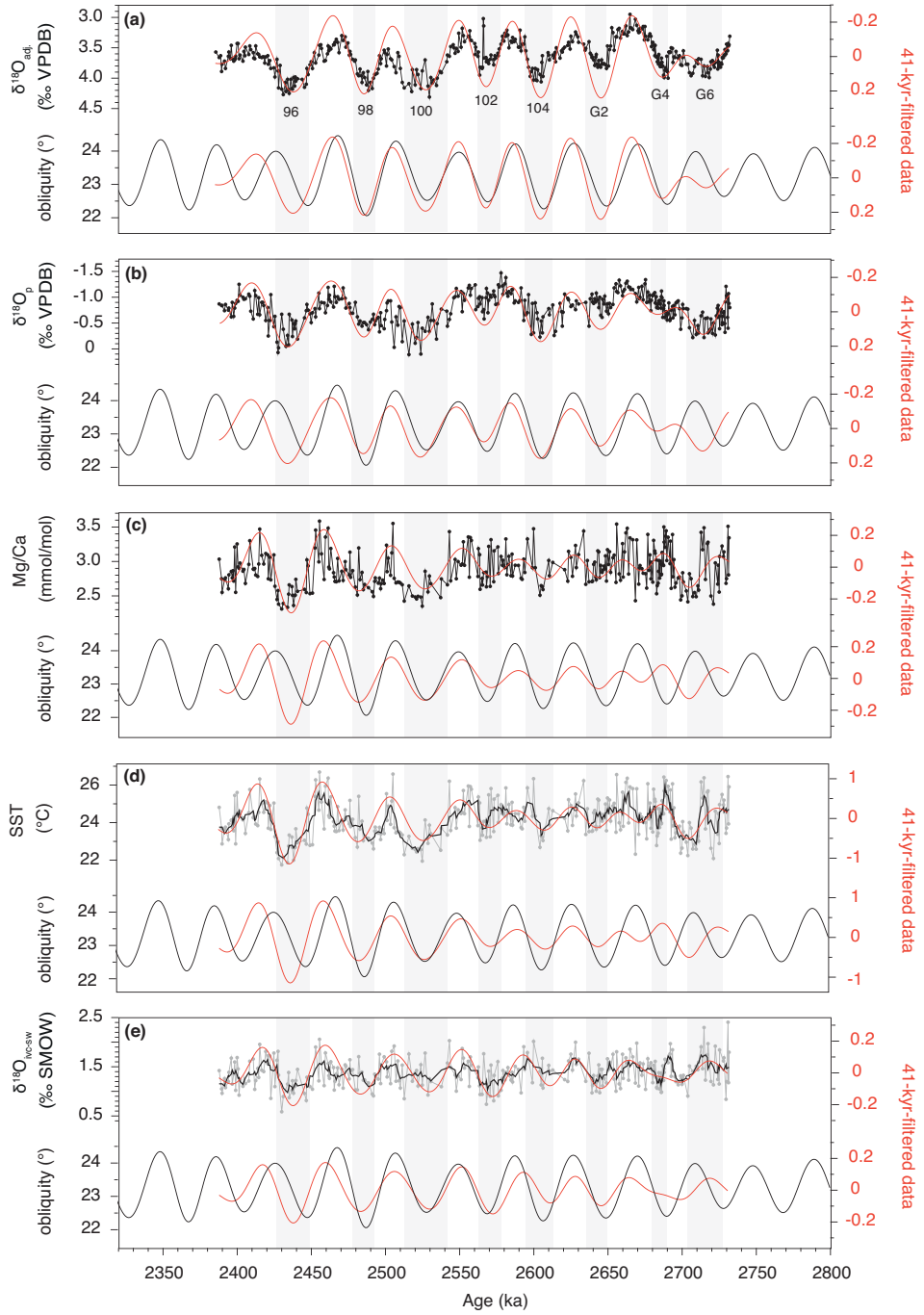

Figure 5.4. 41-kyr-filtered data (red) for Site 849 proxy records for ~2.75–2.4 Ma (MIS G6–95) compared to the astronomical solution for orbital obliquity (black; Laskar et al., 2004) for **(a)** benthic foraminiferal (*C. wuellerstorfi*) $\delta^{18}O$, **(b)** planktic foraminiferal (*G. ruber*) $\delta^{18}O$ ($\delta^{18}O_p$), **(c)** *G. ruber* Mg/Ca, **(d)** *G. ruber* Mg/Ca-based SST estimates, **(e)** ice-volume-adjusted $\delta^{18}O_{sw}$. Grey points in Figure 5.4d–e depict individual data points, black line illustrates the five-point smoothed average of a record. Grey bars highlight glacial periods.

5.4.2 Plio-Pleistocene SST in the Eastern Equatorial Pacific

Our new *G. ruber* Mg/Ca-based SST record from Site 849 documents eight obliquity-paced G-IG oscillations between ~2.75 and ~2.4 Ma (MIS G6–95) (Figures 5.3c–d and 5.4c–d, see also Figure A.2.6 in Appendix A.2). Considering that *G. ruber*-derived temperature estimates from the tropical Pacific most likely represent mean annual SSTs (Lin et al., 1997), our data imply mean annual SSTs ranging from ~22°C during glacial MIS 96 to ~27°C during interglacial MIS 97. Overall, our SST record documents a long-term cooling trend of ~0.7°C across the studied time interval. Glacial-interglacial SST oscillations are of larger amplitude from MIS 100 to 95 (~3–4°C) than during the time interval prior to MIS 100 (<2°C). Comparison of our Plio-Pleistocene SST estimates with modern mean annual SSTs at Site 849 at 20 m water depth (~23.5°C; Boyer et al., 2013), i.e., the assumed mean depth habitat of *G. ruber* (Wang, 2000), indicates slightly warmer values, supporting the overall notion of a warmer-than-present EEP during the late Pliocene and early Pleistocene (e.g., Lawrence et al., 2006; Groeneveld et al., 2014).

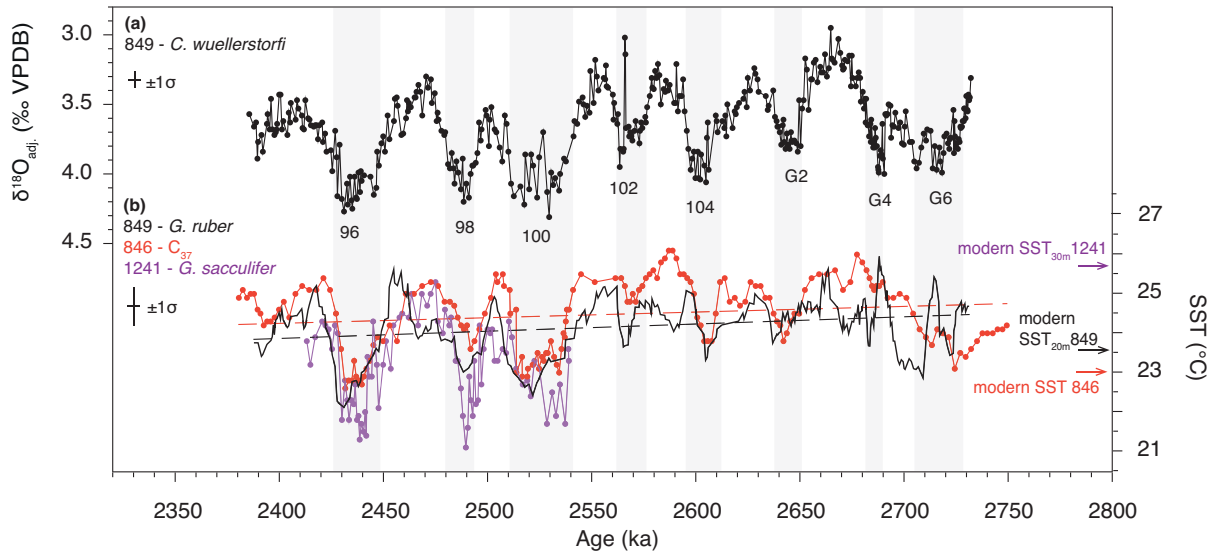

Figure 5.5. East Pacific SST estimates from ODP Sites 849 (black; five-point smoothed; this study) and 846 (red; Lawrence et al., 2006) for MIS G6–95 (~2.75–2.4 Ma) and from ODP Site 1241 (purple; Groeneveld et al., 2014) for MIS 100–95 (~2.55–2.42 Ma). Records from Sites 846 and 1241 are re-tuned to LR04 (Lisiecki and Raymo, 2005), tuning points are provided in Table A.2.2 (Appendix A.2). **(a)** Benthic foraminiferal (*C. wuellerstorfi*) $\delta^{18}O$ stratigraphy for Site 849. **(b)** East Pacific SSTs. While estimates from Site 849 (this study; $Mg/Ca_{G.\ ruber}$-based) and 846 (Lawrence et al., 2006; alkenone-based [C_{37}]) reflect temperatures of the uppermost part of the water column, temperature estimates from Site 1241 (Groeneveld et al., 2014; $Mg/Ca_{G.\ sacculifer}$-based) reflect a water depth of ~30 m (Fairbanks et al., 1982). Thereafter, black, red and purple arrows represent modern mean annual SSTs at Sites 846 (surface water), 849 (20 m water depth) and 1241 (30 m water depth), respectively (Boyer et al., 2013). Dashed lines indicate trends. Horizontal and vertical bars indicate the 1σ standard deviation associated with the age model and the individual Site 849 proxy records, respectively. Grey bars highlight glacial periods.

In terms of G-IG amplitudes, our late Pliocene to early Pleistocene SST record from Site 849 is in good agreement with the pattern shown by the alkenone-derived SST record from Site 846 (Lawrence et al., 2006) and by the *Globigerinoides sacculifer* Mg/Ca-derived SST estimates from Site 1241 (Groeneveld et al., 2014) (Figure 5.5). In terms of absolute values, however, SSTs at Eastern Pacific Warm Pool Site 1241 appear to be substantially colder than expected when compared to modern temperatures at that location. A more southwesterly position of Site 1241 ~2.5 Ma ago can only account for ~0.5°C of this signal (Mix et al., 2003). The temperatures from Site 1241 are also markedly colder than SST estimates from Sites 849 and 846, which may be related to the fact that Site 1241 *G. sacculifer*-based temperature estimates (assumed habitat at ~30 m water depth; Fairbanks et al., 1982) reflect a greater water depth compared to *G. ruber*- and alkenone-derived SSTs. Seasonality may also play a role when comparing these different proxy records. Visual evaluation of Figure 5.5 indicates that the Site 846 SST record leads the Site 849 SST record, suggesting, in agreement with observations made in Chapter 4, that different mechanisms dictate G-IG surface-water variability in these two distinct regions of the highly heterogeneous EEP.

5.4.3 Comparison between west and east tropical Pacific SST records

To explore the possibility of orbitally paced changes in surface-water structure resulting from G-IG changes in the west-east tilt of the thermocline in the Plio-Pleistocene equatorial Pacific Ocean, we evaluate zonal SST changes by comparing our *G. ruber*-based temperature record to that of Medina-Elizalde and Lea (2010) from WPWP Site 806 (see Text A.2.5 in Appendix A.2 for a detailed methodical discussion). Because foraminiferal preservation at Site 806 has been described as typically only moderate to good (Chaisson and Leckie, 1993; Medina-Elizalde and Lea, 2010), dissolution may have reduced foraminiferal Mg/Ca ratios, resulting in an underestimation of absolute SSTs and therefore of the reconstructed zonal SST gradient. Yet relative changes (G-IG cycles in SST at Site 806) should be preserved. However, we cannot rule out the possibility of increased and diminished carbonate dissolution during glacials and interglacials in the WEP during the early Pleistocene, respectively (Sexton and Barker, 2012). The addition of inorganic calcite from sediment pore fluids onto foraminiferal tests (overgrowths) that typically has a much larger Mg/Ca signature than its biogenic counterpart may also play a role for Site 806 *G. ruber* samples. There is, however, no correlation between Fe/Ca and Mn/Ca, diagnostic for microcrystalline overgrowth, to Mg/Ca in *G. ruber* specimens for the herein investigated time interval (Medina-Elizalde and Lea, 2010).

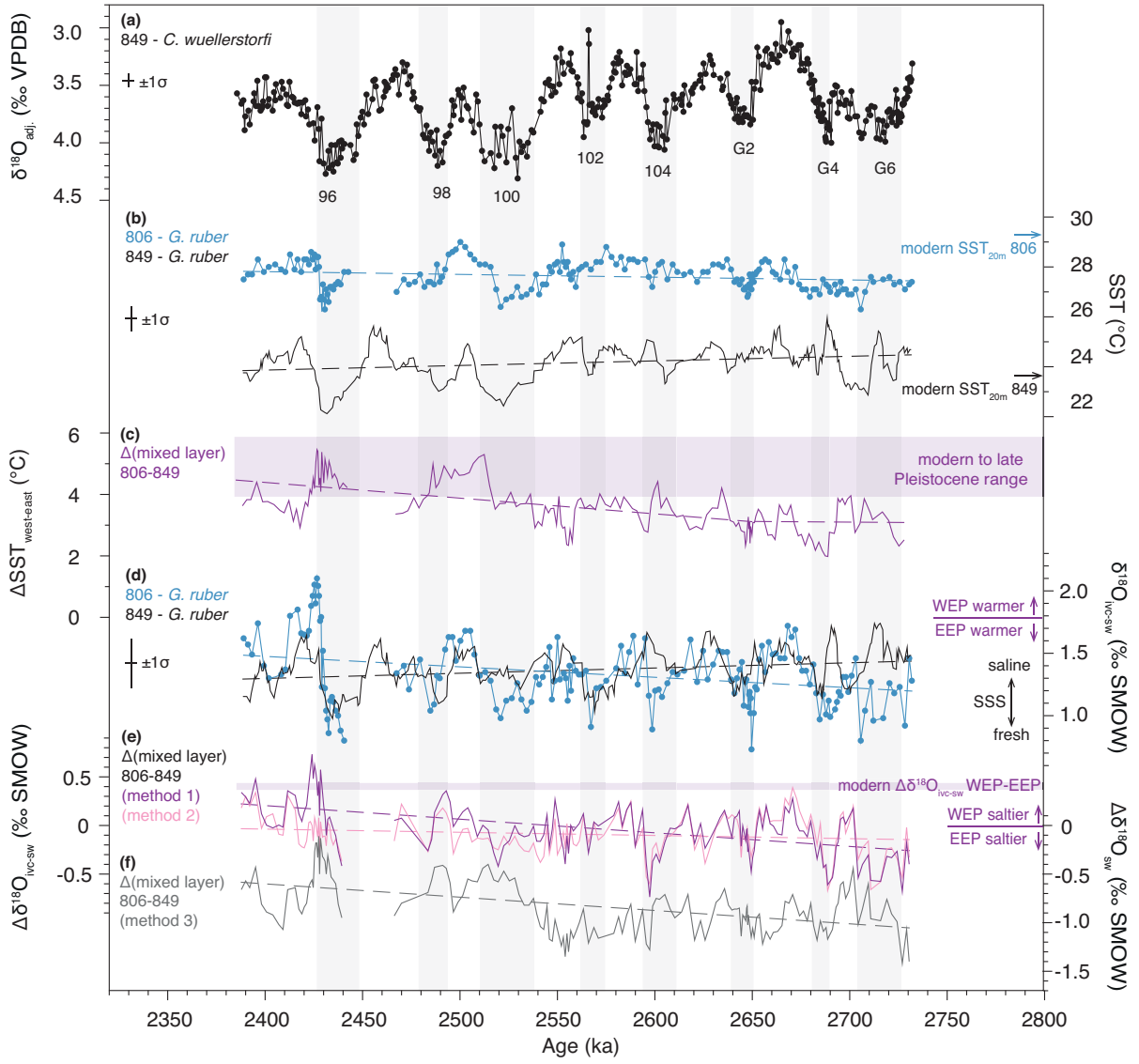

Figure 5.6. High-resolution planktic foraminiferal temperature and salinity proxy data from ODP Site 849 (black; this study) in the EEP and ODP Site 806 (blue; Medina-Elizalde and Lea, 2010) in the WEP based on revised benthic foraminiferal stratigraphies for MIS G6–95 (~2.75–2.4 Ma) (tuning points are provided in Table A.2.2 [Appendix A.2]). **(a)** Benthic foraminiferal (*C. wuellerstorfi*) $\delta^{18}O$ stratigraphy for Site 849. **(b)** *Globigerinoides ruber* Mg/Ca-based SST estimates from Sites 849 in the EEP (black; five-point smoothed; this study) and 806 in the WEP (blue; Medina-Elizalde and Lea, 2010). Black and blue arrows represent modern mean annual SSTs at 20 m water depth for Sites 849 and 806, respectively (Boyer et al., 2013). **(c)** Difference between *G. ruber* Mg/Ca-based SST estimates from Sites 849 in the EEP (this study) and 806 in the WEP (Medina-Elizalde and Lea, 2010) ($\Delta SST_{west\text{-}east}$). Pale purple shaded zone represents the range of the modern (~6°C; Boyer et al., 2013) to late Pleistocene (~4°C; Wara et al., 2005) SST gradients between the EEP and WEP. **(d)** Planktic foraminiferal (*G. ruber*) $\delta^{18}O_{ivc\text{-}sw}$ record from Sites 849 in the EEP (black; five-point smoothed; this study) and 806 in the WEP (blue; Medina-Elizalde and Lea, 2010). **(e)** Difference between $\delta^{18}O_{ivc\text{-}sw}$ from Sites 849 in the EEP (this study) and 806 in the WEP (Medina-Elizalde and Lea, 2010) following method 1 (purple) and method 2 (pink). Pale purple shaded zone represents the modern $\delta^{18}O_{ivc\text{-}sw}$ gradient between the EEP and the WEP (Schmidt et al., 1999). **(f)** Difference between $\delta^{18}O_{sw}$ from Sites 849 in the EEP (this study) and 806 in the WEP (Medina-Elizalde and Lea, 2010) following method 3 (grey). The break at ~2450 ka represents a coring gap in the Site 806 record. Dashed lines indicate trends. Horizontal and vertical bars indicate the 1σ standard deviation associated with the age model and the individual Site 849 proxy records, respectively. Grey bars highlight glacial periods.

Sea-surface temperatures at Sites 849 and 846 in the EEP are on average ~3.5°C cooler than at Site 806 in the WPWP (Figures 5.5b and 5.6b). Both west and east Pacific glacial-interglacial SST (~41 kyr) oscillations were smaller prior to the first three large-amplitude G-IG cycles of iNHG (MIS 100–96). Glacial-interglacial SST amplitudes for MIS 100–96 are on the order of ~3°C in the EEP, slightly larger than the ~2°C amplitude in the WPWP (Figure 5.6b). This observation is in agreement with a previous study for the investigated time interval that compared Site 806 SSTs to east Pacific SSTs from Site 846 (Lawrence et al., 2006; Medina-Elizalde and Lea, 2010).

The zonal SST gradient between EEP Site 849 and WPWP Site 806 (Figure 5.6c) is relatively stable (~3°C) prior to MIS 102 (~2.64 Ma). This gradient increased progressively to ~4.5°C by ~2.4 Ma. Thus, the ~4°C threshold for this gradient proposed by Wara et al. (2005) based on lower-resolution records was crossed ~800 kyr earlier than previously proposed, albeit with the possibility that the gradients that we reconstruct may be slight over-estimates because of the Mg/Ca size-fraction effect (see Chapter 5.3.2). Regardless, reconstructed late Pliocene to early Pleistocene west-to-east ΔSST was significantly smaller than both the late Pleistocene interglacial zonal SST gradient of ~6°C (which approximates modern values) (Boyer et al., 2013) and the late Pleistocene glacial gradient of ~6.5°C (Dyez and Ravelo, 2014). The general increase in zonal ΔSST across our study interval is mostly driven by glacial cooling in the EEP (indicated by alkenone- and planktic foraminifer-derived SST estimates; Figure 5.5b).

Our reconstructed zonal SST gradient, which is strongly coupled to changes in thermocline tilt (see Chapter 5.1), shows no G-IG cyclicity (Figures 5.6c and 5.7a). Therefore, our data do not support the concept of changes in thermocline slope that would signify switches between an El Niño-like and La Niña-like climate state on G-IG timescales. This finding is consistent with those of Bolton et al. (2010a) for MIS 101–95 based on nannofossil assemblages.

5.4.4 Plio-Pleistocene $\delta^{18}O_{ivc\text{-}sw}$ at east Pacific Site 849

The five-point smoothed average of the Site 849 $\delta^{18}O_{ivc\text{-}sw}$ record indicates a clear G-IG 41-kyr cyclicity (Figures 5.3e and 5.4e), with lower $\delta^{18}O_{ivc\text{-}sw}$ during glacials particularly across prominent iNHG glacials MIS 100, 98 and 96. The amplitude of glacial-interglacial cycles in $\delta^{18}O_{ivc\text{-}sw}$ is on the order of ~0.5‰. If we assume that this residual signal represents only relative changes in SSS, this corresponds to ~2.4 practical salinity units (psu) using a modern regional $\delta^{18}O_{sw}$-SSS relationship (Schmidt et al., 1999) (see Figure A.2.7 in Appendix A.2).

Although a ~2.4 psu G-IG amplitude appears reasonable in terms of absolute values (compare Benway et al., 2006), it is important to note that this value should be only regarded as a rough estimate when applying a modern $\delta^{18}O_{sw}$-SSS relationship to past time periods. The long-term trend of the smoothed $\delta^{18}O_{ivc\text{-}sw}$ record indicates a slight decrease over the investigated time interval of ~0.1‰, which could be interpreted as a modest freshening (~0.5 psu) of surface waters in the eastern tropical Pacific across iNHG (Figure 5.6d), although we note that such a change is within the error of the calculations.

Sea-surface salinity is generally controlled by the balance between local evaporation, local precipitation, oceanic salt advection, and fresh-water runoff. An influence of continental fresh-water runoff on SSS can be excluded at Site 849 because of its open-ocean setting. It is more likely that SSS at our study site (as represented by $\delta^{18}O_{ivc\text{-}sw}$) was affected by oceanic salt advection through one or a combination of the following factors: (i) Sea-level-controlled glacioeustatic closure/opening of the Central American Seaway (CAS) (Groeneveld et al., 2014), (ii) changes in upwelling of high-salinity Equatorial Undercurrent waters (either in response to CAS closure or to changes in trade-wind strength), and (iii) changes in precipitation minus evaporation.

Potential influence of CAS closure on Site 849

It has been suggested that glacioeustatic gateway closures of the CAS strongly influenced ocean circulation (Maier-Reimer et al., 1990; Schneider and Schmittner, 2006; Groeneveld et al., 2014). However, we suggest that the influence of temporary full CAS closure as hypothesized for MIS 100 to 98 and 96 (Groeneveld et al., 2014; compare Chapter 4) on our paleoceanographic records from Site 849 can only have been minor. Reasons for this interpretation are three-fold:

(i) CAS closure would have reduced the inflow of warm, high-salinity surface waters from the Caribbean Sea into the EEP and the outflow of cold, low-salinity surface waters from the EEP into the Caribbean Sea (Maier-Reimer et al., 1990; Groeneveld et al., 2014). Thus, CAS closure should act to trap low-salinity waters west of the isthmus and expand the east Pacific fresh pool, leading to SSS variations north of the equatorial upwelling zone that are mainly controlled by CAS throughflow. If the east Pacific fresh pool expanded at least onto the equator in analogue to the modern situation as inferred from Aquarius Sea Surface Salinity images (http://aquarius.nasa.gov), fresher conditions during MIS 100, 99 and 98, increased salinity during MIS 97, and low-salinity conditions toward the end of MIS 96 would be

expected at Site 849, based on temporary CAS closures suggested by Groeneveld et al. (2014). This pattern is, however, not seen in the SSS record from EEP Site 849.

(ii) Any closure of the CAS is likely to have promoted increased equatorial upwelling rates of nutrient-enriched Equatorial Undercurrent waters (Schneider and Schmittner, 2006). Thus, increased export production during MIS 100, 99 and 98, low productivity rates during MIS 97, and enhanced productivity toward the end of MIS 96 would be expected. However, this scenario is not supported by the productivity records from EEP Sites 849 (Chapter 4) or 846 (Lawrence et al., 2006; Bolton et al., 2010a).

(iii) We might expect gateway closures during MIS 100 through 98 and again toward the end of MIS 96 to result in surface-water cooling in the EEP (Groeneveld et al., 2014). However, this pattern is not consistent with SST data from east Pacific Sites 849 (this study) and 846 (Lawrence et al., 2006). These records document substantial glacial-interglacial SST changes between MIS 100, 99 and 98 (Figure 5.5b), whereas, if related to CAS closure, we might also expect low SSTs during MIS 99.

Influence of latitudinal ITCZ migration on Site 849

For Site 849, upwelling intensification, diagnostic of increased easterly trade-wind strength, has been demonstrated from MIS 100 onward, with peak upwelling occurring toward glacial terminations (Chapter 4). We might therefore reasonably expect increased SSSs through the influence of high-salinity Equatorial Undercurrent waters. Yet our data record lower-salinity surface waters for glacials MIS 100, 98 and 96, superimposed on a modest long-term freshening of surface waters in the EEP from MIS G6 through 95 (Figure 5.3e). We suggest that enhanced precipitation during glacials relative to interglacials is responsible for this pattern. This hypothesis invokes an equatorward migration of the Intertropical Convergence Zone (ITCZ) during glacials in the eastern Pacific. The modern ITCZ shows strong seasonal meridional migration toward the warmer hemisphere in response to insolation forcing (Figure 5.1). Paradoxically, however, the ITCZ migrates toward the cooler hemisphere in response to ENSO dynamics on inter-annual timescales, primarily driven by tropical changes in atmospheric energy input (Schneider et al., 2014, and references therein) (see Chapter 5.4.7). Latitudinal ITCZ migration is also inferred from paleo-records in response to changes in inter-hemispheric temperature gradients on millennial through G-IG and secular timescales (e.g., Koutavas and Lynch-Stieglitz, 2003; Benway et al., 2006; Schneider et al., 2014; Hyeong et al., 2016). Strong cooling in the high-northern latitudes during prominent iNHG

glacials (Lawrence et al., 2009) is a plausible mechanism for equatorward (i.e., southward) movement of the ITCZ. The amplitude of suggested G-IG paleosalinity change (~2.4 psu) at Site 849 (Figure 5.3e) in response to ITCZ shifts in the eastern tropical Pacific during iNHG falls in the range of those estimated for late Pleistocene ITCZ-controlled paleosalinity variations of ~2–4 psu (Benway et al., 2006). In light of the strong control exerted by Atlantic Meridional Overturning Circulation on the strength of the global annual mean cross-equatorial temperature gradient, an ITCZ influence on our records is consistent with evidence for major southern component water incursions into the deep North Atlantic (implied Atlantic Meridional Overturning Circulation weakening or shoaling) during MIS G6, 100 and 96 (Lang et al., 2016).

5.4.5 Possible influences on the paleosalinity record from the WPWP

The $\delta^{18}O_{ivc\text{-}sw}$ record from Site 806 in the WPWP varies on 41-kyr timescales (Figure 5.6d). If most of this signal represents changes in local salinity, the Site 806 $\delta^{18}O_{ivc\text{-}sw}$ record indicates fresher conditions during glacials than during interglacials (Figure 5.6d). This is similar to the observation derived from Site 849 in the EEP for prominent iNHG glacial-interglacial cycles. Modeling and proxy data consistently indicate lower-salinity glacial conditions for the Last Glacial Maximum for both the WPWP (e.g., Lea et al., 2000; DiNezio and Tierney, 2013) and the EEP cold tongue (Koutavas and Lynch-Stieglitz, 2003), consistent with our observations for early Pleistocene glacials.

As discussed in Chapter 5.4.4, a southward movement of the ITCZ during glacials may have promoted an increasing influence of the ITCZ rain belt on east Pacific Site 849. A contemporaneous southward displacement of the mean ITCZ in the west Pacific during glacials to a position akin to that observed during modern winter conditions, however, would have prevented a year-round influence of the ITCZ on Site 806 (Figure 5.1). Hence, saltier water would be expected in the WEP during glacials than during interglacials. This scenario is, however, not compatible with the local Site 806 $\delta^{18}O_{ivc\text{-}sw}$ record (Medina-Elizalde and Lea, 2010), which indicates fresher conditions during glacials than during interglacials (Figure 5.6d). There are many different possible explanations for this result, including, for instance, a different Plio-Pleistocene pathway of ITCZ migration in the WEP from today. Additionally, it might be speculated that a glacioeustatically driven exposure of the Sunda Shelf may have influenced the Plio-Pleistocene paleosalinity pattern in the WPWP. The exposure of the Sunda Shelf is an important factor influencing regional glacial climates (Sun

et al., 2000; DiNezio and Tierney, 2013). Pollen assemblages from the continental shelf of the South China Sea document intensified river flows on the exposed Sunda Shelf in response to strengthened winter monsoon precipitation during the Last Glacial Maximum (Sun et al., 2000). Some model results for the Last Glacial Maximum are consistent with this observation, indicating that a change in the Walker circulation driven by weakened atmospheric convection over the WPWP results in (i) increased riverine freshwater flux in response to enhanced precipitation over the exposed land and (ii) increased rainfall in the west Pacific region, thereby reducing SSS over much of the western tropical Pacific (DiNezio and Tierney, 2013). Given the distance between the exposed Sunda Shelf and Site 806 (~5500 km), the latter mechanism is the more plausible of these two explanations for SSS change at Site 806. We note, however, that this interpretation of hydroclimate in the WPWP is contradicted by some other model results summarized in DiNezio and Tierney (2013) and by speleothem records from northern Borneo indicating drier conditions during late Pleistocene glacials rather than during interglacials (Meckler et al., 2012).

5.4.6 Comparison between west and east tropical Pacific $\delta^{18}O_{ivc\text{-}sw}$ records

To provide further clues to potential ITCZ migrations and the apparent lack of glacial-interglacial thermocline-tilt-related changes in SSTs in the equatorial Pacific during the Plio-Pleistocene, we evaluate west-to-east $\delta^{18}O_{ivc\text{-}sw}$ gradients (see Text A.2.5 in Appendix A.2 for detailed methodical discussion).

Robustness of approaches

The three different approaches that we have applied to adjust our records for changes in continental ice volume (see Chapter 5.3.4) yield identical results in terms of G-IG amplitudes and trends of the zonal equatorial Pacific $\delta^{18}O_{ivc\text{-}sw}$ ($\Delta\delta^{18}O_{ivc\text{-}sw}$) and $\delta^{18}O_{sw}$ ($\Delta\delta^{18}O_{sw}$) gradient (Figure 5.6e–f). This observation suggests that this result is robust (albeit lower absolute values are obtained using method 3). For simplification, we refer to method 1 only in the follow-up discussion.

Obliquity oscillations in the zonal Pacific $\delta^{18}O_{ivc\text{-}sw}$ gradient

The zonal Pacific $\delta^{18}O_{ivc\text{-}sw}$ gradient (interpreted to represent changes in the zonal SSS gradient; see Chapters 5.4.4 and 5.4.5) documents saltier surface water by ~2.4 psu (as defined by ~0.5‰) in the EEP than in the WPWP at ~2.75 Ma (Figure 5.6e). Over the studied

time interval, the long-term salinity gradient decreased, disappeared around MIS 100, and increased again from MIS 100 onward.

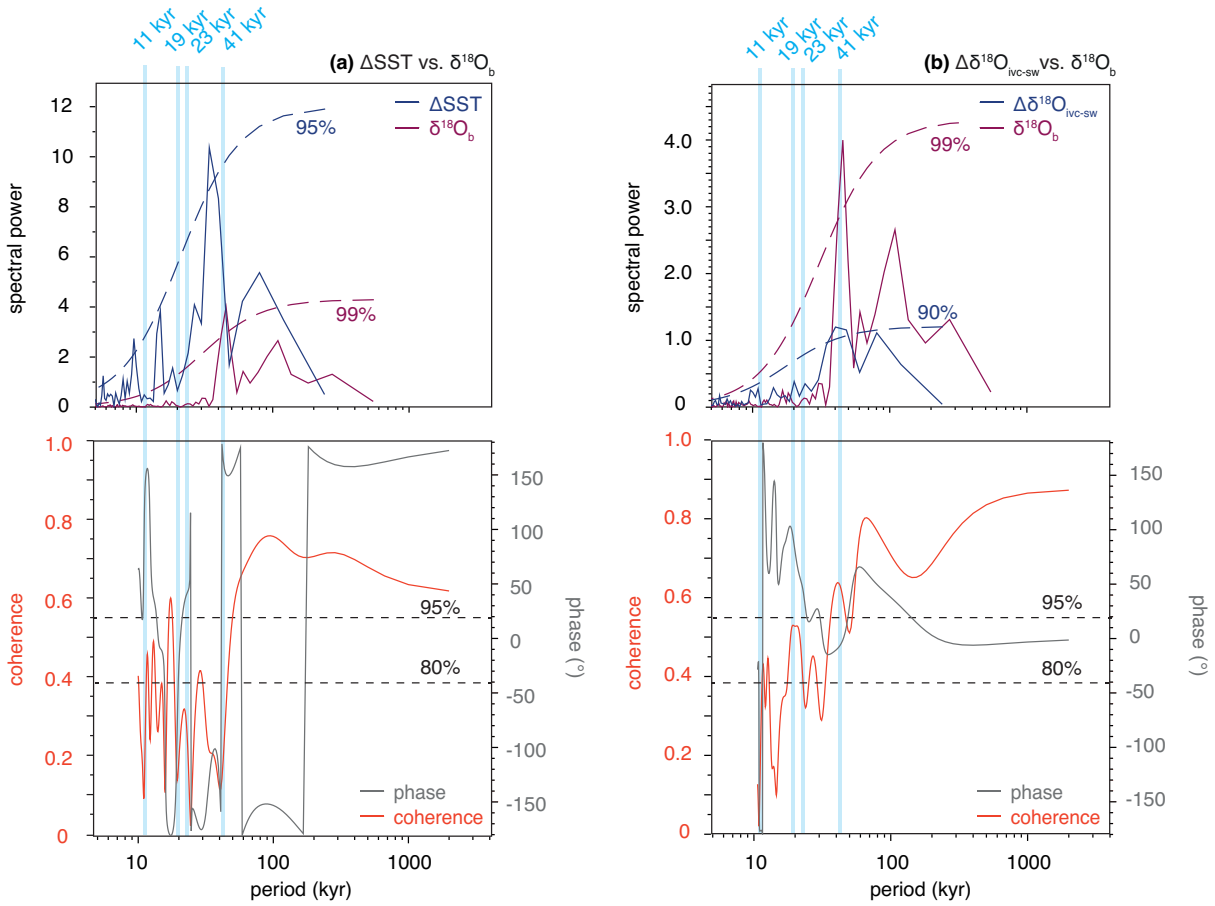

Figure 5.7. (top) Spectral analyses of **(a)** Site 849 $\delta^{18}O_b$ (purple) and tropical Pacific zonal ΔSST (dark blue) and of **(b)** Site 849 $\delta^{18}O_b$ (purple) and tropical Pacific zonal $\Delta\delta^{18}O_{ivc\text{-}sw}$ (method 1) (dark blue) for the time interval ~2.75–2.4 Ma. The highest confidence level is shown for each record (dashed lines). **(bottom)** Blackman-Tukey cross-spectral analyses showing coherence (red) and phase (grey) relationships between global ice volume (Site 849, $\delta^{18}O_b$) and the tropical Pacific zonal **(a)** SST and **(b)** $\delta^{18}O_{ivc\text{-}sw}$ gradient (method 1) between Sites 849 in the EEP and 806 in the WEP spanning the time interval ~2.75–2.4 Ma. Black dashed lines mark 95% and 80% confidence levels. Blue lines indicate obliquity (41 kyr), precessional (23 kyr, 19 kyr) and half-precessional (11 kyr) cycles. Note log scale on x-axes. The $\delta^{18}O_b$-ΔSST cross-spectral analysis indicates no coherency at the 41-kyr band, indicating that the west-to-east Pacific SST gradient is unrelated to obliquity. The existence of 41-kyr cycles in the individual records for Site 849 and 806 $\delta^{18}O_{ivc\text{-}sw}$ calculation is evident in the single spectrum analyses, each showing significant peaks at the 41-kyr band (see Figure A.2.6 in Appendix A.2).

Our new $\Delta\delta^{18}O_{ivc\text{-}sw}$ record provides strong evidence for the existence of ~41-kyr fluctuations in phase with global ice-volume during the entire study interval (Figure 5.7b). If these 41-kyr oscillations were a result of changes in thermocline tilt, we might expect higher-amplitude G-IG surface-water salinity variations in the EEP than in the WPWP (see Chapter 5.1). However, G-IG surface-water salinity variability of similar magnitude in the Eastern and

Western Equatorial Pacific during the most prominent iNHG glacial-interglacial cycles, as evidenced by our data, argues against thermocline-tilt-controlled surface-water dynamics (Figure 5.6d). This result supports our hypothesis that G-IG salinity changes in the tropical Pacific were more likely driven by ITCZ displacement over the EEP. In combination with our orbital-resolution zonal ΔSST record (Figure 5.7a), these findings have important implications for the ongoing debate on the existence of obliquity-paced oscillations from El Niño- to La Niña-like climate states in the tropical Pacific during the Plio-Pleistocene, which we conclude were unlikely during late Pliocene to early Pleistocene G-IG cycles.

5.4.7 Implications for obliquity-paced surface-water dynamics during the Plio-Pleistocene

The typical pattern of seasonal ITCZ migration toward the warmer hemisphere caused by insolation changes is not observed during modern ENSO variability (Schneider et al., 2014). Going from La Niña to El Niño conditions in the modern, the Northern Hemisphere warms more than the Southern Hemisphere. Paradoxically, the ITCZ responds with a southward migration toward the cooler hemisphere, which appears to be primarily driven by tropical changes in atmospheric energy input (Schneider et al., 2014, and references therein). This has important implications for the debate over whether surface-water dynamics in the equatorial Pacific followed glacial-interglacial-scale ENSO-like pattern across iNHG. We interpret local $\delta^{18}O_{ivc\text{-}sw}$ changes in the late Pliocene to early Pleistocene EEP to indicate a northward migration of the ITCZ during interglacials and a southward migration during glacials. This interpretation is supported by both our zonal equatorial Pacific ΔSST (which are unrelated to G-IG cycles; Figure 5.7a) and $\Delta\delta^{18}O_{ivc\text{-}sw}$ estimates (which show a G-IG cyclicity, but suggest an ITCZ movement toward the warmer hemisphere during prominent iNHG glacial-interglacial cycles; Figure 5.7b). Evaluation of the applicability of modern atmospheric ENSO and ITCZ dynamics to these longer G-IG timescales is, however, required.

5.5 Conclusions

We present new high-resolution records from Eastern Equatorial Pacific ODP Site 849 and compare them to west Pacific ODP Site 806 to critically assess the possibility of obliquity-paced changes in surface-water structure, involving changes in Walker Cell circulation,

during the Plio-Pleistocene onset of Northern Hemisphere Glaciation (MIS G6–95, ~2.75–2.4 Ma). The most salient features of our study are as follows:

(i) We find that the west-east equatorial Pacific SST gradient progressively increased across iNHG, mostly driven by glacial cooling in the EEP. The absence of a G-IG cyclicity in the zonal equatorial Pacific SST gradient argues against obliquity-paced fluctuations from El Niño-like to La Niña-like climate states in the equatorial Pacific during the late Pliocene and early Pleistocene.

(ii) In analogy to modern seasonal ITCZ shifts, we propose the reconstructed glacial-interglacial SSS amplitudes (as represented by $\delta^{18}O_{ivc\text{-}sw}$) at Site 849 during most prominent iNHG glacial-interglacial cycles to be related to a glacial southward and interglacial northward displacement of the ITCZ rain belt, respectively.

(iii) The equatorial Pacific SSS gradient (as represented by $\Delta\delta^{18}O_{ivc\text{-}sw}$) is characterized by 41-kyr fluctuations. We speculate that glacial-interglacial north-south migrations of the ITCZ over the EEP as evidenced in the $\delta^{18}O_{ivc\text{-}sw}$ record from Site 849 controlled the $\delta^{18}O_{ivc\text{-}sw}$ gradient in the Pacific during prominent iNHG glacials. These findings have important implications for the debate on possible fluctuations between El Niño-like and La Niña-like climate states on G-IG timescales, which we conclude were unlikely during the late Pliocene and early Pleistocene.

CHAPTER 6

SEA-LEVEL AND DEEP-SEA TEMPERATURE EVOLUTION DURING THE PLIO-PLEISTOCENE INTENSIFICATION OF NORTHERN HEMISPHERE GLACIATION: RECONCILING SIGNALS FROM THE EASTERN EQUATORIAL PACIFIC AND THE NORTH ATLANTIC†

6.1 Introduction

In light of the increasing manifestation of anthropogenic forcing on Earth's climate, it is important to understand the response of ice volume/sea level to global warming on human-relevant (i.e., [sub-]millennial) timescales (e.g., IPCC, 2014; Nicholls et al., 2014). The need for reliable predictions of future sea-level rise is highlighted by the fact that with a sea-level increase of merely 40 cm – a value probably to be reached by the end of the 21st century (IPCC, 2014) – as many as 270 million people presently living in near-coastal lowlands will lose their homes (Mimura, 2013). At the same time, information on the lower-frequency (i.e., orbital-scale) baseline characteristics of sea-level change underlying the short-term variability is required in order to obtain a full mechanistic understanding. In this context, the sea-level variability of the early Pleistocene and late Pliocene can provide unique insight into the processes and mechanisms connected to sea-level change across a wide variety of different timescales, ranging from long-term (Myr) to glacial-interglacial (100–41 kyr) to (sub-) millennial (<1,000 yr).

While several continuous sea-level records with relatively high resolution (i.e., [sub-] millennial-scale) exist for the past 500 kyr (e.g., Siddall et al., 2003; Rohling et al., 2009), markedly less information is yet available on the short-term sea-level variability under warmer-than-present climate conditions of the early Pleistocene and late Pliocene. Continuous, highly resolved records of sea-level change under such climatic boundary

† *Data for this Chapter are provided in Tables B.3.1–B.3.2 (Appendix B.3).*

conditions are, however, needed in order to better understand the evolution of past climates and to reliably predict the effects of future climate change.

The late Pliocene onset and early Pleistocene intensification of Northern Hemisphere Glaciation (iNHG) ~2.9 to ~2.5 Ma ago (e.g., Raymo et al., 1989; Jansen et al., 2000; Bartoli et al., 2006) comprises climatic boundary conditions as they are expected in the context of near-future climate warming and sea-level rise. It encompasses the transition from a warmer Pliocene climate without large Northern Hemisphere ice sheets to a progressively cooler Pleistocene climate characterized by an increasingly stronger response of the climate-cryosphere system to orbital forcing (Lisiecki and Raymo, 2005). Within this climatic evolution, Marine Isotope Stage (MIS) 100 stands out as the first glacial during which the Laurentide Ice Sheet advanced into the midlatitudes (e.g., Balco and Rovey, 2010) comparable to its extension during the Last Glacial Maximum (Bailey et al., 2013). Available sea-level records support this observation. They consistently document a shift toward larger-amplitude sea-level fluctuations (i.e., stronger glacials) for MIS 100–96 (Bintanja and Van de Wal, 2008; de Boer et al., 2014). However, the sea-level estimates as they are yet available for MIS 100–96 cover a wide spectrum from +10 m to -110 m relative to present (Table 6.1), which makes it difficult to reliably constrain the dynamics of the early Pleistocene climate-cryosphere system. In addition, most of the available datasets are limited to orbital-scale resolution, and there is still a paucity of high-resolution records comparable to those of the late Pleistocene (e.g., Siddall et al., 2003; Rohling et al., 2009).

In light of this need for higher resolved data, sea-level and deep-sea temperature change is quantified in this study for the interval ~2.65–2.4 Ma ago (MIS G1–95) based on new, high-resolution benthic foraminiferal (*Oridorsalis umbonatus*) Mg/Ca and stable-isotope records from Ocean Drilling Program (ODP) Site 849 in the Eastern Equatorial Pacific (EEP) and Integrated Ocean Drilling Program (IODP) Site U1313 in the North Atlantic (Figure 6.1). The North Atlantic has been selected for this study because of its proximity to the large dynamic Northern Hemisphere ice sheets; the Pacific Ocean has been selected not only because it represents the largest water body on Earth, but because it is – unlike the Atlantic Ocean – influenced by only one bottom-water mass (Dwyer and Chandler, 2008; Lang et al., 2016).

6.2 Available sea-level estimates covering the intensification of Northern Hemisphere Glaciation

To date, various techniques have been employed for generating sea-level records for different time intervals of the iNHG and based on material from different regions (Table 6.1, Figure 6.1). A brief overview on the sea-level estimates for iNHG as yet available, along with the techniques applied, is given in the following.

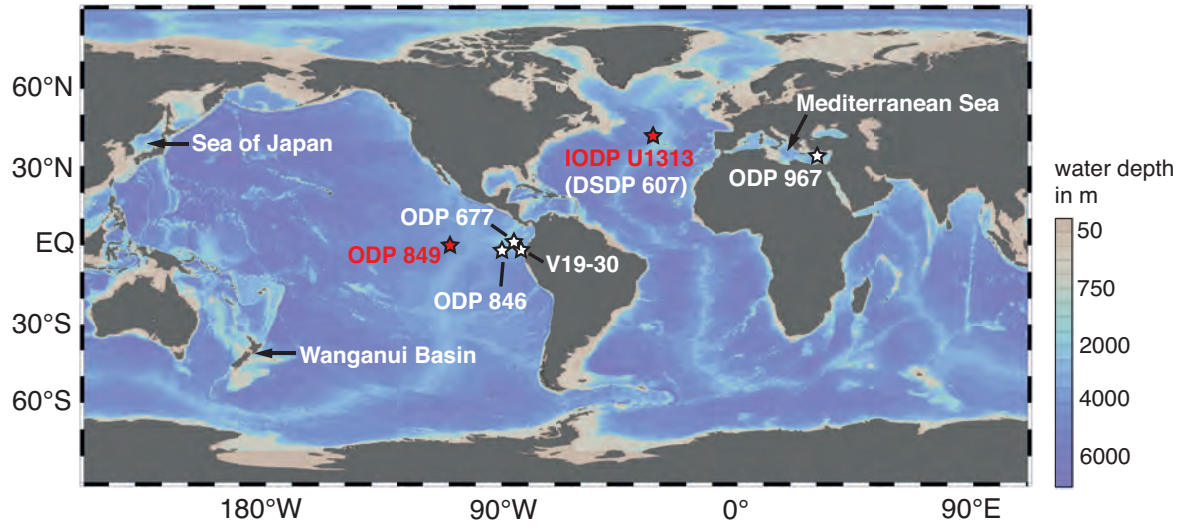

Figure 6.1. Bathymetric map showing the location of ODP Site 849 (red; this study), IODP Site U1313 (red; this study) and other locations (white) mentioned in the text. Water depth (m) after World Ocean Atlas.

6.2.1 Sea-level estimates for glacials (MIS 100 –96)

The most extreme sea-level lowstand estimates (in m below present) of -110 m, -100 m and -80 m for MIS 100, 98 and 96, respectively, derive from sequence stratigraphy applied to continental margins in New Zealand (Naish, 1997). Sea-level lowstand estimates calculated from benthic foraminiferal oxygen isotopes ($\delta^{18}O_b$) (Miller et al., 2011) or paired benthic Mg/Ca and $\delta^{18}O$ analyses (Dwyer et al., 1995; Sosdian and Rosenthal, 2009) suggest values of -55 m to -75 m for MIS 100, -60 m to -70 m for MIS 98, and -60 m to -90 m for MIS 96. Inverse forward modeling based on the LR04 stack of benthic foraminiferal $\delta^{18}O$ records (Lisiecki and Raymo, 2005) has yet yielded an "artificial" sea-level curve comprising the past 5 Myr (Bintanja and Van de Wal, 2008; Lourens et al., 2010; de Boer et al., 2014); the estimated lowstands for glacials MIS 100 through 96 range from -65 m to -75 m (Bintanja and Van de Wal, 2008; Lourens et al., 2010) to more modest values of -35 m to -45 m (de Boer et al., 2014). The latter values are comparable to those inferred from a nonlinear transfer function based on $\delta^{18}O_b$ and sea level, which amount to -35 m, -40 m and -20 m for MIS 100, 98 and 96, respectively (Siddall et al., 2010). The yet most modest sea-level lowstand values

of -15 m for MIS 100 and 98, and +10 m for MIS 96 have recently become available through planktic foraminiferal oxygen-isotope ($\delta^{18}O_p$) analyses in the eastern Mediterranean Sea (Rohling et al., 2014). Regardless of absolute values, aforementioned sea-level records consistently document more conservative sea-level lowstand estimates for glacials prior to MIS 100.

Table 6.1. Summary of sea-level lowstand estimates (in m relative to present) for glacials MIS 104 to 96 from previous studies. Ages reflect peak glacial conditions based on the LR04 stack (Lisiecki and Raymo, 2005).

MIS					Method	Location	Reference
104 2.60 ka	**102** 2.57 ka	**100** 2.52 ka	**98** 2.49 ka	**96** 2.43 ka			
-45	-30	-60	-60	-65	$\delta^{18}O_b$	global (LR04-based)	Miller et al. (2011)
	-10	-35	-40	-20	$\delta^{18}O_b$	East Pacific (ODP Sites 677 and 846, Site V19-30)	Siddall et al. (2010)
0	+30	-15	-15	+10	$\delta^{18}O_p$	Mediterranean Sea	Rohling et al. (2014)
-45	-5	-60	-60	-60	model	global (LR04-based)	Bintanja and Van de Wal (2008)
-25	-5	-45	-35	-40	model	global (LR04-based)	de Boer et al. (2014)
		-75	-70	-65	model	Mediterranean Sea (ODP Site 967)	Lourens et al. (2010)
		-110	-100	-80	sequence stratigraphy	Wanganui Basin, New Zealand	Naish (1997)
-50	-30	-60	-60	-60	sequence stratigraphy	Wanganui Basin, New Zealand	Naish and Wilson (2009)
-55	-80	-80	-60	-55	sequence stratigraphy	Sea of Japan	Cronin et al. (1994)
-65	-65	-75	-70	-90	$Mg/Ca_{ostracodes}$ and $\delta^{18}O_b$	North Atlantic (DSDP Site 607)	Dwyer et al. (1995)
-40	-25	-55	-65	-60	Mg/Ca_b and $\delta^{18}O_b$	North Atlantic (DSDP Site 607)	Sosdian and Rosenthal (2009)

MIS = Marine Isotope Stage, DSDP = Deep Sea Drilling Program, ODP = Ocean Drilling Program

6.2.2 Sea-level estimates for interglacials (MIS G1–95)

Model simulations (Bintanja and Van de Wal, 2008; Lourens et al., 2010; de Boer et al., 2014) and paired Mg/Ca- and $\delta^{18}O$-based records (Sosdian and Rosenthal, 2009; Miller et al., 2011) indicate a sea-level highstand on the order of present-day sea level for interglacials MIS G1 through 95. In line with these results, transfer-function-derived sea-level values do also not exceed present-day sea-level during that time (Siddall et al., 2010). New sea-level estimates from the Mediterranean Sea, however, have challenged these perceptions, indicating highstand values of 40–50 m above present for interglacials MIS G1 through 95 (Rohling et al., 2014).

6.3 Material and methods

6.3.1 Site locations

Deep-sea temperature and sea-level data presented in this study have been generated on sediment cores that were drilled within the framework of ODP Leg 138 in the EEP (Site 849) and IODP Expedition 306 in the North Atlantic (Site U1313) (Figure 6.1; for details see Chapter 3). Site 849 (0°11'N, 110°31'W) is situated ~860 km west of the East Pacific Rise and was drilled at a present-day water depth of 3851 m (Mayer et al., 1992; Mix et al., 1995). Located in the heart of the EEP upwelling zone, it exhibits continuous sedimentation with high sedimentation rates across the target interval (~2.7 cm kyr^{-1}; Chapter 5). Site 849 is located well above the modern (4500–4700 m [Lyle et al., 1995; Pälike et al., 2012]) and Plio-Pleistocene (>4500 m [Pälike et al., 2012]) carbonate compensation depth in the tropical Pacific, which favors carbonate preservation and thus the reconstruction of highly resolved foraminifer-based proxy records (Chapters 4 and 5).

Site U1313 is a reoccupation of Deep Sea Drilling Program Site 607, which constitutes a benchmark mid-depth site for monitoring subpolar North Atlantic climate evolution and has provided important insight into Pleistocene paleoceanography (e.g., Raymo et al., 1989; Raymo et al., 1992). Site U1313 is located in the subpolar North Atlantic ~400 km northwest of the Azores (41°N, 32.5°W) (Figure 6.1). It is situated at the base of the upper western flank of the Mid-Atlantic Ridge in a present-day water depth of 3426 m (Expedition 306 Scientists, 2006) at the southernmost end of the "Ice-rafted debris belt" (Ruddiman, 1977a, b; Chapter 3). Consistently high sedimentation rates on the order of 4–5 cm kyr^{-1} at Site U1313 during the Plio-Pleistocene (Expedition 306 Scientists, 2006) provide the opportunity to work at high temporal resolution.

6.3.2 Sample material and processing

To study Plio-Pleistocene sea-level and deep-sea temperature change centered on MIS G1–95 at Site 849, cores 849C-7H-1-80 cm to 849C-7H-2-21 cm and 849D-6H-5-102 cm to 849D-7H-3-73 (74.17–67.78 m composite depth [mcd]) were investigated. For generating a record at suborbital resolution, 240 samples (sample volume: 20 cm^3) were examined at 2-cm spacing (yielding a resolution of ~800 yr according to the age model presented in Chapter 5). The chronology for the target interval (~2.65–2.4 Ma) follows that presented in Chapter 5, which is based on a high-resolution $\delta^{18}O_b$ (*Cibicidoides wuellerstorfi*) stratigraphy for Site 849 tuned to the LR04 stack (Lisiecki and Raymo, 2005).

For Site U1313, 248 samples were examined at 8-cm spacing (temporal resolution: ~1550 yr according to the age model of Bolton et al. [2010c]), with a higher 4-cm spacing (corresponding to a resolution of ~775 yr) across glacial terminations and a 2-cm spacing (~388 yr) for MIS 100. Samples were investigated along the primary shipboard splice from 125.25 to 114.12 mcd, representing ~2.65–2.4 Ma (cores U1313B-12H-2-118 cm to U1313B-12H-6-120 cm, U1313B-13H-1-74 cm to U1313B-13H-1-127 cm, U1313C-12H-3-112 cm to U1313C-12H-5-52 cm, and U1313C-13H-3-2 cm to U1313C-13H-4-22 cm). A robust age model is already available for the time interval focused upon in this study. It is based on a ~2-kyr resolution $\delta^{18}O_b$ (*C. wuellerstorfi*) stratigraphy (Bolton et al., 2010c) tuned to the LR04 stack (Lisiecki and Raymo, 2005). To achieve high-resolution stable-isotope records (*C. wuellerstorfi* $\delta^{18}O$ and $\delta^{13}C$) across MIS 100 for Site U1313, new data were generated (~388 yr according to the age model of Bolton et al. [2010c]) to supplement lower-resolved (~2 kyr) data published in previous studies (Bolton et al., 2010c; Lang et al., 2014). Therefore, 3–5 *C. wuellerstorfi* specimens were picked from the >150 μm size fraction on a 2-cm resolution from 121.34 to 118.52 mcd.

For sea-level and deep-sea temperature reconstruction, the benthic foraminiferal species *Oridorsalis umbonatus* has been selected because it is, in comparison to other benthic foraminiferal species, less affected by the carbonate-ion effect (Rathmann and Kuhnert, 2008) and therefore appears to be a highly reliable Mg/Ca recorder. Moreover, *O. umbonatus* is easier to clean for Mg/Ca analyses due to its larger chambers compared to other species such as *C. wuellerstorfi*. An average of 12 *O. umbonatus* specimens was picked from the >150 μm dried sediment fraction for both sites. To allow for combined $\delta^{18}O$ and Mg/Ca analyses, tests were cracked, homogenized and split into two subsamples.

6.3.3 Foraminiferal Mg/Ca cleaning and analyses

Subsamples for Mg/Ca analyses were carefully cleaned to remove clay minerals, organic material and re-adsorbed contaminants following the cleaning protocol of Barker et al. (2003). Site 849 samples were analyzed using the Agilent Inductively Coupled Plasma-Optical Emission Spectrometer 720 at the Institute of Earth Sciences, Heidelberg University. Mg/Ca samples from Site U1313 (except for MIS 100) were run on a Thermo Fischer Element High-resolution Inductively Coupled Plasma Mass Spectrometer at the National Oceanography Centre, Southampton (UK). Samples from Site U1313 covering MIS 100 were measured using a Perkin Elmer Optima 4300DV Inductively Coupled Plasma-Optical Emission Spectrometer also at the National Oceanography Centre, Southampton (UK). Reported Mg/Ca

values were normalized relative to the ECRM 752-1 standard reference value of 3.762 mmol/mol (Greaves et al., 2008) to correct for machine offsets. To ensure instrumental precision, an internal consistency standard was monitored at least every 20 samples. Based on replicate measurements, a standard deviation for Mg/Ca of ±0.025 mmol/mol (equals ±0.13°C) for Site 849 samples and ±0.096 mmol/mol (equals ±0.4°C) for Site U1313 samples is obtained. To identify possible contamination by clay particles or diagenetic coatings which might affect foraminiferal Mg/Ca ratios (Barker et al., 2003), elemental ratios of Al/Ca, Fe/Ca and Mn/Ca were screened. Results indicate that the Mg/Ca content of the analyzed tests is unaffected by contamination (see Figures A.3.1 and A.3.2 in Appendix A.3).

6.3.4 Stable-isotope analyses

Stable isotopes of *C. wuellerstorfi* samples from Site U1313 and *O. umbonatus* subsamples from Sites U1313 and 849 were analyzed using a ThermoFinnigan MAT253 gas source mass spectrometer equipped with a Gas Bench II at the Institute of Geosciences, Goethe-University Frankfurt. Values are reported relative to the Vienna Pee Dee Belemnite (VPDB) standard through the analysis of an in-house standard calibrated to NBS-18 and NBS-19. The precession of the $\delta^{18}O$ and $\delta^{13}C$ analyses is better than 0.08‰ and 0.06‰ (at 1σ level), respectively. Analyses of modern (Graham et al., 1981), Cenozoic (Shackleton et al., 1984b) and Turonian (Wendler et al., 2013) tests of *O. umbonatus* suggest that $\delta^{18}O$ and $\delta^{13}C$ values of this species approximate equilibrium with ambient seawater. Also *C. wuellerstorfi* precipitates its shell close to $\delta^{13}C$ equilibrium (Zahn et al., 1986; Mackensen et al., 1993), while $\delta^{18}O$ values of *C. wuellerstorfi* deviate from equilibrium by 0.64‰ (Shackleton et al., 1984b) (see Table 2.1 in Chapter 2).

6.3.5 Paleotemperature and sea-level reconstruction

Mg/Ca ratios from both sites were converted into bottom-water temperature (BWT) estimates following a species-specific equation for *O. umbonatus* (BWT = ln[Mg/Ca/1.008] x [1/0.114]) (Lear et al., 2002). Because this equation is based on oxidative and reductive cleaning of foraminiferal tests, while only oxidative cleaning has been applied for Site 849 and U1313 samples, measured Mg/Ca values were adjusted by reducing each value by 10% (Barker et al., 2003). The oxygen-isotope composition of seawater ($\delta^{18}O_{sw}$, relative to the Standard Mean Ocean Water [SMOW] standard) was then calculated using *O. umbonatus* based $\delta^{18}O$ and BWT estimates ($\delta^{18}O_{sw,\ SMOW} = [(BWT - 16.9)/4.0] + \delta^{18}O_b + 0.27‰$) (Shackleton, 1974; Hut, 1987). Finally, $\delta^{18}O_{sw}$ was converted to sea-level assuming that

0.11‰ change in $\delta^{18}O_{sw}$ is equivalent to a 10 m change in sea-level (Fairbanks and Matthews, 1978). This combined geochemical approach typically yields an uncertainty for sea-level of ~20 m (Sosdian and Rosenthal, 2009; Arbuszewski et al., 2010).

A recent study demonstrates that during late Pliocene glacials the influence of North Atlantic Deep Water became restricted at Site U1313 relative to deep waters derived from high southern latitudes (Lang et al., 2016). Therefore, using a combined approach of $\delta^{18}O$ and Mg/Ca on benthic foraminifera at Site U1313 requires a correction against changing deep-water masses that alternately influence the seafloor on G-IG timescales. Two different methods are applied to adjust the Site U1313 record to hypothesized changes in bottom-water masses. First, foraminifer-derived $\delta^{18}O$ and BWT values used for sea-level reconstruction were adjusted by using a linear regression ($BWT = 5 \times \delta^{18}O_{sw} + 2.6$) between modern North Atlantic Deep Water and Antarctic Bottom Water temperature and $\delta^{18}O_{sw}$ endmembers of 2.6°C and 0.1‰ and 0°C and -0.5‰, respectively (Craig and Gordon, 1965) (hereinafter sl_{CG65}) (see Figure A.3.3 in Appendix A.3). Second, Site U1313 foraminifer-derived $\delta^{18}O$ and BWT values used for sea-level calculation were adjusted by using benthic $\delta^{13}C$-based estimates of the relative abundance of northern- *versus* southern-component waters reconstructed for Site U1313/607 (Lang et al., 2014; Lang et al., 2016) (hereinafter sl_{L16}). For Pacific Ocean Site 849 this correction is not necessary, because deep-water masses that bath the EEP are primarily sourced from the Southern Ocean (Emery, 2003; see also Chapter 3).

6.3.6 Foraminiferal preservation

Although previous studies document that carbonate preservation does not significantly alter foraminifer-derived proxy records across the studied time interval at Sites 849 (Chapters 4 and 5) and U1313 (Expedition 306 Scientists, 2006; Friedrich et al., 2013), the preservation of tests used in this study was examined by scanning electron microscope (SEM) images for selected specimens representing both glacial and interglacial intervals. Close-up views were generated using a LEO 440 SEM at the Institute of Earth Sciences, Heidelberg University, and a ZEISS SIGMA VP-FE-SEM at the Institute of Geosciences, Goethe-University Frankfurt. Results indicate that the preservation is consistently good to acquire high-quality stable-isotope and Mg/Ca data at both sites (Figure 6.2).

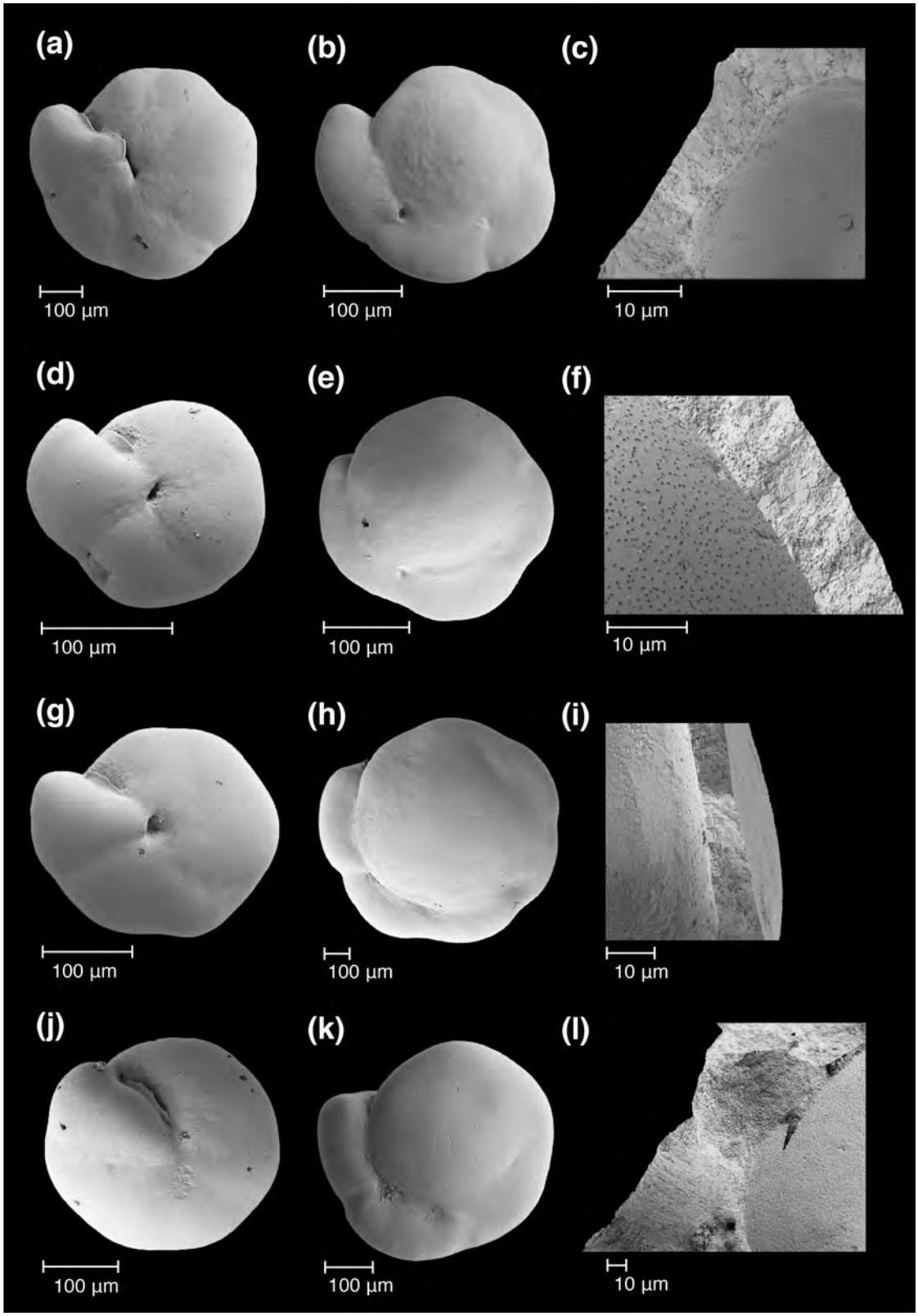

Figure 6.2. Scanning electron microscope micrographs of *Oridorsalis umbonatus* from Site 849 in the Eastern Equatorial Pacific **(a–f)** and from Site U1313 in the North Atlantic **(g–l)**. Both glacial (a–c, g–i) (samples 849D 7H-2 41–43 cm, U1313B 12H-4 124–126 cm) and interglacial (d–e, j–l) (samples 849D 7H-4 103–105 cm, U1313B 12H-5 92–94 cm, U1313B 12-5 98–100 cm) tests are well preserved, allowing for the acquisition of reliable Mg/Ca and stable-isotope data at both sites. Note the preservation of delicate pore channels (c, f, i, l) and a layered wall structure (l) in the close-up views.

6.4 Results

6.4.1 Late Pliocene to early Pleistocene benthic foraminiferal proxy records from Eastern Equatorial Pacific Site 849

Deep-sea $\delta^{18}O$ and $\delta^{13}C$ records

The new high-resolution $\delta^{18}O$ record of the benthic foraminiferal species *O. umbonatus* from Site 849 for the time interval ~2.65–2.4 Ma varies between 2.80‰ and 4.40‰, with a mean value of 3.56‰ (Figure 6.3a). Lowest and highest values are associated with interglacials and

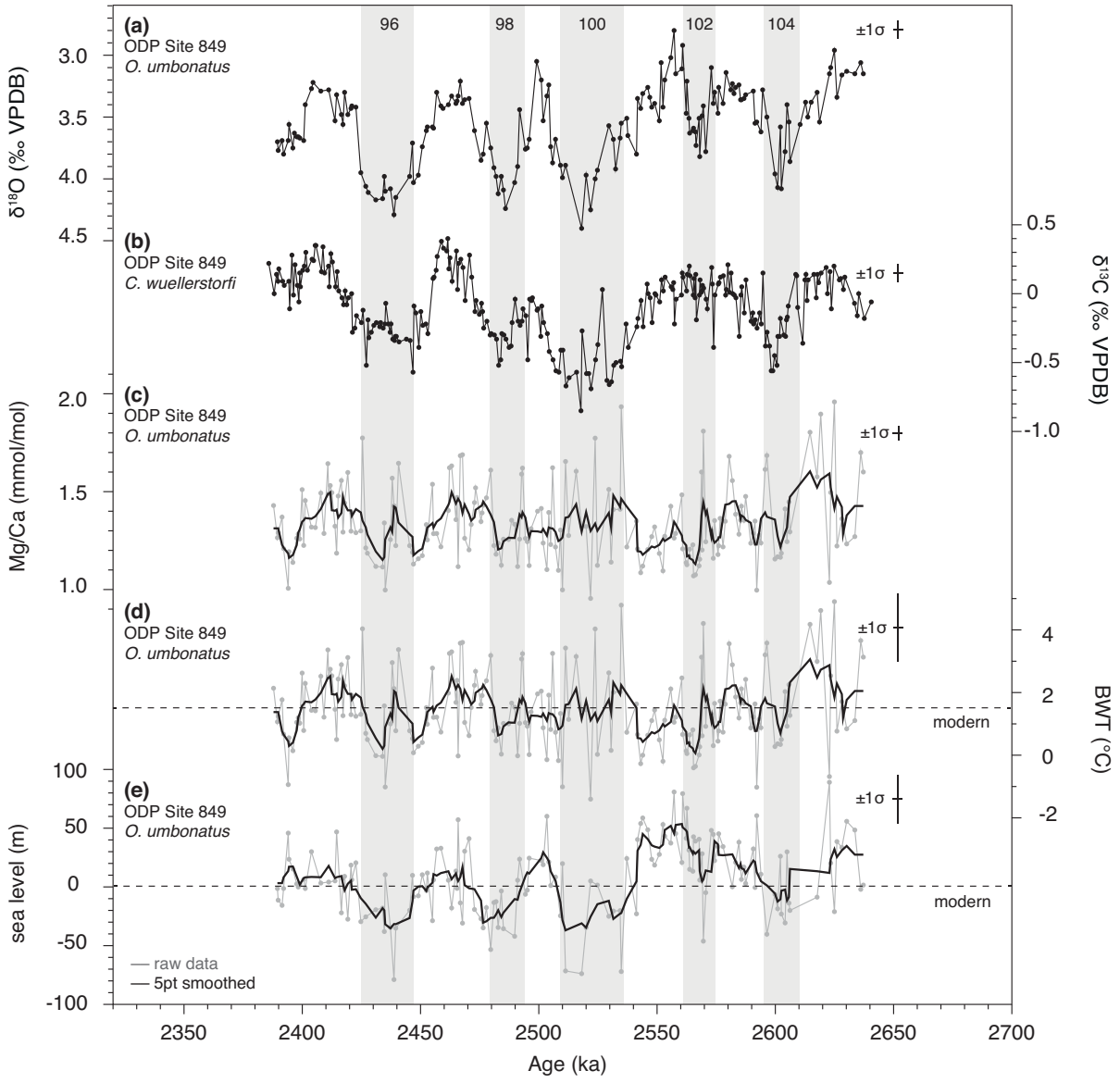

Figure 6.3. High-resolution benthic foraminiferal proxy records from east Pacific Site 849 for MIS G1 to 95. **(a)** *O. umbonatus* $\delta^{18}O$, **(b)** *C. wuellerstorfi* $\delta^{13}C$, **(c)** *O. umbonatus* Mg/Ca, **(d)** *O. umbonatus* Mg/Ca-based estimates of deep-sea temperature in comparison to modern values (dashed line [Locarnini et al., 2013]), **(e)** *O. umbonatus* Mg/Ca- and $\delta^{18}O$-based sea-level record relative to present-day sea level (dashed line). Grey data points in Figure 6.3c–e show raw data, black line represents the five-point smoothed average of a record. Horizontal and vertical bars indicate the 1σ standard deviation associated with the age model and the individual proxy records, respectively. Grey bars mark glacial periods.

glacials, respectively. The $\delta^{18}O$ record of *O. umbonatus* perfectly captures the obliquity-related pattern derived by another benthic foraminiferal (*C. wuellerstorfi*) $\delta^{18}O$ record from Site 849 for the same time interval (Chapter 5). Glacial-interglacial variations in both benthic foraminiferal $\delta^{18}O$ datasets are significantly stronger for MIS 100–96 (>1‰), i.e., during the first strong glacials since the late Pliocene onset of Northern Hemisphere Glaciation, compared to the time interval prior to MIS 100 (<1‰).

The deep-sea $\delta^{13}C$ record of *C. wuellerstorfi* from Site 849 (Figure 6.3b) used in this study to calculate benthic foraminiferal $\delta^{13}C$ gradients between the Atlantic and Pacific Oceans (see Chapter 6.5.2) has already been presented in Chapter 4. In that study it has been hypothesized that benthic (and planktic) foraminiferal $\delta^{13}C$ records at Site 849 are controlled by changes in the isotopic composition of upwelled waters sourced in the high-latitude Southern Ocean for MIS G1–95, with minor G-IG fluctuations prior to MIS 100 and larger-scale G-IG changes from MIS 100 onward. This interpretation is in agreement with previous findings (Tsuchiya et al., 1989; Toggweiler et al., 1991), confirming that the EEP is primarily sourced by high-southern-latitude waters.

Deep-sea temperatures

The five-point smoothed average of the BWT record from Site 849 varies between 0°C and 3.1°C (Figure 6.3c–d) for the time interval ~2.65–2.4 Ma. Average BWTs of ~1.5°C across the studied interval are identical to present-day mean annual deep-sea temperatures at Site 849 (Locarnini et al., 2013). Raw data produce highest and lowest BWT values of 4.9°C and -1.4°C, respectively, and show strong short-term fluctuations with amplitudes of ~2–4°C. Visual evaluation of the smoothed BWT record appears to indicate low-amplitude G-IG variations (<2°C) across the entire investigated time interval.

Sea-level estimates

The five-point smoothed average of the sea-level record from Site 849 follows the obliquity-related G-IG cyclicity given by the Site 849 $\delta^{18}O_b$ record from ~2.65 to 2.4 Ma (Figure 6.3e). Glacial-interglacial amplitudes became more pronounced from MIS 100 onward (~50 m) than prior to MIS 100 (~35 m), contemporaneous with the proposed first significant waxing and waning of Northern Hemisphere ice sheets (e.g., Shackleton et al., 1984a). Mean sea-level highstand estimates were above modern values during the entire study interval, i.e., approximately +35 m for MIS G1, +40 m for MIS 103, +55 m for MIS 101, +30 m for MIS 99, +15 m for MIS 97, and +20 m for MIS 95 (relative to modern values). Sea-level lowstand

estimates (relative to present) were on average -10 m for MIS 104, +5 m for MIS 102, -35 m for MIS 100 and 96, and -25 m for MIS 98 (Table 6.2). Raw data produce peak sea-level lowstand values of approximately -40 m for MIS 104, -45 m for MIS 102, -75 m for MIS 100, -55 m for MIS 98, and -80 m for MIS 96. The negative excursions at 2.44 Ma (MIS 96) to -80 m and at 2.57 Ma (MIS 102) to -45 m, however, are only represented by a single data point, and should therefore be interpreted with caution. Notably, it appears that the onset of significant waxing and waning of Northern Hemisphere ice sheets from MIS 100 through 96 was associated with an average sea-level drop of ~30 m during glacial and ~15 m during interglacial intervals. This pattern is comparable to sea-level evolution during the late Pliocene cooling from 3.2 to 2.7 Ma (Sosdian and Rosenthal, 2009), but, for example, different to the Mid-Pleistocene Transition (~1.2–0.7 Ma) when sea level only dropped during glacial intervals (Sosdian and Rosenthal, 2009).

Table 6.2. Comparison of sea-level lowstand estimates for MIS 104 to 96 derived from previous estimates (see Table 6.1) and from this study (in m relative to present). Ages reflect peak glacial conditions based on the LR04 stack (Lisiecki and Raymo, 2005).

MIS					Reference
104 2.60 ka	**102** 2.57 ka	**100** 2.52 ka	**98** 2.49 ka	**96** 2.43 ka	
0 to -65	+30 to -80	-15 to -110	-15 to -100	+10 to -90	Previous estimates
-80	-60	-110	-125	-130	this study: North Atlantic IODP Site U1313 (sl_{CG65})
-95	-65	-125	-155	-190	this study: North Atlantic IODP Site U1313 (sl_{L16})
-40	-45	-75	-55	-80	this study: East Pacific ODP Site 849 (raw)
-10	+5	-35	-25	-35	this study: East Pacific ODP Site 849 (smoothed)

MIS = Marine Isotope Stage, IODP = Integrated Ocean Drilling Program, ODP = Ocean Drilling Program

6.4.2 Late Pliocene to early Pleistocene benthic foraminiferal proxy records from North Atlantic Site U1313

Deep-sea $\delta^{18}O$ and $\delta^{13}C$ records

The new high-resolution $\delta^{18}O$ record of *O. umbonatus* from North Atlantic Site U1313 varies between 2.51‰ and 4.60‰ across the study interval (~2.65–2.4 Ma) with lower values during interglacial periods and higher values during glacial periods (Figure 6.4a). Overall, the $\delta^{18}O$

record of *O. umbonatus* follows the obliquity-related G-IG cyclicity shown by the *C. wuellerstorfi* $\delta^{18}O$ record from that site (Bolton et al., 2010c). Glacial-interglacial amplitudes became stronger across prominent iNHG glacials (>1‰) compared to the time period prior to MIS 100 (<1‰). Interestingly, the final ~10 kyr of MIS 100 are characterized by an additional increase in $\delta^{18}O$ before $\delta^{18}O$ values decrease rapidly during the following termination.

High-resolution $\delta^{13}C$ data based on *C. wuellerstorfi* from Site U1313 across MIS 100 (this study) perfectly capture the pattern yielded by a lower-resolved record of the same species at the same site (Lang et al., 2014) (Figure 6.4b). In general, lowest values are associated with glacial periods and highest values with interglacial periods. Interglacial values remain relatively constant across the interval of study, while a significant decrease in glacial values during MIS 100, 98 and 96 indicates that G-IG amplitudes become stronger (~1‰) compared to the time interval prior to MIS 100 (~0.5‰). This is comparable to the pattern observed in the deep-sea $\delta^{18}O$ record at the same site (Figure 6.4a), and benthic foraminiferal $\delta^{18}O$ and $\delta^{13}C$ records at EEP Site 849 (Figure 6.3a–b).

Deep-sea temperatures

The new BWT record from Site U1313 fluctuates between a maximum value of 9.5°C and a minimum value of 2.2°C between ~2.65 and 2.4 Ma (Figure 6.4c–d). Interglacial BWTs are on the order of ~6–7°C, with the exception of MIS 97 that yielded the by far warmest temperatures (>7°C, up to 9.5°C) of the entire record. Glacial temperatures during MIS 104 and MIS 100–96 approximate modern mean annual BWT values of 3.4°C at that site (Locarnini et al., 2013), while average BWTs across the studied time interval of ~5.1°C indicate slightly warmer (~1.7°C) than present-day values. This supports the overall notion of a warmer-than-modern global climate during the late Pliocene and early Pleistocene. Visual evaluation of Figure 6.4d indicates obliquity-related G-IG oscillations with an amplitude of ~3.5°C. This trend is stronger across MIS 97, but weak across MIS 102, suggesting that this modest glacial as evidenced in benthic foraminiferal $\delta^{18}O$ (Figure 6.4a) was too subtle to induce larger-scale changes in deep-ocean temperature.

Sea-level estimates

Both approaches for sea-level reconstruction at Site U1313 (see Chapter 6.3.5) show similar trends throughout most of the record (Figure 6.4e). Visual evaluation of Figure 6.4e indicates

a clear G-IG cyclicity in both sea-level records particularly from MIS 100 onward. Prior to MIS 100, interglacial sea-level highstand estimates significantly exceed present-day sea-level values (the fact that this is not documented for MIS 103 is a matter of low sample resolution), while glacial sea-level lowstand estimates remain below modern values. Raw data produce peak sea-level lowstand values (relative to present) of approximately -80 m (sl_{CG65}) and -95 m (sl_{L16}) for MIS 104, and -60 m (sl_{CG65}) and -65 m (sl_{L16}) for MIS 102. From MIS 100 onward, mean sea-level highstand estimates during interglacials approximate modern values. Sea-level values (relative to present) during prominent iNHG glacials are on average -80 m (sl_{CG65}) to -75 m (sl_{L16}) for MIS 100, -85 m (sl_{CG65}) to -80 m (sl_{L16}) for MIS 98, and -100 m (sl_{CG65}) to

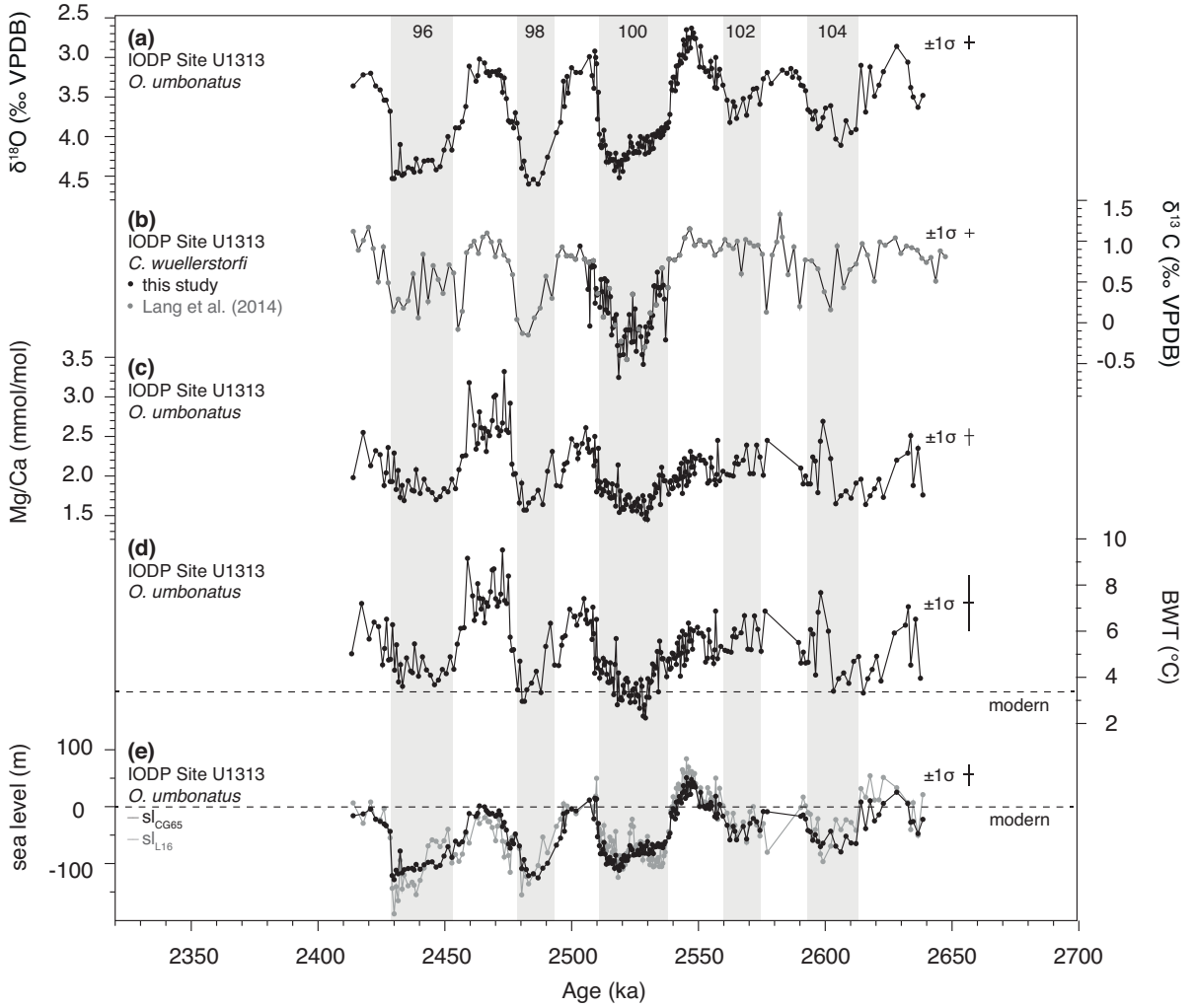

Figure 6.4. High-resolution benthic foraminiferal proxy records from North Atlantic Site U1313 for MIS G1 to 95. **(a)** *O. umbonatus* $\delta^{18}O$, **(b)** high-resolution $\delta^{13}C$ record of *C. wuellerstorfi* for MIS 100 (this study, black) supplemented by the dataset of Lang et al. (2014) (grey), **(c)** *O. umbonatus* Mg/Ca, **(d)** *O. umbonatus* Mg/Ca-based estimates of deep-sea temperature in comparison to modern values (dashed line; Locarnini et al. [2013]), **(e)** *O. umbonatus* Mg/Ca- and $\delta^{18}O$-based sea-level record relative to present-day sea level (dashed line) based on the approach of Craig and Gordon (1965) (sl_{CG65}, black data) and Lang et al. (2016) (sl_{L16}, grey data). Horizontal and vertical bars indicate the 1σ standard deviation associated with the age model and the individual proxy records, respectively. Grey bars mark glacial periods.

-115 m (sl_{L16}) for MIS 96. Raw data produce peak sea-level lowstand values of -110 m (sl_{CG65}) and -125 m (sl_{L16}) for MIS 100, -125 m (sl_{CG65}) and -155 m (sl_{L16}) for MIS 98, and -130 m (sl_{CG65}) and -190 m (sl_{L16}) for MIS 96 (Table 6.2). Although average values remain relatively consistent no matter which water-mass correction is applied, peak sl_{L16} lowstand values reconstructed for MIS 100 and 98 and in particular for MIS 96 appear to be overestimated because they even significantly exceed lowstand estimates for the Last Glacial Maximum by up to ~60 m (Bintanja and Van de Wal, 2008). For simplification, it is therefore only referred to the sl_{CG65} record for Site U1313 in the follow-up discussion.

Sea-level estimates from Site U1313 point to a drop in sea level during both glacial and interglacial intervals of ~50 m and ~25 m, respectively, contemporaneously with the onset of prominent G-IG cycles MIS 100–96. This dictates larger-scale G-IG amplitudes from MIS 100 onward (~100 m) compared to the time interval before (~75 m). This pattern is similar to that observed at Site 607 during the late Pliocene cooling (Sosdian and Rosenthal, 2009), and also reproduces findings from east Pacific Site 849 for the same time interval (see Chapter 6.4.1).

Identical with observations made for the benthic $\delta^{18}O$ record from Site U1313 (see above), the high-resolution sea-level record at Site U1313 for MIS 100 appears to be characterized by an additional sea-level fall ~10 kyr before sea-level increased rapidly during the following termination. A comparable, but more subdued pattern emerges for MIS 96 (Figure 6.4e).

6.5 Discussion

6.5.1 Comparison of North Atlantic and east Pacific deep-sea temperature records

North Atlantic deep-sea temperature records from Site 607 (Sosdian and Rosenthal, 2009) and its reoccupation Site U1313 (this study) show the same trend across the interval of study (Figure 6.5a). Interestingly, the BWT record from Site U1313 is shifted to ~2.7°C higher values compared to BWT estimates derived from Site 607 (Sosdian and Rosenthal, 2009), although the location of theses sites is identical (Figure 6.1). Applying the same calibration as for Site U1313 Mg/Ca data in this study (Lear et al., 2002) to the Site 607 Mg/Ca record presented in Sosdian and Rosenthal (2009), Site 607 BWTs will be shifted to on average 1.1°C higher values. The resulting BWTs are shown in Figure 6.5a. However, Site 607 BWT estimates are still ~1.6°C colder compared to Site U1313. This appears to be a result of significant discrepancies in Mg/Ca raw data (on average ~0.5 mmol/mol), although it remains

peculiar in light of the same locality of these sites. Although the deep-sea Mg/Ca record from Site 607 is based on a composite of *O. umbonatus* and *C. wuellerstorfi* specimens, species-specific differences in Mg/Ca can not account alone for the observed Mg/Ca difference between Sites 607 and U1313, because the interspecific offset between these two species is typically only 0.16 mmol/mol (Sosdian and Rosenthal, 2009). A possible explanation for the observed Mg/Ca offset between Sites 607 and U1313 is that reductive cleaning applied for Site 607 samples dissolved tests and leached Mg more vigorously than the 10%-Mg/Ca-lowering (Barker et al., 2003) assumed in this study to adjust Mg/Ca values for the reductive-cleaning-based BWT calibration (Lear et al., 2002) (see Chapter 6.3.5). This would result in underestimated BWTs at Site 607 and therefore an overestimation of Mg/Ca-based sea-level estimates.

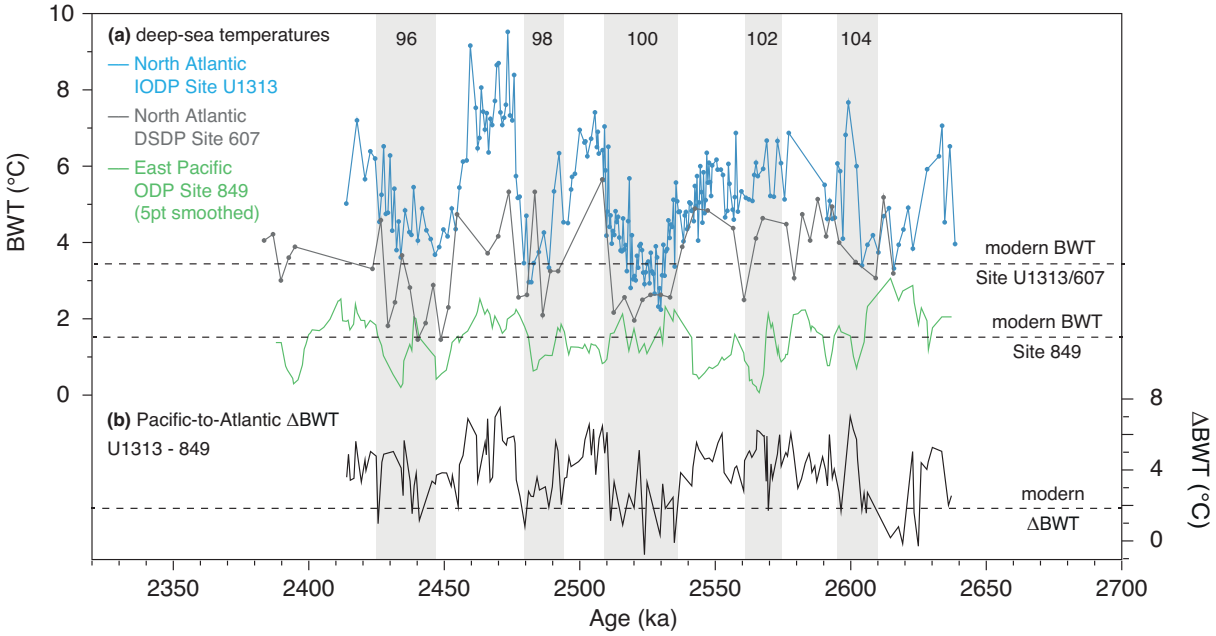

Figure 6.5. **(a)** Comparison of deep-sea temperature records from North Atlantic Site U1313 (blue; this study) and east Pacific Site 849 (green; this study) to deep-sea temperature estimates from Site 607 in the North Atlantic (grey) (Sosdian and Rosenthal, 2009) for the time interval ~2.65–2.4 Ma (MIS G1–95). To facilitate comparison between Sites 849 and U1313 to Site 607, Mg/Ca data from Site 607 (Sosdian and Rosenthal, 2009) were converted into BWTs using the calibration of Lear et al. (2002) instead of the calibration of Sosdian and Rosenthal (2009). Records are plotted with their original age models in alignment to LR04 (Sosdian and Rosenthal, 2009; Bolton et al., 2010c; Chapter 5). Dashed lines indicate modern BWT values at Sites 849 and U1313/607, respectively (Locarnini et al., 2013). **(b)** Pacific-to-Atlantic (Site U1313-to-849) deep-sea temperature gradient (ΔBWT). Dashed line indicates the modern BWT gradient between Site U1313 and Site 849 (Locarnini et al., 2013). Grey bars mark glacial periods.

Deep-sea temperatures derived from east Pacific Site 849 are on average ~4°C colder compared to Site U1313 (Figure 6.5a). The Pacific-to-Atlantic (849-to-U1313) BWT difference, however, is not constant on G-IG timescales. Strong G-IG amplitudes in the North

Atlantic (~3.5°C) compared to rather small-scale fluctuations in the east Pacific (<2°C) imply a diminished Pacific-to-Atlantic BWT gradient during glacials relative to interglacials (Figure 6.5b). This is interpreted to be related to changes in deep-water masses that alternately influence the seafloor on G-IG timescales in the North Atlantic, while the deep east Pacific is permanently bathed by a single water mass from high southern latitudes (see Chapter 6.5.2). In fact, the influence of northern-component waters, which prevail during interglacials at Site U1313, has been demonstrated to be diminished during late Pliocene/early Pleistocene glacials when a ~2.6°C colder (Craig and Gordon, 1965) southern-component water mass advanced into the deep North Atlantic (Lang et al., 2016).

6.5.2 Sea-level reconstruction in the North Atlantic

Comparison of North Atlantic sea-level estimates

In Figure 6.6 the new high-resolution (~388–1550 yr) sea-level record from North Atlantic Site U1313 is compared to a previously published lower-resolved (~3 kyr) record from North Atlantic Site 607 (Sosdian and Rosenthal, 2009). While Site U1313 indicates large-scale sea-level variations on G-IG timescales for MIS 100–96 (~100 m), Site 607 only shows smaller-scale variations (<80 m). This is related to significantly lower glacial sea-level values determined for Site 607 (~60 m below present) compared to Site U1313 (~80–100 m below present). Nevertheless, both records show the same overall trend, with low-amplitude G-IG sea-level fluctuations prior to MIS 100 compared to larger-scale fluctuations from MIS 100 onward. Because both sea-level records derive from the same locality and are based on the same method, not only similar trends are expected, but also comparable (if not identical) absolute values. As outlined above, however, the records exhibit large discrepancies in absolute values particularly for glacial periods. This may be related to one or a combination of the following aspects: (i) Lower temporal resolution for Site 607 compared to Site U1313 such that peak values are perhaps not captured; (ii) significant discrepancies (~0.5 mmol/mol) in the Mg/Ca raw data from Sites 607 and U1313 (see Chapter 6.5.1); (iii) differences in benthic $\delta^{18}O$ data; (iv) missing adjustment for changing deep-water masses for Site 607. The adjustment of sea-level records for different deep-water masses is pivotal to allow for any kind of comparison. Therefore, a new, highly resolved record of the mixing history of deep waters in the North Atlantic is explored in the following. This higher-resolved record allows to verify the lower-resolved record used for sea-level adjustment in this study provided by Lang et al. (2016).

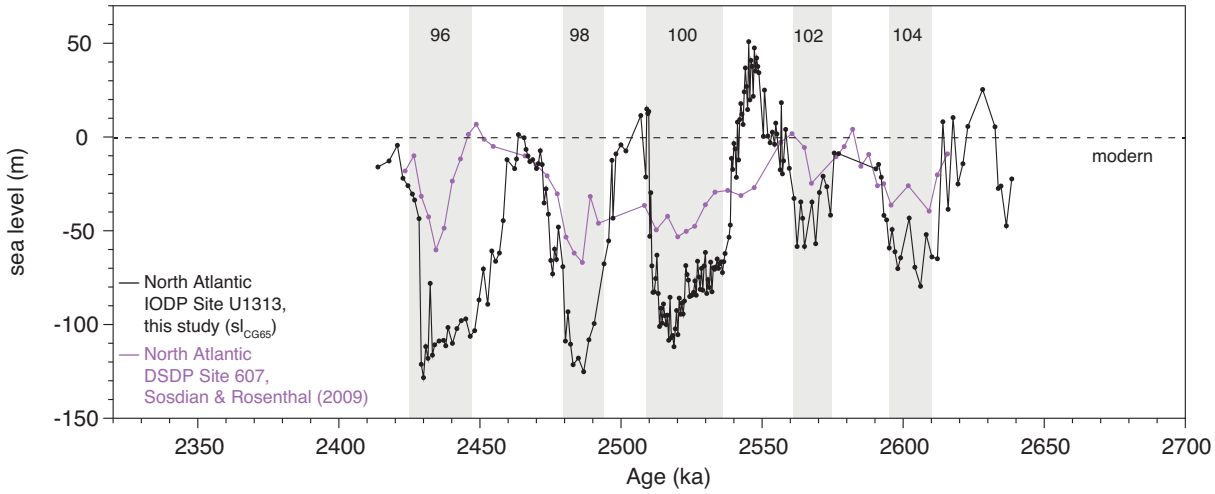

Figure 6.6. Comparison of the new sea-level record from North Atlantic Site U1313 (black; this study) to previous estimates derived from North Atlantic Site 607 (purple) (Sosdian and Rosenthal, 2009). Grey bars mark glacial periods. Black dashed line represents the present-day sea level.

Mixing history of northern- versus southern-sourced deep waters in the North Atlantic

The Site U1313 sea-level estimates presented in Figure 6.4e have been adjusted for changing deep-water masses that alternately influence the deep North Atlantic on G-IG timescales (see Chapter 6.3.5). One of the performed adjustments (sl_{L16}, which is interpreted to yield less realistic values than the sl_{CG65} solution; see Chapter 6.4.2) is based on a record that describes percentages of northern-component waters (%NCW) at Site U1313 (Lang et al., 2016). The applied %NCW record is, however, of much lower resolution (~4 kyr) compared to the sample resolution for Site U1313 (mean: ~910 yr) such that short-term variations are perhaps not captured.

To obtain a more detailed picture of the deep-water mixing history in the North Atlantic on Site U1313 sample resolution, two independent %NCW records were generated by comparing North Atlantic and Eastern Equatorial Pacific BWT and deep-sea $\delta^{13}C$ across iNHG (Figure 6.7). Therefore two major assumptions have been made: (i) A Pacific-to-Atlantic BWT and $\delta^{13}C$ gradient of 0°C and 0‰ or less, respectively, indicates that both sites were bathed by the same, i.e., southern-sourced, water mass; (ii) a difference of 6°C and 1.2‰ or more (mean interglacial value), respectively, is related to 100% southern-sourced waters at Site 849 and 100% northern-sourced waters at Site U1313 (purple bars in Figure 6.7a and 6.7c). Any mixture between these endmembers is likely to reflect a mixture of southern- and northern-sourced deep waters in the North Atlantic.

Both the new high-resolution BWT- (Figure 6.7a–b) and δ^{13}C-gradient-based (Figure 6.7c–d) records of %NCW at Site U1313 indicate changing deep-water masses that alternately influence the seafloor on G-IG timescales in the North Atlantic. Although new records for Site U1313 show a much more detailed variability than the lower-resolution record of Lang et al. (2016), they confirm the overall trend of that dataset. All records indicate an overall decreasing influence of northern-sourced deep waters at Site U1313 relative to deep waters derived from high southern latitudes during glacials compared to interglacials. While the record of Lang et al. (2016) indicates 100% NCW over most of the interglacial periods, new records generated in this study show a small amount of southern-sourced waters at Site U1313. This, however, depends on the definition of the upper endmember (6°C and 1.2‰) for the %NCW calculation (see above). If defined with lower values, the interglacial amount of %NCW would be shifted to higher percentages.

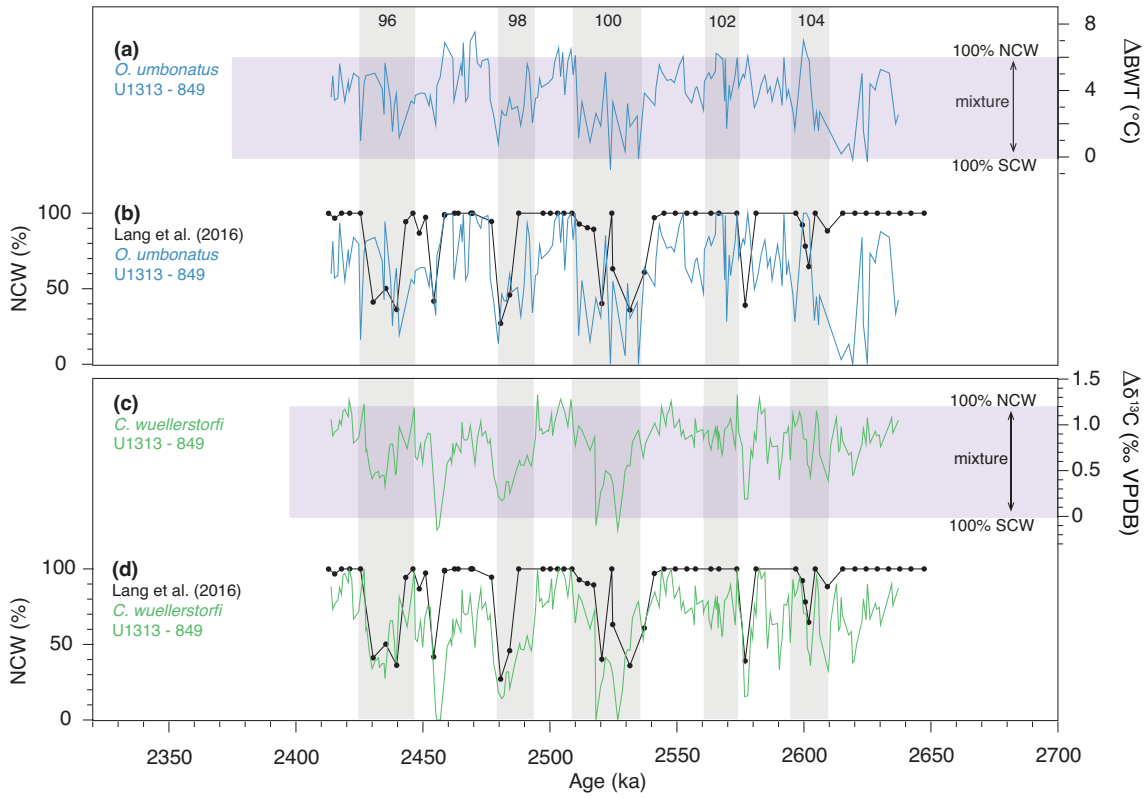

Figure 6.7. Estimates of northern- *versus* southern-sourced deep waters at North Atlantic Site U1313 for MIS G1–95 based on Pacific-to-Atlantic temperature (top; blue) and deep-sea δ^{13}C (bottom; green) gradients (ΔBWT and $\Delta\delta^{13}$C). The BWT gradient in Figure 6.7a is based on data presented in this study (Figures 6.3d and 6.4d). The benthic foraminiferal δ^{13}C gradient in Figure 6.7c is derived from (i) data for Site U1313 presented in this study supplemented by the dataset of Lang et al. (2014) (Figure 6.4b), and (ii) data for Site 849 presented in Figure 6.3b. Results are compared to previous %NCW estimates of Lang et al. (2016) (black). Horizontal purple bars in Figures 6.7a and 6.7c mark a mixture between northern- (NCW) and southern-sourced (SCW) waters (see text for explanation). Vertical grey bars mark glacial periods.

In contrast to the Atlantic Ocean, the Pacific Ocean is primarily sourced by deep waters derived from the high southern latitudes (see Chapter 6.5.1) and thus is not influenced by changes in deep-ocean circulation. This significantly improves sea-level estimates based on benthic foraminiferal geochemistry. Therefore, sea-level estimates from EEP Site 849, for which a water-mass correction is not necessary, are explored in the following.

6.5.3 Comparison of east Pacific sea-level estimates with previous records

When comparing the new sea-level record from Site 849 in the east Pacific to a recently published sea-level record from the eastern Mediterranean Sea (Rohling et al., 2014) it is important to note that sea-level values reconstructed for the Mediterranean Sea as shown in Figure 6.8 should be considered with caution. This is because these estimates may also reflect changes in the morphology of the Strait of Gibraltar that may have occurred throughout the Plio-Pleistocene (Rohling et al., 2014, and references therein). In fact, sea-level estimates from Site 849 indicate much lower values in comparison to the sea-level data from the Mediterranean Sea (Rohling et al., 2014), particularly from MIS 100 onward (Figure 6.8). Nevertheless, both records show comparable details, indicating short periods of sea-level increase during glacials MIS 100 and 96. The fact that this pattern is not reflected in modeling data (Bintanja and Van de Wal, 2008; de Boer et al., 2014) (Figure 6.8) may be a matter of resolution.

A comparison of the new sea-level record from Site 849 to the model-based sea-level record of de Boer et al. (2014) shows that both records are consistent (within the error of calculations) in terms of absolute values and G-IG amplitudes over most of the investigated time interval (Figure 6.8). While glacial sea-level values from Site 849 perfectly match these modeling data and are also comparable to other estimates from the east Pacific (Siddall et al., 2010), glacial values are lower than estimates based on other modeling data (Bintanja and Van de Wal, 2008; Lourens et al., 2010) or sequence stratigraphy (Cronin et al., 1994; Naish, 1997) (Tables 6.1 and 6.2). Interglacial sea-level estimates from Site 849, however, are up to 50 m (MIS 101) higher than values derived from modeling studies (Bintanja and Van de Wal, 2008; de Boer et al., 2014), which do not exceed present-day values. This also dictates that model simulations (Bintanja and Van de Wal, 2008; de Boer et al., 2014) only indicate a sea-level drop associated with glacials across iNHG, while both a glacial and interglacial sea-level fall is documented in the new record from EEP Site 849.

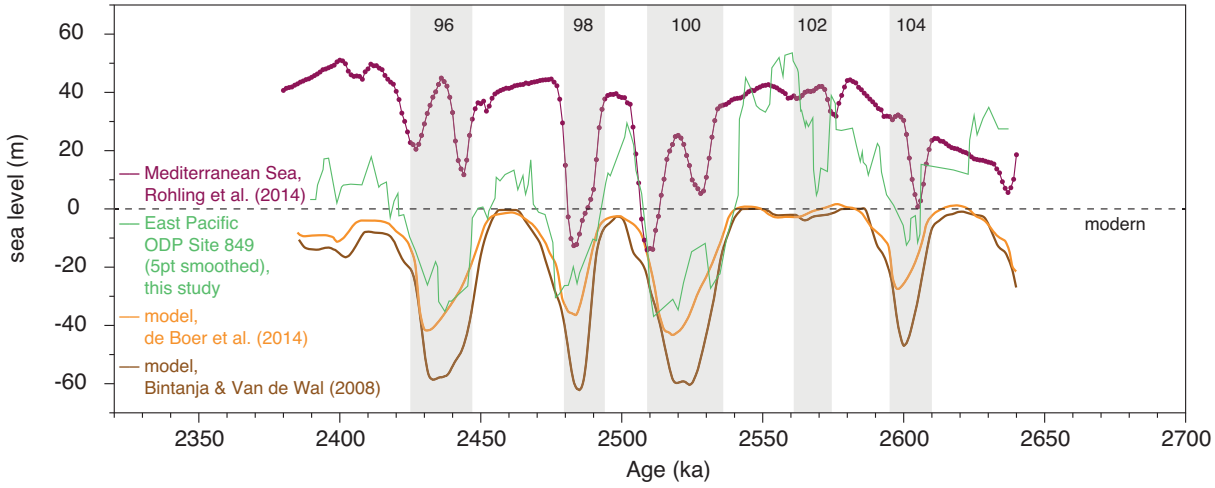

Figure 6.8. Comparison of the new sea-level record from east Pacific Site 849 (green; this study) to previous estimates derived from the Mediterranean Sea (purple) (Rohling et al., 2014) and from model simulations of Bintanja and Van de Wal (2008) (brown) and de Boer et al. (2014) (orange). Grey bars mark glacial periods. Black dashed line represents the present-day sea level.

6.6 Implications for global ice-volume dynamics during the Plio-Pleistocene intensification of Northern Hemisphere Glaciation

Table 6.2 and Figure 6.9 compare new high-resolution sea-level records from the North Atlantic and the EEP. Interglacial sea-level highstand values are within the error of calculations consistent (except for interglacial MIS 103, where data for Site U1313 are lacking). Although glacial sea-level estimates show substantial discrepancies (80–120 m; see also Figure A.3.4 in Appendix A.3), both records exhibit the same overall trend and form an envelope for the global sea-level model of Bintanja and Van de Wal (2008), with estimates from Site 849 and Site U1313 representing the lower and higher boundaries, respectively. The observed differences between Sites 849 and U1313 may be due to the correction required for Site U1313 because of changing deep-water masses, which increases the uncertainty of this record.

In comparison to the global sea-level model of Bintanja and Van de Wal (2008), new sea-level estimates from the EEP and the North Atlantic reveal a more detailed picture of late Pliocene/early Pleistocene ice-sheets dynamics as outlined in the following. In this context it is important to note that the internal structure of a glacial from the Site U1313 sea-level record as described below remains consistent no matter which water-mass correction is applied.

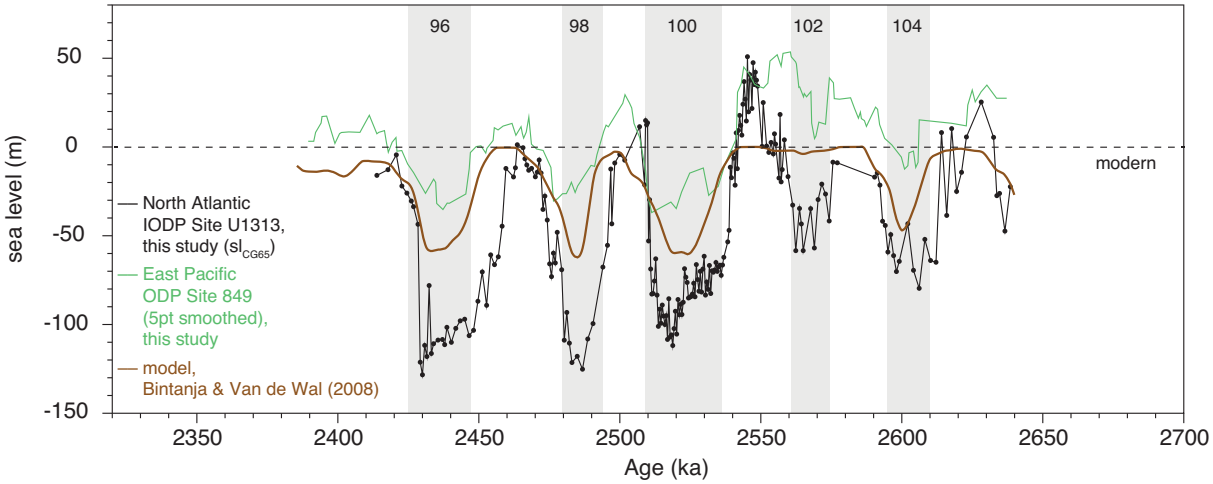

Figure 6.9. Comparison between sea-level records from east Pacific Site 849 (green; this study), North Atlantic Site U1313 (black; this study) and model simulations (brown) (Bintanja and Van de Wal, 2008). Grey bars mark glacial periods. Black dashed line represents the present-day sea level.

6.6.1 Glacial and interglacial sea-level drop across the intensification of Northern Hemisphere Glaciation

The new records show an average sea-level drop of ~80–150 m into glacial MIS 100, i.e., the first strong glacial during iNHG. The sea-level drop exceeds the modeling-derived value by at least 20 m (Bintanja and Van de Wal, 2008). Moreover, sea-level records from Sites 849 and U1313 consistently demonstrate that hypothesized waxing and waning of Northern Hemisphere ice sheets from MIS 100 through 96 was associated with a sea-level drop not only during glacial, but also during interglacial intervals (Figure 6.9). This indicates an increase in global ice-volume also during interglacials periods, thereby challenging model results. Remarkably, the observed glacial and interglacial increase in ice-volume appears not to be associated with a similar pattern in deep sea-temperature evolution (Figure 6.5a). This suggests that deep-ocean cooling may not have played an important role for iNHG.

6.6.2 Internal anatomy of early Pleistocene glacials

For MIS 100, both studied sites demonstrate (notwithstanding the lower resolution for Site 849) that the final ~10 kyr of this glacial are characterized by an additional drop in sea level before sea level rose rapidly during the following termination (Figure 6.10). A comparable, but more subdued pattern emerges during MIS 96 as evidenced by the North Atlantic sea-level record. This structure is strikingly similar to late Pleistocene glacial periods (Clark et al., 2009). During the Last Glacial Maximum, for instance, mid- and high-latitude Northern Hemisphere ice sheets and the West Antarctic Ice Sheet already reached their maximum

extent 2.5 kyr before actual sea-level lowstand, while remaining ice sheets including the Laurentide Ice Sheet continued to grow (Clark et al., 2009). It may be speculated whether the final sea-level drop observed for MIS 100 indicates – in analogy to the Last Glacial Maximum – the ongoing advance of some ice sheets, perhaps including the Laurentide Ice Sheet, while other ice sheets (such as the West Antarctic Ice Sheet) already reached their maximum extent ~10 kyr before the termination.

New high-resolution sea-level data in particular from North Atlantic Site U1313 (but also from the lower-resolved Site 849 record) document the overall "sawtooth"-like pattern of a gradual sea-level fall/ice-sheet buildup into glacial periods followed by a rapid sea-level increase/ice-sheet melt during the deglaciation ("termination") of MIS 100 and 96 (Figures 6.4e and 6.10). Average rates of sea-level rise at Site U1313 of 1.3 m per century are observed from 2.52 to 2.51 Ma (MIS 100) and from 2.43 to 2.42 Ma (MIS 96). The main deglaciation phase of MIS 98 occurred from 2.48 to 2.47 Ma at lower rates. Thus this glacial has a symmetric shape rather than a "sawtooth"-like structure. Aforementioned observations are consistent with a previous study (Lourens et al., 2010). Further, Lourens et al. (2010) found that the terminations of MIS 100 and 96 occurred during maximum obliquity, while the deglaciation of MIS 98 was associated with a minimum in obliquity. Data generated in this study, however, do not support this observation: A comparison between the new sea-level record from Site U1313 and an astronomical solution for obliquity (Laskar et al., 2004) (see Figure A.3.5 in Appendix A.3) does not show this pattern, but rather shows an in-phase oscillation between obliquity and sea level/ice volume.

Rates of sea-level change of 1.3 m per century for MIS 100 and 96 are comparable to those of late Pleistocene terminations (MIS 5e: 1.6 m per century [Rohling et al., 2007]; Last Glacial Maximum: 0.6–1.2 m per century [Waelbroeck et al., 2002; Bintanja and Van de Wal, 2008; Lambeck et al., 2014]) (Figure 6.10). This implies that mechanisms hypothesized to have triggered terminations of late Pleistocene glacials may have also operated during prominent iNHG glacials MIS 100 and 96. Rapid deglaciations in the late Pleistocene occur via a series of complex feedback mechanisms (see Denton et al., 2010 for a review) triggered by a maximum in Northern Hemisphere insolation. A comparison between the sea-level record from Site U1313 and an astronomical solution for Northern Hemisphere insolation (Laskar et al., 2004) indicates that the onset of the termination of MIS 100 was in fact associated with an insolation maximum (see Figure A.3.5 in Appendix A.3). The termination of MIS 96 also began during times of generally high (albeit not maximum) insolation. The termination of MIS 98, however, does not comply with this pattern as it is associated with an insolation

minimum. This is unlikely a coincidence because this glacial also does not indicate a "sawtooth"-like pattern. In contrast, the strikingly close correspondence between Northern Hemisphere insolation maxima and rapid terminations that causes a "sawtooth"-like glacial structure suggests that MIS 100 and 96 were early attempts of Earth's climate to shift into the late Pleistocene asymmetric G-IG cyclicity as it was finally established only ~1.5 Myr later.

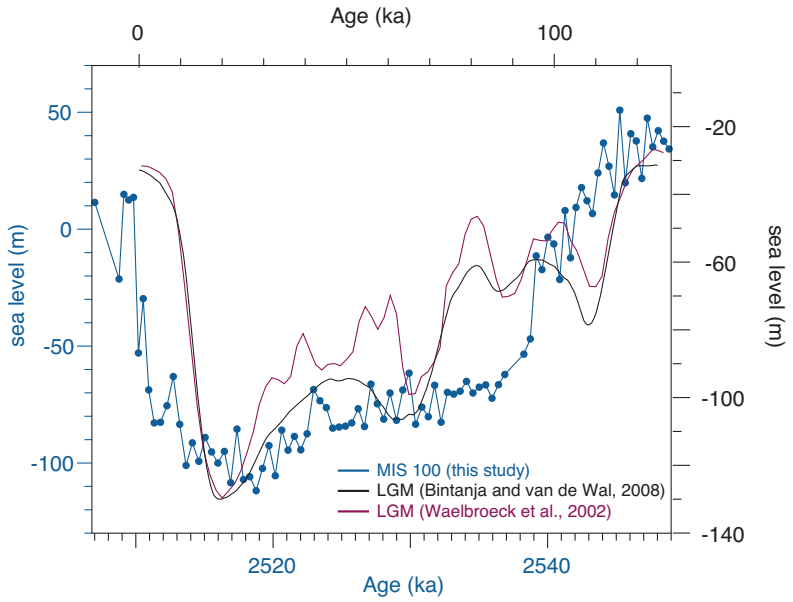

Figure 6.10. Comparison of sea-level records from the early Pleistocene (MIS 100) and the Last Glacial Maximum. Blue: Benthic foraminiferal (*O. umbonatus*) $\delta^{18}O$- and Mg/Ca-based sea-level estimates from North Atlantic Site U1313 for MIS 100 (2.55–2.51 Ma). Black and purple: Sea-level data derived from model results (Bintanja and Van de Wal, 2008) and benthic $\delta^{18}O$-coral transfer functions (Waelbroeck et al., 2002) for the Last Glacial Maximum. Note different axes (left and lower axes in blue for the record from Site U1313 for MIS 100; right and upper axes in black for model [Bintanja and Van de Wal, 2008] and proxy data [Waelbroeck et al., 2002] for the Last Glacial Maximum).

6.6.3 Vulnerability of the "stable" East Antarctic Ice Sheet

Amplitudes in G-IG-scale sea-level change became twice as high during prominent iNHG glacials MIS 100 through 96 compared to prior glacials (Figure 6.9). A sea-level increase into interglacials recorded at Site 849 and particularly at Site U1313 of ~50 m to ~100 m, respectively, has important implications for the ongoing debate on the contribution of the "stable" East Antarctic Ice Sheet to global sea-level evolution during warmer-than-modern climatic conditions (Cook et al., 2013; DeConto and Pollard, 2016). The ice volume of the Greenland Ice Sheet and the West Antarctic Ice Sheet corresponds to ~7.4 m (Vaughan et al., 2013) and ~5 m (Lythe and Vaughan, 2001) of sea-level equivalents, respectively. Accordingly, complete melting of Greenland and West Antarctic Ice Sheets would account for ~12.4 m eustatic sea-level rise. Considering that other factors relevant for sea-level change

on G-IG timescales (such as thermal expansion of seawater, variations in groundwater and lake storage) can only account for <10 m of sea-level increase (Miller et al., 2005; Dutton et al., 2015), a sea-level rise of ~50 to 100 m from full glacial to full interglacial conditions as evidenced by the new records for MIS 100 through 96 (Figure 6.9) implies – in addition to an assumed collapse of Greenland and West Antarctic Ice Sheets (Dutton et al., 2015) – at least a partial retreat of the East Antarctic Ice Sheet.

While traditionally the East Antarctic Ice Sheet was believed to have been stable for the past 14 Myr (Barrett, 2013; and references therein), modeling and geological evidence consistently suggest some retreat around the margins in warm Pliocene times (Cook et al., 2013; DeConto and Pollard, 2016). A key mechanism for the mass loss of ice shelves connected to the marine-based West Antarctic Ice Sheet lies in warmer ocean temperatures and thus basal melting (Pritchard et al., 2012). Both sedimentary evidence (Cook et al., 2013) and model simulations (Pritchard et al., 2012) indicate that ice-shelf melting in response to warmer ocean temperatures possibly also occurs in low-lying areas at the edge of the continental-based East Antarctic Ice Sheet. These findings, which are consistent with observations of this study, are supported by model simulations that highlight the vulnerability of Antarctic ice sheets, producing a 11.3 m contribution of the West and East Antarctic Ice Sheets to mean global sea-level rise during the warm Pliocene (DeConto and Pollard, 2016).

6.7 Conclusions

New high-resolution benthic foraminiferal $\delta^{18}O$- and Mg/Ca-based proxy records from Eastern Equatorial Pacific ODP Site 849 and North Atlantic IODP Site U1313 are presented to reconstruct deep-sea temperature and sea-level change across Plio-Pleistocene iNHG (~2.65–2.4 Ma). The most salient features are as follows:

(i) Deep-sea temperatures in the EEP were on average ~4°C colder than in the North Atlantic across the study interval. Large G-IG amplitudes in the North Atlantic (~3.5°C) compared to rather small-scale fluctuations in the EEP (<2°C) imply a diminished Pacific-to-Atlantic temperature gradient during glacials relative to interglacials. This indicates changing deep-water masses that alternately influenced the seafloor on G-IG timescales in the North Atlantic (northern- *versus* southern-sourced waters), while the deep east Pacific was only bathed by a single, southern-sourced water mass.

(ii) New sea-level estimates from the EEP and the North Atlantic exhibit the same overall trend and form an envelope for the global sea-level model of Bintanja and Van de Wal (2008)

for the study interval. Sea-level lowstand estimates from Site 849 are more subdued (peak values of ~55 to 85 m below present) than those from Site U1313 (peak values of ~110 to 130 m below present) for prominent G-IG cycles MIS 100 through 96, while sea-level highstand estimates are consistent (~0–30 m above present). The records from both sites show that iNHG was associated with a drop in sea-level and thus an increase in global ice volume during both glacial and interglacial intervals.

(iii) The internal structure of MIS 100 and 96 is strikingly similar to that of late Pleistocene glacials (asymmetric "sawtooth" pattern, rapid terminations, final drop in sea level ~10 kyr before the following termination). This implies a similar mechanistic behavior of early and late Pleistocene ice-sheet dynamics controlled by Northern Hemisphere insolation.

(iv) A sea-level rise of ~50 to 100 m into interglacials as evidenced from new records for MIS 100 through 96 implies complete melting of Greenland and West Antarctic Ice Sheets and at least a partial retreat of the "stable" East Antarctic Ice Sheet, hinting at its future vulnerability under a warmer-than-present climate.

CHAPTER 7

FINAL SUMMARY AND OUTLOOK

7.1 Final summary

In this thesis, sediment cores from the Eastern Equatorial Pacific (Site 849) and the North Atlantic (Site U1313) that were drilled within the framework of Ocean Drilling Program Leg 138 and Integrated Ocean Drilling Program Expedition 306, respectively, were investigated. New proxy records from these cores – mainly based on benthic and planktic foraminiferal stable isotopes ($\delta^{18}O$ and $\delta^{13}C$) and Mg/Ca ratios – were generated for the time interval ~2.75–2.4 Ma (corresponding to Marine Isotope Stages [MIS] G6–95). They provide insight into the processes and mechanisms involved in glacial-interglacial- (G-IG) to (sub-) millennial-scale climate fluctuations and sea-level variability during past times of "near-modern" paleogeography and warmer-than-present climatic boundary conditions. A brief summary of the thesis is given in the following.

The first study presented in this thesis focuses on changes in primary productivity in the Eastern Equatorial Pacific (EEP) upwelling system during the intensification of Northern Hemisphere Glaciation (iNHG) from ~2.65 to 2.4 Ma (MIS G1–95) (**Chapter 4**). The upwelling system in the EEP is an important component in Earth's atmospheric and marine carbon budget (e.g., Schlitzer, 2004; Takahashi et al., 2009) as it supports >10% of the present-day global ocean primary production (Pennington et al., 2006). Hence this region is an ideal natural laboratory to identify how primary productivity changes relate to climate fluctuations. It is controversially debated whether changes in EEP productivity predominantly depend on trade wind strength-controlled upwelling intensity (e.g., Cleaveland and Herbert, 2007; Etourneau et al., 2010) or on nutrient transport from the high southern latitudes via oceanic teleconnections (Lawrence et al., 2006; Etourneau et al., 2013). To test the competing hypotheses for G-IG changes in productivity during Plio-Pleistocene iNHG, new records of carbon isotopes in benthic and planktic foraminiferal calcite and sand-accumulation rates from Site 849 covering the time interval ~2.65–2.4 Ma (MIS G1–95) were generated.

The new data show a clear G-IG cyclicity from MIS 100 onward, with productivity levels increasing during full glacial conditions and peaking at glacial terminations. Two mechanisms

were identified that controlled the observed primary productivity pattern in the EEP: (i) Variations in nutrient delivery from high southern latitudes – presumably controlled by productivity rates and thus sea-ice extent in the Southern Ocean –; and (ii) changes in trade-wind-driven upwelling intensity in the EEP connected to Laurentide Ice Sheet retreats. More precisely, primary productivity changes in the EEP were shown to be regulated by enhanced nutrient delivery from the high southern latitudes during full glacial conditions, superimposed by intensified regional upwelling toward glacial terminations from MIS 100 onward.

The second study presented in this thesis focuses on G-IG changes in equatorial Pacific surface-water structure during Plio-Pleistocene iNHG (**Chapter 5**). During the Pliocene, the Pacific warm pool was greatly expanded relative to today, giving rise to a surface-ocean temperature field akin to modern El Niño conditions. The iNHG marks the transition from this warm Pliocene climate state to a climate state that approximates modern conditions, with strong upwelling in the east of the basin and stronger zonal temperature and primary productivity gradients. In this study, the possibility of an obliquity-paced El Niño-Southern Oscillation-like variability during Plio-Pleistocene iNHG (Philander and Fedorov, 2003; Fedorov et al., 2006) – which plays a major role in the modern global climate system – is critically assessed. Therefore, new high-resolution (~800 yr) planktic foraminiferal Mg/Ca- and $\delta^{18}O$-based sea-surface temperature and salinity records from EEP Site 849 were generated for ~2.75–2.4 Ma (MIS G6–95) and compared to west Pacific Site 806 (Medina-Elizalde and Lea, 2010).

The generated data indicate that the zonal (west-to-east) sea-surface temperature gradient increased by ~1.5°C from ~2.75 to ~2.4 Ma through EEP cooling. No G-IG pattern is evident in this gradient, which argues against obliquity-paced fluctuations from El Niño-like to La Niña-like climate states. On the other hand, obliquity-paced oscillations in the surface-water salinity gradient are documented. These oscillations originate from a response to a glacial southward and interglacial northward migration of the Intertropical Convergence Zone over the EEP. These new data have important implications for the ongoing debate on possible fluctuations between El Niño-like and La Niña-like climate states on G-IG timescales (Philander and Fedorov, 2003; Lee and Poulsen, 2005; Fedorov et al., 2006; Bolton et al., 2010a), indicating that such a variability was unlikely during the late Pliocene and early Pleistocene.

The third study presented in this thesis (**Chapter 6**) focuses on the reconstruction of high-resolution sea-level records under warmer-than-modern (late Pliocene/early Pleistocene)

climatic boundary conditions that are not only important for understanding past climate evolution, but also for reliably predicting future sea-level rise. For this purpose, new (sub-) millennial-scale benthic foraminiferal $\delta^{18}O$- and Mg/Ca-based sea-level records have been generated for EEP Site 849 and North Atlantic Site U1313 covering ~2.65–2.4 Ma (MIS G1–95).

The sea-level lowstand estimates for prominent iNHG glacials MIS 100–96 show substantially lower values for Site 849 than for Site U1313 (peak values of ~55–85 m *versus* ~110–130 m below present), while interglacial sea-level highstand estimates are rather consistent (~0–30 m above present). In comparison to previous estimates, the new record from Site 849 is comparable to model-based sea-level data (de Boer et al., 2014) for the investigated time interval, while values for Site U1313 appear to be overestimated. This is most likely related to uncertainties in the Site U1313 sea-level record when correcting for changing (northern- *versus* southern-sourced) deep-water masses. Nevertheless, sea-level evolution determined for MIS 100 and 96 is strikingly reminiscent of late Pleistocene glacials (asymmetric "sawtooth" pattern, rapid terminations, final drop in sea level ~10 kyr before the following termination). This implies a similar mechanistic behavior of early and late Pleistocene ice sheets, i.e., a series of complex feedback mechanisms triggered by a maximum in Northern Hemisphere insolation (Denton et al., 2010). Remarkably, a ~50–100 m sea-level rise into early Pleistocene interglacials has been reconstructed. These values imply complete melting of Greenland and West Antarctic Ice Sheets and at least a partial retreat of the "stable" East Antarctic Ice Sheet, hinting at its future vulnerability.

7.2 Future perspectives

The work carried out within the framework of this thesis demonstrates the potential in particular of Site 849 for the generation of reliable benthic and planktic foraminifer-based geochemical proxy data at high temporal resolution (Chapter 7.1). Continuous sedimentation with constantly high sedimentation rates (2.5–3 cm kyr^{-1}) (Mayer et al., 1992; Mix et al., 1995), high carbonate content (Hagelberg et al., 1995), abundant occurrence of foraminifera, and the possibility to work at maximum stratigraphic precision (Mix et al., 1995; see Figure 7.1a) over the past 5 Myr at Site 849 provide optimum preconditions to extend the generated data of this study over several G-IG cycles. Beyond the research questions outlined in Chapter 1, other issues of interest have emerged over the course of this work. Aspects that merit attention for future study are presented in the following.

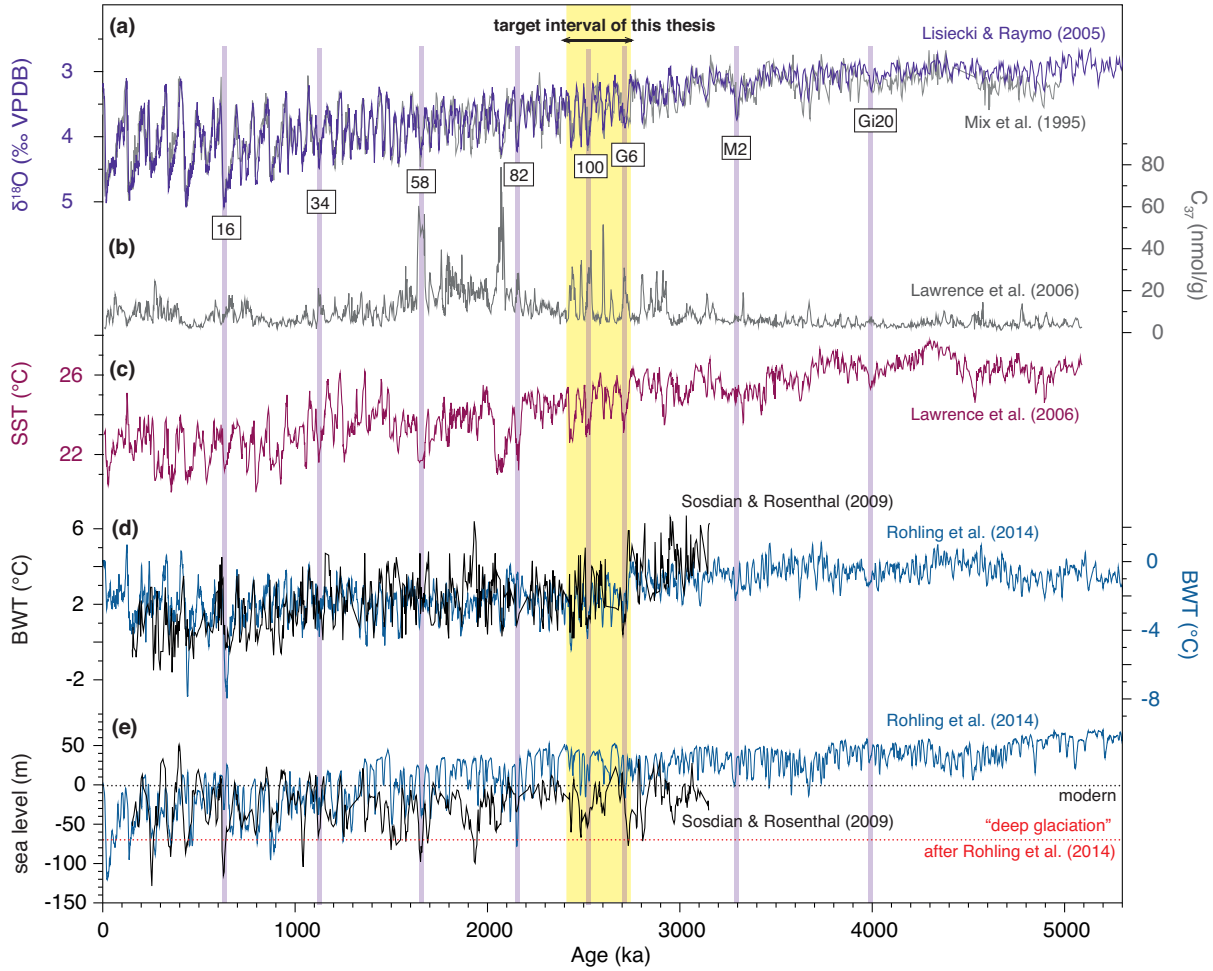

Figure 7.1. Overview of climatic records for the past 5.3 Myr. **(a)** Benthic foraminiferal $\delta^{18}O$ (purple: LR04 stack [Lisiecki and Raymo, 2005], grey: Data from Site 849 [Mix et al., 1995]). **(b)** Alkenone-based proxy record for primary productivity changes (C_{37}) from east Pacific Site 846 (Lawrence et al., 2006). **(c)** Alkenone-based sea-surface temperature (SST) estimates from east Pacific Site 846 (Lawrence et al., 2006). **(d)** Relative changes in bottom-water temperature (BWT) in the Mediterranean Sea (blue) (Rohling et al., 2014) and absolute BWT estimates for the North Atlantic (black) (Sosdian and Rosenthal, 2009). Note different axes. **(e)** Sea-level estimates relative to present derived from the Mediterranean Sea (blue) (Rohling et al., 2014) and the North Atlantic (black) (Sosdian and Rosenthal, 2009). Black dashed line indicates present-day sea level. Red dashed line indicates a "deep glaciation" (as defined by a sea-level lowering to 70 m below present following Rohling et al. [2014]). Yellow shading indicates the target interval of this thesis (~2.75–2.4 Ma, MIS G6–95). Selected glacials are named for reference.

Primary Productivity. The new data presented in Chapter 4 provide information on the mechanisms that controlled changes in primary productivity across iNHG in the Eastern Equatorial Pacific, a region of major importance for surface ocean-atmosphere CO_2 exchange. Detailed work on productivity proxy records on a comparable temporal resolution as in this thesis for the same time interval at multiples sites would allow for a global synthesis. Such information is needed to understand potential links between upwelling-/productivity-controlled changes in atmospheric CO_2 to iNHG.

Since modern primary productivity changes in the EEP are primarily controlled by trade-wind-driven upwelling strength (e.g., Bjerknes, 1969), changes in both nutrient supply in the upwelled water mass and upwelling intensity drove EEP productivity fluctuations across iNHG (Chapter 4). This raises the question when during Earth's history upwelling strength became the prominent factor controlling productivity fluctuations at that site. Such information is needed to identify potential relationships between upwelling-/productivity-controlled changes in atmospheric CO_2 and the stronger response of the climate/cryosphere system to orbital forcing toward the late Pleistocene. This issue could be addressed by extending the productivity record for Site 849 by several G-IG cycles. For this purpose, Site 849 bears a decisive advantage over nearby Site 846 – for which a productivity record for the past ~5 Myr already exists (Lawrence et al., 2006) (Figure 7.1b) – through being located west of the East Pacific Rise and thus being independent from local oceanography or continental influence (Mix et al., 1995; Messié and Chavez, 2011; Messié and Chavez, 2012).

Surface-water structure. Chapter 5 indicates that fluctuations between El Niño- and La Niña-like climate states on G-IG timescales were unlikely during the late Pliocene and early Pleistocene, although they are suggested by modeling studies for the Plio-Pleistocene. Another key interval to advance this debate and to critically assess the observed model-data-mismatch is the late Pleistocene with its large-amplitude G-IG cycles. Therefore, records of surface-water properties comparable to those presented in Chapter 5 (i.e., temperature and salinity) could be generated for Site 849 and compared to a west Pacific site covering several late Pleistocene G-IG cycles after the Mid-Pleistocene Transition. Although a sea-surface temperature record for the past ~5 Myr is already available (Lawrence et al., 2006) (Figure 7.1c), Site 849 might be better suited for this purpose because of its open-ocean position (see above).

Sea level and deep-sea temperature. Sea-level data from Site 849 as presented in Chapter 6 document a shift to stronger glacials for MIS 100 to 96. The observed trend is supported by several traditional deep-sea $\delta^{18}O$-based sea-level estimates (Bintanja and Van de Wal, 2008; Sosdian and Rosenthal, 2009; de Boer et al., 2014). However, new millennial-resolution deep-sea temperature and sea-level records derived from a planktic foraminiferal $\delta^{18}O$ stack from the eastern Mediterranean Sea (Wang et al., 2010; Rohling et al., 2014) that is independent from the deep-sea $\delta^{18}O$ concept challenges this perspective (Figure 7.1d–e). These data indicate that the first "deep glacial" (as defined by a sea-level value of 70 m below present after Rohling et al. [2014]) occurred ~500 kyr later than previously proposed, i.e., at ~2.15 Ma (MIS 82). The change observed in deep-sea $\delta^{18}O$ at ~2.7 Ma (MIS G6), previously

interpreted to represent a first significant sea-level drop (Dwyer et al., 1995; Sosdian and Rosenthal, 2009), is hypothesized to be more likely related to bottom-water cooling (Rohling et al., 2014). This raises the question whether and to what degree the observed discrepancies are due to methodological inconsistencies, which casts doubt on the fidelity of previously available sea-level reconstructions. Validation could be achieved through a refined approach for sea-level reconstruction through integrating the traditionally used benthic $\delta^{18}O$- and Mg/Ca-based approach with "clumped-isotope" paleothermometry. This would allow for a more accurate quantification of bottom-water temperatures and therefore sea level. Besides shedding new light on the opposing views on the actual first occurrence of "deep glacials", it will significantly refine the quality of yet available sea-level reconstructions for the late Pliocene to early Pleistocene.

LIST OF REFERENCES

Adelseck, C.G., Anderson, T.F. (1978). The late Pleistocene record of productivity fluctuations in the eastern equatorial Pacific Ocean. Geology, 6, 388–391.

Adkins, J.F., McIntyre, K., Schrag, D.P. (2002). Salinity, temperature, and $\delta^{18}O$ of the glacial deep ocean. Science, 298, 1769–1773.

Anand, P., Elderfield, H., Conte, M.H. (2003). Calibration of Mg/Ca thermometry in planktonic foraminifera from a sediment trap time series. Paleoceanography 18, 1050, doi:1010.1029/2002PA000846.

Arbuszewski, J., Demenocal, P., Kaplan, A., Farmer, E.C. (2010). On the fidelity of shell-derived $\delta^{18}O_{seawater}$ estimates. Earth Planet. Sci. Lett., 300, 185–196.

Arnold, A.J., Parker, W.C. (1999). Biogeography of planktonic foraminifera. In Modern foraminifera, edited by Sen Gupta, B.K., pp. 103–122, Kluwer Academic Publishers, Dordrecht, Boston.

Aurahs, R., Treis, Y., Darling, K., Kucera, M. (2011). A revised taxonomic and phylogenetic concept for the planktonic foraminifer species *Globigerinoides ruber* based on molecular and morphometric evidence. Mar. Micropaleontol., 79, 1–14.

Bahr, A., Kaboth, S., Jiménez-Espejo, F.J., Sierro, F.J., Voelker, A.H.L., Lourens, L., Röhl, U., Reichart, G.J., Escutia, C., Hernández-Molina, F.J., Pross, J., Friedrich, O. (2015). Persistent monsoonal forcing of Mediterranean Outflow Water dynamics during the late Pleistocene. Geology, 43, 951–954.

Bailey, I., Bolton, C.T., DeConto, R.M., Pollard, D., Schiebel, R., Wilson, P.A. (2010). A low threshold for North Atlantic ice rafting from "lowslung slippery" late Pliocene ice sheets. Paleoceanography, 25, PA1212, doi:10.1029/2009PA001736.

Bailey, I., Foster, G.L., Wilson, P.A., Jovane, L., Storey, C.D., Trueman, C.N., Becker, J. (2012). Flux and provenance of ice-rafted debris in the earliest Pleistocene sub-polar North Atlantic Ocean comparable to the Last Glacial Maximum. Earth Planet. Sci. Lett., 341–344, 222–233.

Bailey, I., Hole, G.M., Foster, G.L., Wilson, P.A., Storey, C.D., Trueman, C.N.,Raymo, M.E. (2012). An alternative suggestion for the Pliocene onset of major northern hemisphere glaciation based on the geochemical provenance of North Atlantic Ocean ice-rafted debris. Quaternary Sci. Rev., 75, 181–194.

Balco, G., Rovey, C.W. (2010). Absolute chronology for major Pleistocene advances of the Laurentide Ice Sheet. Geology, 38(9), 795–798.

Barker, S., Greaves, M., Elderfield, H. (2003). A study of cleaning procedures used for foraminiferal Mg/Ca paleothermometry. Geochem. Geophys. Geosyst.,*4*(9), 8407, doi:10.1029/2003GC000559.

Barreiro, M., Philander, G., Pacanowski, R., Fedorov, A. (2005). Simulations of warm tropical conditions with application to middle Pliocene atmospheres. Clim. Dynam., 26, 349–365.

Barrett, P.J. (2013). Resolving views on Antarctic Neogene glacial history – the Sirius debate. Earth Env. Sci. T. R. So., 104, 31–53.

Bartlein, P.J., Anderson, K.H., Anderson, P.M., Edwardsm, M.E., Mock, C.J., Thompson, R.S., Webb, R.S., Webb, T., Whitlock, C. (1998). Paleoclimate simulations for North America over the past 21,000 years: Features of the simulated climate and comparisons with paleoenvironmental data. Quaternary Sci. Rev., 17, 549–585.

Bartoli, G., Sarnthein, M., Weinelt, M., Erlenkeuser, H., Garbe-Schönberg, D., Lea, D.W. (2005). Final closure of Panama and the onset of northern hemisphere glaciation. Earth Planet. Sci. Lett., 237, 33–44.

Bartoli, G., Sarnthein, M., Weinelt, M. (2006). Late Pliocene millennial-scale climate variability in the northern North Atlantic prior to and after the onset of Northern Hemisphere glaciation. Paleoceanography, 21, PA4205, doi:4210.1029/ 2005PA001185.

Bassinot, F.C., Beaufort, L., Vincent, E., Labeyrie, L.D., Rostek, F., Müller, P.J., Quidelleur, X., Lancelot, Y. (1994). Coarse fraction fluctuations in pelagic carbonate sediments from the tropical Indian Ocean: A 1500-kyr record of carbonate dissolution. Paleoceanography, 9, 579–600, doi:10.1029/94PA00860.

Bé, A.W.H., Tolderlund, D.S. (1971). Distribution and ecology of living planktonic foraminifera in surface waters of the Atlantic and Indian oceans. In Micropaleontology of the Oceans, edited by Funnell, B.M., Riedel, W.R., pp. 105–149, Cambridge University Press, London.

Bé, A.W.H. (1977). An egological, zoogeographic and taxonomic review of recent planktonic foraminifera. In Oceanic Micropaleontology, edited by Ramsay, A.T.S., pp. 1–100, Academic Press, London.

Bé, A.W.H. (1980). Gametogenic calcification in a spinose planktonic foraminifer, *Globigerinoides sacculifer*. Mar. Micropaleontol., 5, 283–310.

Beaulieu, S.E. (2002). Accumulation and fate of phytodetritus on the seafloor. Oceanogr. Mar. Biol., 40, 171–232.

Bemis, B.E., Spero, H.J., Bijma, J., Lea, D.W. (1998). Reevaluation of the oxygen isotopic composition of planktonic foraminifera: Experimental results and revised paleotemperature equations. Paleoceanography, 13, 150–160.

Bender, M.L., Lorens, R.B., Williams, D.F. (1975). Sodium, magnesium, and strontium in the tests of planktonic foraminifera. Micropaleontology, 21, 448–459.

Benway, H.M., Mix, A.C., Haley, B.A., Klinkhammer, G.P. (2006). Eastern Pacific Warm Pool paleosalinity and climate variability: 0–30 kyr. Paleoceanography, 21, PA3008, doi:3010.1029/2005PA001208.

Berger, W.H., Adelseck, C.G., Mayer, L.A. (1976). Distribution of carbonate in surface sediments of the Pacific Ocean. J. Geophys. Res., 81, 2617–2627.

Berger, W.H., Bonneau, M.-C., Parker, F.L. (1982). Foraminifera on the deep-sea floor: Lysocline and dissolution rate. Oceanol. Acta, 5, 249–258.

Berger, W., Vincent, E. (1986). Deep-sea carbonates: Reading the carbon-isotope signal. Geol. Rundsch., 75, 249–269.

Berger, W.H., Jansen, E. (1994). Mid-Pleistocene climate shift: The Nansen connection. In The polar oceans and their role in shaping the global environment, edited by Johannessen, O.M., Muench, R.D., Overland, J.E., pp. 295–311, doi:210.1029/GM1085p0295b, AGU, Washington.

Berstad, I.M., Sejrup, H.P., Klitgaard-Kristensen, D., Haflidason, H. (2003). Variability in temperature and geometry of the Norwegian Current over the past 600 yr: Stable isotope and grain size evidence from the Norwegian margin. J. Quat. Sci., 18(7), 591–602.

Bijma, J., Erez, J., Hemleben, C. (1990a). Lunar and semi-lunar reproductive cycles in some spinose planktonic foraminifera. J. Foramin. Res., 20, 117–127.

Bijma, J., Faber, W.W., Hemleben, C. (1990b). Temperature and salinity limits for growth and survival of some planktonic foraminifers in laboratory cultures. J. Foramin. Res., 20, 95–116.

Billups, K., Channell, J.E.T., Zachos, J. (2002). Late Oligocene to early Miocene geochronology and paleoceanography from the subantarctic South Atlantic. Paleoceanography, 17(1), 1004, doi:10.1029/2000PA000568.

Bintanja, R., Van de Wal, R. (2008). North American ice-sheet dynamics and the onset of 100,000-year glacial cycles. Nature, 454, 869–872.

Bjerknes, J. (1969). Atmospheric teleconnections from the equatorial Pacific. Mon. Weather Rev., 97(3), 163–172.

Bolton, C.T., Gibbs, S.J., Wilson, P.A. (2010a). Evolution of nutricline dynamics in the equatorial Pacific during the late Pliocene. Paleoceanography, 25, PA1207, doi:1210.1029/2009PA001821.

Bolton, C.T., Lawrence, K.T., Gibbs, S.J., Wilson, P.A., Cleaveland, L.C., Herbert, T.D. (2010b). Glacial-interglacial productivity changes recorded by alkenones and microfossils in late Pliocene eastern equatorial Pacific and Atlantic upwelling zones. Earth Planet. Sci. Lett., 295(3–4), 401–411.

Bolton, C.T., Wilson, P.A., Bailey, I., Friedrich, O., Beer, C.J., Becker, J., Baranwal, S., Schiebel, R. (2010c). Millennial-scale climate variability in the subpolar North Atlantic Ocean during the late Pliocene. Paleoceanography, 25, PA4218, doi:10.1029/2010PA001951.

Bolton, C.T., Lawrence, K.T., Gibbs, S.J., Wilson, P.A., Herbert, T.D. (2011). Biotic and geochemical evidence for a global latitudinal shift in ocean biogeochemistry and export productivity during the late Pliocene. Earth Planet. Sci. Lett., 308(1–2), 200–210.

Boltovskoy, E. (1964). Seasonal occurrences of some living foraminifera in Puerto Deseado (Patagonia, Argentina). J. Conseil, 29, 136–145.

Bonn, W.J., Gingele, F.X., Grobe, H., Mackensen, A., Fütterer, D.K. (1998). Paleoproductivity at the Antarctic continental margin: Opal and barium records for the last 400 ka. Palaeo3, 139(3–4), 195–211.

Bosak, T., Lahr, D.J.G., Pruss, S.B., Macdonald, F.A., Gooday, A.J., Dalton, L., Matys, E.D. (2011). Possible early foraminiferans in post-Sturtian (716–635 Ma) cap carbonates. Geology, 40, 67–70.

Bouvier-Soumagnac, Y., Duplessy, J.C. (1985). Carbon and oxygen isotopic composition of planktonic foraminifera from laboratory culture, plankton tows and recent sediment: implications for the reconstruction of paleoclimatic conditions and of the global carbon cycle. J. Foramin. Res., 15, 302–320.

Boyer, T.P., et al. (2013). World Ocean Database 2013, edited by S. Levitus, Ed., U.S. Gov. Print. Off., Washington, D.C., NOAA Atlas NESDIS, 72., 209 pp.

Boyle, E.A., Keigwin, L.D. (1985). Comparision of Atlantic and Pacific paleochemical records for the last 215,000 years - changes in deep ocean circulation and chemical inventories. Earth Planet. Sci. Lett., 76, 135–150.

Broecker, W.S. (1991). The great ocean conveyor. Oceanography, 4, 78–89.

Brown, S.J., Elderfield, H. (1996). Variations in Mg/Ca and Sr/Ca ratios of planktonic foraminifera caused by postdepositional dissolution: Evidence of shallow Mg-dependent dissolution. Paleoceanography, 11, 543–551.

Burton, E., Walter, L.M. (1991). The effects of pCO_2 and temperature on magnesium incorporation in calcite in seawater and $MgCl_2$-$CaCl_2$ solutions. Geochim. Cosmochim. Ac., 55, 777–785.

Cane, M.A., Molnar, P. (2001). Closing of the Indonesian seaway as a precursor to east African aridification around 3–4 million years ago. Nature, 411, 157–162.

Cannariato, K.G., Ravelo, A.C. (1997). Pliocene-Pleistocene evolution of eastern tropical Pacific surface water circulation and thermocline depth. Paleoceanography, 12, 805–820.

Chaisson, W.P., Leckie, R.M. (1993). High resolution Neogene planktonic foraminifer biostratigraphy of Site 806, Ontong Jave Plateau (western equatorial Pacific). In Proceedings of the Ocean Drilling Program, Sci. Results, 130, pp. 137–178, Ocean Drill. Program, College Station, Tex.

Charles, C.D., Froelich, P.N., Zibello, M.A., Matlock, R.A., Morley, J.J. (1991). Biogenic opal in Southern Ocean sediments over the last 450,000 years: Implications for surface water chemistry and circulation. Paleoceanography, 6, 697–728, doi:10.1029/91PA02477.

Clark, P.U., Pollard, D. (1998). Origin of the Middle Pleistocene transition by ice sheet erosion of regolith. Paleoceanography, 13, 1–9, doi:10.1029/97PA02660.

Clark, P.U., Archer, D., Pollard, D., Blum, J.D., Rial, J.A., Brovkin, V., Mix, A.C., Pisias, N.G., Roy, M. (2006). The middle Pleistocene transition: characteristics, mechanisms, and implications for long-term changes in atmospheric pCO_2. Quaternary Sci. Rev., 25, 3150–3184.

Clark, P.U., Dyke, A.S., Shakun, J.D., Carlson, A.E., Clark, J., Wohlfarth, B., Mitrovica, J.X., Hostetler, S.W., McCabe, A.M. (2009). The Last Glacial Maximum. Science, 325, 710–714.

Cleaveland, L.C., Herbert, T.D. (2007). Coherent obliquity band and heterogeneous precession band responses in early Pleistocene tropical sea surface temperatures. Paleoceanography, 22, PA2216, doi:10.1029/2006PA001370.

Coale, K.H., et al. (1996). A massive phytoplankton bloom induced by an ecosystem-scale iron fertilization experiment in the equatorial Pacific Ocean. Nature, 383, 495–501.

COHMAP Members (1988). Climatic changes of the last 18,000 years: Observations and model simulations. Science, 241(4869), 1043–1052.

Cook, C.P., et al. (2013). Dynamic behaviour of the East Antarctic ice sheet during Pliocene warmth. Nat. Geosci., 6, 765–769.

Corliss, B.H., McCorkle, D.C., Higdon, D.M. (2002). A time series study of the carbon isotopic composition of deep-sea benthic foraminifera. Paleoceanography, 17, doi:10.1029/2001PA000664.

Craig, H. (1961). Standard for reporting concentrations of deuterium and oxygen-18 in natural waters. Science, 133, 1833–1834.

Craig, H., Gordon, L.I. (1965). Deuterium and oxygen-18 variations in the ocean and the marine atmosphere. In Stable isotopes in oceanographic studies and paleotemperatures, edited by Tongiorgi, E., pp. 9–130, Spoletto, Pisa, Italy.

Cramer, B.S., Toggweiler, J.R., Wright, J.D., Katz, M.E., Miller, K.G. (2009). Ocean overturning since the Late Cretaceous: Inferences from a new benthic foraminiferal isotope compilation. Paleoceanography, 24, PA4216, doi:10.1029/2008PA001683.

Cronin, T.M., Whatley, F., Wood, A., Tsukagoshi, A., Ikeya, N., Brouwers, E.M., Briggs Jr., W.M. (1993). Microfaunal evidence for elevated pliocene temperatures in the Arctic Ocean. Paleoceanography, 8, 161–173.

Cronin, T.M., Kitamura, A., Ikeya, N., Watanabe, M., Kamiya, T. (1994). Late Pliocene climate change 3.4–2.3 Ma: Paleoceanographic record from the Yabuta Formation, Sea of Japan. Palaeo3, 108, 437–455.

Culver, S.J., Buzas, M.A. (1999). Biogeography of neritic benthic foraminifera. In Modern foraminifera, edited by Sen Gupta, B.K., pp. 93–102, Kluwer Academic Publishers, Dordrecht, Boston.

Curry, W.B., Oppo, D.W. (2005). Glacial water mass geometry and the distribution of $\delta^{13}C$ of ΣCO_2 in the western Atlantic Ocean. Paleoceanography, 20, PA1017, doi:10.1029/2004PA001021.

Darling, K.F., Kucera, M., Wade, C.M., von Langen, P., Pak, D. (2003). Seasonal distribution of genetic types of planktonic foraminifer morphospecies in the Santa Barbara Channel and its paleoceanographic implications. Paleoceanography, 18, 1032, doi:1010.1029/2001PA000723.

de Boer, B., Lourens, L.J., Van de Wal, R.S. (2014). Persistent 400,000-year variability of Antarctic ice volume and the carbon cycle is revealed throughout the Plio-Pleistocene. Nat. Comm., 5, doi:10.1038/ncomms3999.

de Garidel-Thoron, T., Rosenthal, Y., Bassinot, F., Beaufort, L. (2005). Stable sea surface temperatures in the western Pacific warm pool over the past 1.75 million years. Nature, 433, 294–298.

DeConto, R.M., Pollard, D., Wilson, P.A., Pälike, H., Lear, C.H., Pagani, M. (2008). Thresholds for Cenozoic bipolar glaciation. Nature, 455(7213), 652–656.

DeConto, R.M., Pollard, D. (2016). Contribution of Antarctica to past and future sea-level rise. Nature, 531, 591–597.

Dekens, P.S., Lea, D.W., Pak, D.K., Spero, H.J. (2002). Core top calibration of Mg/Ca in tropical foraminifera: Refining paleotemperature estimation. Geochem. Geophys. Geosys., 3, doi:10.1029/2001GC000200.

Dekens, P.S., Ravelo, A.C., McCarthy, M.D. (2007). Warm upwelling regions in the Pliocene warm period. Paleoceanography, 22, PA3211, doi:10.1029/2006PA001394.

Denton, G., Anderson, R., Toggweiler, J., Edwards, R., Schaefer, J., Putnam, A. (2010). The last glacial termination. Science, 328, 1652–1656.

Deuser, W.G., Ross, E.H., Hemleben, C., Spindler, M. (1981). Seasonal changes in species composition, numbers, mass, size, and isotopic composition of planktonic foraminifera settling into the deep Sargasso Sea. Palaeo3, 33, 103–127.

Diester-Haass, L., Meyers, P.A., Vidal, L. (2002). The late Miocene onset of high productivity in the Benguela Current upwelling system as part of a global pattern. Mar. Geol., 180, 87–103.

DiNezio, P.N., Tierney, J.E. (2013). The effect of sea level on glacial Indo-Pacific climate. Nat. Geosci., 6, 485–491.

Dolan, A.M., Haywood, A.M., Hill, D.J., Dowsett, H.J., Hunter, S.J., Lunt, D.J., Pickering, S.J. (2011). Sensitivity of Pliocene ice sheets to orbital forcing. Palaeo3, 309, 98–110.

Dowsett, H.J., Robinson, M.M., Foley, K.M. (2009). Pliocene three-dimensional global ocean temperature reconstruction. Climate of the Past, 5, 769–783.

Dowsett, H.J., et al. (2013). Sea surface temperature of the mid-Piacenzian ocean: A data-model comparison. Scientific Reports, 3, doi:10.1038/srep02013.

Drever, J.I., Li, Y.-H., Maynard, J.B. (1988). Geochemical cycles: The continental crust and the oceans. In Chemical cycles in the evolution of the earth, edited by C.B. Gregor, pp. 17–53, Wiley, New York.

Duplessy, J.-C., Lalou, C., Vinot, A.C. (1970). Differential isotopic fractionation in benthic foraminifera and paleotemperatures reassessed. Science, 168, 250–251.

Duplessy, J.-C., Shackleton, N.J., Matthews, R.K., Prell, W., Ruddiman, W.F., Caralp, M., Hendy, C.H. (1984). $\delta^{13}C$ record of benthic foraminifera in the last interglacial ocean: Implications for the carbon cycle and the global deep water circulation. Quaternary Res., 21, 225–243.

Duplessy, J.-C., Labeyrie, L., Waelbroeck, C. (2002). Constraints on the oxygen isotopic enrichment between the Last Glacial Maximum and the Holocene: Paleoceanographic implications. Quaternary Sci. Rev., 21, 315–330.

Dutton, A., Carlson, A.E., Long, A.J., Milne, G.A., Clark, P.U., DeConto, R., Horton, B.P., Rahmstorf, S., Raymo, M.E. (2015). Sea-level rise due to polar ice-sheet mass loss during past warm periods. Science, 349, doi:10.1126/science.aaa4019.

Dwyer, G.S., Cronin, T.M., Baker, P.A., Raymo, M.E., Buzas, J.S., Correge, T. (1995). North Atlantic deepwater temperature change during late Pliocene and late Quaternary climatic cycles. Science, 270, 1347–1351.

Dwyer, G.S., Chandler, M.A. (2008). Mid-Pliocene sea level and continental ice volume based on coupled benthic Mg/Ca palaeotemperatures and oxygen isotopes. Philos. T. Roy. Soc. A, 367, 157–168.

Dyez, K.A., Ravelo, A.C. (2014). Dynamical changes in the tropical Pacific warm pool and zonal SST gradient during the Pleistocene. Geophys. Res. Lett., 41, 7626–7633.

Edgar, K.M., Pälike, H., Wilson, P.A. (2013). Testing the impact of diagenesis on the $\delta^{18}O$ and $\delta^{13}C$ of benthic foraminiferal calcite from a sediment burial depth transect in the equatorial Pacific. Paleoceanography, 28, 468–480.

Eggins, S., De Deckker, P., Marshall, J. (2003). Mg/Ca variation in planktonic foraminifera tests: Implications for reconstructing palaeo-seawater temperature and habitat migration. Earth Planet. Sci. Lett., 212, 291–306.

Eguchi, N.O., Kawahata, H., Taira, A. (1999). Seasonal response of planktonic foraminifera to surface ocean condition: Sediment trap results from the central NorthPacific Ocean. J. Oceanogr., 55, 681–691.

Ehlert, C., Grasse, P., Frank, M. (2013). Changes in silicate utilisation and upwelling intensity off Peru since the Last Glacial Maximum – insights from silicon and neodymium isotopes. Quaternary Sci. Rev., 72, 18–35.

Elderfield, H., Ganssen, G. (2000). Past temperature and $\delta^{18}O$ of surface ocean waters inferred from foraminiferal Mg/Ca ratios. Nature, 405, 422–445.

Elderfield, H., Vautravers, M., Cooper, M. (2002). The relationship between shell size and Mg/Ca, Sr/Ca, $\delta^{18}O$, and $\delta^{13}C$ of species of planktonic foraminifera. Geochem. Geophys. Geosyst., 3(8), 1052, doi:10.1029/2001GC000194.

Eldrett, J.S., Harding, I.C., Wilson, P.A., Butler, E., Roberts, A.P. (2007). Continental ice in Greenland during the Eocene and Oligocene. Nature, 446, 176–179.

Emanuele, D., Ferretti, P., Palumbo, E., Amore, F.O. (2015). Sea-surface dynamics and palaeoenvironmental changes in the North Atlantic Ocean (IODP Site U1313) during Marine Isotope Stage 19 inferred from coccolithophore assemblages. Palaeo3, 430, 104–117.

Emery, W.J. (2003). Water types and water masses. In Encyclopedia of Atmospheric Sciences, edited by Holton, J.R., Curry, J.A., Pyle, J.A., pp. 1556–1567, Elsevier.

Emiliani, C. (1955). Pleistocene temperatures. J. Geol., 538–578.

Etourneau, J., Schneider, R., Blanz, T., Martinez, P. (2010). Intensification of the Walker and Hadley atmospheric circulations during the Pliocene-Pleistocene climate transition. Earth Planet. Sci. Lett., 297(1–2), 103–110.

Etourneau, J., Ehlert, C., Frank, M., Martinez, P., Schneider, R. (2012). Contribution of changes in opal productivity and nutrient distribution in the coastal upwelling systems to Late Pliocene/Early Pleistocene climate cooling. Clim. Past, 8(5), 1435–1445.

Etourneau, J., Robinson, R.S., Martinez, P., Schneider, R. (2013). Equatorial Pacific peak in biological production regulated by nutrient and upwelling during the late Pliocene/early Pleistocene cooling. Biogeosciences, 10(8), 5663–5670.

Expedition 306 Scientists (2006). Site U1313. In North Atlantic climate, Proc. Integr. Ocean Drill. Program 303/306, doi:10.2204/iodp.proc.303306.112.2006.

Fairbanks, R.G., Matthews, R.K. (1978). The marine oxygen isotopic record in Pleistocene coral, Barbados, West Indies. Quaternary Res., 10, 181–196.

Fairbanks, R.G., Sverdlove, M., Free, R., Wiebe, P., Bé, W. (1982). Vertical distribution and isotopic fractionation of living planktonic foraminifera from the Panama Basin. Nature, 298, 841–844.

Fantle, M.S., DePaolo, D.J. (2005). Variations in the marine Ca cycle over the past 20 million years. Earth Planet. Sci. Lett., 237, 102–117.

Fantle, M.S., DePaolo, D.J. (2006). Sr isotopes and pore fluid chemistry in carbonate sediment of the Ontong Java Plateau: Calcite recrystallization rates and evidence for a rapid rise in seawater Mg over the last 10 million years. Geochim. Cosmochim. Ac., 70, 3883–3904.

Fedorov, A.V., Philander, S.G. (2000). Is El Niño changing? Science, 288, 1997–2002.

Fedorov, A.V., Dekens, P.S., McCarthy, M., Ravelo, A.C., deMenocal, P.B., Barriero, M., Pacanowski, R.C., Philander, S.G. (2006). The Pliocene paradox (mechanisms for a permanent El Niño). Science, 312, 1485–1489.

Fedorov, A.V., Burls, N.J., Lawrence, K.T., Peterson, L.C. (2015). Tightly linked zonal and meridional sea surface temperature gradients over the past five million years. Nat. Geosci., 8, 975–980.

Ferguson, J., Henderson, G., Kucera, M., Rickaby, R. (2008). Systematic change of foraminiferal Mg/Ca ratios across a strong salinity gradient. Earth Planet. Sci. Lett., 265, 153–166.

Fiedler, P.C. (2002). Environmental change in the eastern tropical Pacific Ocean: review of ENSO and decadal variability. Mar. Ecol-Prog. Ser., 244, 265–283.

Filippelli, G.M., Latimer, J.C., Murray, R.W., Flores, J.A. (2007). Productivity records from the Southern Ocean and the equatorial Pacific Ocean: Testing the glacial shelf-nutrient hypothesis. Deep Sea Res. II, 54(21–22), 2443–2452.

Fisher, G., Wefer, G. (1999). Use of proxies in paleoceanography – Examples from the South Atlantic. Springer-Verlag, Heidelberg, Berlin, 735 pp.

Flores, J.A., Sierro, F.J., Raffi, I. (1995). Evolution of the calcareous nannofossil assemblage as a response to the paleoceanographic changes in the eastern equatorial Pacific Ocean from 4 to 2 Ma (Leg 138, Sites 849 and 852). In Proceedings of the Ocean Drilling Program, Sci. Results, 138, pp. 163–176, Ocean Drill. Program, College Station, Tex.

Flores, J.A., Filippelli, G.M., Sierro, F.J., Latimer, J. (2012). The "White Ocean" hypothesis: A late Pleistocene Southern Ocean governed by coccolithophores and driven by phosphorus. Front. Microbiol., 3, 233, doi:10.3389/fmicb.2012.00233.

Fraile, I., Mulitza, S., Schulz, M. (2009). Modeling planktonic foraminiferal seasonality: Implications for sea-surface temperature reconstructions. Mar. Micropaleontol., 72, 1–9, doi:10.1016/j.marmicro.2009.1001.1003.

Franco-Fraguas, P., Costa, K.B., Antonio, F., Toledo, L. (2011). Stable isotope/test size relationship in *Cibicidoides wuellerstorfi*. Brazilian Journal of Oceanography, 59, 287-291.

Frank, M., Reynolds, B.C., O'Nions, R.K. (1999). Nd and Pb isotopes in Atlantic and Pacific water masses before and after closure of the Panama gateway. Geology, 27, 1147–1150.

Fratantoni, D.M. (2001). North Atlantic surface circulation during the 1990's observed with satellite-tracked drifters. J. Geophys. Res.-Oceans, 106, 22067–22093.

Friedrich, O., Hemleben, C. (2007). Early Maastrichtian benthic foraminiferal assemblages from the western North Atlantic (Blake Nose) and their relation to paleoenvironmental changes. Mar. Micropaleontol., 62, 31–44.

Friedrich, O., Erbacher, J., Moriya, K., Wilson, P.A., Kuhnert, H. (2008a). Warm saline intermediate waters in the Cretaceous tropical Atlantic Ocean. Nat. Geosci., 1, 453–457.

Friedrich, O., Norris, R.D., Bornemann, A., Beckmann, B., Pälike, H., Worstell, P., Hofmann, P., Wagner, T. (2008b). Cyclic changes in Turonian to Coniacian planktic foraminiferal assemblages from the tropical Atlantic Ocean. Mar. Micropaleontol., 68, 299–313.

Friedrich, O., Schiebel, R., Wilson, P.A., Weldeab, S., Beer, C.J., Cooper, M.J., Fiebig, J. (2012). Influence of test size, water depth, and ecology on Mg/Ca, Sr/Ca, $\delta^{18}O$ and $\delta^{13}C$ in nine modern species of planktic foraminifers. Earth Planet. Sci. Lett., 319, 133–145.

Friedrich, O., Wilson, P.A., Bolton, C.T., Beer, C.J., Schiebel, R. (2013). Late Pliocene to early Pleistocene changes in the North Atlantic Current and suborbital-scale sea-surface temperature variability. Paleoceanography, 28, 274–282.

Ganeshram, R.S., Pedersen, T.F., Calvert, S.E., McNeill, G.W. Fontugne, M.R. (2000). Glacial-interglacial variability in denitrification in the world's oceans: Causes and consequence. Paleoceanography, 15, 361–376, doi:10.1029/1999PA000422.

Garcia, H.E., Locarnini, R.A., Boyer, T.P., Antonov, J.I., Baranova, O.K., Zweng, M.M., Reagan, J.R., Johnson, D.R. (2014). World Ocean Atlas 2013, Vol. 4: Dissolved Inorg. Nutr. (Phosphate, Nitrate, Silic.), edited by S. Levitus, U.S. Gov. Print. Off., Washington, D.C., NOAA Atlas NESDIS, 76, 25 pp.

Gibbard, P.L., Head, M.J., Walker, M.J.C. (2010). Formal ratification of the Quaternary System/Period and the Pleistocene Series/Epoch with a base at 2.58 Ma. J. Quat. Sci., 25(2), 96–102.

Gradstein, F.M., Ogg, J.G. (2012). The chronostratigraphic scale. In The geological timescale, edited by Gradstein, F.M., Ogg, J.G., Schmitz, M.D., Ogg, G.M., pp. 31–42, Elsevier, Amsterdam.

Graham, D.W., Corliss, B.H., Bender, M.L., Keigwin, L.D. (1981). Carbon and oxygen isotopic disequilibria of recent deep-sea benthic foraminifera. Mar. Micropaleontol., 6, 483–497.

Greaves, M., et al. (2008). Interlaboratory comparison study of calibration standards for foraminiferal Mg/Ca thermometry. Geochem. Geophys. Geosyst., 9, Q08010, doi:08010.01029/02008GC001974.

Groeneveld, J., Hathorne, E.C., Steinke, S., DeBey, H., Mackensen, A., Tiedemann, R. (2014). Glacial induced closure of the Panamanian Gateway during Marine Isotope Stages (MIS) 95–100. Earth Planet. Sci. Lett., 404, 296–306.

Hadley, G. (1735). Concerning the cause of the general trade-winds. Phil. Trans., 39, 58–62.

Hagelberg, T.K., Pisias, N.G., Mayer, L.A., Shackleton, N.J., Mix, A.C. (1995). Spatial and temporal variability of Late Neogene Equatorial Pacific carbonate: Leg 138. In Proceedings of the Ocean Drilling Program, Sci. Results, 138, pp. 321–336, Ocean Drill. Program, College Station, Tex.

Hallock, P. (1999). Symbiont-bearing foraminifera. In Modern foraminifera, edited by Sen Gupta, B.K., pp. 123–139, Kluwer Academic Publishers, Dordrecht, Boston.

Hammer, Ø., Harper, D.A.T., Ryan, P.D. (2001). PAST: Paleontological statistics software package for education and data analysis. Palaeontol. Electron., 4, 1–9.

Harrison, T.M., Copeland, P., Kidd, W.S.F., Yin, A. (1992). Raising Tibet. Science, 255, 1663–1670.

Haug, G.H., Tiedemann, R. (1998). Effect of the formation of the Isthmus of Panama on Atlantic Ocean thermohaline circulation. Nature, 393, 673–676.

Haug, G.H., Sigman, D.M., Tiedemann, R., Pedersen, T.F., Sarnthein, M. (1999). Onset of permanent stratification in the subarctic Pacific Ocean. Nature, 401, 779–782.

Haug, G.H., et al. (2005). North Pacific seasonality and the glaciation of North America 2.7 million years ago. Nature, 433, 821–825.

Hayes, C.T., Anderson, R.F., Fleisher, M.Q. (2011). Opal accumulation rates in the equatorial Pacific and mechanisms of deglaciation. Paleoceanography, 26, PA1207, doi:10.1029/2010PA002008.

Hemleben, C., Spindler, M., Anderson, O. (1989). Modern planktonic foraminifera. Springer-Verlag, New York, 363 pp.

Hemleben, C., Bijma, J. (1994). Foraminiferal population dynamics, stable isotopes and paleo-environment in the Red Sea and the North Atlantic. In Carbon cycling in the glacial ocean: Constrains on the ocean's role in global change, edited by Zahn, R., Kaminski, M., Labeyrie, L., Pedersen, T., pp. 145–166, Elsevier, New York.

Hennissen, J.A.I., Head, M.J., De Schepper, S., Groeneveld, J. (2014). Palynological evidence for a southward shift of the North Atlantic current at ~2.6 Ma during the intensification of late Cenozoic Northern Hemisphere glaciation. Paleoceanography, 29, 564–580, doi:10.1002/2013PA002543.

Hennissen, J.A.I., Head, M.J., De Schepper, S., Groeneveld, J. (2015). Increased seasonality during the intensification of Northern Hemisphere glaciation at the Pliocene-Pleistocene boundary ~2.6 Ma. Quaternary Sci. Rev., 129, 321–332.

Herguera, J.C., Berger, W.H. (1991). Paleoproductivity from benthic foraminifera abundance: Glacial to postglacial change in the westequatorial Pacific. Geology, 19, 1173–1176.

Hillenbrand, C.-D., Fütterer, D.K. (2001). Neogene to Quaternary deposition of opal on the continental rise west of the Antarctic Peninsula, ODP Leg 178, Sites 1095, 1096 and 1101. In Proceedings of the Ocean Drilling Program, Sci. Results, 178, pp. 1–33, Ocean Drill. Program, College Station, Tex.

Hillenbrand, C.-D., Cortese, G. (2006). Polar stratification: A critical view from the Southern Ocean. Palaeo3, 242(3–4), 240–252.

Hodell, D.A., Venz, K.A., Charles, C.D., Ninnemann, U.S. (2003). Pleistocene vertical carbon isotope and carbonate gradients in the South Atlantic sector of the Southern Ocean. Geochem. Geophys. Geosyst., 4(1), 1004, doi:10.1029/2002GC000367.

Holbourn, A., Kuhnt, W., Frank, M., Haley, B.A. (2013). Changes in Pacific Ocean circulation following the Miocene onset of permanent Antarctic ice cover. Earth Planet. Sci. Lett., 365, 38–50.

Hönisch, B., Allen, K.A., Lea, D.W., Spero, H.J., Eggins, S.M., Arbuszewski, J., deMenocal, P., Rosenthal, Y., Russell, A.D., Elderfield, H. (2013). The influence of salinity on

Mg/Ca in planktic foraminifers – Evidence from cultures, core-top sediments and complementary $\delta^{18}O$. Geochim. Cosmochimi. Ac., 121, 196–213.

Hovan, S.A. (1995). Late Cenozoic atmospheric circulation intensity and climatic history recorded by eolian deposition in the eastern equatorial Pacific Ocean, Leg 138. In Proceedings of the Ocean Drilling Program, Sci. Results, 138, pp. 615–625, Ocean Drill. Program, College Station, Tex.

Hovan, S.A. (2013). Grain-size variations, eolian material and accumulation rates in sediments from ODP Hole 138-849B. doi:10.1594/PANGAEA.807833.

Hut, G. (1987). Consultant's group meeting on stable isotope reference samples for geochemical and hydrological investigations. Report to the Director General, International Atomic Energy Agency, Vienna, 42 pp.

Hyeong, K., Kuroda, J., Seo, I., Wilson, P.A. (2016). Response of the Pacific inter-tropical convergence zone to global cooling and initiation of Antarctic glaciation across the Eocene Oligocene Transition. Sci. Rep., 6, doi:10.1038/srep30647.

IPCC, 2014. Climate Change 2014: Synthesis Report. IPCC, Geneva, Switzerland, 151 pp.

Jansen, E., Fronval, T., Rack, F., Channell, J.E.T. (2000). Pliocene-Pleistocene ice rafting history and cyclicity in the Nordic Seas during the last 3.5 Myr. Paleoceanography, 15, 709–721.

Jarvis, I.A.N., Gale, A.S., Jenkyns, H.C., Pearce, M.A. (2006). Secular variation in Late Cretaceous carbon isotopes: A new $\delta^{13}C$ carbonate reference curve for the Cenomanian-Campanian (99.6–70.6 Ma). Geol. Mag., 143, 561–608.

Johnson, T.C. (1972). Ocean-floor erosion in the equatorial Pacific. Geol. Soc. Am. Bull., 83(10), 3121–3144.

Johnson, T.C., Hamilton, E.L., Berger, W.H. (1977). Physical properties of calcareous ooze: Control by dissolution at depth. Mar. Geol., 24, 259–277.

Jonkers, L., Kučera, M. (2015). Global analysis of seasonality in the shell flux of extant planktonic Foraminifera. Biogeosciences, 12, 2207–2226.

Jorissen, F.J., Stigter, H.C., Widmark, J.G.V. (1995). A conceptual model explaining benthic foraminiferal microhabitats. Mar. Micropaleontol., 26, 3–15.

Kaiho, K. (1998). Phylogeny of deep-sea calcareous trochospiral benthic foraminifera: evolution and diversification. Micropaleontology, 44, 291–311.

Karas, C., Nürnberg, D., Gupta, A.K., Tiedemann, R., Mohan, K., Bickert, T. (2009). Mid-Pliocene climate change amplified by a switch in Indonesian subsurface throughflow. Nat. Geosci., 2, 434–438, doi:10.1038/NGEO520.

Keigwin, L.D. (1982). Isotopic paleoceanography of the Caribbean and east Pacific: Role of Panama uplift in Late Neogene time. Science, 217, 350–353.

Kemle von Mücke, S., Oberhänsli, H. (1999). The distribution of living planktic foraminifera in relation to southeast Atlantic oceanography. In Use of Proxies in Paleoceanography: Examples From the South Atlantic, edited by G. Fischer, G. Wefer, pp. 91–115, Springer, Berlin.

Kennett, J.P., Thunnell, R.C. (1975). Global increase in Quaternary explosive volcanism. Science, 187, 497–503.

Kennett, J.P., McBirney, A.R., Thunnell, R.C. (1977). Episodes of Cenozoic volcanism in the circum-Pacific region. Journal of Vulcanology and Geothermal Research, 2, 145–163.

Kessler, W.S. (2006). The circulation of the eastern tropical Pacific: A review. Prog. Oceanogr., 69, 181–217.

Kienast, S.S., Calvert, S.E., Pedersen, T.F. (2002). Nitrogen isotope and productivity variations along the northeast Pacific margin over the last 120 kyr: Surface and subsurface paleoceanography. Paleoceanography, 17(4), 1055, doi:10.1029/ 2001PA000650.

Kısakürek, B., Eisenhauer, A., Böhm, F., Garbe-Schönberg, D., Erez, J. (2008). Controls on shell Mg/Ca and Sr/Ca in cultured planktonic foraminiferan, *Globigerinoides ruber* (white). Earth Planet. Sci. Lett., 273, 260–269.

Kleiven, H.F., Jansen, E., Fronval, T., Smith, T.M. (2002), Intensification of Northern Hemisphere glaciations in the circum Atlantic region (3.5–2.4 Ma) - Ice-rafted detritus evidence. Palaeo3, 184, 213–223.

Koutavas, A., Lynch-Stieglitz, J. (2003). Glacial-interglacial dynamics of the eastern equatorial Pacific cold tongue-Intertropical Convergence Zone system reconstructed from oxygen isotope records. Paleoceanography, 18, 1089, doi:1010.1029/2003PA000894.

Kucera, M., et al. (2005). Reconstruction of sea-surface temperatures from assemblages of planktonic foraminifera: multi-technique approach based on geographically constrained calibration data sets and its application to glacial Atlantic and Pacific Oceans. Quaternary Sci. Rev., 24, 951–998.

Kucera, M. (2007). Planktonic foraminifera as tracers of past oceanic environments. In Proxies in Late Cenozoic paleoceanography, edited by Hillaire-Marcel, C., De Vernal, A., pp. 213–262, Elsevier, Amsterdam.

Kuroyanagi, A., Tsuchiya, M., Kawahata, H., Kitazato, H. (2008). The occurrence of two genotypes of the planktonic foraminifer *Globigerinoides ruber* (white) and paleo-environmental implications. Mar. Micropaleontol., 68, 236–243.

Kutzbach, J.E., Guetter, P.J., Behling, P.J., Selin, R. (1993). Simulated climatic changes: Results of the COHMAP climate-model experiments. In Global climates since the Last Glacial Maximum, edited by H.E. Wright Jr. et al., pp. 24–93, Univ. of Minnesota Press, Minneapolis.

Kutzbach, J.E., Ruddiman, W.F. (1993). Model description, external forcing, and surface boundary conditions. In Global Climates Since the Last Glacial Maximum, edited by H.E. Wright Jr. et al., pp. 12–23, Univ. of Minnesota Press, Minneapolis.

Lalicata, J.J., Lea, D.W. (2011). Pleistocene carbonate dissolution fluctuations in the eastern equatorial Pacific on glacial timescales: Evidence from ODP Hole 1241. Mar. Micropaleontol., 79(1–2), 41–51.

Lambeck, K., Rouby, H., Purcell, A., Sun, Y., Sambridge, M. (2014). Sea level and global ice volumes from the Last Glacial Maximum to the Holocene. P. Natl. Acad. Sci., 111, 15296–15303.

Lang, D.C., et al. (2014). The transition on North America from the warm humid Pliocene to the glaciated Quaternary traced by eolian dust deposition at a benchmark North Atlantic Ocean drill site. Quaternary Sci. Rev., 93, 125–141.

Lang, D.C., Bailey, I., Wilson, P.A., Chalk, T., Foster, G., Gutjahr, M. (2016). Incursions of southern-sourced water into the deep North Atlantic during late Pliocene glacial intensification. Nat. Geosci., 9, doi:10.1038/NGEO2688.

Laskar, J., Robutel, P., Joutel, F., Gastineau, M., Correia, A.C.M., Levrard, B. (2004). A long-term numerical solution for the insolation quantities of the Earth. Astron. Astrophys., 428, 261–285, doi:10.1051/0004-6361:20041335.

Lawrence, K.T., Liu, Z., Herbert, T.D. (2006). Evolution of the eastern tropical Pacific through Plio-Pleistocene glaciation. Science, 312, 79–83.

Lawrence, K.T., Herbert, T.D., Brown, C.M., Raymo, M.E., Haywood, A.M. (2009). High-amplitude variations in North Atlantic sea surface temperature during the early Pliocene warm period. Paleoceanography, 24, PA2218, doi:10.1029/2008PA001669.

Lawrence, K.T., Sigman, D.M., Herbert, T.D., Riihimaki, C.A., Bolton, C.T., Martinez-Garcia, A., Rosell-Mele, A., Haug, G.H. (2013). Timetransgressive North Atlantic productivity changes upon Northern Hemisphere glaciation. Paleoceanography, 28, 740–751, doi:10.1002/2013PA002546.

Le, J., Shackleton, N.J. (1992). Carbonate dissolution fluctuations in the western equatorial Pacific during the late Quaternary. Paleoceanography, 7, 21–42, doi:10.1029/91PA02854.

Le, J., Mix, A.C., Shackleton, N.J. (1995). Late Quaternary paleoceanography in the eastern equatorial Pacific Ocean from planktonic foraminifers: A high-resolution record from Site 846. In Proceedings of the Ocean Drilling Program, Sci. Results, 138, pp. 675–693, Ocean Drill. Program, College Station, Tex.

Lea, D.W., Mashiotta, T.A., Spero, H.J. (1999). Controls on magnesium and strontium uptake in planktonic foraminifera determined by live culturing. Geochim. Cosmochim. Ac., 63, 2369–2379.

Lea, D.W., Pak, D.K., Spero, H.J. (2000). Climate impact of late Quaternary equatorial Pacific sea surface temperature variations. Science, 289, 1719–1724.

Lear, C.H., Elderfield, H., Wilson, P.A. (2000). Cenozoic deep-sea temperatures and global ice volumes from Mg/Ca in benthic foraminiferal calcite. Science, 287, 269–272.

Lear, C.H., Rosenthal, Y., Slowey, N. (2002). Benthic foraminiferal Mg/Ca-paleothermometry: A revised core-top calibration. Geochim. Cosmochim. Ac., 66, 3375–3387.

Lear, C.H., Rosenthal, Y., Coxall, H.K., Wilson, P.A. (2004). Late Eocene to early Miocene ice sheet dynamics and the global carbon cycle. Paleoceanography, 19, PA4015, doi:4010.1029/2004PA001039.

Lear, C.H., Coxall, H.K., Foster, G.L., Lunt, D.J., Mawbey, E.M., Rosenthal, Y., Sosdian, S.M., Thomas, E., Wilson, P.A. (2015). Neogene ice volume and ocean temperatures: Insights from infaunal foraminiferal Mg/Ca paleothermometry. Paleoceanography, 30, doi:10.1002/2015PA002833.

Lee, S.Y., Poulsen, C.J. (2005). Tropical Pacific climate response to obliquity forcing in the Pleistocene. Paleoceanography, 20, PA4010, doi:4010.1029/2005PA001161.

Levin, L.A., Gooday, A.J. (2003). The Deep Atlantic Ocean. In Ecosystems of the deep oceans, edited by Tyler, P.A., pp. 111–178, Elsevier, Amsterdam, New York.

Lhomme, N., Clarke, G.K.C. (2005). Global budget of water isotopes inferred from polar ice sheets. Geophys. Res. Lett., 32, L20502, doi:20510.21029/22005GL023774.

Lin, H.-L., Peterson, L.C., Overpeck, J.T., Trumbore, S.E., Murray, D.W. (1997). Late Quaternary climate change from $\delta^{18}O$ records of multiple species of planktonic foraminifera: High-resolution records from the Anoxic Cariaco Basin, Venezuela. Paleoceanography, 12, 415–427.

Lisiecki, L.E., Raymo, M.E. (2005). A Pliocene-Pleistocene stack of 57 globally distributed benthic $\delta^{18}O$ records. Paleoceanography, 20, PA1003, doi:10.1029/2004PA001071.

Locarnini, R.A., et al. (2013). World Ocean Atlas 2013, Vol. 1: Temperature, edited by S. Levitus and A. Mishonov, U.S. Gov. Print. Off., Washington, D.C., NOAA Atlas NESDIS, 73, 40 pp.

Loubere, P. (2000). Marine control of biological production in the eastern equatorial Pacific Ocean. Nature, 406, 497–500.

Lourens, L.J., Becker, J., Bintanja, R., Hilgen, F.J., Tuenter, E., Van de Wal, R.S.W., Ziegler, M. (2010). Linear and non-linear response of late Neogene glacial cycles to obliquity forcing and implications for the Milankovitch theory. Quaternary Sci. Rev., 29, 352–365.

Lukas, R. (1986). The termination of the Equatorial Undercurrent in the Easterm Pacific. Prog. Oceanogr., 16, 63–90.

Lunt, D.J., Foster, G.L., Haywood, A.M., Stone, E.J. (2008a). Late Pliocene Greenland glaciation controlled by a decline in atmospheric CO_2 levels. Nature, 454(7208), 1102–1106.

Lunt, D.J., Valdes, P.J., Haywood, A., Rutt, I.C. (2008b). Closure of the Panama Seaway during the Pliocene: Implications for climate and Northern Hemisphere glaciation. Clim. Dynam., 30, 1–18.

Luthi, D., et al. (2008). High-resolution carbon dioxide concentration record 650,000-800,000 years before present. Nature, 453, 379–382.

Lyle, M., Dadey, K.A., Farrell, J.W. (1995). The late Miocene (11–8 Ma) eastern Pacific carbonate crash: Evidence for reorganization of ddep-water circulation by the closure of the Panama Gateway. In Proceedings of the Ocean Drilling Program, Sci. Results, 138, pp. 821–838, Ocean Drill. Program, College Station, Tex.

Lyle, M., Mix, A., Pisias, N. (2002). Patterns of $CaCO_3$ deposition in the eastern tropical Pacific Ocean for the last 150 kyr: Evidence for a southeast Pacific depositional spike during marine isotope stage (MIS) 2. Paleoceanography, 17, doi:10.1029/ 2000PA00538.

Lyle, M., Baldauf, J. (2015). Biogenic sediment regimes in the Neogene equatorial Pacific, IODP Site U1338: Burial, production, and diatom community. Palaeo3, 433, 106–128.

Lythe, M.B., Vaughan, D.G. (2001). BEDMAP: A new ice thickness and subglacial topographic model of Antarctica. J. Geophys. Res.-Sol. Ea., 106, 11335–11351.

Ma, Z., Ravelo, A.C., Liu, Z., Zhou, L., Paytan, A. (2015). Export production fluctuations in the eastern equatorial Pacific during the Pliocene-Pleistocene: Reconstruction using

barite accumulation rates. Paleoceanography, 30, 1455–1469, doi:10.1002/2015PA002860.

Mackensen, A., Hubberten, H.-W., Bickert, T., Fischer, G., Fütterer, D.K. (1993). The $\delta^{13}C$ in benthic foraminiferal tests of *Fontbotia wuellerstorfi* (Schwager) relative to the $\delta^{13}C$ of dissolved inorganic carbon in southern ocean deep water: Implications for glacial ocean circulation models. Paleoceanography, 8, 587–610, doi:10.1029/93PA01291.

Mackensen, A., Bickert, T. (1999). Stable carbon isotopes in benthic foraminifera: Proxies for deep and bottom water circulation and new production. In Use of Proxies in Paleoceanography: Examples From the South Atlantic, edited by G. Fischer, G. Wefer, pp. 229–254, Springer, Berlin.

Mackensen, A., Rudolph, M., Kuhn, G. (2001). Late Pleistocene deep-water circulation in the sub-antarctic eastern Atlantic. Global Planet. Change, 30, 197–229.

Maier-Reimer, E., Mikolajewicz, U., Crowley, T. (1990). Ocean general circulation model sensitivity experiment with an open Central American Isthmus. Paleoceanography, 5, 349–366.

Marchitto, T.M., Lynch-Stieglitz, J., Hemming, S.R. (2005). Deep Pacific $CaCO_3$ compensation and glacial-interglacial atmospheric CO_2. Earth Planet. Sci. Lett., 231(3–4), 317–336.

Marchitto, T.M., Bryan, S.P., Curry, W.B., McCorkle, D.C. (2007). Mg/Ca temperature calibration for the benthic foraminifer *Cibicidoides pachyderma*. Paleoceanography, 22, PA1203, doi:1210.1029/2006PA001287.

Markovic, S., Paytan, A., Wortmann, U.G. (2015). Pleistocene sediment offloading and the global sulfur cycle. Biogeosciences, 12, 3043–3060, doi:10.5194/bg-12-3043-2015.

Martinez-Boti, M.A., Foster, G.L., Chalk, T.B., Rohling, E.J., Sexton, P.F., Lunt, D.J., Pancost, R.D., Badger, M.P., Schmidt, D.N. (2015). Plio-Pleistocene climate sensitivity evaluated using high-resolution CO_2 records. Nature, 518, 49–54.

Mashiotta, T.A., Lea, D.W., Spero, H.J. (1999). Glacial-interglacial changes in Subantarctic sea surface temperature and $\delta^{18}O$-water using foraminiferal Mg. Earth Planet. Sci. Lett., 170, 417–432.

Maslin, M.A., Haug, G.H., Sarnthein, M., Tiedemann, R., Erlenkeuser, H., Stax, R. (1995). Northwest Pacific Site 882: The initiation of Northern Hemisphere Glaciation. In Proceedings of the Ocean Drilling Program, Sci. Results, 145, pp. 315–329, Ocean Drill. Program, College Station, Tex..

Maslin, M.A., Li, X.S., Loutre, M.-F., Berger, A. (1998). The contribution of orbital forcing to the progressive intensification of Northern Hemisphere Glaciation. Quaternary Sci. Rev., 17, 411–426.

Mathien-Blard, E., Bassinot, F. (2009). Salinity bias on the foraminifera Mg/Ca thermometry: Correction procedure and implications for past ocean hydrographic reconstructions. Geochem., Geophys., Geosyst., 10, Q12011, doi:12010.11029/12008GC002353.

Mayer, L., et al. (1985). Site 572. In Proceedings of the Deep Sea Drilling Project, Initial Rep., 85, pp. 33–135, Deep Sea Drill. Proj., Washington, D.C.

Mayer, L., et al. (1992). Site 849. In Proceedings of the Ocean Drilling Program, Initial Rep., 138, pp. 735–807, Ocean Drill. Program, College Station, Tex.

McConnaughey, T. (1989). ^{13}C and ^{18}O isotopic disequilibrium in biological carbonates: I. Patterns. Geochim. Cosmochim. Ac., 53, 151–162.

McConnell, M.C., Thunell, R.C. (2005). Calibration of the planktonic foraminiferal Mg/Ca paleothermometer: Sediment trap results from the Guaymas Basin, Gulf of California. Paleoceanography, 20, doi:10.1029/2004PA001077.

McGee, D., Marcantonio, F., Lynch-Stieglitz, J. (2007). Deglacial changes in dust flux in the eastern equatorial Pacific. Earth Planet. Sci. Lett., 257(1–2), 215–230.

McPhaden, M.J., Zebiak, S.E., Glantz, M.H. (2006). ENSO as an integrating concept in earth science. Science, 314, 1740–1745.

Meckler, A.N., Clarkson, M.O., Cobb, K.M., Sodemann, H., Adkins, J.F. (2012). Interglacial hydroclimate in the tropical west Pacific through the Late Pleistocene. Science, 336, 1301–1304.

Medina-Elizalde, M., Lea, D.W., Fantle, M.S. (2008). Implications of seawater Mg/Ca variability for Plio-Pleistocene tropical climate reconstruction. Earth Planet. Sci. Lett. 269, 585–595.

Medina-Elizalde, M., Lea, D.W. (2010). Late Pliocene equatorial Pacific. Paleoceanography, 25, PA2208, doi:2210.1029/2009PA001780.

Messié, M., Chavez, F.P. (2011). Global modes of sea surface temperature variability in relation to regional climate indices. J. Climate, 24, 4314–4331.

Messié, M., Chavez, F.P. (2012). A global analysis of ENSO synchrony: The oceans biological response to physical forcing. J. Geophys. Res., 117, C09001, doi:09010.01029/02012JC007938.

Milankovitch, M. (1941). Kanon der Erdbestrahlung und seine Auswirkung auf das Eiszeitenproblem. Special Publications of the Royal Serbian Academy, Belgrad, 633 pp.

Miller, K.G., Kominz, M.A., Browning, J.V., Wright, J.D., Mountain, G.S., Katz, M.E., Sugarman, P.J., Cramer, B.S., Christie-Blick, N., Pekar, S.F. (2005). The Phanerozoic record of global sea-level change. Science, 310, 1293–1298.

Miller, K.G., Mountain, G.S., Wright, J.D., Browning, J.V. (2011). A 180-million-year record of sea level and ice volume variations from continental margin and deep-sea isotopic records. Oceanography, 24, 40–53.

Miller, K.G., Wright, J.D., Browning, J.V., Kulpecz, A., Kominz, M., Naish, T.R., Cramer, B.S., Rosenthal, Y., Peltier, W.R., Sosdian, S. (2012). High tide of the warm Pliocene: Implications of global sea level for Antarctic deglaciation. Geology, 40, 407–410.

Mimura, N. (2013). Sea-level rise caused by climate change and its implications for society. P. Jpn. Acad. B-Phys., 89, 281–301.

Mitsuguchi, T., Matsumoto, E., Abe, O., Uchida, T., Isdale, P.J. (1996). Mg/Ca thermometry in coral skeletons. Science, 274, 961–963.

Mix, A.C., Pisias, N.G., Rugh, W., Wilson, J., Morey, A., Hagelberg, T.K. (1995). Benthic foraminifer stable isotope record from Site 849 (0–5 Ma): Local and global climate changes. In Proceedings of the Ocean Drilling Program, Sci. Results, 138, pp. 371–412, Ocean Drill. Program, College Station, Tex.

Mix, A.C., et al. (2003). Proceedings of the Ocean Drilling Program, Init. Reports, 202. Ocean Drill. Program, College Station, Tex.

Molnar, P., Cane, M.A. (2002). El Niño's tropical climate and teleconnections as a blueprint for pre-Ice Age climates. Paleoceanography, 17, 1021, doi:1010.1029/2001PA000663.

Mortlock, R.A., Charles, C.D., Froelich, P.N., Zibello, M.A., Saltzmann, J., Hays, J.D., Burckle, L.H. (1991). Evidence for lower productivity in the Antarctic Ocean during last glaciation. Nature, 351, 220–223.

Mucci, A. (1987). Influence of temperature on the composition of magnesian calcite overgrowths precipitated from seawater. Geochim. Cosmochim. Ac., 51, 1977–1984.

Mudelsee, M., Raymo, M.E. (2005). Slow dynamics of the northern hemisphere glaciation. Paleoceanography, 20, PA4022, doi:4010.1029/2005PA001153.

Murray, J.W. (1991). Ecology and palaeoecology of benthic foraminifera. Longman, New York, 397 pp.

Murray, R.W., Knowlton, C., Leinen, M., Mix, A.C., Polsky, C.H. (2000). Export production and carbonate dissolution in the central equatorial Pacific Ocean over the past 1 Myr. Paleoceanography, 15, 570–592, doi:10.1029/1999PA000457.

Naafs, B.D.A., Stein, R., Hefter, J., Khélifi, N., De Schepper, S., Haug, G.H. (2010). Late Pliocene changes in the North Atlantic current. Earth Planet. Sci. Lett., 298, 434–442.

Naafs, B.D.A., Hefter, J., Acton, G., Haug, G.H., Martínez-Garcia, A., Pancost, R., Stein, R. (2012). Strengthening of North American dust sources during the late Pliocene (2.7 Ma). Earth Planet. Sci. Lett., 317, 8–19.

Naafs, B.D.A., Hefter, J. Stein, R. (2013). Millennial-scale ice rafting events and Hudson Strait Heinrich(-like) events during the late Pliocene and Pleistocene: A review. Quaternary Sci. Rev., 80, 1–28, doi:10.1016/j.quascirev.2013.08.014.

Naish, T.R. (1997). Constraints on the amplitude of late Pliocene eustatic sea-level fluctuations: new evidence from the New Zealand shallow-marine sediment record. Geology, 25, 1139–1142.

Naish, T.R., Wilson, G.S. (2009). Constraints on the amplitude of Mid-Pliocene (3.6–2.4 Ma) eustatic sea-level fluctuations from the New Zealand shallow-marine sediment record. Phil. Trans. R. Soc. A, 367, 169–187.

Nakai, S., Halliday, A.N., Rea, D.K. (1993). Provenance of dust in the Pacific Ocean. Earth Planet. Sci. Lett., 119, 143–157.

Nicholls, R.J., Hanson, S.E., Lowe, J.A., Warrick, R.A., Lu, X., Long, A.J. (2014). Sea-level scenarios for evaluating coastal impacts. WIREs Clim. Change, 5, 129–150.

Nürnberg, C.C., Bohrmann, G., Schlüter, M. (1997). Barium accumulation in the Atlantic sector of the Southern Ocean: Results from 190,000-year records. Paleoceanography, 12, 594–603, doi:10.1029/97PA01130.

Nürnberg, D., Bijma, J., Hemleben, C. (1996). Assessing the reliability of magnesium in foraminiferal calcite as a proxy for water mass temperatures. Geochim. Cosmochim. Ac., 60, 803–814.

Oomori, T., Kaneshima, H., Maezato, Y. (1987). Distribution coefficient of Mg^{2+} ions between calcite and solution at 10–50°C. Mar. Chem., 20, 327–336.

Oster, J.L., Ibarra, D.E., Winnick, M.J., Maher, K. (2015). Steering of westerly storms over western North America at the Last Glacial Maximum. Nat. Geosci., 8(3), 201–205.

Pados, T., Spielhagen, R.F. (2014). Species distribution and depth habitat of recent planktic foraminifera in Fram Strait, Arctic Ocean. Polar Res., 33, http://dx.doi.org/10.3402/polar.v3433.22483.

Pagani, M., Liu, Z., LaRiviere, J., Ravelo, A.C. (2010). High earth-system climate sensitivity determined from Pliocene carbon dioxide concentrations. Nat. Geosci., 3, 27–30.

Paillard, D., Labeyrie, L., Yiou, P. (1996). Macintosh program performs time-series analysis. Eos Trans. AGU, 77(39), 379, doi:10.1029/1096EO00259.

Pälike, H., et al. (2012). A Cenozoic record of the equatorial Pacific carbonate compensation depth. Nature, 488(7413), 609–614.

Park, R., Epstein, S. (1960). Carbon isotope fractionation during photosynthesis. Geochim. Cosmochim. Ac., 21, 110–126.

Pawlowski, J., Holzmann, M., Berney, C., Fahrni, J., Gooday, A.J., Cedhagen, T., Habura, A., Bowser, S.S. (2003). The evolution of early foraminifera. P. Natl. Acad. Sci., 100, 11494–11498.

Paytan, A., Lyle, M., Mix, A.C., Chase, Z. (2004). Climatically driven changes in oceanic processes throughout the equatorial Pacific. Paleoceanography, 19, PA4017, doi:10.1029/2004PA001024.

Pearson, P.N., Ditchfield, P.W., Singano, J., Harcourt-Brown, K.G., Nicholas, C.J., Olsson, R.K., Shackleton, N.J., Hall, M.A. (2001). Warm tropical sea surface temperatures in the Late Cretaceous and Eocene epochs. Natrue, 413, 481–470.

Pelet, R. (1987). A model of organic sedimentation on present-day continental margins. Geological Society London, Special Publications, 26, 167–180.

Pennington, J.T., Mahoney, K.L., Kuwahara, V.S., Kolber, D.D., Calienes, R., Chavez, F.P. (2006). Primary production in the eastern tropical Pacific: A review. Prog. Oceanogr., 69(2–4), 285–317.

Pflaumann, U., et al. (2003). Glacial North Atlantic: Sea-surface conditions reconstructed by GLAMAP 2000. Paleoceanography, 18, 1065, doi:1010.1029/2002PA000774.

Philander, S.G., Fedorov, A.V. (2003). Role of tropics in changing the response to Milankovich forcing some three million years ago. Paleoceanography, 18(2), 1045, doi:1010.1029/2002PA00083.

Pichat, S., Sims, K.W.W., François, R., McManus, J.F., Brown Leger, S., Albarède, F. (2004). Lower export production during glacial periods in the equatorial Pacific derived from $(^{231}Pa/^{230}Th)_{xs,0}$ measurements in deep-sea sediments. Paleoceanography, 19, PA4023, doi:10.1029/2003PA000994.

Pierre, C., Saliege, J.F., Urrutiaguer, M.J., Giraudeau, J. (2001). Stable isotope record of the last 500 k.y. at Site 1087 (Southern Cape Basin). In Proceedings of the Ocean Drilling Program, Sci. Results, 175, pp. 1–22, Ocean Drill. Program, College Station, Tex.

Pisias, N.G., Mayer, L.A., Mix, A.C. (1995). Paleoceanography of the eastern equatorial Pacific during the Neogene: Synthesis of Leg 138 drilling results. In Proceedings of the Ocean Drilling Program, Sci. Results, 138, pp. 5–21, Ocean Drill. Program, College Station, Tex.

Pisias, N.G., Mix, A.C. (1997). Spatial and temporal oceanographic variability of the eastern equatorial Pacific during the Late Pleistocene: Evidence from radiolaria microfossils. Paleoceanography, 12, 381–393, doi:10.1029/97PA00583.

Poore, H.R., Samworth, R., White, N.J., Jones, S.M., McCave, I.N. (2006). Neogene overflow of Northern Component Water at the Greenland-Scotland Ridge. Geochem. Geophys. Geosyst., 7, Q06010, doi:10.1029/2005GC001085.

Pritchard, H.D., Ligtenberg, S.R., Fricker, H.A., Vaughan, D.G., van den Broeke, M.R., Padman, L. (2012). Antarctic ice-sheet loss driven by basal melting of ice shelves. Nature, 484, 502–505.

Prueher, L.M., Rea, D.K. (1998). Rapid onset of glacial conditions in the subarctic North Pacific region at 2.67 Ma: Clues to causality. Geology, 26, 1027–1030.

Pusz, A.E., Thunell, R.C., Miller, K.G. (2011). Deep water temperature, carbonate ion, and ice volume changes across the Eocene-Oligocene climate transition. Paleoceanography, 26, PA2205, doi:10.1029/2010PA001950.

Rahmstorf, S. (1997). Risk of sea-change in the Atlantic. Nature, 388, 825–826.

Rathmann, S., Kuhnert, H. (2008). Carbonate ion effect on Mg/Ca, Sr/Ca and stable isotopes on the benthic foraminifera *Oridorsalis umbonatus* off Namibia. Mar. Micropaleontol., 66, 120–133.

Rausch, S., Böhm, F., Bach, W., Klügel, A., Eisenhauer, A. (2013). Calcium carbonate veins in ocean crust record a threefold increase of seawater Mg/Ca in the past 30 million years. Earth Planet. Sci. Lett., 362, 215–224.

Ravelo, A.C., Fairbanks, R.G. (1992). Oxygen isotopic composition of multiple species of planktonic foraminifera: Recorders of the modern photic zone temperature gradient. Paleoceanography, 7, 815–831, doi:10.1029/92PA02092.

Ravelo, A.C., Fairbanks, R.G. (1995). Carbon isotopic fractionation in multiple species of planktonic-foraminifera from core-tops in the tropical Atlantic. J. Foramin. Res., 25, 53–74.

Ravelo, A.C., Andreasen, D.H. (1999). Using planktonic foraminifera as monitors of the tropical surface ocean. In Reconstructing ocean history - a window into the future, edited by Abrantes, F., Mix, A., pp. 217–244, Plenum Press, New York.

Ravelo, A.C., Andreasen, D.H., Lyle, M., Lyle, A.O., Wara, M.W. (2004). Regional climate shifts caused by gradual global cooling in the Pliocene epoch. Nature, 429, 263–267.

Ravelo, A.C., Hillaire-Marcel, C. (2007). The use of oxygen and carbon isotopes of foraminifera in paleoceanography. In Proxies in late Cenozoic paleoceanography, edited by Hillaire-Marcel, C., De Vernal, A., pp. 735–764, Elsevier, Amsterdam.

Ravelo, A.C., Lawrence, K.T., Fedorov, A.V., Ford, H.L. (2014). Comment on "A 12-million-year temperature history of the tropical Pacific Ocean". Science, 436, 1467, doi:10.1126/science.1257618.

Raymo, M.E., Ruddiman, W.F., Froelich, P.N. (1988). Influence of late Cenozoic mountian buidling on ocean geochemical cycles. Geology, 16, 649–653.

Raymo, M.E., Ruddiman, W.F., Backman, J., Clement, B.M., Martinson, D.G. (1989). Late Pliocene variation in Northern Hemisphere ice sheets and North Atlantic deep water circulation. Paleoceanography, 4, 413–446.

Raymo, M.E., Hodell, D., Jansen, E. (1992). Response of deep ocean circulation to initiation of Northern Hemisphere glaciation (3–2 Ma). Paleoceanography, 7, 645–672.

Raymo, M.E., Ruddiman, W.F. (1992). Tectonic forcing of late Cenozoic climate. Nature, 359, 117–122.

Raymo, M.E. (1994). The initiation of Northern Hemisphere Glaciation. Annu. Rev. Earth Pl. Sc., 22, 353–383.

Raymo, M.E., Grant, B., Horowitz, M., Rau, G.H. (1996). Mid-Pliocene warmth: stronger greenhouse and stronger conveyor. Mar. Micropaleontol., 27, 313–326.

Regenberg, M., Nürnberg, D., Schönfeld, J., Reichart, G.-J. (2007). Early diagenetic overprint in Caribbean sediment cores and its effect on the geochemical composition of planktonic foraminifera. Biogeosciences, 4, 957–973.

Regenberg, M., Regenberg, A., Garbe-Schönberg, D., Lea, D.W. (2014). Global dissolution effects on planktonic foraminiferal Mg/Ca ratios controlled by the calcite-saturation state of bottom waters. Paleoceanography, 29, doi:10.1002/2013PA002492.

Reverdin, G., Niiler, P.P., Valdimarsson, H. (2003). North Atlantic Ocean surface currents. J. Geophys. Res., 108, doi:3010.1029/2001JC001020.

Reynolds, L., Thunell, R.C. (1985). Seasonal succession of planktonic foraminifera in the subpolar North Pacific. J. Foraminiferal Res., 15, 282–301.

Rind, D. (1998). Latitudinal temperature gradients and climate change. J. Geophys. Res., 103, 5943–5971.

Rippert, N., Nürnberg, D., Raddatz, J., Maier, E., Hathorne, E., Bijma, J., Tiedemann, R. (2016). Constraining foraminiferal calcification depths in the western Pacific warm pool. Mar. Micropaleontol., 128, 14–27.

Robinson, M.M., Dowsett, H.J., Chandler, M.A. (2008). Pliocene role in assessing future climate impacts. Eos, Transactions American Geophysical Union, 89, 501–502.

Rohling, E.J., Cooke, S. (1999). Stable oxygen and carbon isotope ratios in foraminiferal carbonate. In Modern foraminifera, edited by Sen Gupta, B.K., pp. 239–258, Kluwer Academic, Dordrecht, Boston.

Rohling, E.J., Grant, K., Hemleben, C., Siddall, M., Hoogakker, B.A.A., Bolshaw, M., Kucera, M. (2007). High rates of sea-level rise during the last interglacial period. Nat. Geosci., 1, 38–42.

Rohling, E.J., Grant, K., Bolshaw, M., Roberts, A.P., Siddall, M., Hemleben, C., Kucera, M. (2009). Antarctic temperature and global sea level closely coupled over the past five glacial cycles. Nat. Geosci., 2, 500–504.

Rohling, E.J., Foster, G.L., Grant, K.M., Marino, G., Roberts, A.P., Tamisiea, M.E., Williams, F. (2014). Sea-level and deep-sea-temperature variability over the past 5.3 million years. Nature, 508, 477–482.

Ruddiman, W.F. (1977a). Late Quaternary deposition of ice-rafted sand in the subpolar North Atlantic (lat 40° to 65° N). Geol. Soc. Am. Bull., 88, 1813–1827.

Ruddiman, W.F. (1977b). North Atlantic icerafting: A major change at 75,000 years before the present. Science, 196, 1208–1211.

Russell, A.D., Hönisch, B., Spero, H.J., Lea, D.W. (2004). Effects of seawater carbonate ion concentration and temperature on shell U, Mg, and Sr in cultured planktonic foraminifera. Geochim. Cosmochim. Ac., 68, 4347–4361.

Sadekov, A., Eggins, S.M., De Deckker, P., Kroon, D. (2008). Uncertainties in seawater thermometry deriving from intratest and intertest Mg/Ca variability in *Globigerinoides ruber*. Paleoceanography, 23, PA1215, doi:1210.1029/2007PA001452.

Saraswat, R. (2015). Non-destructive foraminiferal paleoclimatic proxies: A brief insight. Proc. Indian Natl. Sci. Acad., 81(2), 381–395.

Sarmiento, J.L., et al. (2004). Response of ocean ecosystems to climate warming. Global Biogeochem. Cycles, 18, GB3003, doi:10.1029/2003GB002134.

Sarnthein, M., Fenner, J. (1988). Global wind-induced change of deep-sea sediment budgets, new ocean production and CO_2 reservoirs ca. 3.3–2.35 Ma BP. Philos. Trans. R. Soc. London A, 318, 487–504.

Sarnthein, M.K., Winn, K., Duplessy, J.C., Fontugne, M.R. (1988). Global variations of surface ocean productivity in low and mid-latitudes: Influence of CO_2. Paleoceanography, 3, 361–399, doi:10.1029/PA003i003p00361.

Savin, S.M., Douglas, R.G. (1973). Stable isotope and trace element geochemistry of recent planktonic foraminifera from the South Pacific. Geol. Soc. Am. Bull., 84, 2337–2342.

Saynal, A., Hemming, N.G., Hanson, G.N., Broecker, W.S. (1995). Evidence for a higher pH in the glacial ocean from boron isotopes in foraminifera. Nature, 373, 234–236.

Schiebel, R., Hemleben, C. (2000). Interannual variability of planktic foraminiferal populations and test flux in the eastern North Atlantic Ocean (JGOFS). Deep Sea Res., 47, 1809–1852.

Schiebel, R. (2002). Planktic foraminiferal sedimentation and the marine calcite budget. Global Biogeochemical Cycles, 16, doi:10.1029/2001GB001459.

Schiebel, R., Schmuker, B., Alves, M., Hemleben, C. (2002). Tracking the recent and late Pleistocene Azores front by the distribution of planktic foraminifers. J. Marine Syst., 37, 213–227.

Schiebel, R., Hemleben, C. (2005). Modern planktic foraminifera. Paläontologische Zeitschrift, 79, 135–148.

Schlitzer, R. (2004). Export production in the equatorial and North Pacific derived from dissolved oxygen, nutrient and carbon data. J. Oceanogr., 60, 53–62.

Schmidt, G.A., Bigg, G.R., Rohling, E.J. (1999). Global Seawater Oxygen-18 Database - v1.21. http://data.giss.nasa.gov/o18data/.

Schneider, B., Schmittner, A. (2006). Simulating the impact of the Panamanian seaway closure on ocean circulation, marine productivity and nutrient cycling. Earth Planet. Sci. Lett., 246, 367–380.

Schneider, T., Bischoff, T., Haug, G.H. (2014). Migrations and dynamics of the intertropical convergence zone. Nature, 513, 45–53.

Seki, O., Foster, G.L., Schmidt, D.N., Mackensen, A., Kawamura, K., Pancost, R.D. (2010). Alkenone and boron-based Pliocene pCO_2 records. Earth Planet. Sci. Lett., 292, 201–211.

Sen Gupta, B.K. (1999a). Modern Foraminifera. Kluwer Academic Publishers, Dordrecht, Boston, 371 pp.

Sen Gupta, B.K. (1999b). Systematics of modern foraminifera. In Modern foraminifera, edited by Sen Gupta, B.K., pp. 7–36, Kluwer Academic Publishers, Dordrecht, Boston.

Sepulchre, P., Arsouze, T., Donnadieu, Y., Dutay, J.-C., Jaramillo, C., Le Bras, J., Martin, E., Montes C., Waite, A.J. (2014). Consequences of shoaling of the

Central American Seaway determined from modeling Nd isotopes. Paleoceanography, 29, 176–189, doi:10.1002/2013PA002501.

Sexton, P.F., Wilson, P.A., Pearson, P.N. (2006). Microstructural and geochemical perspectives on planktic foraminiferal preservation: "Glassy" versus "Frosty". Geochem. Geophys. Geosyst., 7, Q12P19, doi:10.1029/2006GC001291.

Sexton, P.F., Barker, S. (2012). Onset of "Pacific-style" deep-sea sedimentary carbonate cycles at the mid-Pleistocene transition. Earth Planet. Sci. Lett., 321–322, 81–94.

Shackleton, N.J. (1974). Attainment of isotopic equilibrium between ocean water and the benthonic foraminifera genus *Uvigerina*: Isotopic changes in the ocean during the last glacial. Colloques Internationaux du Centre National de la Recherche Scientifique, 219, 203–210.

Shackleton, N.J., Hall, M.A. (1984). Oxygen and carbon isotope stratigraphy of Deep Sea Drilling Project Hole 552A: Plio-Pleistocene Glacial History. In Proceedings of the Deep Sea Drilling Project, Initial Rep., 81, pp. 599–609, Deep Sea Drill. Proj., Washington, D.C.

Shackleton, N.J., Backman, J., Zimmerman, H., Kent, D.V., Hall, M., Roberts, D., Schnitker, D., Baldauf, J., Desprairies, A., Homrighausen, R. (1984a). Oxygen isotope calibration of the onset of ice-rafting and history of glaciation in the North Atlantic region. Nature, 307, 620–623.

Shackleton, N.J., Hall, M.A., Boersma, A. (1984b). Oxygen and carbon isotope data from Leg 74 foraminifers. In Proceedings of the Deep Sea Drilling Project, Initial Rep., 74, pp. 599–612, Deep Sea Drill. Proj., Washington, D.C.

Shackleton, N.J., Hall, M.A., Pate, D. (1995). Pliocene stable isotope stratigraphy of Site 846. In Proceedings of the Ocean Drilling Program, Sci. Results, 138, pp. 337–355, Ocean Drill. Program, College Station, Tex.

Siddall, M., Rohling, E.J., Almogi-Labin, A., Hemleben, C., Meischner, D., Schmelzer, I., Smeed, D.A. (2003). Sea-level fluctuations during the last glacial cycle. Nature, 423, 853–858.

Siddall, M., Hönisch, B., Waelbroeck, C., Huybers, P. (2010). Changes in deep Pacific temperature during the mid-Pleistocene transition and Quaternary. Quaternary Sci. Rev., 29, 170–181.

Sigman, D.M., Jaccard, S.L., Haug, G.H. (2004). Polar ocean stratification in a cold climate. Nature, 428, 59–63.

Snider, L.J., Burnett, B.R., Hessler, R.R. (1984). The composition and distribution of meiofauna and nanobiota in a central North Pacific deep-sea area. Deep Sea Res., 31, 1225–1249.

Sosdian, S., Rosenthal, Y. (2009). Deep-sea temperature and ice volume changes across the Pliocene-Pleistocene climate transitions. Science, 325, 306–310.

Spero, H.J., Parker, S.L. (1985). Photosynthesis in the symbiotic planktonic foraminifer *Orbulina universa* and its potential contribution to oceanic primary productivity. J. Foramin. Res., 15, 273–281.

Spero, H.J., Williams, D.F. (1988). Extracting environmental information from planktonic foraminiferal $\delta^{13}C$ data. Nature, 335, 717–719.

Spero, H.J., Lea, D.W. (1993). Intraspecific stable isotope variability in the planktic foraminifera *Globigerinoides sacculifer*: Results from laboratory experiments. Mar. Micropaleontol., 22, 221–234.

Spero, H.J., Lea, D.W. (1996). Experimental determination of stable isotope variability in *Globigerina bulloides:* implications for paleoceanographic reconstructions. Mar. Micropaleontol., 28, 231–246.

Spero, H.J., Bijma, J., Lea, D.W., Bemis, B.E. (1997). Effect of seawater carbonate concentration on foraminiferal carbon and oxygen isotopes. Nature, 390, 497–500.

Spero, H.J., Mielke, K.M., Kalve, E.M., Lea, D.W., Pak, D.K. (2003). Multispecies approach to reconstructing eastern equatorial Pacific thermocline hydrography during the past 360 kyr. Paleoceanography, 18(1), 1022, doi:10.1029/2002PA000814.

Spicer, R.A., Harris, N.B.W., Widdowson, M., Herman, A.B., Guo, S., Valdes, P.J., Wolfe, J.A., Kelley, S.P. (2003). Constant elevation of southern Tibet over the past 15 million years. Nature, 421, 622–624.

Srokosz, M.A., Bryden, H.L. (2015). Observing the Atlantic Meridional Overturning Circulation yields a decade of inevitable surprises. Science, 348, doi:10.1126/ science.1255575.

Stancin, A., Gleason, J., Rea, D., Owen, R., Moorejr, T., Blum, J., Hovan, S. (2006). Radiogenic isotopic mapping of late Cenozoic eolian and hemipelagic sediment distribution in the east-central Pacific. Earth Planet. Sci. Lett., 248(3–4), 840–850.

Stein, R., Hefter, J., Grützner, J., Voelker, A., Naafs, B.D.A. (2009). Variability of surface water characteristics and Heinrich-like events in the Pleistocene midlatitude North Atlantic Ocean: Biomarker and XRD records from IODP Site U1313 (MIS 16–9). Paleoceanography, 24, PA2203, doi:2210.1029/2008PA001639.

Steinhardt, J., Cléroux, C., de Nooijer, L.J., Brummer, G.J., Zahn, R., Ganssen, G., Reichart, G.J. (2015). Reconciling single-chamber Mg/Ca with whole-shell $\delta^{18}O$ in surface to deep-dwelling planktonic foraminifera from the Mozambique Channel. Biogeosciences, 12, 2411–2429.

Steinke, S., Chiu, H.Y., Yu, P.S., Shen, C.C., Löwemark, L., Mii, H.S., Chen, M.T. (2005). Mg/Ca ratios of two *Globigerinoides ruber* (white) morphotypes: Implications for reconstructing past tropical/subtropical surface water conditions. Geochem. Geophys. Geosyst., 6, Q11005, doi:10.1029/2005GC000926.

Steph, S., Tiedemann, R., Groeneveld, J., Sturm, A., Nürnberg, D. (2006). Pliocene changes in tropical east Pacific upper ocean stratification: response to tropical gateways? In Proceedings of the Ocean Drilling Program, Sci. Results, 202, doi:10.2973/ odp.proc.sr.202.211.2006, Ocean Drill. Program, College Station, Tex.

Steph, S., Tiedemann, R., Prange, M., Groeneveld, J., Schulz, M., Timmermann, A., Nürnberg, D., Rühlemann, C., Saukel, C., Haug, G.H. (2010). Early Pliocene increase in thermohaline overturning: A precondition for the development of the modern equatorial Pacific cold tongue. Paleoceanography, 25, PA2202, doi:10.1029/2008PA001645.

Stokes, W.L. (1955). Another look at the ice age. Science, 122, 815–821.

Sun, X., Li, X., Chen, X. (2000). The vegetation and climate at the last glaciation on the emerged continental shelf of the South China Sea. Palaeo3, 160, 301–316.

Takahashi, T., et al. (2002). Global air-sea CO_2 flux based on climatological surface ocean pCO_2, and seasonal biological and temperature effects. Deep Sea Res. II, 49, 1601–1622.

Takahashi, T., et al. (2009). Climatological mean and decadal change in surface ocean pCO_2, and net sea-air CO_2 flux over the global oceans. Deep Sea Res., II, 56(8–10), 554–577.

Tedesco, K., Thunell, R. (2003). Seasonal and interannual variations in planktonic foraminiferal flux and assemblage composition in the Cariaco Basin. J. Foramin. Res. 33, 192–210.

Thompson, P.R., Bé, A.W.H., Duplessy, J.C., Shackleton, N.J. (1979). Disappearance of pink-pigmented *Globigerinoides ruber* at 120.000 yr BP in the Indian and Pacific Oceans. Nature, 280, 554–558.

Toggweiler, J.R., Sarmiento, J.L. (1985). Glacial to interglacial changes in atmospheric carbon dioxide: The role of ocean surface water in high latitudes. In The Carbon Cycle and Atmospheric CO: Natural Variations Archean to Present, Geophys. Monogr. Ser., 32, pp. 163–184, AGU, Washington, D.C.

Toggweiler, J.R., Dixon, K., Broecker, W.S. (1991). The Peru upwelling and the ventilation of the south Pacific thermocline. J. Geophys. Res., 96, 20467–20497, doi:10.1029/91JC02063.

Tolderlund, D.S., Bé, A.W.H. (1971). Seasonal distribution of planktonic foraminifera in the western Northern Atlantic. Micropaleontology, 17, 297–329.

Tsuchiya, M., Lukas, R., Fine, A.R., Firing, E., Lindstrom, E.J. (1989). Source waters of the Pacific equatorial undercurrent. Prog. Oceanogr., 23, 101–147.

Urey, H.C. (1947). The thermodynamic properties of isotopic substances. J. Chem. Soc., 562–581.

van de Flierdt, T., Frank, M., Lee, D.-C., Halliday, A.N., Reynolds, B.C., Hein, J.R. (2004). New constraints on the sources and behavior of neodymium and hafnium in seawater from Pacific Ocean ferromanganese crusts. Geochim. Cosmochim. Ac., 68(19), 3827–3843.

van der Zwaan, G.J. (1999). Benthic foraminifers: proxies or problems? A review of paleocological concepts. Earth-Sci. Rev., 46, 216–236.

Vaughan, D.G., et al. (2013). Observations: Cryosphere. In Climate Change 2013: The Physical Science Basis. Contribution of Working Group I to the Fifth Assessment Report of the Intergovernmental Panel on Climate Change, edited by Stocker, T.F., Qin, D., Plattner, G.-K., Tignor, M., Allen, S.K., Boschung, J., Nauels, A., Xia, Y., Bex, V., Midgley, P.M., pp. 317–382, Cambridge University Press, Cambridge, United Kingdom, New York, USA.

Vickermann, K. (1992). The diversity and ecological significance of protozoa. Biodivers. Conserv., 1, 334–341.

Voelker, A.H.L., Rodrigues, T., Billups, K., Oppo, D., McManus, J., Stein, R., Hefter, J., Grimalt, J.O. (2010). Variations in mid-latitude North Atlantic surface water properties during the mid-Brunhes (MIS 9–14) and their implications for the thermohaline circulation. Climate of the Past, 6, 531–552.

Voigt, S., Hilbrecht, H. (1997). Late Cretaceous carbon isotope stratigraphy in Europe: Correlation and relations with sea level and sediment stability. Palaeo3, 134, 39–59.

Waddell, L.M., Hendy, I.L., Moore, T.C., Lyle, M.W. (2009). Ventilation of the abyssal Southern Ocean during the late Neogene: A new perspective from the subantarctic Pacific. Paleoceanography, 24, PA3206, doi:10.1029/2008PA001661.

Waelbroeck, C., Labeyrie, L., Michel, E., Duplessy, J.C., McManus, J., Lambeck, K., Balbon, E., Labracherie, M. (2002). Sea-level and deep water temperature changes derived from benthic foraminifera isotopic records. Quaternary Sci. Rev., 21, 295–305.

Wang, B., Wu, R., Lukas, R. (2000). Annual adjustment of the thermocline in the tropical Pacific Ocean. J. Climate, 13, 596–616.

Wang, L. (2000). Isotopic signals in two morphotypes of *Globigerinoides ruber* (white) from the South China Sea: Implications for monsoon climate change during the last glacial cycle. Palaeo3, 161, 381–394.

Wang, P., Tian, J., Lourens, L.J. (2010). Obscuring of long eccentricity cyclicity in Pleistocene oceanic carbon isotope records. Earth Planet. Sci. Lett., 290, 319–330.

Wara, M.W., Ravelo, A.C., Delaney, M.L. (2005). Permanent El Niño-like conditions during the Pliocene warm period. Science, 309, 758–761.

Watson, A.J., Garabato, A.C.N. (2006). The role of Southern Ocean mixing and upwelling in glacial-interglacial atmospheric CO_2 change. Tellus, Ser. B, 58, 73–75.

Wendler, I., Huber, B.T., MacLeod, K.G., Wendler, J.E. (2013). Stable oxygen and carbon isotope systematics of exquisitely preserved Turonian foraminifera from Tanzania - Understanding isotopic signatures in fossils. Mar. Micropaleontol., 102, 1–33.

Wilke, I., Meggers, H., Bickert, T. (2009). Depth habitats and seasonal distributions of recent planktic foraminifers in the Canary Islands region (29°N) based on oxygen isotopes. Deep Sea Res. I, 56, 89–106.

Willeit, M., Ganopolski, A., Calov, R., Robinson, A., Maslin, M. (2015). The role of CO_2 decline for the onset of Northern Hemisphere glaciation. Quaternary Sci. Rev., 119, 22–34.

Winckler, G., Anderson, R.F., Fleisher, M.Q., McGee, D., Mahowald, N. (2008). Covariant glacial-interglacial dust fluxes in the equatorial Pacific and Antarctica. Science, 320, 93–96.

Wu, G., Herguera, J.C., Berger, W.H. (1990). Differential dissolution: Modification of late Pleistocene oxygen isotope records in the western equatorial Pacific. Paleoceanography, 5, 581–594, doi:10.1029/PA005i004p00581.

Wyrtki, K. (1966). Oceanography of the eastern equatorial Pacific Ocean. Oceanogr. Mar. Biol., Annual Review, 4, 33–68.

Wyrtki, K. (1981). An estimate of equatorial upwelling in the Pacific. J. Phys. Oceanogr., 11, 1205–1214.

Zachos, J.C., Stott, L.D., Lohmann, K.C. (1994). Evolution of early Cenozoic marine temperatures. Paleoceanography, 9, 353–387.

Zachos, J.C., Pagani, M., Sloan, L., Thomas, E., Billups, K. (2001). Trends, rhythms, and aberrations in global climate 65 Ma to present. Science, 292, 686–693.

Zachos, J.C., Dickens, G.R., Zeebe, R.E. (2008). An early Cenozoic perspective on greenhouse warming and carbon-cycle dynamics. Nature, 451, 279–283.

Zahn, R., Winn, K., Sarnthein, M. (1986). Benthic foraminiferal $\delta^{13}C$ and accumulation rates of organic carbon: *Uvigerina peregrina* group and *Cibicidoides wuellerstorfi*. Paleoceanography, 1, 27–42, doi:10.1029/PA001i001p00027.

Zhang, Y.G., Pagani, M., Liu, Z. (2014). A 12-million-year temperature history of the tropical Pacific Ocean. Science, 344, 84–87.

Ziegler, C.L., Murray, R.W., Plank, T., Hemming, S.R. (2008). Sources of Fe to the equatorial Pacific Ocean from the Holocene to Miocene. Earth Planet. Sci. Lett., 270(3–4), 258–270.

APPENDIX A.1

SUPPORTING INFORMATION FOR CHAPTER 4

Supporting Chapter 4 of this thesis, which reports on glacial-interglacial primary productivity changes in the Eastern Equatorial Pacific upwelling system during the Plio-Pleistocene, this appendix contains nine figures, two tables and additional references.

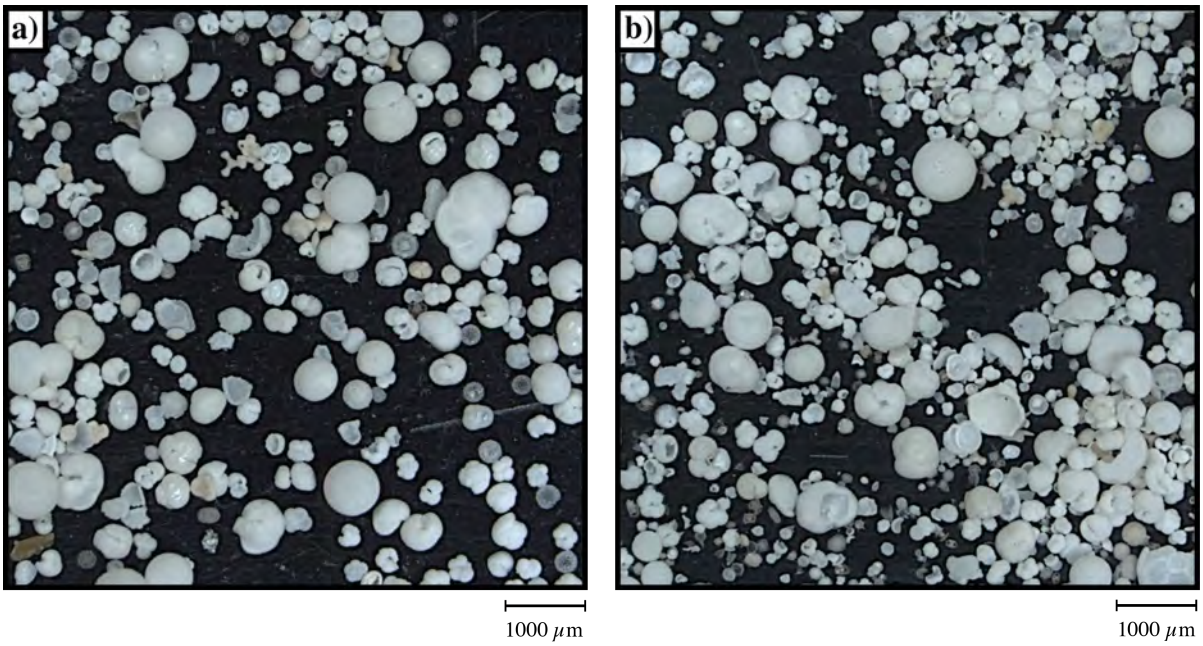

Figure A.1.1. Photographs of the **(a)** interglacial and **(b)** glacial >63 μm dried sediment fraction (sand fraction) from Site 849, indicating that the vast majority of this size fraction consists of planktic foraminifera and radiolarians (together with rare benthic foraminifera). Thus it appears reasonable to assume that variations in the sand fraction predominantly reflect changes in the relative abundance of zooplankton (planktic foraminifera and radiolarians).

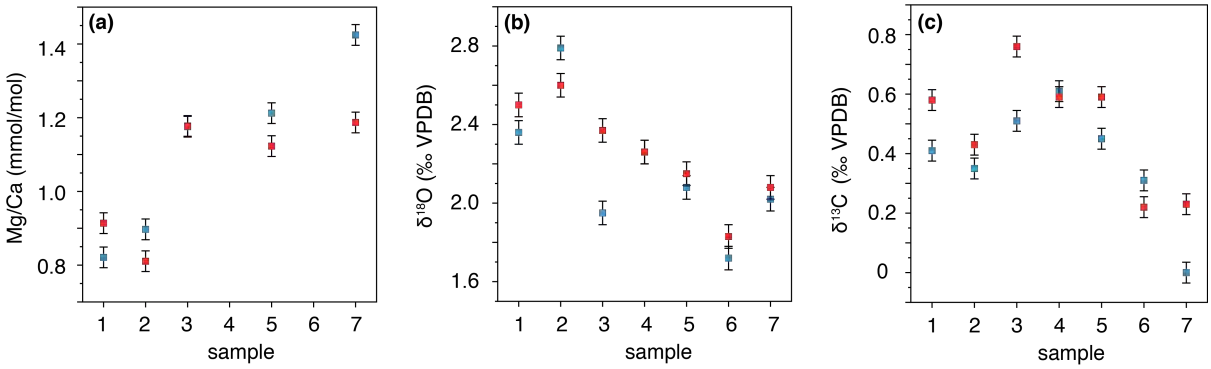

Figure A.1.2. Relationship of the coiling direction of *Globorotalia crassaformis* specimens (blue: sinistral, red: dextral) and **(a)** Mg/Ca, **(b)** $\delta^{18}O$, and **(c)** $\delta^{13}C$ for samples 849D-6H-6-53 cm to 849D-6H-6-55 cm (1), 849D-6H-6-68 cm to 849D-6H-6-70 cm (2), 849C-7H-1-80 cm to 849C-7H-1-82 cm (3), 849C-7H-1-91 cm to 849C-7H-1-93 cm (4), 849C-7H-2-15 cm to 849C-7H-2-17 cm (5), 849D-7H-1-31 cm to 849D-7H-1-33 cm (6), and 849D-7H-1-42 cm to 849D-7H-1-44 cm (7). Comparison between $\delta^{18}O$, $\delta^{13}C$ and Mg/Ca measurements of sinistral and dextral coiling forms within the same samples indicates that there is no consistent offset in all three parameters between specimens with different coiling directions. This allows to combine the results form sinistrally and dextrally coiling forms without applying an intertaxon adjustment factor.

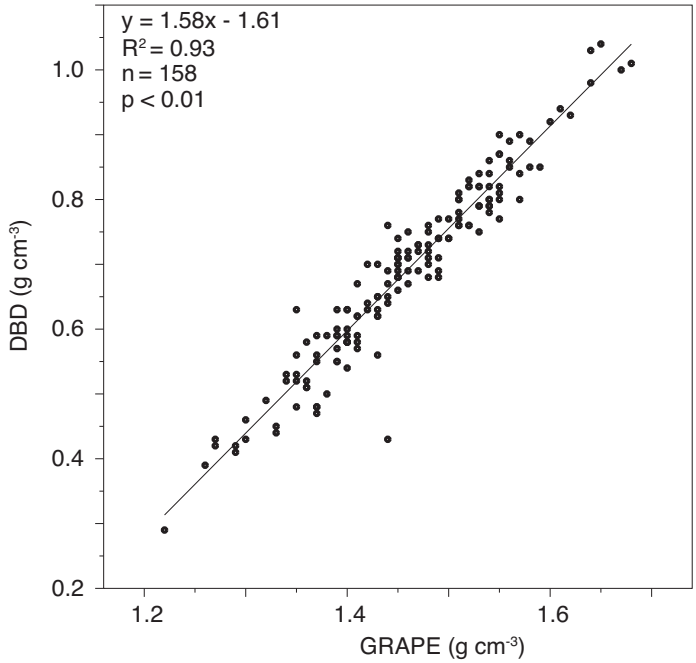

Figure A.1.3. Cross plot between DBD (Hovan, 2013) and GRAPE (IODP JANUS database [Mayer et al., 1992]) for 158 samples (n = 158) of the uppermost 356 m (~10 Myr) of Hole 849B (849B-1H to 849B-37X). The relationship between DBD and GRAPE (DBD [g cm^{-3}] = 1.58 x GRAPE [g cm^{-3}] - 1.61) has been applied to calculate out of high-resolution GRAPE-density shipboard measurements a high-resolution DBD dataset for the investigated time interval (~2.65–2.4 Ma) at Site 849. The calculated relationship is statistically significant at the 95% confidence level (R^2 = 0.93, p <0.01).

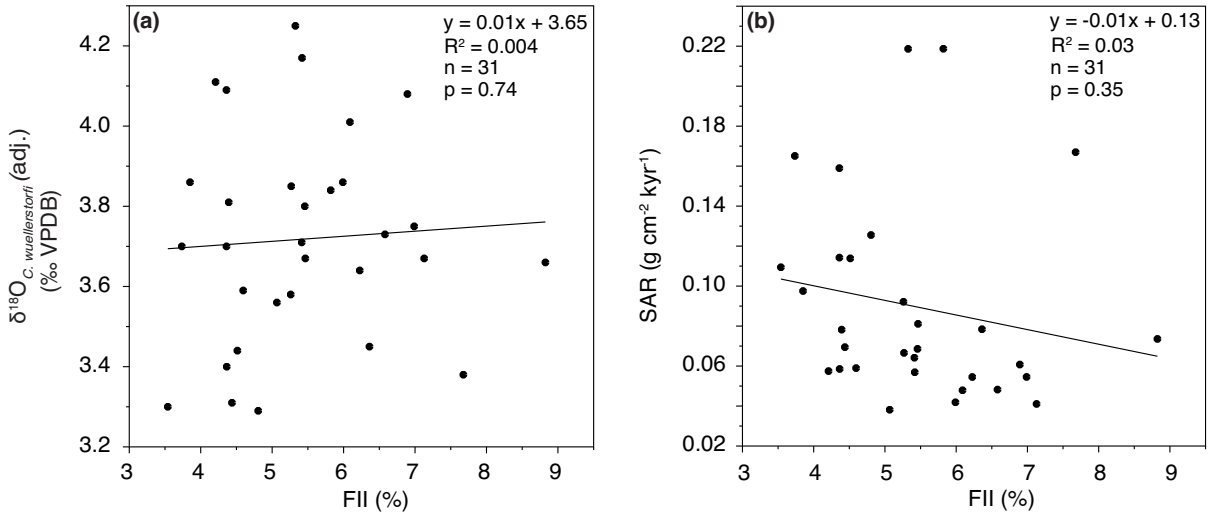

Figure A.1.4. (**a)** Cross plot between $\delta^{18}O_b$ (‰ VPDB) and FFI (%) from Site 849 (n = 31). A lack of a statistically significant correlation at the 95% confidence level between both datasets (R^2 = 0.004, p >0.05) confirms that fragmentation is unrelated to G-IG cycles. (**b)** Cross plot between SAR (g cm^{-2} kyr^{-1}) and FFI (%) from Site 849 (n =31). A lack of a statistically significant correlation at the 95% confidence level between both datasets (R^2 = 0.03, p >0.05) confirms that SARs are not an artifact of carbonate dissolution.

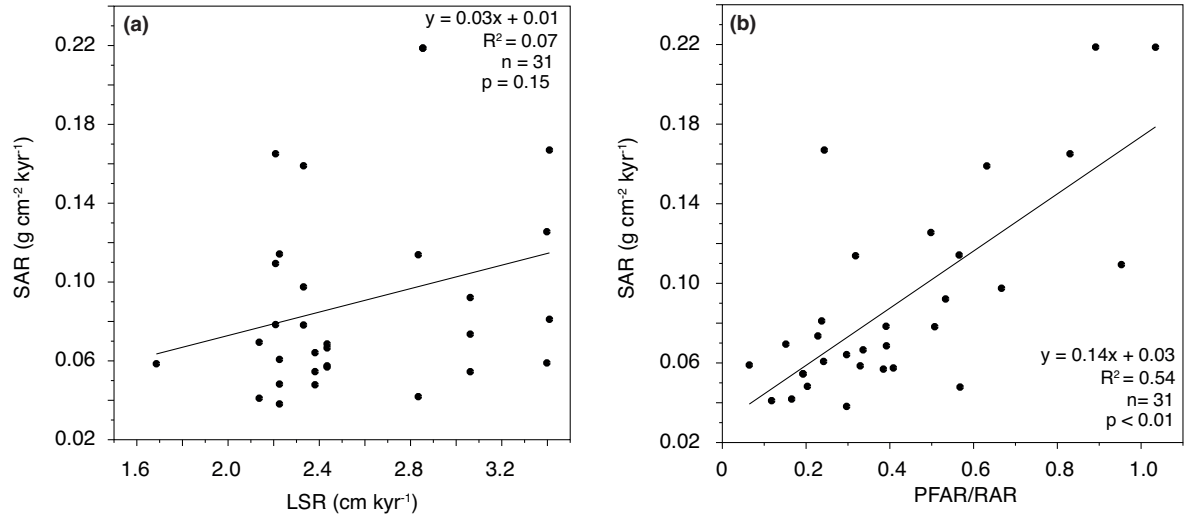

Figure A.1.5. (**a)** Cross plot between SAR and LSR from Site 849. A lack of statistically significant correlation at the 95% confidence level (R^2 = 0.07, p >0.05) indicates that increasing SARs (increasing export productivity) do not result in elevated sedimentation rates. Thus, there must be a counterbalancing factor to smooth out the expected sedimentation-rate increase. (**b)** Cross plot between SAR and PFAR/RAR ratio from Site 849. Statistically significant covariance at the 95% confidence level (R^2 = 0.54, p <0.01) between both parameters gives evidence that there is a stronger increase in the number of planktic foraminifera compared to the number of radiolarians during times of elevated SARs (increasing productivity). Decreases (increases) in the fraction of poorly packed spinose radiolarians during glacials (interglacials) act to cancel out productivity-related changes in sedimentation rates.

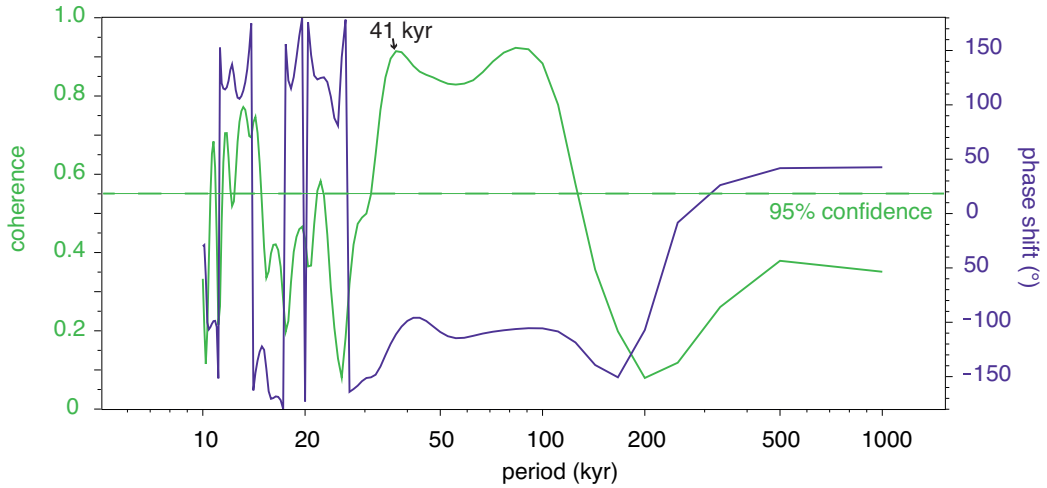

Figure A.1.6. Blackman-Tukey cross-spectral analysis for the identification of phase shifts at the 95% confidence level. Coherence (green) and phase (purple) relationship between productivity records from Site 849 (SAR; this study) and 846 (C_{37} alkenone accumulation rates; Lawrence et al. [2006]) for the time interval from ~2.65 to 2.4 Ma are plotted on log scales. The orbital 41 kyr period is marked. Negative values in this phase plot indicate that the productivity proxy record from Site 849 (SAR) lags the productivity proxy record from Site 846 (C_{37} alkenone accumulation rates [Lawrence et al., 2006]), i.e., by -95.2° (equal to -11 kyr) for the 41 kyr period. In combination with the observation that productivity at Site 849 lags global ice volume by ~9.5 kyr (Chapter 4), these findings are in agreement with observations from Lawrence et al. (2006), indicating that C_{37} alkenone accumulation rates oscillate nearly in phase with benthic $\delta^{18}O$ with a lead of ~2 to 3 kyr.

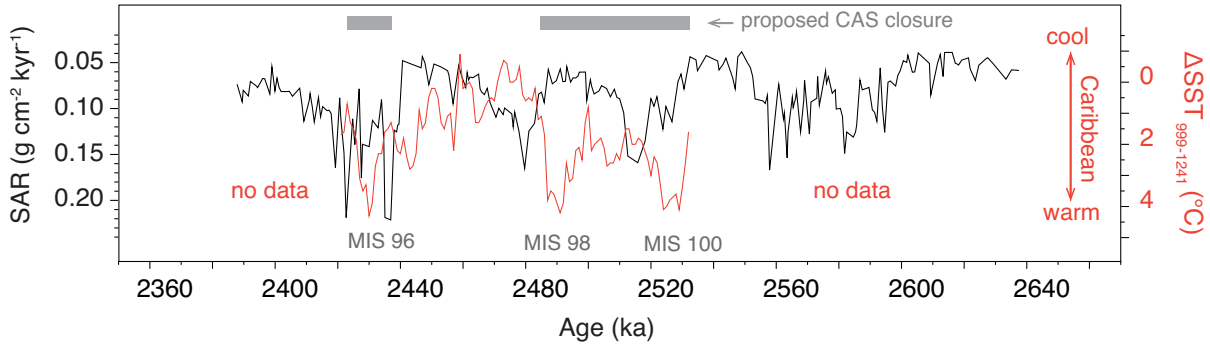

Figure A.1.7. Sand-accumulation rate (productivity) changes from Site 849 (black, this study) and sea-surface temperature (SST) differences between Site 999 (Caribbean Sea) and Site 1241 (EEP) for MIS 100, 98 and 96 (red [Groeneveld et al., 2014]). A warming in the Caribbean Sea (evidenced by increased SST gradients between Sites 999 and 1241) suggests, in combination with changes in relative salinity and water-column stratification at Sites 999 and 1241, a temporary glacioeustatic gateway closure from MIS 100 to 98 and toward the end of MIS 96 (grey bars [Groeneveld et al., 2014]). Assuming that the proposed CAS closure leads to an intensification of the EEP upwelling system (Schneider and Schmittner, 2006), this would result in increased export production from MIS 100 to 96, low productivity rates during MIS 97, and again enhanced productivity toward the end of MIS 96. However, this is not consistent with our SAR record from Site 849. Therefore, we suggest that the influence of upwelling intensification in response to temporary CAS closure at Site 849 plays only a minor role in regulating G-IG upwelling changes across the studied time interval.

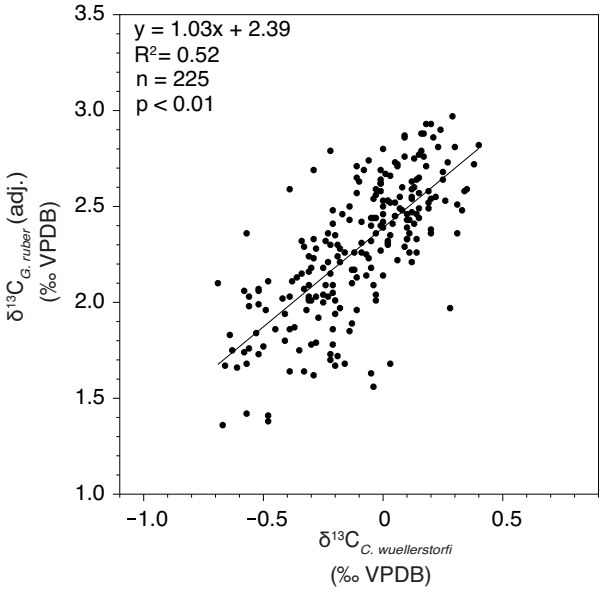

Figure A.1.8. $\delta^{13}C$ cross plot for the planktic foraminifera *G. ruber* ($\delta^{13}C$ values adjusted after Spero et al. [2003]) and the benthic foraminifera *C. wuellerstorfi* from Site 849. Statistical significant covariance at the 95% confidence level (R^2 = 0.52, p <0.01) between $\delta^{13}C$ of the planktic and the benthic species gives evidence that both are affected by the same initial water mass. The $\delta^{13}C$ values of the benthic species are shifted to ~2.39‰ lower values compared to the planktic $\delta^{13}C$ probably as a result of prevailing local primary productivity and the influence of a water mass with a higher degree of remineralization.

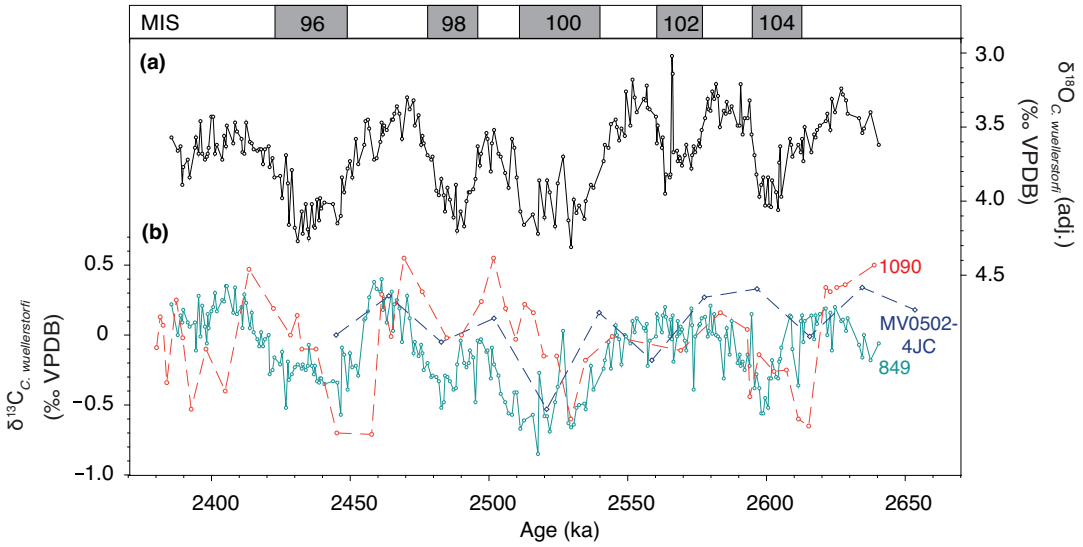

Figure A.1.9. Comparison of benthic $\delta^{13}C$ from ODP Site 849 (this study) to benthic $\delta^{13}C$ from South Pacific Site MV0502-4JC and South Atlantic ODP Site 1090 (re-tuned; see Table A.1.2) for the time interval from ~2.65 to 2.4 Ma. (**a)** $\delta^{18}O$ record of the benthic foraminifera *C. wuellerstorfi* from Site 849. (**b)** $\delta^{13}C$ record of the benthic foraminifera *C. wuellerstorfi* from Sites 849 (green), MV0502-4JC (blue [Waddell et al., 2009]) and 1090 (red [Hodell et al., 2003]). Site MV0502-4JC (50°20'S, 148°08'W, 4286 m) is located within the trajectory of AABW from its source area to the EEP, thus giving an idea of the initial carbon-isotope signature for upwelled waters in the EEP. Although the record from Site MV0502-4JC has a rather low resolution, it shows clearly that G-IG changes in $\delta^{13}C_b$ exhibit the same pattern as at Site 849 from MIS 100 onward, confirming that $\delta^{13}C_b$ values recorded at Site 849 bear a high-latitude signature. $\delta^{13}C_b$ values of Site MV0502-4JC are slightly elevated compared to those of Site 849, which reflects a closer proximity to the source area and therefore a lower

degree of deep-sea remineralization. Site 1090 is located in the South Atlantic (42°55'S, 8°54'E, 3702 m), not on the direct trajectory of AABW from the Southern Ocean to the EEP, however this site is accepted as the best endmember of Southern Ocean waters (Billups et al., 2002; Pusz et al., 2011). Displaying a higher resolution compared to Site MV0502-4JC and a complete $\delta^{13}C_b$ record throughout the studied succession, similar $\delta^{13}C_b$ variations at Site 1090 compared to Site 849 confirm that Site 849 records a high-latitude signal.

Table A.1.1. Age model tie-points used in this study for ODP Site 849 for the time interval from ~2.65 to 2.4 Ma (MIS G1 to 95). Depth (in meters) is on the composite scale (mcd) for combined drill holes.

Site 849	
Depth (mcd)	**Age (ka)**
68.96	2427.14
69.56	2449.91
70.22	2479.81
70.51	2492.50
70.95	2509.96
71.61	2540.82
72.19	2562.58
72.68	2575.74
73.24	2594.93
73.73	2613.61
74.16	2637.46

Table A.1.2. Age model tie-points used in this study for ODP Sites 846 and 1090 for the time interval from ~2.65 to 2.4 Ma (MIS G1 to 95). Depth (in meters) is on the composite scale (mcd) for combined drill holes.

Site 846	
Depth (mcd)	**Age (ka)**
91.06	2386.74
92.07	2406.04
92.77	2428.22
94.22	2449.93
95.05	2479.79
95.85	2495.08
96.36	2510.97
97.79	2537.24
98.78	2563.17
99.05	2567.65
100.61	2594.16
101.65	2612.30

Site 1090	
Depth (mcd)	**Age (ka)**
51.99	2396.06
52.30	2418.47
52.51	2428.89
52.74	2450.53
52.98	2475.56
53.13	2492.92
53.36	2506.61
53.62	2539.35
53.70	2558.35
53.78	2579.19
54.10	2598.08
54.66	2632.93

Table A.1.3. Proxy records from ODP Site 849, listed by increasing age. Depth (mcd): Meters composite depth was used to join samples from both cores 849C and 849D onto an idealized depth scale (Hagelberg et al., 1992). Age (ka): The age was calculated by tuning the benthic oxygen-isotope record together with the oxygen-isotope data from Mix et al. (1995) to the LR04 stack (Lisiecki and Raymo, 2005). FFI (%): The planktic foraminiferal fragmentation index was calculated after Le and Shackleton (1992). PFAR (planktic foraminiferal accumulation rate, number of specimens $cm^{-2}\,yr^{-1}$): PFARs were calculated according to Herguera and Berger (1991), where PF is the number of planktic foraminifera. RAR (radiolarian accumulation rate, number of specimens $cm^{-2}\,yr^{-1}$): RARs were calculated according to Herguera and Berger (1991), where R is the number of radiolarians.

Depth (mcd)	**Age (ka)**	**FFI (%)**	**PFAR (PF $cm^{-2}\,yr^{-1}$)**	**RAR (R $cm^{-2}\,yr^{-1}$)**
67.78	2387.85	8.83	19.99	87.58
68.12	2398.96	6.23	9.17	47.49
68.48	2410.83	5.26	18.30	34.32
68.83	2422.67	5.82	778.97	873.77
69.18	2435.06	5.33	249.28	240.97
69.33	2440.68	6.09	15.74	27.73
69.65	2452.88	6.99	39.37	204.71
69.78	2459.50	5.41	6.80	22.92
69.91	2465.43	6.36	263.83	674.72
70.02	2470.50	3.54	403.81	423.73
70.22	2479.67	3.74	81.05	97.62
70.39	2487.22	4.21	20.03	49.04
70.48	2491.05	5.42	58.35	151.71
70.58	2495.13	5.27	26.63	79.23
70.72	2500.66	5.46	204.15	520.95
70.85	2505.83	4.39	165.85	327.01
71.08	2515.79	4.36	386.38	611.77
71.19	2520.95	3.85	273.74	410.61
71.31	2526.71	4.36	53.61	94.80
71.41	2531.52	6.89	37.75	156.10
71.62	2541.30	6.58	100.48	494.69
71.80	2548.96	5.07	2.53	8.53
72.04	2557.88	7.68	136.90	562.11
72.33	2566.47	5.46	82.15	346.29
72.68	2575.75	4.60	25.57	397.26
72.89	2582.52	4.80	63.85	128.19
73.16	2592.13	4.51	301.94	948.96
73.44	2602.01	5.99	124.96	754.83
73.70	2612.38	7.13	42.56	361.77
73.92	2623.57	4.44	15.69	103.39
74.17	2637.51	4.36	165.78	503.40

Additional references

Billups, K., Channell, J.E.T., Zachos, J. (2002). Late Oligocene to early Miocene geochronology and paleoceanography from the subantarctic South Atlantic. Paleoceanography, 17, PA1004, doi:1010.1029/2000PA000568.

Groeneveld, J., Hathorne, E.C., Steinke, S., DeBey, H., Mackensen, A., Tiedemann, R. (2014). Glacial induced closure of the Panamanian Gateway during Marine Isotope Stages (MIS) 95–100. Earth Planet. Sci. Lett., 404, 296–306.

Hagelberg, T., et al. (1992). Development of composite depth sections for Sites 844 through 854. In Proceedings of the Ocean Drilling Program, Initial Rep., 138, pp. 79–85, Ocean Drill. Program, College Station, Tex.

Herguera, J.C., Berger, W.H. (1991). Paleoproductivity from benthic foraminifera abundance: Glacial to postglacial change in the west-equatorial Pacific. Geology, 19, 1173–1176.

Hodell, D.A., Venz, K.A., Charles, C.D., Ninnemann, U.S. (2003). Pleistocene vertical carbon isotope and carbonate gradients in the South Atlantic sector of the Southern Ocean. Geochem. Geophys. Geosyst., 4(1), 1–19.

Hovan, S.A. (1995). Late Cenozoic atmospheric circulation intensity and climatic history recorded by eolian deposition in the eastern equatorial Pacific Ocean, Leg 138. In Proceedings of the Ocean Drilling Program, Sci. Results, 138, pp. 615–625, Ocean Drill. Program, College Station, Tex.

Hovan, S.A. (2013). Grain-size variations, eolian material and accumulation rates in sediments from ODP Hole 138-849B, doi:10.1594/PANGAEA.807833.

Lawrence, K.T., Liu, Z., Herbert, T.D. (2006). Evolution of the eastern tropical Pacific through Plio-Pleistocene glaciation. Science, 312, 79–83.

Le, J., Shackleton, N.J. (1992). Carbonate dissolution fluctuations in the western equatorial Pacific during the late Quaternary. Paleoceanography, 7(1), 21–42.

Lisiecki, L.E., Raymo, M.E. (2005). A Pliocene-Pleistocene stack of 57 globally distributed benthic $\delta^{18}O$ records. Paleoceanography, 20, PA1003, doi:1010.1029/2004PA001071.

Mayer, L., et al. (1992). Site 849. In Proceedings of the Ocean Drilling Program, Initial Rep., 138, pp. 735–807, Ocean Drill. Program, College Station, Tex.

Mix, A.C., Pisias, N.G., Rugh, W., Wilson, J., Morey, A., Hagelberg, T.K. (1995). Benthic foraminifer stable isotope record from Site 849 (0–5 Ma): Local and global climate changes. In Proceedings of the Ocean Drilling Program, Sci. Results, 138, pp. 371–412, Ocean Drill. Program, College Station, Tex.

Paillard, D., Labeyrie, L., Yiou, P. (1996). Macintosh program performs time-series analysis. Eos Trans. AGU, 77(39), 379, doi:10.1029/1096EO00259.

Pusz, A.E., Thunell, R.C., Miller, K.G. (2011). Deep water temperature, carbonate ion, and ice volume changes across the Eocene-Oligocene climate transition. Paleoceanography, 26, PA2205, doi:2210.1029/2010PA001950.

Schneider, B., Schmittner, A. (2006). Simulating the impact of the Panamanian seaway closure on ocean circulation, marine productivity and nutrient cycling. Earth Planet. Sci. Lett., 246, 367–380.

Shackleton, N.J., Hall, M.A. (1984). Oxygen and carbon isotope stratigraphy of Deep Sea Drilling Project Hole 552A: Plio-Pleistocene Glacial History. In Proceedings of the Deep Sea Drilling Project, Initial Rep., 81, pp. 599–609, Deep Sea Drill. Proj., Washington, D.C.

Spero, H.J., Mielke, K.M., Kalve, E.M., Lea, D.W., Pak, D.K. (2003). Multispecies approach to reconstructing eastern equatorial Pacific thermocline hydrography during the past 360 kyr. Paleoceanography, 18(1), doi:10.1029/2002PA000814.

Waddell, L.M., Hendy, I.L., Moore, T.C., Lyle, M.W. (2009). Ventilation of the abyssal Southern Ocean during the late Neogene: A new perspective from the subantarctic Pacific. Paleoceanography, 24, PA3206, doi:3210.1029/2008PA001661.

APPENDIX A.2

SUPPORTING INFORMATION FOR CHAPTER 5

Supporting Chapter 5 of this thesis, which reports on glacial-interglacial (G-IG) changes in equatorial Pacific surface-water structure during the Plio-Pleistocene, this appendix contains an extended description of methods, additional discussions, seven figures, two tables and additional references.

Text A.2.1: Preservation of foraminiferal tests

Numerous studies suggest a significant influence of calcite dissolution on planktic foraminiferal Mg/Ca ratios, which lowers their initial Mg/Ca signal with increasing water depth of test deposition linked to $\Delta[CO_3^{2-}]$ of overlying bottom waters (e.g., Lea et al., 2000; Regenberg et al., 2014). Initial Mg/Ca ratios are only preserved in bottom waters with $\Delta[CO_3^{2-}]$ above 21.3±6.6 μmol kg^{-1}, which equals a water depth <0.5 km in the Eastern Equatorial Pacific (EEP) (Regenberg et al., 2014). Mg/Ca ratios below this threshold are, perhaps, underestimated (Regenberg et al., 2014).

To evaluate the preservation of planktic foraminiferal tests used for Mg/Ca and $\delta^{18}O$ analyses at Site 849, we extended the planktic foraminiferal fragmentation index (FFI) presented in Chapter 4 back to ~2.75 Ma. The FFI was calculated from aliquots of the >150 μm size fraction following Le et al. (1995):

FFI [%] = (number of fragments/8) x (number of fragments/8 + complete tests)$^{-1}$ x 100%

Low-resolution shipboard investigations on core-catcher material indicate poor preservation of planktic foraminiferal tests at Site 849 (Mayer et al., 1992). However, these observations are not compatible with findings for our target interval. First, scanning electron microscope (SEM) images of the planktic foraminifer *Globigerinoides ruber* from both glacial and interglacial samples in our target interval (Chapter 4) demonstrate that the preservation is consistently good and therefore allows to acquire high-quality Mg/Ca and $\delta^{18}O$ data (see Sexton et al., 2006). Second, relatively low mean FFIs at Site 849 (~6%) across our study

interval compared to previously published FFIs from Site 846 for the last 0.8 Myr (~9% [Le et al., 1995]) and from Site 849 for the last G-IG cycle (~6 to 18% [Marchitto et al., 2005]) indicate only a minor effect of carbonate dissolution on planktic foraminiferal tests (Figure A.2.1a–b). Third, FFIs at Site 849 show no G-IG cyclicity over the entire study interval (Figure A.2.1c), which is in line with the findings presented in Chapter 4.

However, since selective removal of Mg from planktic foraminiferal calcite commences much earlier than a FFI record or SEM images may indicate, Mg/Ca-based proxy records should generally be interpreted with caution, potentially slightly being underestimated with respect to sea-surface temperatures (SST).

Text A.2.2: Evaluation of contamination and diagenetic overgrowth for foraminiferal Mg/Ca ratios

To monitor contamination of clays or diagenetic coatings not removed during the Mg/Ca cleaning process, we monitored Al, Fe and Mn contents (Figure A.2.2). Samples with anomalously high Al/Ca, Fe/Ca or Mn/Ca ratios were rejected.

Al/Ca ratios of >0.1 mmol/mol indicate the presence of detrital clay that was not sufficiently removed during the cleaning process (Barker et al., 2003). Since in most of our samples Al/Ca ratios are close to the detection limit of the ICP-OES, we chose to only discard samples with anomalously high Al/Ca ratios.

Fe/Ca and Mn/Ca values of 0.1 mmol/mol are critical for indicating contamination with Fe-oxide or Mn-oxide coatings (Barker et al., 2003). With the exception of few samples, Fe/Ca values commonly do not exceed this critical value and therefore indicate no contamination by Fe-rich overgrowth (Figure A.2.2a, A.2.2c).

Mn/Ca ratios were higher than the critical ratio of 0.1 mmol/mol given by Barker et al. (2003) (Figure A.2.2c). Since previous foraminiferal Mg/Ca studies also showed Mn/Ca values exceeding 0.1 mmol/mol (e.g., Bahr et al., 2011; 2013), the critical threshold value provided by Barker et al. (2003) may possibly not be applicable for all sediment types foraminiferal tests were selected from. Regardless, Mg/Ca-based temperature estimates may be biased in the case that foraminiferal tests were overgrown by microcrystalline Ca-carbonates during early diagenesis (Regenberg et al., 2007; Groeneveld et al., 2008). For Site 849 samples, there is a lack of statistically significant correlation between Mg/Ca *vs.* Mn/Ca ($R^2 = 0.04$) (Figure A.2.2b), which infers that Mg/Ca ratios are not biased by Mn/Ca coatings. Also SEM images of both glacial and interglacial *G. ruber* tests considerably rule out an overgrowth by

diagenetic crystals (Chapter 4). Furthermore, diagenetic overgrowth typical for Mg/Mn ratios of ~0.1 mol/mol (Barker et al., 2003, and references therein) (Figure A.2.2c) might change temperature estimates by on average ~0.6°C, but does not affect the shape of the Mg/Ca record and the Mg/Ca-based temperature estimates given that consistently enhanced Mn/Ca ratios of ~1.4 mmol/mol indicate diagenetic alteration homogenously across the entire investigated sediment column. If the diagenetic front would not have affected the entire herein investigated sediment column homogenously, this excess is still much smaller than the discussed G-IG temperature amplitudes. Although we cannot completely rule out the possibility of diagenetically induced changes within the foraminiferal tests because of significantly enhanced Mn/Ca ratios, we conclude with reasonable certainty that early diagenetic overprinting has not severely affected the presented data and therefore is not the primary reason for the observed G-IG temperature differences for Marine Isotope Stages (MIS) G6–95 at Site 849.

Text A.2.3: Sea-surface temperature calculation for ODP Site 849

We converted Mg/Ca ratios (mmol/mol) of *G. ruber* into SSTs (°C) following the species-specific equation for *G. ruber* provided by Lea et al. (2000) (Table A.2.1). This equation is based on oxidative and reductive cleaning of foraminiferal tests, while we only applied oxidative cleaning for Site 849 samples. Because reductive cleaning lowers Mg/Ca values by 10–15% (Barker et al., 2003; Pena et al., 2005), we adjusted measured Mg/Ca values by reducing each value by 10% (equal to ~1°C). Subtracting a value of 15% would lower SSTs by additional ~0.5°C, but would not affect the overall trend of the record and therefore would have minimal impact on the discussion presented in this study.

Other calibrations we considered are summarized in Table A.2.1 and Figure A.2.3 and discussed in the following.

We decided against the species-specific Atlantic calibrations for *G. ruber* given by Elderfield and Ganssen (2000), Anand et al. (2003) and Regenberg et al. (2009), because all these equations provide much lower mean SSTs than expected when comparing to present-day SSTs (~23°C [Locarnini et al., 2013]) and Plio-Pleistocene mean SST estimates (~24.5°C [Lawrence et al., 2006]) in the EEP realm. Further we did not apply the species-specific southeast Pacific calibration for *G. ruber* provided by Sadekov et al. (2009), because this equation is only based on the final chamber of *G. ruber*, while we use complete foraminiferal tests in our study.

In light of the species-specific Pacific equation for *G. ruber*, we prefer the calibration provided by Lea et al. (2000) instead of the equation given by Dekens et al. (2002). The latter would result in the same overall shape, but is shifted toward ~1°C higher values (Figure A.2.3). The reason for this decision is threefold: First, the coretop calibration of Dekens et al. (2002) includes a water-depth correction for carbonate dissolution. We suggest, however, that the influence of dissolution on our sample material is of minor importance (see above), thus a water-depth/dissolution-correction factor seems to be negligible. Second, the equation provided by Dekens et al. (2002) is based on coretop samples from the Western Equatorial Pacific (WEP), whereas the calibration of Lea et al. (2000) is based on sample material from the EEP, i.e., the location of this study. Third, Mg/Ca based SST estimates of Site 806 presented by Medina-Elizalde and Lea (2010), to which we compare our record from Site 849, are also calculated according to the relationship of Lea et al. (2000), facilitating data comparison.

In general the calculation of Mg/Ca-derived SSTs is based on the assumption that seawater Mg/Ca has remained constant throughout the interval of study. Because both elements are conservative elements with a residence time longer than 1 Myr (Fantle and DePaolo, 2005, 2006), we argue that the Mg/Ca ratio of seawater has been fairly constant over the time interval investigated in this study (~350 kyr). We are aware that Medina-Elizalde et al. (2008) developed an adjustment for Mg/Ca-based SST estimates compensating past changes in seawater Mg/Ca. However, we do not favor using this correction here, because seawater Mg/Ca estimates for the investigated time interval are only poorly constrained (Fantle and DePaolo, 2006; Rausch et al., 2013). Regardless, applying this correction would result in ~1°C warmer absolute Mg/Ca-based SSTs for the investigated time interval, but is not affecting the overall trend of the record (compare Medina-Elizalde and Lea, 2010), and therefore would have minimal impact on the discussion presented in this study.

Text A.2.4: $\delta^{18}O_{sw}$ and $\delta^{18}O_{ivc\text{-}sw}$ reconstruction for ODP Site 849

To reconstruct surface-water salinity changes (as defined by $\delta^{18}O_{ivc\text{-}sw}$) at Site 849, we calculated the oxygen-isotope composition of seawater ($\delta^{18}O_{sw}$ in ‰ Standard Mean Ocean Water, SMOW) by extracting the component of Mg/Ca-derived SSTs (°C) from the planktic foraminiferal $\delta^{18}O$ record (‰ VPDB) using the high-light (HL) paleotemperature equation determined for *Orbulina universa* (Bemis et al., 1998) and converted foraminiferal $\delta^{18}O$ to SMOW by adding 0.27‰ (Hut, 1987) ($\delta^{18}O_{sw,\,SMOW} = [(SST - 14.9)/4.8] + \delta^{18}O_{calcite} + 0.27$). Applying the low-light (LL) calibration (Bemis et al., 1998) results in 0.33‰ lower values

compared to the HL calibration, but does not affect the general trend and therefore the interpretation of our record. We preferred the HL equation to calculate $\delta^{18}O_{sw}$, because it has been demonstrated that in areas with warm annual SSTs, i.e., close to the equator, *G. ruber*-based $\delta^{18}O_{sw}$ estimates are best described with this calibration (Wang et al., 1995; Thunell et al., 1999; Bemis et al., 2000).

The resulting planktic foraminiferal $\delta^{18}O_{sw}$ record reflects continental ice volume and local salinity variability. To estimate sea-surface salinity (SSS) (as defined by ice-volume adjusted sea-water $\delta^{18}O$ [$\delta^{18}O_{ivc\text{-}sw}$]), two different methods have been applied:

Method 1: To calculate $\delta^{18}O_{ivc\text{-}sw}$, the ice-volume effect from planktic foraminiferal $\delta^{18}O_{sw}$ was removed by subtracting an estimation of the global Plio-Pleistocene ice-volume (given by benthic $\delta^{18}O$ at Site 849) within the same sample. First, the $\delta^{18}O_b$ record was normalized to the modern $\delta^{18}O_{sw}$ value of 3.6‰ (Lisiecki and Raymo, 2005). Based on the approach that the difference in $\delta^{18}O_b$ between the Last Glacial Maximum and the Holocene was ~1.6‰ (Shackleton et al., 1983), while the difference in global ice volume only was ~1.0–1.2‰ (Fairbanks, 1989; Schrag et al., 1996), we assume that the benthic $\delta^{18}O$ signal accounted to ~75% for the last G-IG ice-volume difference, yielding the following equation:

$$\delta^{18}O_{ivc\text{-}sw} = \delta^{18}O_{sw} - 0.75 \times (\delta^{18}O_b - 3.6‰)$$

This relationship has successfully been applied in several Plio-Pleistocene studies, demonstrating that this approximation is not only valid for the Holocene period, but also for the Pliocene-Pleistocene epoch (compare Groeneveld et al., 2006; Karas et al., 2009).

Method 2: $\delta^{18}O_{ivc\text{-}sw}$ was calculated by subtracting a new eustatic sea-level reconstruction of ocean $\delta^{18}O$ (Rohling et al., 2014) from the $\delta^{18}O_{sw}$ record. Therefore, the $\delta^{18}O$ record provided by Rohling et al. (2014) was interpolated on the resolution given by the Site 849 $\delta^{18}O_{sw}$ record.

Text A.2.5: Calculation of zonal Pacific SSS and SST gradients

To determine paleosalinity changes (as defined by $\delta^{18}O_{ivc\text{-}sw}$) at Site 806, we converted the LL-equation-based $\delta^{18}O_{sw}$ record from Site 806 provided by Medina-Elizalde and Lea (2010) to a "HL-$\delta^{18}O_{sw}$ record" (Bemis et al., 1998) (in order to stay consistent with the methodology applied for Site 849; see above), and calculated $\delta^{18}O_{ivc\text{-}sw}$ following both method 1 (but applying the Site 806 benthic $\delta^{18}O$ record [Karas et al., 2009]) and method 2 (see above).

Sea-surface temperature, $\delta^{18}O_{ivc\text{-}sw}$ and $\delta^{18}O_{sw}$ gradients between the Western and Eastern Equatorial Pacific were calculated after (i) linear interpolation of Site 849 SST, $\delta^{18}O_{ivc\text{-}sw}$ and

$\delta^{18}O_{sw}$ raw data on the resolution given by Site 806 (~1.9 kyr for the time interval ~2.75–2.4 Ma), and after (ii) smoothing of the resulting Site 849 records using a 5-point moving average to avoid high-frequency noise, to compensate correlation uncertainties for gradient calculation, and to account for the difference in sample resolution (~800 yr at Site 849 *vs.* ~1.9 kyr at Site 806).

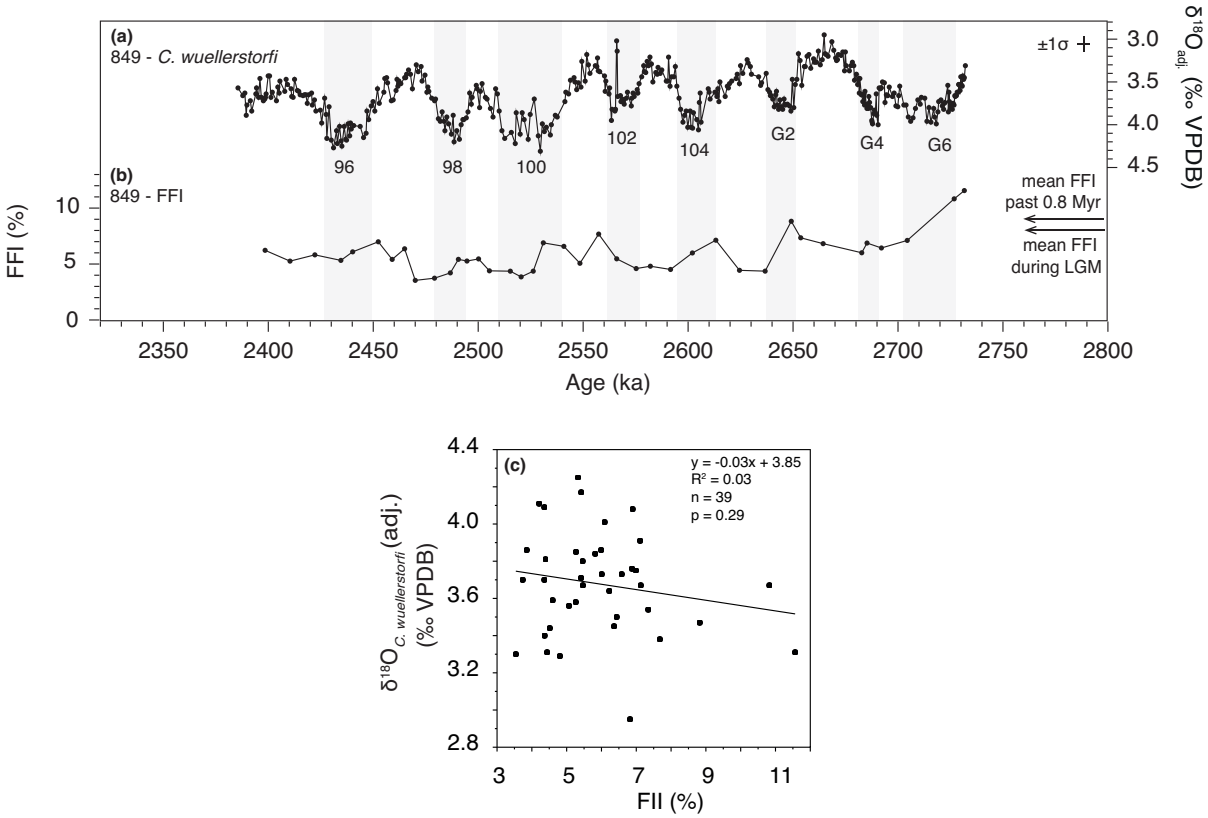

Figure A.2.1. Proxy record for evaluating calcite dissolution at Site 849 between ~2.75 and 2.4 Ma. **(a)** Benthic foraminiferal (*C. wuellerstorfi*) $\delta^{18}O$ record (‰ VPDB) from Site 849. The record consists of new data supplemented by published data of Mix et al. (1995). Bars indicate the 1σ standard deviation. **(b)** Dissolution proxy record (percentage planktic foraminiferal fragmentation [FFI]) from Site 849. Arrows depict mean FFIs for the past 0.8 Myr at Site 846 (~9% [Le et al., 1995]) and for the Last Glacial Maximum at Site 849 (~8% [Marchitto et al., 2005]). Holocene FFIs reach ~16% at Site 849 (Marchitto et al., 2005) and ~30% (Le et al., 1995) at Site 846. Grey bars in Figure A.2.1a–b highlight glacial periods. **(c)** Cross plot between $\delta^{18}O_b$ (‰ VPDB) and FFI (%) from Site 849 (n = 39). A lack of a statistically significant correlation at the 95% confidence level between both data sets (R^2 = 0.03, p >0.05) confirms that fragmentation is unrelated to G-IG cycles.

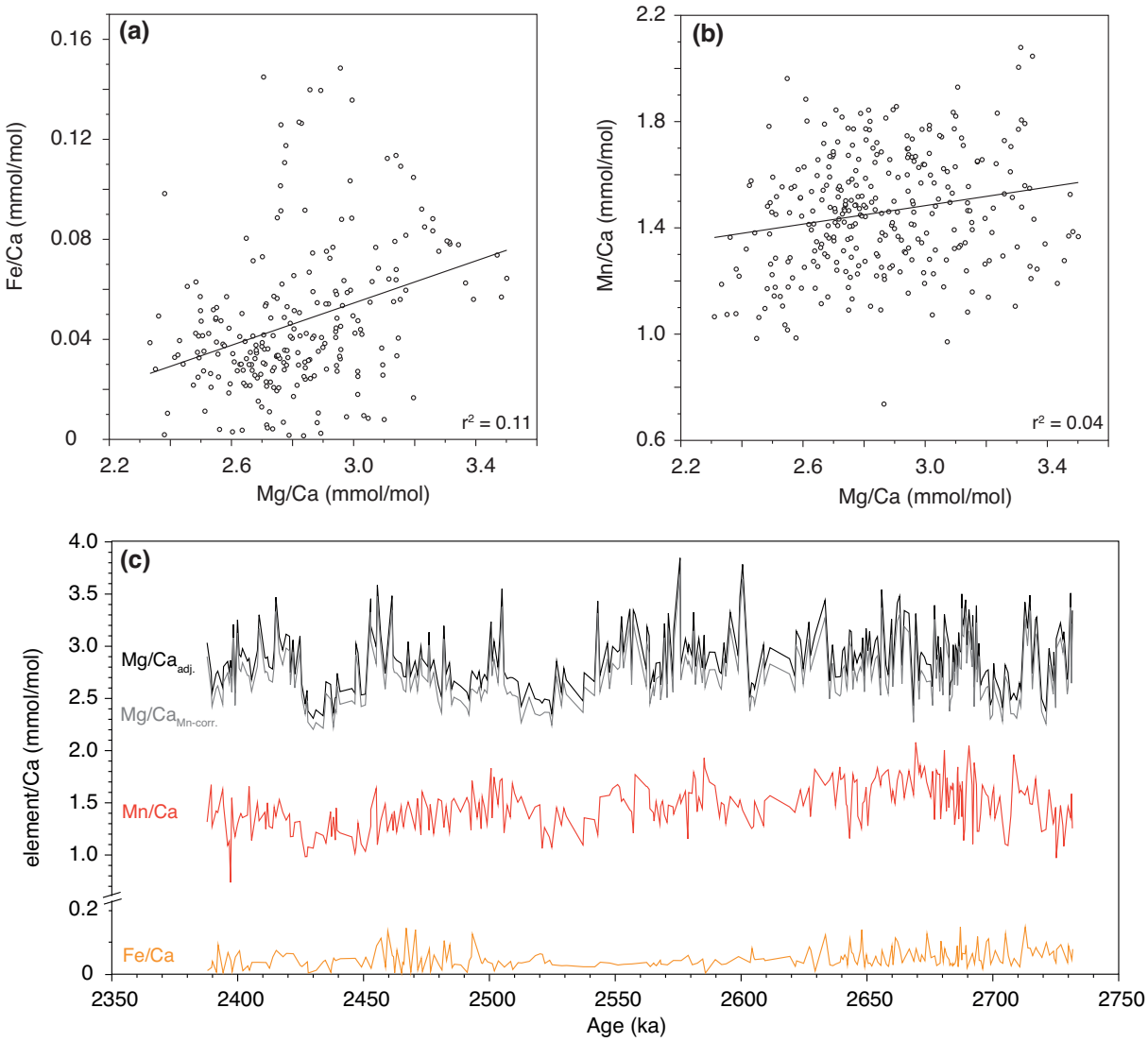

Figure A.2.2. Evaluation of the influence of potential contaminations on the Mg/Ca ratio for *G. ruber*. **(a)** Cross plot between Mg/Ca and Fe/Ca. Note that Fe/Ca values commonly do not exceed the critical value of 0.1 mmol/mol indicative for contamination with Fe-oxide coatings (Barker et al., 2003). **(b)** Cross plot between Mg/Ca and Mn/Ca. Although Mn/Ca values exceed the critical value of 0.1 mmol/mol and therefore might indicate contamination with Mn-oxide coatings (Barker et al., 2003), there is a lack of statistically significant correlation between Mg/Ca *vs.* Mn/Ca. Therefore we consider that Mn-oxide coatings or Mn-carbonates did not considerably alter measured Mg contents. **(c)** Downcore Mg/Ca ratios (black; normalized relative to the ECRM752-1 standard applying the Mg/Ca reference value of 3.762 mmol/mol [Greaves et al., 2008]), Mg/Ca ratios corrected for Mn-bearing overgrowths using the assumption of a Mn:Mg ratio of 1:1 (grey), Mn/Ca ratios (red) and Fe/Ca ratios (orange).

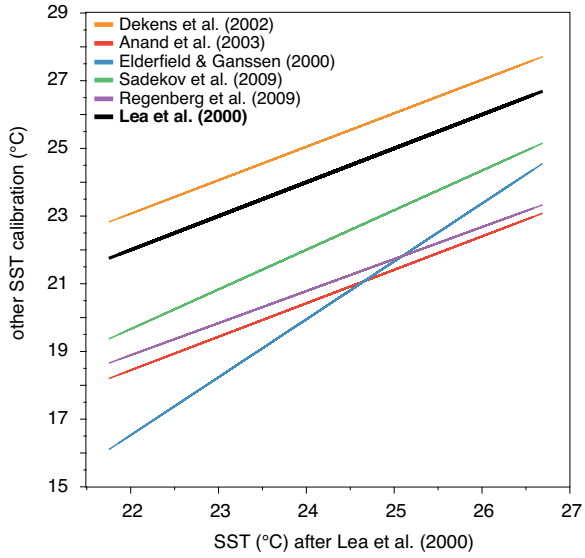

Figure A.2.3. Comparison of different SST calibrations relative to the calibration of Lea et al. (2000) used in this study (black line) for the temperature range 21–27°C. For equations based on reductive cleaning of foraminiferal tests (Lea et al., 2000; Dekens et al., 2002), measured Mg/Ca values were adjusted by reducing 10% (Barker et al., 2003). See Text A.2.3 for explanation.

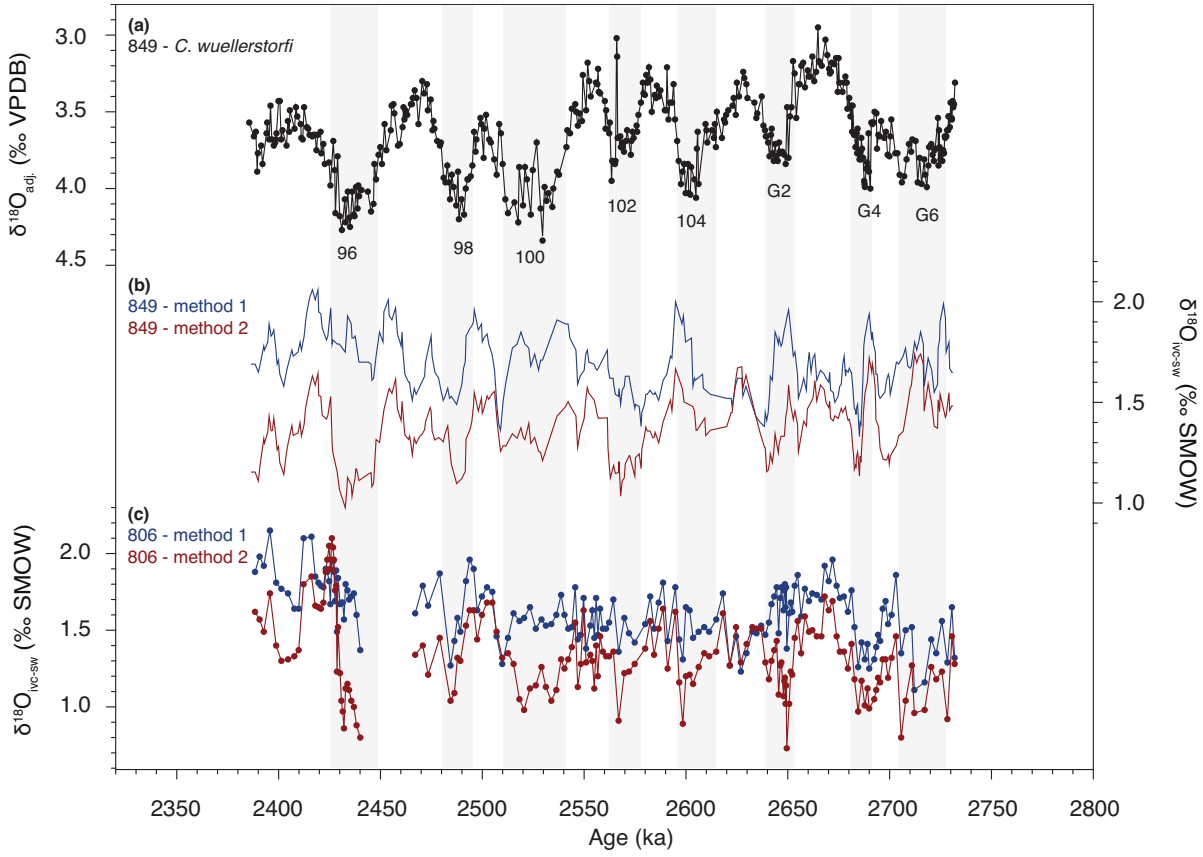

Figure A.2.4. Comparison between two different methods for $\delta^{18}O_{ivc\text{-}sw}$ calculations for Sites 849 and 806 for the time interval ~2.75–2.4 Ma. **(a)** Benthic foraminiferal (*C. wuellerstorfi*) $\delta^{18}O$ stratigraphy for Site 849. **(b)** Planktic foraminiferal (*G. ruber*) $\delta^{18}O_{ivc\text{-}sw}$ record (five-point smoothed) from Site 849 (this study) for method 1 (blue) and method 2 (red). **(c)** Planktic foraminiferal (*G. ruber*) $\delta^{18}O_{ivc\text{-}sw}$ record from Site 806 (Medina-Elizalde and Lea, 2010) for method 1 (blue) and method 2 (red). See text A.2.4 for explanation.

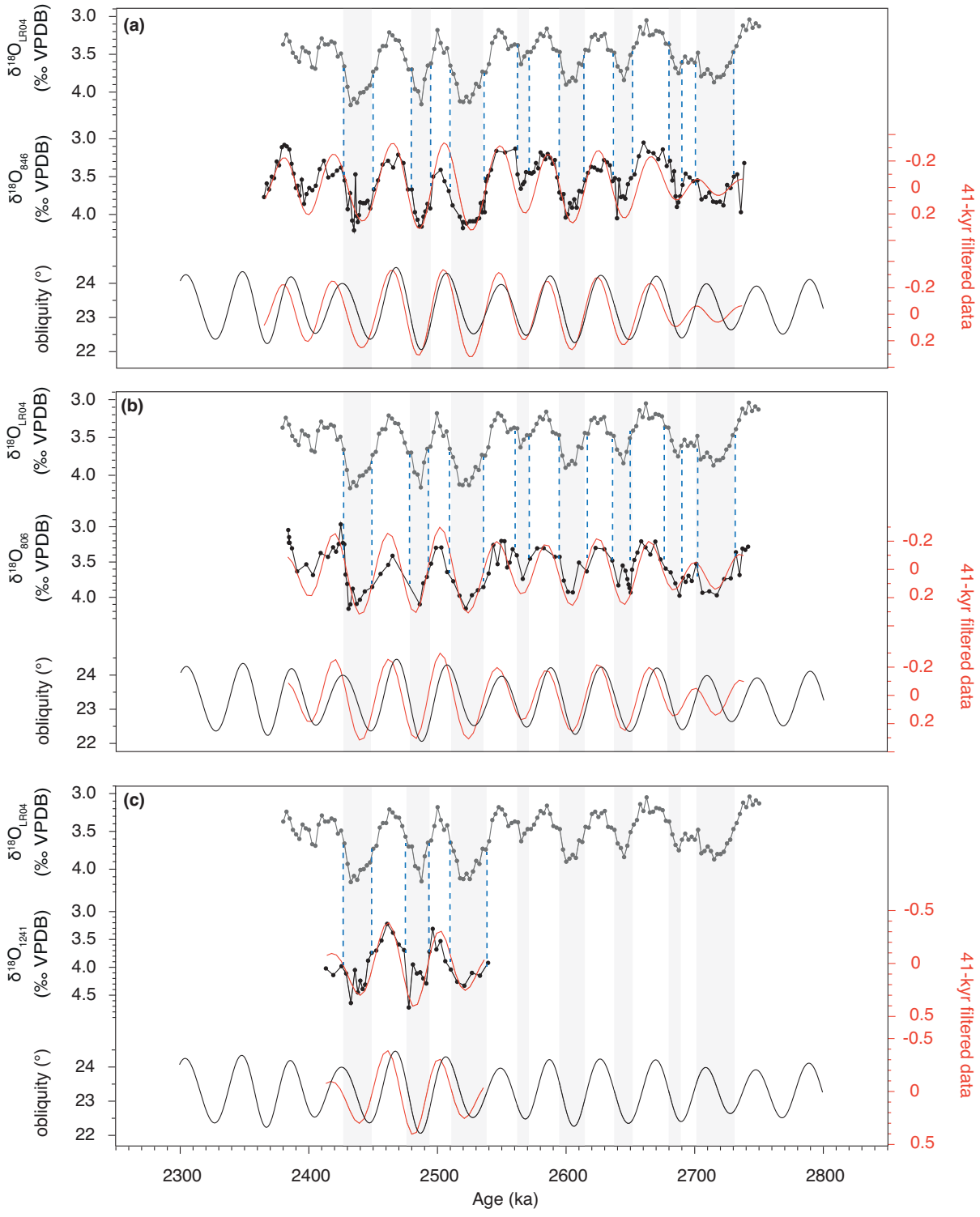

Figure A.2.5. Revised age models (tuned to the LR04 stack [Lisiecki and Raymo, 2005]) for **(a)** ODP Site 846 (Shackleton et al., 1995) and **(b)** ODP Site 806 (Karas et al., 2009) spanning ~2.75–2.4 Ma and for **(c)** ODP Site 1241 (Tiedemann et al., 2007) for ~2.55–2.42 Ma. Blue dashed lines show the tie points used for tuning (provided in Table A.2.2). Further, benthic foraminiferal $\delta^{18}O$ records from Sites 846, 806 and 1241 were filtered with a band-pass Gaussian filter centered on 0.024 kyr^{-1} with a bandwidth of 0.01 kyr^{-1} (red) and compared to the astronomical solution for orbital obliquity (black) (Laskar et al., 2004). Grey bars highlight glacial periods.

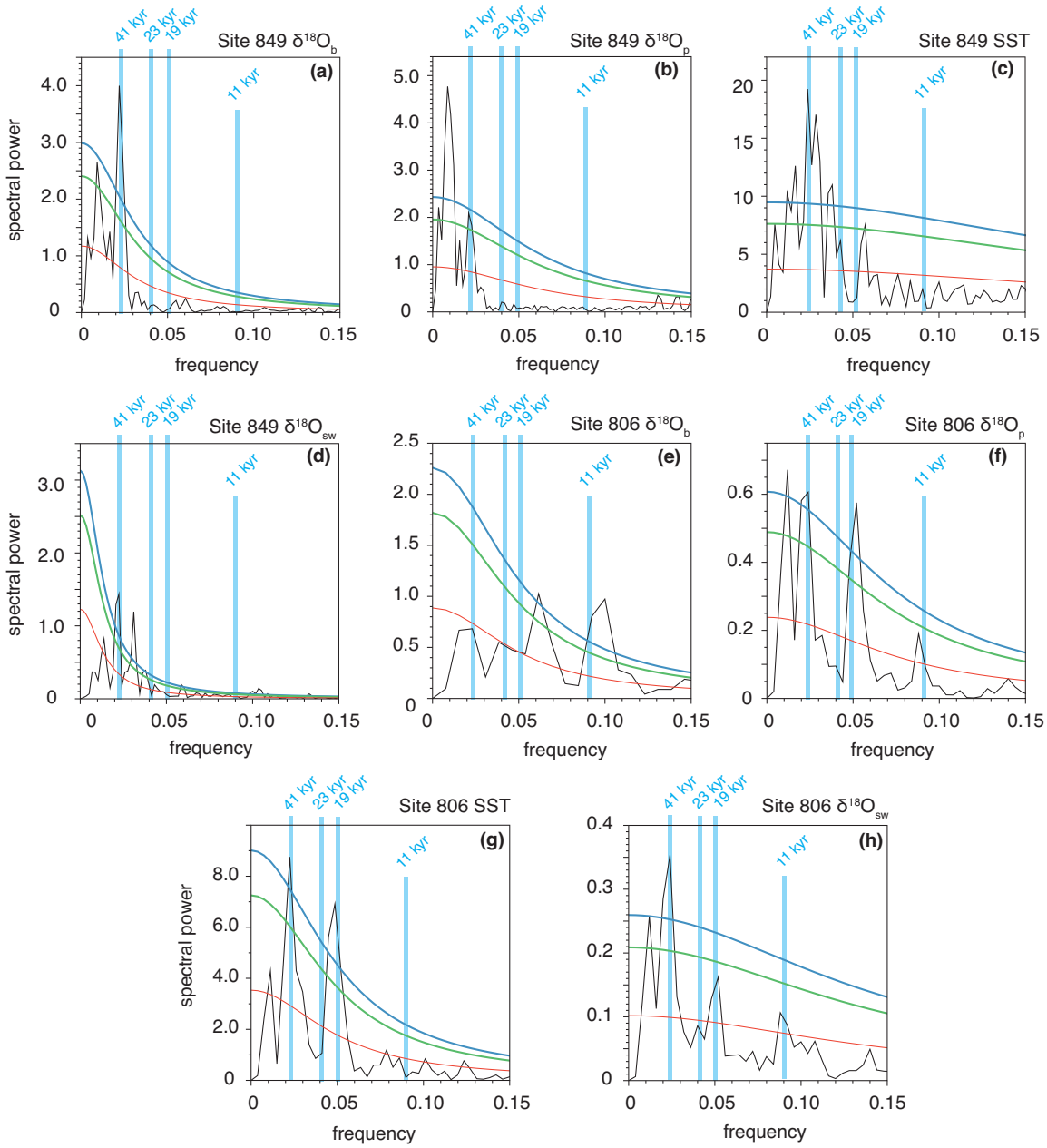

Figure A.2.6. Spectral analyses of Site 849 (a–d) and Site 806 (e–h) proxy records used for $\delta^{18}O_{ivc\text{-}sw}$ calculations for the time interval ~2.75–2.4 Ma (MIS G6–95). **(a)** Site 849 benthic foraminiferal $\delta^{18}O$, **(b)** Site 849 planktic foraminiferal $\delta^{18}O$, **(c)** Site 849 SST, **(d)** Site 849 seawater $\delta^{18}O$, **(e)** Site 806 benthic foraminiferal $\delta^{18}O$, **(f)** Site 806 planktic foraminiferal $\delta^{18}O$, **(g)** Site 806 SST, and **(h)** Site 806 seawater $\delta^{18}O$. Light blue bars represent 41 kyr cycles (obliquity), 23 kyr and 19 kyr cycles (precession), and 11 kyr cycles (half-precession). Spectral analyses were carried out using PAST version 3.11 (Hammer et al., 2001). Proxy records were detrended and fitted against the red-noise background from autoregressive (AR1) process (red line). Blue and green lines represent 95% and 90% confidence levels, respectively. Results confirm the existence of 41 kyr cycles in all records, excluding the possibility that the 41 kyr signal in the $\Delta\delta^{18}O_{ivc\text{-}sw}$ record (Figure 5.7b in Chapter 5) is a result of circularity.

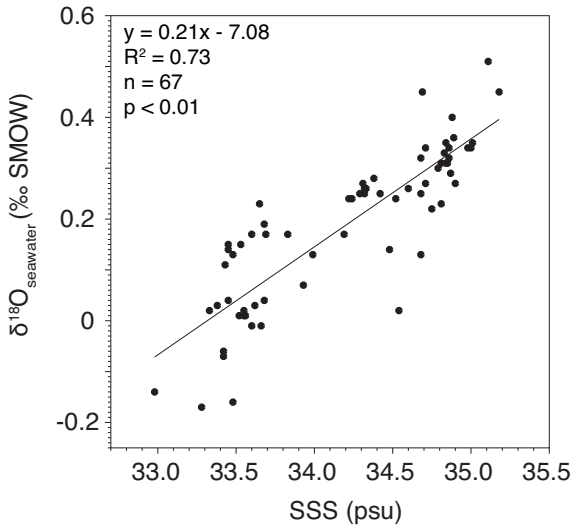

Figure A.2.7. Cross plot between modern surface-water $\delta^{18}O$ (‰ SMOW) and surface-water salinity (psu) in the east Pacific (15°N to 15°S, 125°W to 95°W) (Schmidt et al., 1999). According to the linear correlation of $\delta^{18}O_{sw} = 0.21 \times SSS - 7.08$, a salinity increase of 1 psu corresponds to a 0.21‰ increase in surface-water $\delta^{18}O$ in the modern EEP.

Table A.2.1. Species-specific Mg/Ca-based temperature calibrations for *Globigerinoides ruber*.

Reference	Grain size	Location and sample type	Cleaning method	Calibration
Anand et al. (2003)	250–350 µm	N Atlantic sediment trap	O	$Mg/Ca = 0.449 \times e^{0.09 \times SST}$
Dekens et al. (2002)	250–350 µm	WEP coretop	R/O	$Mg/Ca = 0.38 \times e^{0.09 \times (SST-[0.61 \times d]-1.6)}$
Elderfield and Ganssen (2000)		N Atlantic coretop	O	$Mg/Ca = 0.52 \times e^{0.1 \times SST}$
Lea et al. (2000)	**250–350 µm**	**EEP coretop**	**R/O**	**$Mg/Ca = 0.3 \times e^{0.089 \times SST}$**
Regenberg et al. (2009)	355–400 µm	Atlantic and Caribbean coretop	O	$Mg/Ca = 0.4 \times e^{0.094 \times SST}$
Sadekov et al. (2009)		SE Pacific coretop		$Mg/Ca = 0.53 \times e^{0.076 \times SST}$

R = reductive cleaning; O = oxidative cleaning; WEP = Western Equatorial Pacific; d = core depth in km; Mg/Ca in mmol/mol; SST in °C.

Table A.2.2. Age model tie-points used in this study for ODP Sites 849, 846 and 806 for the time interval ~2.75–2.4 Ma (MIS G6–95) and for ODP Site 1241 for the time interval ~2.55–2.42 Ma (MIS 100–95). Depth (in meter) is on the composite scale (mcd) for combined drill holes.

Site 849		Site 846		Site 806		Site 1241	
Depth (mcd)	**Age (ka)**	**Depth (mcd)**	**Age (ka)**	**Depth (mcd)**	**Age (ka)**	**Depth (mcd)**	**Age (ka)**
68.96	2427.14	92.77	2428.22	55.90	2427.34	57.98	2428.18
69.56	2449.91	94.22	2449.93	56.56	2447.20	58.81	2448.80
70.22	2479.81	95.05	2479.79	57.21	2474.99	59.43	2474.75
70.51	2492.50	95.85	2495.08	57.74	2493.29	60.13	2493.96
70.95	2509.96	96.36	2510.97	58.25	2510.35	60.61	2509.96
71.61	2540.82	97.79	2537.24	58.82	2537.60	61.11	2538.86
72.19	2562.58	98.78	2563.17	59.44	2558.65		
72.68	2575.74	99.05	2567.65	59.90	2571.67		
73.23	2594.61	100.61	2594.16	60.37	2596.30		
73.73	2615.21	101.65	2612.30	61.09	2618.53		
74.18	2637.53	102.72	2637.44	61.47	2637.54		
74.59	2651.76	103.53	2652.76	61.94	2650.23		
75.27	2680.08	104.32	2680.13	62.49	2677.54		
75.78	2690.82	105.04	2690.22	62.95	2690.28		
76.13	2703.75	105.50	2703.85	63.41	2703.62		
76.88	2729.78	106.50	2731.84	63.93	2730.65		

Additional References

Anand, P., Elderfield, H., Conte, M.H. (2003). Calibration of Mg/Ca thermometry in planktonic foraminifera from a sediment trap time series. Paleoceanography, 18, 1050, doi:1010.1029/2002PA000846.

Bahr, A., Nürnberg, D., Schönfeld, J., Garbe-Schönberg, D. (2011). Hydrological variability in Florida Straits during Marine Isotope Stage 5 cold events. Paleoceanography, 26, PA2214, doi:10.1029/2010PA002015.

Bahr, A., Nürnberg, D., Karas, C., Grützner, J. (2013). Millennial-scale versus long-term dynamics in the surface and subsurface of the western North Atlantic Subtropical Gyre during Marine Isotope Stage 5. Glob. Planet. Change, 111, 77–87.

Barker, S., Greaves, M., Elderfield, H. (2003). A study of cleaning procedures used for foraminiferal Mg/Ca paleothermometry. Geochem. Geophys. Geosyst., 4(9), 8407, doi:10.1029/2003GC000559.

Bemis, B.E., Spero, H.J., Bijma, J., Lea, D.W. (1998). Reevaluation of the oxygen isotopic composition of planktonic foraminifera: Experimental results and revised paleotemperature equations. Paleoceanography, 13, 150–160.

Bemis, B.E., Spero, H.J., Lea, D.W., Bijma, J. (2000). Temperature influence on the carbon isotopic composition of *Globigerina bulloides* and *Orbulina universa* (planktonic foraminifera). Mar. Micropaleontol., 38, 213–228.

Dekens, P.S., Lea, D.W., Pak, D.K., Spero, H.J. (2002). Core top calibration of Mg/Ca in tropical foraminifera: Refining paleotemperature estimation. Geochem. Geophys. Geosyst., 3(4), doi:10.1029/2001GC000200.

Elderfield, H., Ganssen, G. (2000). Past temperature and $\delta^{18}O$ of surface ocean waters inferred from foraminiferal Mg/Ca ratios. Nature, 405, 422–445.

Fairbanks, R.G. (1989). A 17,000-year glacio-eustatic sea level record: influence of glacial melting rates on the Younger Dryas event and deep-ocean circulation. Nature, 342, 637–642.

Fantle, M.S., DePaolo, D.J. (2005). Variations in the marine Ca cycle over the past 20 million years. Earth Planet. Sci. Lett., 237, 102–117.

Fantle, M.S., DePaolo, D.J. (2006). Sr isotopes and pore fluid chemistry in carbonate sediment of the Ontong Java Plateau: Calcite recrystallization rates and evidence for a rapid rise in seawater Mg over the last 10 million years. Geochim. Cosmochim. Ac., 70, 3883–3904.

Greaves, M., et al. (2008). Interlaboratory comparison study of calibration standards for foraminiferal Mg/Ca thermometry. Geochem. Geophys. Geosyst., 9, Q08010, doi:08010.01029/02008GC001974.

Groeneveld, J., Steph, S., Tiedemann, R., Garbe-Schönberg, D., Nürnberg, D., Sturm, A. (2006). Pliocene mixed-layer oceanography for Site 1241, using combined Mg/Ca and $\delta^{18}O$ analyses of *Globigerinoides sacculifer*. Proceedings of the Ocean Drilling Program, Sci. Results, 202, doi:10.2973/odp.proc.sr.202.209.2006, Ocean Drill. Program, College Station, Tex.

Groeneveld, J., Nürnberg, D., Tiedemann, R., Reichart, G.-J., Steph, S., Reuning, L., Crudeli, D., Mason, P. (2008). Foraminiferal Mg/Ca increase in the Caribbean during the Pliocene: Western Atlantic Warm Pool formation, salinity influence, or diagenetic overprint? Geochem. Geophys. Geosyst., 9, Q01P23, doi:10.1029/2006GC001564.

Groeneveld, J., Hathorne, E.C., Steinke, S., DeBey, H., Mackensen, A., Tiedemann, R. (2014). Glacial induced closure of the Panamanian Gateway during Marine Isotope Stages (MIS) 95–100. Earth Planet. Sci. Lett., 404, 296–306.

Hammer, Ø., Harper, D.A.T., Ryan, P.D. (2001). PAST: Paleontological statistics software package for education and data analysis. Palaeontol. Electron., 4, 1–9.

Hut, G. (1987). Consultant's group meeting on stable isotope reference samples for geochemical and hydrological investigations. Report to the Director General, International Atomic Energy Agency, Vienna, 42 pp.

Karas, C., Nürnberg, D., Gupta, A.K., Tiedemann, R., Mohan, K., Bickert, T. (2009). Mid-Pliocene climate change amplified by a switch in Indonesian subsurface throughflow. Nat. Geosci., 2, 434–438.

Laskar, J., Robutel, P., Joutel, F., Gastineau, M., Correia, A.C.M., Levrard, B. (2004). A long-term numerical solution for the insolation quantities of the Earth. Astron. Astrophys., 428, 261–285, doi:10.1051/0004-6361:20041335.

Lawrence, K.T., Liu, Z., Herbert, T.D. (2006). Evolution of the eastern tropical Pacific through Plio-Pleistocene glaciation. Science, 312, 79–83.

Le, J., Mix, A.C., Shackleton, N.J. (1995). Late Quaternary paleoceanography in the eastern equatorial Pacific Ocean from planktonic foraminifers: A high-resolution record from Site 846. In Proceedings of the Ocean Drilling Program, Sci. Results, 138, pp. 675–693, Ocean Drill. Program, College Station, Tex.

Lea, D.W., Pak, D.K., Spero, H.J. (2000). Climate impact of late Quaternary equatorial Pacific sea surface temperature variations. Science, 289, 1719–1724.

Lisiecki, L.E., Raymo, M.E. (2005). A Pliocene-Pleistocene stack of 57 globally distributed benthic $\delta^{18}O$ records. Paleoceanography, 20, PA1003, doi:1010.1029/2004PA001071.

Locarnini, R.A., et al. (2013). World Ocean Atlas 2013, Vol. 1: Temperature, edited by S. Levitus and A. Mishonov, U.S. Gov. Print. Off., Washington, D.C., NOAA Atlas NESDIS, 73, 40 pp.

Marchitto, T.M., Lynch-Stieglitz, J., Hemming, S.R. (2005). Deep Pacific $CaCO_3$ compensation and glacial-interglacial atmospheric CO_2. Earth Planet. Sci. Lett., 231(3–4), 317–336.

Mayer, L., et al. (1992). Site 849. In Proceedings of the Ocean Drilling Program, Initial Rep., 138, pp. 735–807, Ocean Drill. Program, College Station, Tex.

Medina-Elizalde, M., Lea, D.W., Fantle, M.S. (2008). Implications of seawater Mg/Ca variability for Plio-Pleistocene tropical climate reconstruction. Earth Planet. Sci. Lett., 269, 585-595.

Medina-Elizalde, M., Lea, D.W. (2010). Late Pliocene equatorial Pacific. Paleoceanography, 25, PA2208, doi:2210.1029/2009PA001780.

Mix, A.C., Pisias, N.G., Rugh, W., Wilson, J., Morey, A., Hagelberg, T.K. (1995). Benthic foraminifer stable isotope record from Site 849 (0–5 Ma): Local and global climate changes. In Proceedings of the Ocean Drilling Program, Sci. Results, 138, pp. 371–412, Ocean Drill. Program, College Station, Tex.

Pena, L.D., Calvo, E., Cacho, I., Eggins, S., Pelejero, C. (2005). Identification and removal of Mn-Mg-rich contaminant phases on foraminiferal tests: Implications for Mg/Ca past temperature reconstructions. Geochem. Geophys. Geosyst., 6, Q09P02, doi:10.1029/2005GC000930.

Rausch, S., Böhm, F., Bach, W., Klügel, A., Eisenhauer, A. (2013). Calcium carbonate veins in ocean crust record a threefold increase of seawater Mg/Ca in the past 30 million years. Earth Planet. Sci. Lett., 362, 215–224.

Regenberg, M., Nürnberg, D., Schönfeld, J., Reichart, G.-J. (2007). Early diagenetic overprint in Caribbean sediment cores and ist effect on the geochemical composition of planktonic foraminifera. Biogeosciences, 4, 957–973.

Regenberg, M., Steph, S., Nürnberg, D., Tiedemann, R., Garbe-Schönberg, D. (2009). Calibrating Mg/Ca ratios of multiple planktonic foraminiferal species with $\delta^{18}O$-calcification temperatures: Paleothermometry for the upper water column. Earth Planet. Sci. Lett., 278, 324–336.

Regenberg, M., Regenberg, A., Garbe-Schönberg, D., Lea, D.W. (2014). Global dissolution effects on planktonic foraminiferal Mg/Ca ratios controlled by the calcite-saturation state of bottom waters. Paleoceanography, 29, 127–142, doi:10.1002/2013PA002492.

Rohling, E.J., Foster, G.L., Grant, K.M., Marino, G., Roberts, A.P., Tamisiea, M.E., Williams, F. (2014). Sea-level and deep-sea-temperature variability over the past 5.3 million years. Nature, 508, 477–482.

Sadekov, A., Eggins, S.M., De Deckker, P., Ninnemann, U., Kuhnt, W., Bassinot, F. (2009). Surface and subsurface seawater temperature reconstruction using Mg/Ca microanalysis of planktonic foraminifera *Globigerinoides ruber, Globigerinoides sacculifer,* and *Pulleniatina obliquiloculata*. Paleoceanography, 24, PA3201, doi:3210.1029/2008PA001664.

Schmidt, G.A., Bigg, G.R., Rohling, E.J. (1999). Global Seawater Oxygen-18 Database - v1.21. http://data.giss.nasa.gov/o18data/.

Schrag, D.P., Hampt, G., Murray, D.W. (1996). Pore fluid constraints on the temperature and oxygen isotopic composition of the glacial ocean. Science, 272, 1930–1932.

Sexton, P.F., Wilson, P.A., Pearson, P.N. (2006). Microstructural and geochemical perspectives on planktic foraminiferal preservation: "Glassy" versus "Frosty". Geochem. Geophys. Geosyst., 7, Q12P19, doi:10.1029/2006GC001291.

Shackleton, N.J., Imbrie, J., Hall, M. (1983). Oxygen and carbon isotope record of East Pacific core V19-30: implications for the formation of deep water in the late Pleistocene North Atlantic. Earth Planet. Sci. Lett., 65, 233–244.

Shackleton, N.J., Hall, M.A., Pate, D. (1995). Pliocene stable isotope stratigraphy of Site 846. In Proceedings of the Ocean Drilling Program, Sci. Results, 138, pp. 337–355, Ocean Drill. Program, College Station, Tex.

Thunell, R., Tappa, E., Pride, C., Kincaid, E. (1999). Sea-surface temperature anomalies associated with the 1997–1998 El Niño recorded in the oxygen isotope composition of planktonic foraminifera. Geology, 27, 843–846.

Wang, L., Sarnthein, M., Duplessy, J.C., Erlenkeuser, H., Jung, S., Pflaumann, U. (1995). Paleo sea surface salinities in the low-latitude Atlantic: The $\delta^{18}O$ record of *Globigerinoides ruber* (white). Paleoceanography, 10, 749–761.

APPENDIX A.3

SUPPORTING INFORMATION FOR CHAPTER 6

Supporting Chapter 6 of this thesis, which reports on Plio-Pleistocene sea-level and deep-sea temperature evolution, this appendix contains five figures and additional references.

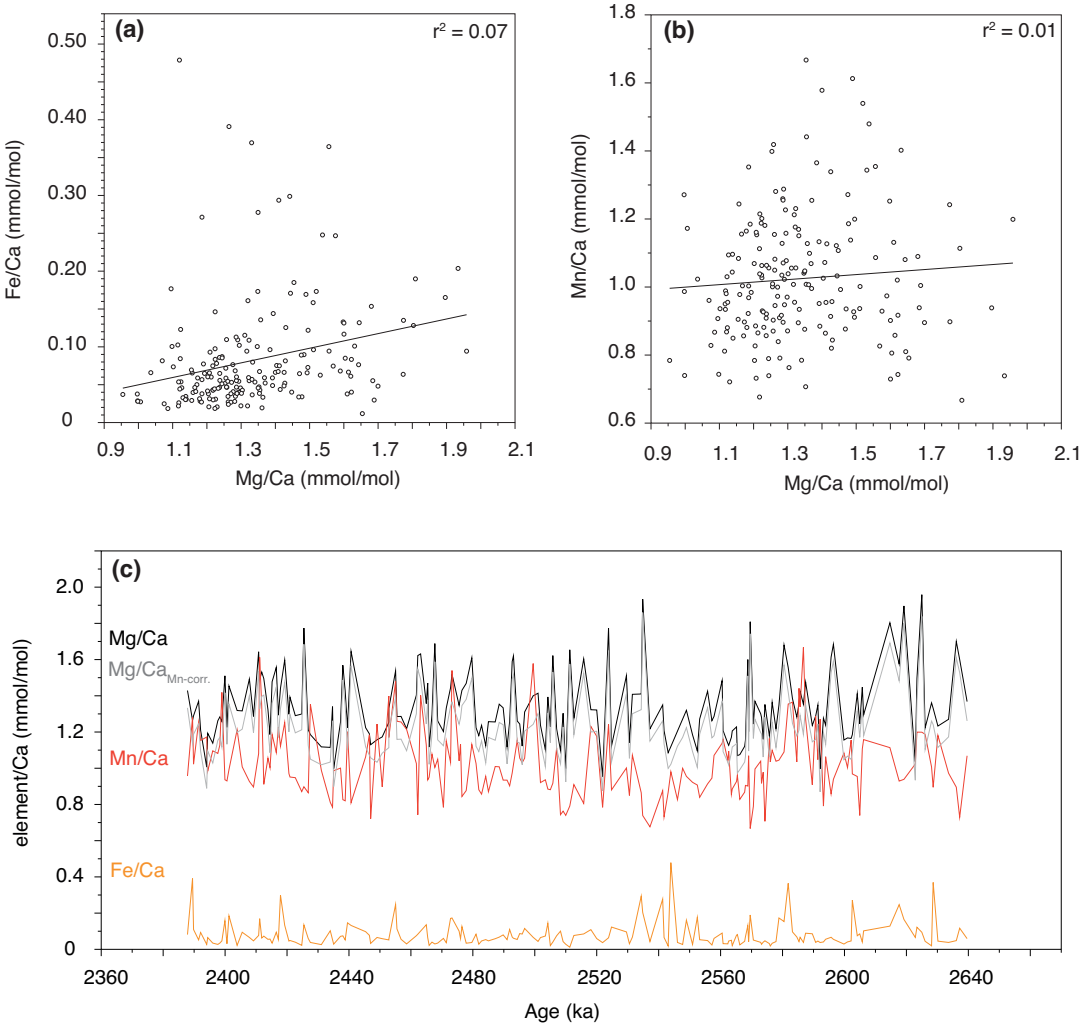

Figure A.3.1. Evaluation of the influence of potential contaminations on the Mg/Ca ratio for *Oridorsalis umbonatus* at east Pacific Site 849 through monitoring Al/Ca, Fe/Ca and Mn/Ca ratios. Samples with anomalously high Al/Ca, Fe/Ca or Mn/Ca ratios were rejected. Note that in most of the investigated samples Al/Ca ratios are below the detection limit and therefore not shown in this figure. **(a)** Cross plot between Mg/Ca and Fe/Ca. **(b)** Cross plot between Mg/Ca and Mn/Ca. Although Mn/Ca and some Fe/Ca values exceed the

critical value of 0.1 mmol/mol and therefore might indicate contamination with Mn-oxide and Fe-oxide coatings, respectively (Barker et al., 2003; see also Appendix A.2), there is a lack of statistically significant correlation between Mg/Ca *vs.* Mn/Ca (R^2 = 0.01) and Mg/Ca *vs.* Fe/Ca (R^2 = 0.07). Therefore it can be considered that Mn- and Fe-oxide coatings or Mn-carbonates did not considerably alter measured Mg contents. **(c)** Downcore Mg/Ca ratios (black; normalized relative to the ECRM752-1 standard [Greaves et al., 2008]), Mg/Ca ratios corrected for Mn-bearing overgrowths using the assumption of a Mn:Mg ratio of 1:1 (grey), Mn/Ca ratios (red) and Fe/Ca ratios (orange). Diagenetic overgrowth typical for Mg/Mn ratios of ~0.1 mol/mol (Barker et al., 2003, and references therein) might change temperature estimates by on average ~0.7°C, but does not affect the shape of the Mg/Ca record (black *vs.* grey line) and the Mg/Ca-based temperature estimates.

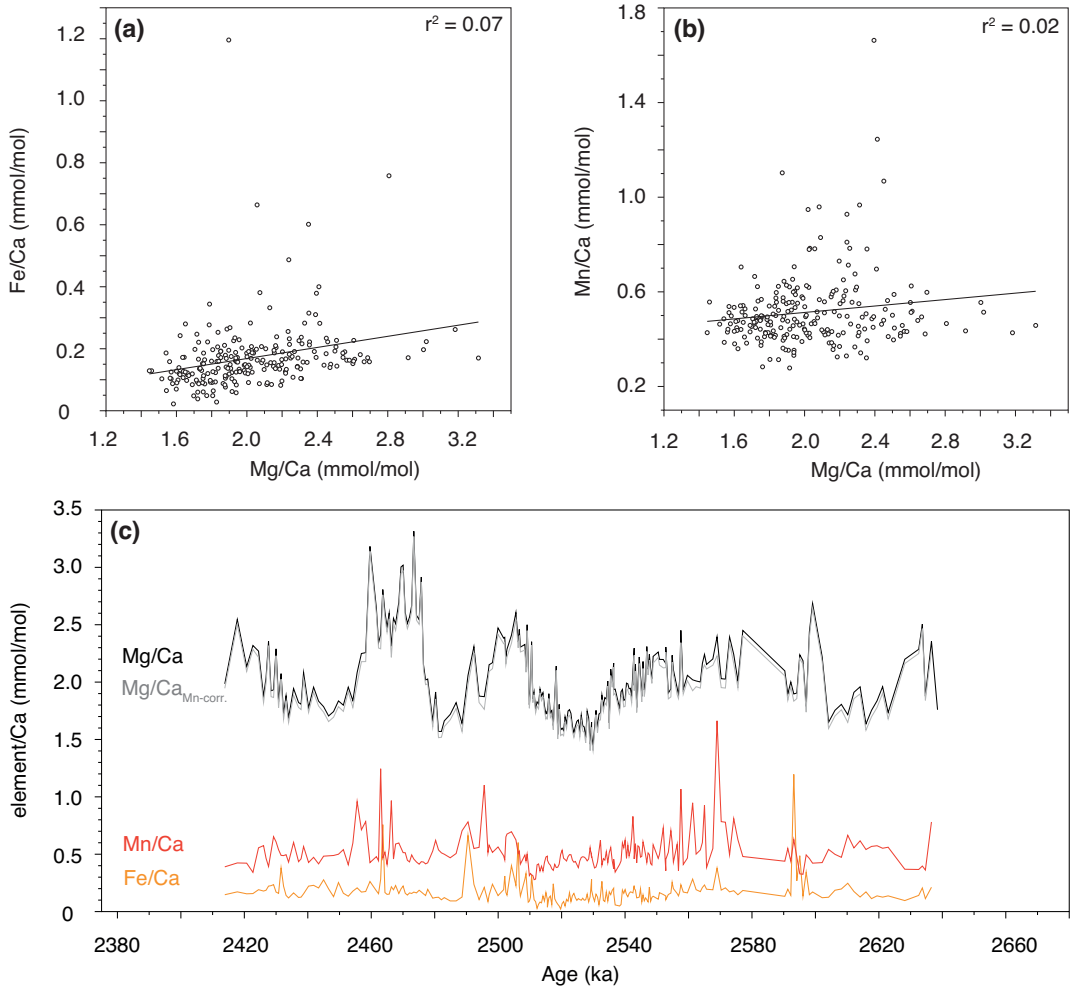

Figure A.3.2. Evaluation of the influence of potential contaminations on the Mg/Ca ratio for *Oridorsalis umbonatus* at North Atlantic Site U1313 through monitoring Al/Ca, Fe/Ca and Mn/Ca ratios. Samples with anomalously high Al/Ca, Fe/Ca or Mn/Ca ratios were rejected. Note that in most of the investigated samples Al/Ca ratios are below the detection limit and therefore not shown in this figure. **(a)** Cross plot between Mg/Ca and Fe/Ca. **(b)** Cross plot between Mg/Ca and Mn/Ca. Although Mn/Ca and Fe/Ca values exceed the critical value of 0.1 mmol/mol and therefore might indicate contamination with Mn-oxide and Fe-oxide coatings, respectively (Barker et al., 2003; see also Appendix A.2), there is a lack of statistically significant correlation between Mg/Ca *vs.* Mn/Ca (R^2 = 0.02) and Mg/Ca *vs.* Fe/Ca (R^2 = 0.07). Therefore it can be considered that Mn- and Fe-oxide coatings or Mn-carbonates did not considerably alter measured Mg contents. **(c)** Downcore Mg/Ca ratios (black; normalized relative to the ECRM752-1 standard [Greaves et al., 2008]), Mg/Ca ratios corrected for Mn-bearing overgrowths using the assumption of a Mn:Mg ratio of 1:1 (grey), Mn/Ca ratios (red) and Fe/Ca ratios (orange). Diagenetic overgrowth typical for Mg/Mn ratios of ~0.1 mol/mol (Barker et al., 2003, and references therein) might change temperature estimates by on average ~0.7°C, but does not affect the shape of the Mg/Ca record (black *vs.* grey line) and the Mg/Ca-based temperature estimates.

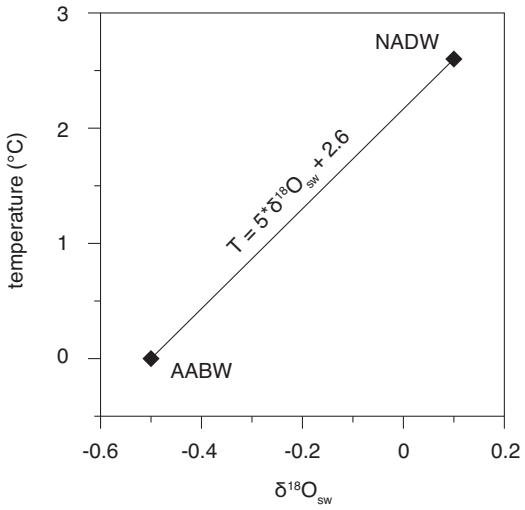

Figure A.3.3. Linear regression between modern North Atlantic Deep Water (NADW) and Antarctic Bottom Water (AABW) temperature and $\delta^{18}O_{sw}$ endmembers of 2.6°C and 0.1‰ and 0°C and -0.5‰, respectively (Craig and Gordon, 1965).

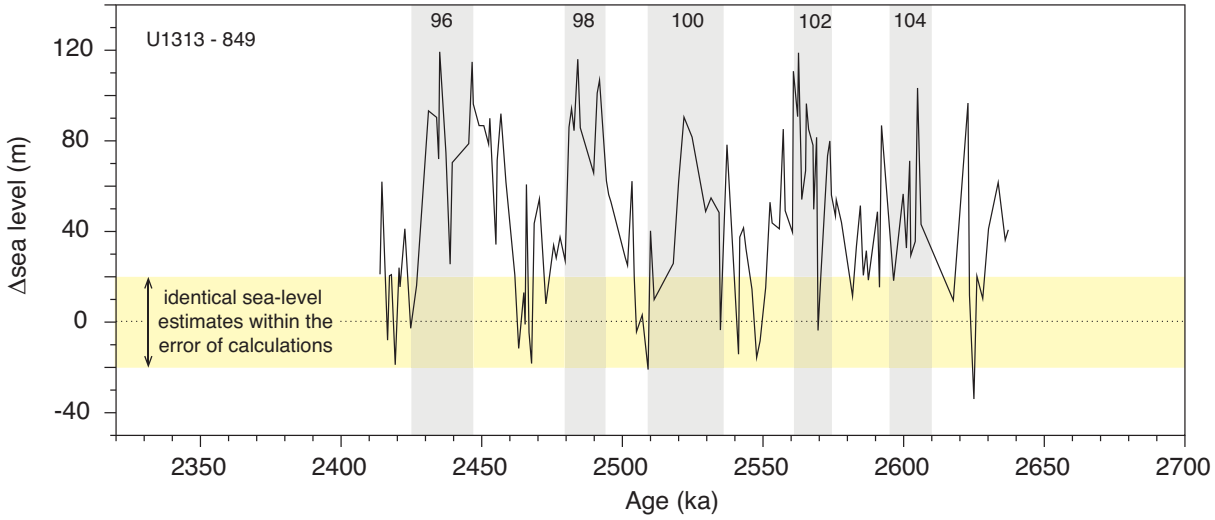

Figure A.3.4. Differences and similarities in sea-level estimates for North Atlantic IODP Site U1313 and Eastern Equatorial Pacific ODP Site 849 for ~2.65 to 2.4 Ma. Yellow bar marks the range of similar estimates for both sites within the error of calculations.

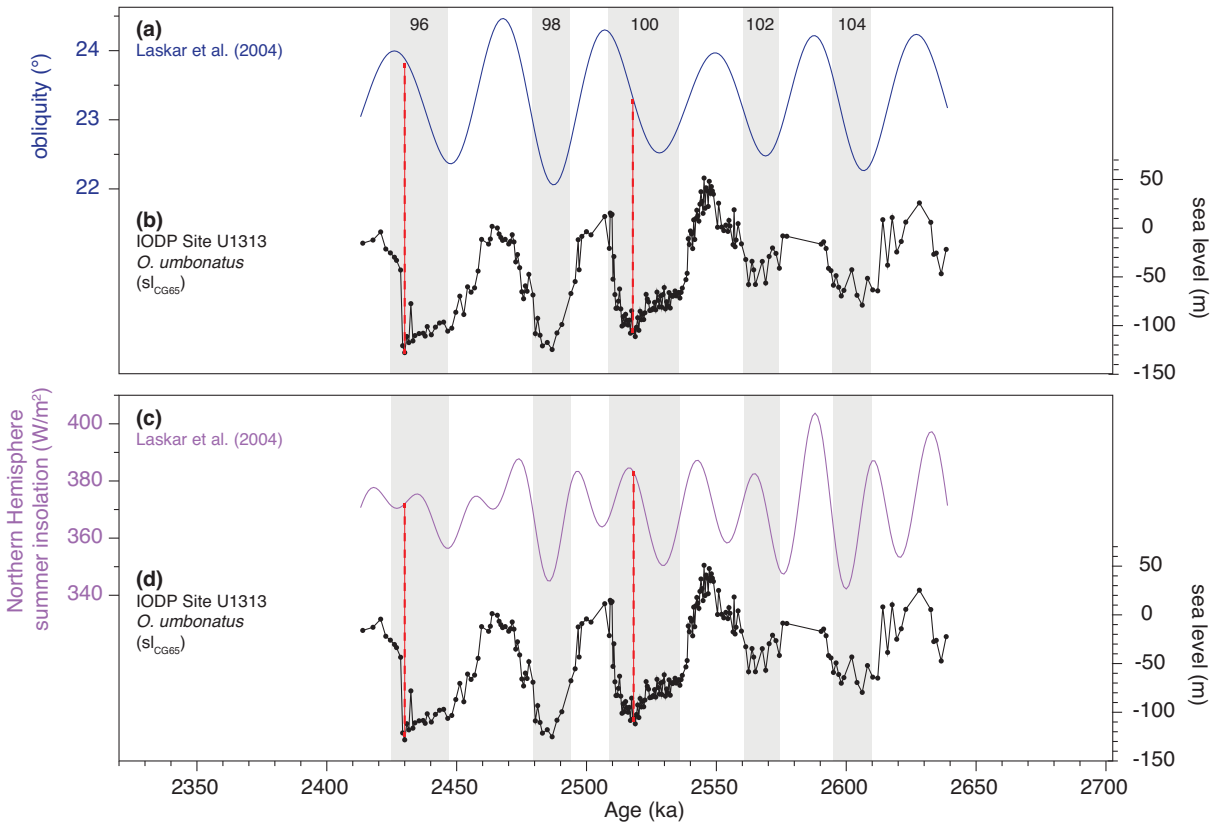

Figure A.3.5. Sea-level record from Site U1313 (black) (corrected after Craig and Gordon [1965]) compared to astronomical solutions from Laskar et al. (2004) for orbital obliquity (blue; top) and Northern Hemisphere summer insolation (purple; bottom). Red lines mark the onset of glacial (MIS 100 and 96) terminations. Grey bars mark glacial period.

Additional references

Barker, S., Greaves, M., Elderfield, H. (2003). A study of cleaning procedures used for foraminiferal Mg/Ca paleothermometry. Geochem. Geophys. Geosys., 4, doi:10.1029/2003GC000559.

Craig, H., Gordon, L.I. (1965). Deuterium and oxygen-18 variations in the ocean and the marine atmosphere. In Stable isotopes in oceanographic studies and paleotemperatures, edited by Tongiorgi, E., pp. 9–130, Spoletto, Pisa, Italy.

Greaves, M., et al. (2008). Interlaboratory comparison study of calibration standards for foraminiferal Mg/Ca thermometry. Geochem. Geophys. Geosys., 9, Q08010, doi:08010.01029/02008GC001974.

Laskar, J., Robutel, P., Joutel, F., Gastineau, M., Correia, A.C.M., Levrard, B. (2004). A long-term numerical solution for the insolation quantities of the Earth. Astron. Astrophys., 428, 261–285, doi:10.1051/0004-6361:20041335.

APPENDIX B.1

DATA TABLE FOR CHAPTER 4

Table B.1.1. Site 849 benthic foraminiferal (*Cibicidoides wuellerstorfi*) $\delta^{18}O$ and benthic (*C. wuellerstorfi*) and planktic (*Globorotalia crassaformis, Globigerinoides ruber*) foraminiferal $\delta^{13}C$, linear sedimentation rates (LSR), sand-accumulation rates (SAR) and dry bulk density (DBD) for ~2.65 to 2.4 Ma. $\delta^{18}O$ values of *C. wuellerstorfi* and $\delta^{13}C$ values of *G. ruber* are adjusted for species-specific offset from equilibrium by the addition of +0.64‰ (Shackleton and Hall, 1984) and +0.94‰ (Spero et al., 2003), respectively. *Cibicidoides wuellerstorfi* stable-isotope data marked with*) are from Mix et al. (1995).

Site	Hole	Core	Section	Top (cm)	Bottom (cm)	Depth *) (cm)	Depth (mcd)	Age (ka)	$\delta^{18}O_{C.\ wuellerstorfi}$ (‰ VPDB)	$\delta^{13}C_{C.\ wuellerstorfi}$ (‰ VPDB)	$\delta^{13}C_{G.\ crassaformis}$ (‰ VPDB)	$\delta^{13}C_{G.\ ruber}$ (‰ VPDB)	LSR (cm kyr^{-1})	SAR (g cm^{-2} kyr^{-1})	DBD (g cm^{-3})	
849	D	6	5			96	67.71	2385.57	3.57	0.22			3.06			*)
849	D	6	5	102	104		67.78	2387.85	3.66	0.00	0.89	2.80	3.06	0.074	0.698	
849	D	6	5			106	67.81	2388.83	3.63	0.14			3.06		0.711	*)
849	D	6	5	106	108		67.83	2389.49	3.89	0.09	0.94	2.87	3.06	0.093	0.724	
849	D	6	5	108	110		67.84	2389.81	3.77	0.18	0.97	2.93	3.06	0.080	0.801	
849	D	6	5	114	116		67.89	2391.45	3.72	0.09	0.89	2.86	3.06	0.086	0.773	
849	D	6	5	116	118		67.91	2392.10	3.84	0.06	0.81	2.72	3.06	0.070	0.722	
849	D	6	5	121	123		67.97	2394.06	3.64	0.09	0.86	2.76	3.06	0.076	0.743	
849	D	6	5	123	125		67.98	2394.39	3.57	-0.11		2.71	3.06	0.077	0.681	
849	D	6	5			126	68.01	2395.37	3.68	0.28			3.06		0.706	*)
849	D	6	5	127	129		68.03	2396.02	3.46	-0.01	0.90	2.69	3.06	0.067	0.738	
849	D	6	5	129	131		68.05	2396.67	3.68	0.21	0.96	2.86	3.06	0.068	0.732	
849	D	6	5	132	134		68.08	2397.65	3.72	0.06	0.87	2.71	3.06		0.782	
849	D	6	5	134	136		68.10	2398.31	3.70	-0.06	0.88	2.74	3.06	0.084	0.814	
849	D	6	5			136	68.11	2398.64	3.68	0.15			3.06		0.730	*)
849	D	6	5	137	139		68.12	2398.96	3.64	0.05	0.97	2.73	3.06	0.055	0.646	
849	D	6	5	139	141		68.15	2399.94	3.43	0.17	0.82	2.76	3.06	0.081	0.841	
849	D	6	5	141	143		68.17	2400.60	3.43	0.20	0.91	2.93	3.06	0.067	0.640	
849	D	6	5	143	145		68.19	2401.26	3.68	0.30		2.81	3.06	0.077	0.831	
849	D	6	5	146	148		68.21	2401.91	3.62	0.17		2.88	3.06	0.082	0.863	
849	D	6	6	1	3		68.27	2403.88	3.72	0.25	0.95	2.68	3.06	0.081	0.896	
849	D	6	6	3	5		68.29	2404.54	3.56	0.24	0.79	2.90	3.06	0.081	0.888	
849	D	6	6			6	68.31	2405.20	3.63	0.35			3.06		0.851	*)
849	D	6	6	6	8		68.32	2405.53	3.49	0.35	0.88	2.59	3.06	0.087	0.814	
849	D	6	6	13	15		68.39	2407.84	3.61	0.16	0.89	2.88	3.06	0.078	0.747	
849	D	6	6	15	17		68.41	2408.50	3.47	0.34	0.65	2.58	3.06	0.094	0.679	

Site	Hole	Core	Section	Top (cm)	Bottom (cm)	Depth *) (cm)	Depth (mcd)	Age (ka)	$\delta^{18}O_{C.\ wuellerstorfi}$ (‰ VPDB)	$\delta^{13}C_{C.\ wuellerstorfi}$ (‰ VPDB)	$\delta^{13}C_{G.\ crassaformis}$ (‰ VPDB)	$\delta^{13}C_{G.\ ruber}$ (‰ VPDB)	LSR (cm kyr^{-1})	SAR (g cm^{-2} kyr^{-1})	DBD (g cm^{-3})	
849	D	6	6	17	19		68.43	2409.17	3.53	0.15	0.65	2.44	3.06	0.114	0.774	
849	D	6	6	22	24		68.48	2410.83	3.58	0.20	0.54	2.38	3.06	0.092	0.733	
849	D	6	6	24	26		68.49	2411.16	3.67	0.05	0.57		2.85	0.084	0.649	
849	D	6	6	26	27		68.51	2411.83	3.68	0.29	0.62	2.97	2.85	0.097	0.766	
849	D	6	6	28	30		68.53	2412.50	3.47	0.23	0.76	2.81	2.85	0.115	0.741	
849	D	6	6	31	33		68.57	2413.84	3.60	0.05	0.68	2.45	2.85	0.088	0.739	
849	D	6	6	33	35		68.59	2414.51	3.61	0.16	0.53	2.79	2.85	0.109	0.814	
849	D	6	6	36	37		68.61	2415.18	3.65	0.02	0.58	2.31	2.85	0.098	0.738	
849	D	6	6	38	40		68.65	2416.53	3.66	-0.03	0.54	2.56	2.85	0.102	0.739	
849	D	6	6	41	43		68.67	2417.21	3.65	-0.08	0.63	2.69	2.85	0.102	0.747	
849	D	6	6	43	45		68.69	2417.89	3.65	0.02	0.55	2.30	2.85	0.105	0.642	
849	D	6	6			46	68.71	2418.57	3.75	-0.08			2.85		0.661	*)
849	D	6	6	48	50		68.73	2419.25	3.65	-0.03	0.41	2.04	2.85	0.164	0.681	
849	D	6	6	51	53		68.77	2420.61	3.63	0.00	0.45	2.39	2.85	0.088	0.730	
849	D	6	6	53	55		68.78	2420.96	3.77	-0.28	0.41	2.28	2.85	0.110	0.803	
849	D	6	6	56	57		68.81	2421.99	3.71	-0.25	0.43	2.04	2.85	0.148	0.725	
849	D	6	6	57	59		68.83	2422.67	3.84	-0.16	0.43	2.26	2.85	0.219	0.807	
849	D	6	6	63	65		68.89	2424.75	3.83	-0.21	0.41	1.86	2.85	0.111	0.727	
849	D	6	6	66	67		68.91	2425.44	3.98	-0.12	0.60	2.17	2.85	0.139	0.738	
849	D	6	6	68	70		68.95	2426.84	3.69	-0.52	0.35	2.07	2.85	0.079	0.861	
849	D	6	6	71	73		68.97	2427.54	3.88	-0.19	0.50	1.72	2.85	0.176	0.875	
849	D	6	6	73	75		68.98	2427.89	4.16	-0.32	0.62	1.96	2.85	0.139	0.845	
849	D	6	6			76	69.01	2428.95	3.79	-0.28			2.85		0.812	*)
849	D	6	6	78	80		69.04	2430.01	4.18	-0.23	0.58	2.21	2.85	0.141	0.779	
849	D	6	6	81	82		69.07	2431.08	4.27	-0.21	0.21	2.09	2.85	0.113	0.875	
849	D	6	6			86	69.11	2432.51	4.07	-0.24			2.85		0.826	*)
849	D	6	6	86	87		69.12	2432.88	4.22	-0.21	0.67	1.78	2.85	0.121	0.776	
849	D	6	6	89	91		69.15	2433.96	4.02	-0.25	0.63	2.00	2.85	0.090	0.771	
849	D	6	6	91	93		69.17	2434.69	4.19	-0.22	0.61	1.70	2.85	0.135	0.822	
849	D	6	6	93	95		69.18	2435.06	4.25	-0.07	0.48	2.14	2.85	0.219	0.847	
849	D	6	6			96	69.21	2436.16	4.02	-0.22			2.85		0.860	*)
849	D	6	6	97	98		69.23	2436.90	4.17	-0.28	0.42	1.79	2.85	0.221	0.866	
849	D	6	6	98	100		69.24	2437.27	4.18	-0.22	0.57	1.73	2.85	0.191	0.897	
849	D	6	6	100	102		69.26	2438.02	3.99	-0.33	0.53	2.07	2.85	0.124	0.827	
849	D	6	6	102	104		69.28	2438.77	4.13	-0.34	0.65	2.15	2.85	0.125	0.757	
849	D	6	6	104	105		69.29	2439.15	3.98	-0.31	0.54	2.09	2.38	0.118	0.788	
849	D	6	6	105	107		69.30	2439.53	4.05	-0.31	0.43	2.03	2.38	0.117	0.818	
849	D	6	6	108	110		69.33	2440.68	4.01	-0.35	0.52	1.75	2.38	0.048	0.801	
849	D	6	6			116	69.41	2443.79	4.02	-0.33			2.38		0.739	*)
849	D	6	6	120	121		69.45	2445.38	4.15	-0.34	0.46	2.32	2.38		0.676	
849	D	6	6	122	124		69.48	2446.59	4.10	-0.57	0.55	2.36	2.38	0.056	0.660	

Site	Hole	Core	Section	Top (cm)	Bottom (cm)	Depth *) (cm)	Depth (mcd)	Age (ka)	$\delta^{18}O_{C.\ wuellerstorfi}$ (‰ VPDB)	$\delta^{13}C_{C.\ wuellerstorfi}$ (‰ VPDB)	$\delta^{13}C_{G.\ crassaformis}$ (‰ VPDB)	$\delta^{13}C_{G.\ ruber}$ (‰ VPDB)	LSR (cm kyr^{-1})	SAR (g cm^{-2} kyr^{-1})	DBD (g cm^{-3})	
849	D	6	6	124	126		69.49	2447.00	3.84	-0.09	0.53	2.31	2.38	0.043	0.675	
849	D	6	6	126	127		69.51	2447.82	3.94	-0.14	0.56	2.50	2.38	0.050	0.667	
849	D	6	6	128	130		69.54	2449.06	3.78	-0.39	0.53	2.03	2.38	0.074	0.752	
849	D	6	6	131	133		69.56	2449.89	3.73	-0.13	0.66	2.17	2.38		0.589	
849	D	6	6	133	135		69.58	2450.74	3.84	-0.23	0.73	2.36	2.38	0.052	0.651	
849	D	6	6			136	69.61	2452.02	3.58	-0.22			2.38		0.702	*)
849	D	6	6	139	140		69.65	2452.88	3.75	-0.29	0.61	2.69	2.38	0.055	0.673	
849	D	6	6	141	143		69.68	2455.05	3.62	0.11	0.59	2.43	2.38	0.059	0.594	
849	D	6	6	143	145		69.69	2455.49	3.46	0.12		2.55	2.38	0.064	0.631	
849	D	6	6			146	69.71	2456.38	3.45	0.17			2.38		0.668	*)
849	D	6	6	147	149		69.72	2456.82	3.51	0.27	0.82	2.73	2.38	0.095	0.705	
849	C	7	1	80	82		69.76	2458.61	3.72	0.38	0.51	2.72	2.38	0.053	0.743	
849	C	7	1	82	84		69.78	2459.50	3.71	0.33	0.52	2.48	2.38	0.064	0.741	
849	D	6	7	4	7		69.81	2460.86	3.60	0.31	0.51	2.36	2.38	0.077	0.758	
849	C	7	1	86	88		69.82	2461.31	3.47	0.40	0.55	2.82	2.38	0.061	0.730	
849	D	6	7	8	10		69.83	2461.77	3.55	0.18	0.76	2.71	2.38	0.069	0.676	
849	C	7	1	88	90		69.84	2462.22	3.49	0.26	0.61	2.53	2.38	0.066	0.815	
849	C	7	1	91	93		69.86	2463.14	3.52	0.09	0.61	2.29	2.38	0.066	0.675	
849	C	7	1	93	95		69.90	2464.97	3.45	0.31	0.56	2.51	2.38	0.063	0.708	
849	D	6	7	17	19		69.91	2465.43	3.45	0.03	0.56	2.35	2.21	0.078	0.801	
849	C	7	1	96	98		69.92	2465.89	3.41	0.22	0.44	2.55	2.21	0.082	0.730	
849	C	7	1	98	100		69.94	2466.81	3.36	0.25	0.35	2.64	2.21	0.085	0.858	
849	D	6	7	22	24		69.96	2467.73	3.41	0.19	0.40	2.58	2.21	0.078	0.724	
849	C	7	1	103	104		69.98	2468.65	3.58	-0.05	0.40	2.44	2.21	0.094	0.679	
849	C	7	1	106	108		70.02	2470.50	3.30	0.28	0.36	1.97	2.21	0.109	0.765	
849	C	7	1	108	110		70.04	2471.42	3.38	0.12	0.32	2.59	2.21	0.100	0.743	
849	C	7	1	111	113		70.07	2472.80	3.32	-0.13	0.39	2.10	2.21	0.107	0.741	
849	C	7	1	113	115		70.08	2473.26	3.49	-0.05	0.27	2.18	2.21	0.099	0.648	
849	C	7	1			116	70.11	2474.65	3.42	-0.15			2.21		0.690	*)
849	C	7	1	116	118		70.13	2475.56	3.62	-0.07	0.29	2.25	2.21	0.106	0.733	
849	C	7	1	118	120		70.14	2476.02	3.56	-0.13		1.89	2.21	0.120	0.754	
849	C	7	1	120	122		70.15	2476.48	3.61	-0.25	0.23	2.18	2.21	0.104	0.776	
849	C	7	1	122	124		70.18	2477.85	3.69	-0.20		2.01	2.21	0.125	0.774	
849	C	7	1			126	70.21	2479.22	3.72	-0.30			2.21		0.800	*)
849	C	7	1	126	128		70.22	2479.67	3.70	-0.29	0.29	2.23	2.21	0.165	0.826	
849	C	7	1	128	130		70.25	2481.03	3.93	-0.30	0.22	2.18	2.21	0.124	0.760	
849	C	7	1	131	133		70.27	2481.93	3.96	-0.33	0.16	1.64	2.21	0.121	0.708	
849	C	7	1	133	135		70.29	2482.82	3.85	-0.52	0.12	1.99	2.21	0.116	0.844	
849	C	7	1			136	70.31	2483.71	3.96	-0.48			2.21		0.787	*)
849	C	7	1	136	138		70.32	2484.15	4.07	-0.29		1.62	2.21	0.084	0.730	
849	C	7	1	138	140		70.34	2485.04	3.91	-0.30	0.17	2.01	2.21	0.082	0.776	

Site	Hole	Core	Section	Top (cm)	Bottom (cm)	Depth *) (cm)	Depth (mcd)	Age (ka)	$\delta^{18}O_{C.\ wuellerstorfi}$ (‰ VPDB)	$\delta^{13}C_{C.\ wuellerstorfi}$ (‰ VPDB)	$\delta^{13}C_{G.\ crassaformis}$ (‰ VPDB)	$\delta^{13}C_{G.\ ruber}$ (‰ VPDB)	LSR (cm kyr^{-1})	SAR (g cm^{-2} kyr^{-1})	DBD (g cm^{-3})	
849	C	7	1	141	143		70.36	2485.91	3.99	-0.33		2.29	2.21	0.093	0.735	
849	C	7	1	143	145		70.39	2487.22	4.11	-0.39		1.64	2.43	0.057	0.637	
849	C	7	1			146	70.41	2488.08	3.89	-0.38			2.43		0.702	*)
849	C	7	1	146	148		70.42	2488.51	4.20	-0.21	0.09	2.05	2.43	0.073	0.768	
849	C	7	1	148	150		70.45	2489.79	4.07	-0.04	0.20	1.56	2.43	0.070	0.774	
849	C	7	2	1	3		70.48	2491.05	4.17	-0.20	0.24	1.94	2.43	0.057	0.781	
849	C	7	2	3	5		70.50	2491.88	4.00	-0.23	0.40	2.03	2.43	0.071	0.793	
849	C	7	2	5	7		70.52	2492.71	3.94	-0.20	0.34	1.67	2.43	0.070	0.705	
849	C	7	2	7	9		70.53	2493.11	3.94	-0.11	0.50	1.96	2.43	0.054	0.716	
849	C	7	2	9	11		70.56	2494.33	3.92	-0.16	0.61	1.68	2.43	0.071	0.841	
849	C	7	2	11	13		70.58	2495.13	3.85	-0.48	0.41	2.11	2.43	0.067	0.792	
849	C	7	2	13	15		70.60	2495.93	3.63	-0.04	0.45	2.09	2.43	0.067	0.743	
849	C	7	2	15	17		70.62	2496.72	3.76	-0.05	0.45	1.63	2.43	0.065	0.842	
849	C	7	2	17	19		70.63	2497.12	3.68	-0.03	0.52	2.01	2.43	0.060	0.763	
849	D	7	1	21	23		70.68	2499.09	3.54	-0.12	0.35	2.26	2.43	0.060	0.692	
849	D	7	1	23	25		70.69	2499.48	3.58	-0.11	0.36	2.13	2.43	0.091	0.694	
849	D	7	1	26	28		70.72	2500.66	3.80	-0.31	0.29	2.01	2.43	0.069	0.623	
849	D	7	1	28	30		70.73	2501.05	3.61	-0.09	0.26	2.26	2.43	0.076	0.692	
849	D	7	1	31	33		70.75	2501.84	3.52	-0.21	0.31	2.48	2.33	0.084	0.668	
849	D	7	1	33	35		70.79	2503.42	3.68	-0.29	0.17	2.33	2.33	0.081	0.645	
849	D	7	1	36	38		70.81	2504.22	3.70	-0.42	0.11	2.02	2.33	0.075	0.676	
849	D	7	1	40	42		70.85	2505.83	3.81	-0.48	0.04	1.38	2.33	0.078	0.660	
849	D	7	1	42	44		70.88	2507.06	3.91	-0.56	0.00	1.76	2.33	0.087	0.558	
849	D	7	1	46	47		70.91	2508.30	3.58	-0.57	0.27	1.68	2.33	0.079	0.668	
849	D	7	1	47	49		70.93	2509.15	3.64	-0.41	0.20	1.80	2.33	0.088	0.698	
849	D	7	1	50	52		70.95	2510.00	3.84	-0.41	0.27	1.94	2.33	0.089	0.653	
849	D	7	1	52	54		70.98	2511.30	4.07	-0.67	0.21	1.36	2.33	0.105	0.749	
849	D	7	1	56	58		71.01	2512.62	4.16	-0.61	0.34	1.66	2.33	0.152	0.782	
849	D	7	1	62	64		71.08	2515.79	4.09	-0.57	0.10	1.42	2.33	0.159	0.733	
849	D	7	1			67	71.12	2517.65	4.22	-0.85			2.33		0.748	*)
849	D	7	1	67	69		71.13	2518.11	3.86	-0.27	0.19	1.92	2.33	0.136	0.763	
849	D	7	1	71	73		71.17	2520.00	4.11	-0.58	0.22	1.74	2.33	0.089	0.702	
849	D	7	1	73	74		71.19	2520.95	3.86	-0.58	0.26	2.06	2.33	0.098	0.790	
849	D	7	1	76	78		71.21	2521.90	3.94	-0.69	0.29	2.10	2.33	0.087	0.626	
849	D	7	1	78	80		71.25	2523.82	4.17	-0.48	0.13	1.41	2.33	0.122	0.694	
849	D	7	1	82	84		71.27	2524.78	3.88	-0.37	0.26	1.87	2.33	0.098	0.725	
849	D	7	1	86	88		71.31	2526.71	3.70	0.03	0.22	1.68	2.23	0.114	0.672	
849	D	7	1	88	90		71.35	2528.63	4.13	-0.63	0.29	1.75	2.23	0.071	0.670	
849	D	7	1	91	93		71.37	2529.60	4.31	-0.66	0.25	1.67	2.23	0.063	0.657	
849	D	7	1	93	95		71.39	2530.56	3.99	-0.64	0.23	1.83	2.23	0.079	0.798	
849	D	7	1	96	98		71.41	2531.52	4.08	-0.52	0.25	1.73	2.23	0.061	0.616	

Site	Hole	Core	Section	Top (cm)	Bottom (cm)	Depth *) (cm)	Depth (mcd)	Age (ka)	$\delta^{18}O_{C.\ wuellerstorfi}$ (‰ VPDB)	$\delta^{13}C_{C.\ wuellerstorfi}$ (‰ VPDB)	$\delta^{13}C_{G.\ crassaformis}$ (‰ VPDB)	$\delta^{13}C_{G.\ ruber}$ (‰ VPDB)	LSR (cm kyr^{-1})	SAR (g cm^{-2} kyr^{-1})	DBD (g cm^{-3})	
849	D	7	1	98	100		71.43	2532.47	4.03	-0.50	0.14	1.77	2.23	0.044	0.575	
849	D	7	1	101	102		71.47	2534.38	4.12	-0.49	0.28	1.96	2.23	0.047	0.551	
849	D	7	1	102	104		71.48	2534.85	4.00	-0.53	0.30	1.84	2.23	0.059	0.586	
849	D	7	1			107	71.52	2536.73	3.89	-0.22			2.23		0.591	*)
849	D	7	1	109	111		71.54	2537.65	3.91	-0.39	0.25	1.86	2.23	0.042	0.422	
849	D	7	1	117	118		71.62	2541.30	3.73	-0.24	0.41	2.09	2.23	0.048	0.509	
849	D	7	1	118	120		71.63	2541.74	3.62	-0.18	0.48	2.21	2.23	0.058	0.596	
849	D	7	1	121	123		71.66	2543.07	3.64	-0.05	0.46	2.32	2.23	0.052	0.684	
849	D	7	1	123	125		71.68	2543.94	3.48	-0.24	0.48	2.32	2.23	0.045	0.683	
849	D	7	1			127	71.72	2545.65	3.45	0.07			2.23		0.680	*)
849	D	7	1	127	128		71.73	2546.07	3.50	0.00	0.60	2.14	2.23	0.066	0.678	
849	D	7	1	128	130		71.75	2546.91	3.59	-0.03	0.47	2.36	2.23	0.079	0.697	
849	D	7	1	131	133		71.77	2547.74	3.51	-0.21	0.60	2.41	2.23	0.044	0.716	
849	D	7	1	133	135		71.80	2548.96	3.56	0.00	0.64	2.50	2.23	0.038	0.700	
849	D	7	1			136	71.81	2549.36	3.26	-0.01			2.23		0.683	*)
849	D	7	1	139	140		71.85	2550.95	3.49	-0.06	0.75	2.23	2.23	0.051	0.665	
849	D	7	1	141	143		71.87	2551.72	3.18	0.10	0.51	2.46	2.23	0.055	0.689	
849	D	7	1	143	145		71.89	2552.49	3.30	0.02	0.71	2.53	3.41	0.065	0.673	
849	D	7	1	147	149		71.91	2553.24	3.40	0.12	0.66	2.21	3.41	0.090	0.703	
849	D	7	2	1	3		71.98	2555.80	3.31	0.05	0.68	2.52	3.41	0.092	0.733	
849	D	7	2	3	5		72.00	2556.50	3.32	0.03	0.55	2.66	3.41	0.094	0.763	
849	D	7	2			6	72.01	2556.85	3.22	0.08			3.41		0.695	*)
849	D	7	2	6	8		72.02	2557.20	3.37	-0.22	0.42	2.79	3.41	0.085	0.627	
849	D	7	2	8	10		72.04	2557.88	3.38	-0.04	0.42	2.54	3.41	0.167	0.769	
849	D	7	2			16	72.11	2560.17	3.43	-0.01	0.67		3.41		0.742	*)
849	D	7	2	17	18		72.12	2560.49	3.61	0.15		2.77	3.41	0.081	0.714	
849	D	7	2	18	20		72.13	2560.80	3.49	0.12	0.64	2.54	3.41	0.074	0.610	
849	D	7	2	21	23		72.18	2562.32	3.64	0.02	0.49	2.32	3.41	0.112	0.695	
849	D	7	2	23	25		72.19	2562.62	3.57	0.14	0.47	2.46	3.41	0.105	0.678	
849	D	7	2	26	28		72.22	2563.48	3.95	0.20	0.41	2.54	3.41	0.154	0.784	
849	D	7	2	28	30		72.23	2563.77	3.82	0.13	0.43	2.41	3.41	0.126	0.683	
849	D	7	2	31	33		72.28	2565.14	3.84	-0.01	0.58	2.62	3.41	0.088	0.736	
849	D	7	2	33	35		72.29	2565.41	3.82	0.11	0.65	2.36	3.41	0.099	0.788	
849	D	7	2			36	72.31	2565.95	3.02	-0.03			3.41		0.769	*)
849	D	7	2	36	38		72.32	2566.21	3.14	0.14	0.54	2.26	3.41	0.089	0.751	
849	D	7	2	38	40		72.33	2566.47	3.67	-0.19	0.65	2.30	3.41	0.081	0.643	
849	D	7	2	41	43		72.38	2567.77	3.66	-0.01	0.51	2.64	3.41	0.126	0.652	
849	D	7	2	43	45		72.39	2568.03	3.73	0.10	0.55	2.39	3.41	0.118	0.660	
849	D	7	2			46	72.41	2568.54	3.70	0.01			3.41		0.686	*)
849	D	7	2	46	48		72.42	2568.79	3.71	0.02	0.61	2.53	3.41	0.090	0.711	
849	D	7	2	48	50		72.43	2569.05	3.73	0.06	0.54	2.22	3.41	0.069	0.686	

Site	Hole	Core	Section	Top (cm)	Bottom (cm)	Depth *) (cm)	Depth (mcd)	Age (ka)	$\delta^{18}O_{C.\ wuellerstorfi}$ (‰ VPDB)	$\delta^{13}C_{C.\ wuellerstorfi}$ (‰ VPDB)	$\delta^{13}C_{G.\ crassaformis}$ (‰ VPDB)	$\delta^{13}C_{G.\ ruber}$ (‰ VPDB)	LSR (cm kyr^{-1})	SAR (g cm^{-2} kyr^{-1})	DBD (g cm^{-3})	
849	D	7	2	51	53		72.45	2569.56	3.76	0.04	0.61	2.41	3.40	0.089	0.690	
849	D	7	2	53	55		72.49	2570.58	3.69	-0.04	0.56	2.44	3.40	0.128	0.694	
849	D	7	2	56	58		72.51	2571.10	3.62	-0.11	0.59	2.65	3.40	0.093	0.627	
849	D	7	2	62	63		72.58	2572.94	3.78	0.19	0.53	2.52	3.40	0.089	0.689	
849	D	7	2	63	65		72.59	2573.21	3.69	0.07	0.59	2.55	3.40	0.065	0.566	
849	D	7	2	66	68		72.61	2573.76	3.63	-0.39	0.69	2.59	3.40	0.096	0.765	
849	D	7	2	68	70		72.63	2574.32	3.67	-0.01	0.60	2.40	3.40	0.087	0.711	
849	D	7	2	71	73		72.68	2575.75	3.59	0.07	0.56	2.49	3.40	0.059	0.651	
849	D	7	2	73	75		72.69	2576.05	3.63	0.08	0.52	2.60	3.40	0.072	0.591	
849	D	7	2	76	78		72.71	2576.65	3.52	0.12		2.63	3.40	0.065	0.670	
849	D	7	2	78	80		72.75	2577.89	3.44	0.13	0.70	2.60	3.40	0.083	0.694	
849	D	7	2	81	83		72.78	2578.84	3.31	-0.01	0.51	2.62	3.40	0.080	0.707	
849	D	7	2	83	85		72.79	2579.17	3.38	0.03	0.38	2.52	3.40	0.101	0.721	
849	D	7	2			86	72.81	2579.82	3.39	0.21			3.40		0.723	*)
849	D	7	2	87	88		72.83	2580.48	3.26	0.01	0.48	2.67	3.40	0.100	0.726	
849	D	7	2	88	90		72.85	2581.15	3.31	0.15	0.46	2.49	3.40	0.109	0.728	
849	D	7	2	91	93		72.87	2581.83	3.21	0.00	0.46	2.42	3.40	0.149	0.765	
849	D	7	2	93	95		72.89	2582.52	3.29	-0.01	0.47	2.27	3.40	0.126	0.717	
849	D	7	2	96	98		72.91	2583.21	3.50	-0.03	0.36	2.44	3.40		0.708	
849	D	7	2	98	100		72.95	2584.61	3.39	-0.31	0.42	2.16	3.40	0.131	0.782	
849	D	7	2	101	103		72.97	2585.31	3.41	-0.01	0.32	2.58	3.40	0.126	0.815	
849	D	7	2	103	105		72.98	2585.67	3.33	0.05	0.36	2.45	2.83	0.118	0.725	
849	D	7	2	106	107		73.01	2586.74	3.40	-0.14	0.22	2.43	2.83	0.069	0.646	
849	D	7	2	107	109		73.03	2587.45	3.36	0.10	0.35	2.43	2.83	0.080	0.678	
849	D	7	2	113	115		73.09	2589.61	3.49	-0.20	0.24	2.35	2.83	0.077	0.728	
849	D	7	2			116	73.11	2590.33	3.49	-0.14			2.83		0.736	*)
849	D	7	2	116	118		73.12	2590.69	3.21	-0.22	0.24	2.30	2.83	0.101	0.743	
849	D	7	2	118	120		73.14	2591.41	3.55	-0.19	0.26	2.24	2.83	0.104	0.747	
849	D	7	2	121	123		73.16	2592.13	3.44	-0.25	0.24		2.83	0.114	0.695	
849	D	7	2	123	125		73.19	2593.21	3.44	-0.14	0.26	1.85	2.83	0.056	0.624	
849	D	7	2	126	128		73.21	2593.92	3.32	-0.22	0.20	2.15	2.83	0.100	0.815	
849	D	7	2	128	130		73.23	2594.63	3.55	0.15	0.65	2.65	2.83	0.126	0.822	
849	D	7	2	130	132		73.26	2595.69	3.69	-0.38	0.15	2.11	2.83	0.071	0.741	
849	D	7	2	132	134		73.28	2596.39	3.82	-0.28	0.21	2.03	2.83	0.070	0.670	
849	D	7	2			136	73.31	2597.43	3.97	-0.38			2.83		0.655	*)
849	D	7	2	136	138		73.33	2598.13	3.89	-0.56	0.19	1.98	2.83	0.075	0.640	
849	D	7	2	138	140		73.35	2598.83	3.84	-0.56	0.16	2.03	2.83	0.064	0.642	
849	D	7	2	141	143		73.37	2599.53	4.03	-0.45		1.86	2.83	0.059	0.643	
849	D	7	2	143	145		73.40	2600.59	3.84	-0.52	0.24	2.06	2.83	0.048	0.642	
849	D	7	2			146	73.41	2600.94	4.03	-0.31			2.83		0.661	*)
849	D	7	2	146	148		73.43	2601.66	4.04	-0.31	0.33	2.24	2.83	0.050	0.681	

Site	Hole	Core	Section	Top (cm)	Bottom (cm)	Depth *) (cm)	Depth (mcd)	Age (ka)	$\delta^{18}O_{C.\ wuellerstorfi}$ (‰ VPDB)	$\delta^{13}C_{C.\ wuellerstorfi}$ (‰ VPDB)	$\delta^{13}C_{G.\ crassaformis}$ (‰ VPDB)	$\delta^{13}C_{G.\ ruber}$ (‰ VPDB)	LSR (cm kyr^{-1})	SAR (g cm^{-2} kyr^{-1})	DBD (g cm^{-3})	
849	D	7	2	148	149		73.44	2602.01	3.86	-0.18	0.45	2.28	2.83	0.042	0.700	
849	D	7	3	1	3		73.48	2603.47	3.94	-0.30	0.60	1.78	2.83	0.060	0.720	
849	D	7	3	3	5		73.50	2604.21	4.06	-0.31	0.35	2.02	2.83	0.060	0.739	
849	D	7	3			6	73.51	2604.58	3.74	-0.19			2.14		0.784	*)
849	D	7	3	6	8		73.52	2604.96	3.63	-0.17	0.46	2.46	2.14	0.048	0.828	
849	D	7	3	8	10		73.53	2605.34	3.97	-0.09	0.51	2.42	2.14	0.039	0.751	
849	D	7	3			16	73.61	2608.50	3.58	0.14			2.14		0.770	*)
849	D	7	3	16	18		73.62	2608.91	3.62	0.13	0.49	2.75	2.14	0.051	0.790	
849	D	7	3	18	20		73.63	2609.33	3.70	-0.10	0.67	2.63	2.14	0.085	0.769	
849	D	7	3	21	23		73.68	2611.48	3.62	-0.36	0.22	2.13	2.14	0.051	0.726	
849	D	7	3	23	25		73.70	2612.38	3.67	0.10	0.58	2.33	2.14	0.041	0.683	
849	D	7	3			26	73.71	2612.83	3.58	0.14			2.14		0.766	*)
849	D	7	3	26	28		73.72	2613.29	3.73	-0.05	0.54	2.40	2.14	0.065	0.848	
849	D	7	3	28	30		73.73	2613.76	3.50	0.10			2.14	0.039	0.623	
849	D	7	3	31	33		73.78	2616.18	3.67	0.14		2.64	2.14	0.039	0.616	
849	D	7	3	33	35		73.80	2617.18	3.55	-0.03	0.60	2.59	2.14	0.051	0.717	
849	D	7	3	35	36		73.81	2617.69	3.57	0.14	0.72	2.33	2.14	0.051	0.675	
849	D	7	3	37	38		73.82	2618.21	3.52	0.08	0.57	2.48	2.14	0.053	0.634	
849	D	7	3	38	40		73.84	2619.25	3.49	0.15	0.66	2.57	2.14	0.047	0.594	
849	D	7	3	41	43		73.88	2621.38	3.46	0.19	0.71	2.49	2.14	0.045	0.611	
849	D	7	3	43	45		73.89	2621.92	3.41	0.00	0.68	2.46	2.14	0.057	0.705	
849	D	7	3			46	73.91	2623.02	3.52	0.16			2.14		0.742	*)
849	D	7	3	46	48		73.92	2623.57	3.31	-0.11		2.57	2.14	0.069	0.779	
849	D	7	3	48	50		73.94	2624.69	3.40	0.20	0.59	2.36	2.14	0.053	0.632	
849	D	7	3	51	53		73.98	2626.96	3.24	0.10	0.51	2.33	1.69	0.046	0.706	
849	D	7	3	53	55		73.99	2627.53	3.28	0.11	0.54	2.26	1.69	0.045	0.781	
849	D	7	3			56	74.01	2628.68	3.32	0.03			1.69		0.754	*)
849	D	7	3	56	58		74.02	2629.26	3.41	0.12	0.53	2.47	1.69	0.051	0.728	
849	D	7	3	63	65		74.09	2633.36	3.44	-0.07	0.58		1.69	0.068	0.774	
849	D	7	3			66	74.11	2634.54	3.54	-0.16			1.69		0.747	*)
849	D	7	3	66	68		74.12	2635.14	3.51	0.00	0.51	2.53	1.69	0.058	0.719	
849	D	7	3	71	73		74.17	2637.51	3.40	-0.18	0.46	1.97	1.69	0.059	0.808	
849	D	7	3			76	74.21	2640.47	3.62	-0.06			1.69		0.784	*)

Additional references

Mix, A.C., Pisias, N.G., Rugh, W., Wilson, J., Morey, A., Hagelberg, T.K. (1995). Benthic foraminifer stable isotope record from Site 849 (0–5 Ma): Local and global climate changes. In Proceedings of the Ocean Drilling Program, Sci. Results, 138, pp. 371–412, Ocean Drill. Program, College Station, Tex.

Shackleton, N.J., Hall, M.A. (1984). Oxygen and carbon isotope stratigraphy of Deep Sea Drilling Project Hole 552A: Plio-Pleistocene Glacial History. In Proceedings of the Deep Sea Drilling Project, Initial Rep., 81, pp. 599–609, Deep Sea Drill. Proj., Washington, D.C.

Spero, H.J., Mielke, K.M., Kalve, E.M., Lea, D.W., Pak, D.K. (2003). Multispecies approach to reconstructing eastern equatorial Pacific thermocline hydrography during the past 360 kyr. Paleoceanography, 18(1), 1022, doi:10.1029/2002PA000814.

APPENDIX B.2

DATA TABLES FOR CHAPTER 5

Table B.2.1. Site 849 benthic foraminiferal (*Cibicidoides wuellerstorfi*) $\delta^{18}O$ together with planktic foraminiferal (*Globigerinoides ruber*) $\delta^{18}O$ and Mg/Ca as a proxy for sea-surface temperature (SST) and the oxygen-isotope composition of seawater ($\delta^{18}O_{seawater}$) for ~2.75 to 2.4 Ma. The latter was further corrected for global ice volume ($\delta^{18}O_{sw\text{-}ivc}$). $\delta^{18}O$ values of *C. wuellerstorfi* are adjusted for species-specific offset from equilibrium by the addition of +0.64‰ (Shackleton and Hall, 1984). *Cibicidoides wuellerstorfi* stable-isotope data marked with*) are from Mix et al. (1995). Reported Mg/Ca values of *G. ruber* are normalized to the ECRM752-1 standard. Further this table includes linear sedimentation rates (LSR) and a planktic foraminiferal fragmentation index (FFI).

Site	Hole	Core	Section	Top (cm)	Bottom (cm)	Depth *) (cm)	Depth (mcd)	Age (ka)	$\delta^{18}O_{C.\ wuellerstorfi}$ (‰ VPDB)	$\delta^{18}O_{G.\ ruber}$ (‰ VPDB)	$Mg/Ca_{G.\ ruber}$ (mmol mol^{-1})	SST (°C)	$\delta^{18}O_{seawater}$ (‰ SMOW)	$\delta^{18}O_{sw\text{-}ivc}$ (‰ SMOW)	LSR (cm kyr^{-1})	FFI (%)	
849	D	6	5			96	67.71	2385.57	3.57						3.0618		*)
849	D	6	5	102	104		67.78	2387.85	3.66	-0.87	3.03	24.81	1.47	1.42	3.0618		
849	D	6	5			106	67.81	2388.83	3.63						3.0618		*)
849	D	6	5	106	108		67.83	2389.49	3.89	-0.84	2.75	23.70	1.27	1.05	3.0618		
849	D	6	5	108	110		67.84	2389.81	3.77	-0.84	2.55	22.87	1.09	0.96	3.0618		
849	D	6	5	114	116		67.89	2391.45	3.72	-0.74	2.74	23.65	1.35	1.26	3.0618		
849	D	6	5	116	118		67.91	2392.10	3.84	-0.86	2.76	23.76	1.26	1.08	3.0618		
849	D	6	5	121	123		67.97	2394.06	3.64	-0.75	2.60	23.09	1.23	1.20	3.0618		
849	D	6	5	123	125		67.98	2394.39	3.57	-0.79	2.81	23.93	1.37	1.39	3.0618		
849	D	6	5			126	68.01	2395.37	3.68						3.0618		*)
849	D	6	5	127	129		68.03	2396.02	3.46	-0.62	2.85	24.13	1.57	1.68	3.0618		
849	D	6	5	129	131		68.05	2396.67	3.68	-0.90	2.76	23.75	1.21	1.15	3.0618		
849	D	6	5	131	132		68.06	2397.16			2.87	24.17			3.0618		
849	D	6	5	132	134		68.08	2397.65	3.72	-0.63	2.72	23.57	1.44	1.35	3.0618		
849	D	6	5	134	136		68.10	2398.31	3.70	-0.79	3.21	25.45	1.67	1.60	3.0618		
849	D	6	5			136	68.11	2398.64	3.68						3.0618		*)
849	D	6	5	137	139		68.12	2398.96	3.64	-0.88	2.55	22.87	1.05	1.02	3.0618	6.23	
849	D	6	5	139	141		68.15	2399.94	3.43	-0.94	3.25	25.60	1.56	1.69	3.0618		
849	D	6	5	141	143		68.17	2400.60	3.43	-0.92	2.92	24.39	1.33	1.46	3.0618		
849	D	6	5	143	145		68.19	2401.26	3.68	-1.25	2.90	24.31	0.98	0.92	3.0618		
849	D	6	5	146	148		68.21	2401.91	3.62	-1.04	2.98	24.60	1.25	1.24	3.0618		
849	D	6	6	1	3		68.27	2403.88	3.72	-1.00	2.86	24.15	1.20	1.10	3.0618		
849	D	6	6	3	5		68.29	2404.54	3.56	-0.96	2.88	24.25	1.26	1.29	3.0618		
849	D	6	6			6	68.31	2405.20	3.63						3.0618		*)

Site	Hole	Core	Section	Top (cm)	Bottom (cm)	Depth *) (cm)	Depth (mcd)	Age (ka)	$\delta^{18}O_{C.\ wuellerstorfi}$ (‰ VPDB)	$\delta^{18}O_{G.\ ruber}$ (‰ VPDB)	$Mg/Ca_{G.\ ruber}$ (mmol mol^{-1})	SST (°C)	$\delta^{18}O_{seawater}$ (‰ SMOW)	$\delta^{18}O_{sw\text{-}ivc}$ (‰ SMOW)	LSR (cm kyr^{-1})	FFI (%)	
849	D	6	6	6	8		68.32	2405.53	3.49	-0.97	2.68	23.43	1.08	1.16	3.0618		
849	D	6	6	13	15		68.39	2407.84	3.61	-1.06	2.96	24.53	1.22	1.21	3.0618		
849	D	6	6	15	17		68.41	2408.50	3.47	-1.02	3.30	25.76	1.51	1.61	3.0618		
849	D	6	6	17	19		68.43	2409.17	3.53	-0.73					3.0618		
849	D	6	6	22	24		68.48	2410.83	3.58	-0.58	2.89	24.27	1.64	1.66	3.0618	5.26	
849	D	6	6	24	26		68.49	2411.16	3.67		2.88	24.25			2.8539		
849	D	6	6	26	27		68.51	2411.83	3.68	-1.13	2.90	24.30	1.10	1.04	2.8539		
849	D	6	6	28	30		68.53	2412.50	3.47	-1.03	2.80	23.93	1.12	1.22	2.8539		
849	D	6	6	31	33		68.57	2413.84	3.60	-0.67	2.78	23.84	1.46	1.47	2.8539		
849	D	6	6	33	35		68.59	2414.51	3.61	-0.99	2.96	24.55	1.29	1.28	2.8539		
849	D	6	6	36	37		68.61	2415.18	3.65	-0.66	3.47	26.32	1.99	1.95	2.8539		
849	D	6	6	38	40		68.65	2416.53	3.66	-0.90	3.09	25.02	1.47	1.43	2.8539		
849	D	6	6	41	43		68.67	2417.21	3.65	-0.90					2.8539		
849	D	6	6	43	45		68.69	2417.89	3.65	-0.84	2.96	24.55	1.44	1.40	2.8539		
849	D	6	6			46	68.71	2418.57	3.75						2.8539		*)
849	D	6	6	48	50		68.73	2419.25	3.65	-0.55	3.12	25.11	1.85	1.81	2.8539		
849	D	6	6	51	53		68.77	2420.61	3.63	-0.80	3.10	25.04	1.59	1.56	2.8539		
849	D	6	6	53	55		68.78	2420.96	3.77	-0.25	2.75	23.70	1.85	1.73	2.8539		
849	D	6	6	56	57		68.81	2421.99	3.71	-0.55	3.06	24.91	1.81	1.72	2.8539		
849	D	6	6	57	59		68.83	2422.67	3.84	-1.05	2.73	23.64	1.04	0.86	2.8539	5.82	
849	D	6	6	63	65		68.89	2424.75	3.83	-0.43	3.10	25.04	1.95	1.78	2.8539		
849	D	6	6	66	67		68.91	2425.44	3.98	-0.63	2.64	23.25	1.38	1.10	2.8539		
849	D	6	6	68	70		68.95	2426.84	3.69	-0.13	2.45	22.40	1.70	1.63	2.8539		
849	D	6	6	71	73		68.97	2427.54	3.88	0.07	2.58	22.98	2.02	1.81	2.8539		
849	D	6	6	73	75		68.98	2427.89	4.16	-0.02	2.38	22.09	1.75	1.33	2.8539		
849	D	6	6			76	69.01	2428.95	3.79						2.8539		*)
849	D	6	6	78	80		69.04	2430.01	4.18	-0.67	2.31	21.75	1.02	0.59	2.8539		
849	D	6	6	81	82		69.07	2431.08	4.27	-0.38	2.39	22.14	1.40	0.89	2.8539		
849	D	6	6			86	69.11	2432.51	4.07						2.8539		*)
849	D	6	6	86	87		69.12	2432.88	4.22	-0.05					2.8539		
849	D	6	6	89	91		69.15	2433.96	4.02	-0.26	2.33	21.86	1.46	1.15	2.8539		
849	D	6	6	91	93		69.17	2434.69	4.19	-0.08	2.53	22.75	1.83	1.38	2.8539		
849	D	6	6	93	95		69.18	2435.06	4.25	-0.67	2.66	23.34	1.36	0.87	2.8539	5.33	
849	D	6	6			96	69.21	2436.16	4.02						2.8539		*)
849	D	6	6	97	98		69.23	2436.90	4.17	-0.56	2.64	23.23	1.44	1.02	2.8539		
849	D	6	6	98	100		69.24	2437.27	4.18	-0.24	2.51	22.68	1.65	1.22	2.8539		
849	D	6	6	100	102		69.26	2438.02	3.99	-0.49	2.36	22.00	1.26	0.96	2.8539		
849	D	6	6	102	104		69.28	2438.77	4.13	-0.39	2.51	22.66	1.50	1.10	2.8539		
849	D	6	6	104	105		69.29	2439.15	3.98	-0.49	2.51	22.69	1.40	1.12	2.3812		
849	D	6	6	105	107		69.30	2439.53	4.05	-0.54	2.74	23.67	1.56	1.22	2.3812		
849	D	6	6	108	110		69.33	2440.68	4.01	-0.19	2.57	22.93	1.75	1.45	2.3812	6.09	

Site	Hole	Core	Section	Top (cm)	Bottom (cm)	Depth *) (cm)	Depth (mcd)	Age (ka)	$\delta^{18}O_{C.\ wuellerstorfi}$ (‰ VPDB)	$\delta^{18}O_{G.\ ruber}$ (‰ VPDB)	$Mg/Ca_{G.\ ruber}$ (mmol mol^{-1})	SST (°C)	$\delta^{18}O_{seawater}$ (‰ SMOW)	$\delta^{18}O_{sw\text{-}ivc}$ (‰ SMOW)	LSR (cm kyr^{-1})	FFI (%)	
849	D	6	6			116	69.41	2443.79	4.02						2.3812		*)
849	D	6	6	120	121		69.45	2445.38	4.15	-0.60	2.59	23.06	1.37	0.96	2.3812		
849	D	6	6	122	124		69.48	2446.59	4.10	-0.74	2.55	22.86	1.19	0.81	2.3812		
849	D	6	6	124	126		69.49	2447.00	3.84	-0.86	3.02	24.78	1.47	1.29	2.3812		
849	D	6	6	126	127		69.51	2447.82	3.94	-0.75	2.94	24.45	1.51	1.25	2.3812		
849	D	6	6	128	130		69.54	2449.06	3.78	-0.68	2.53	22.79	1.23	1.10	2.3812		
849	D	6	6	131	133		69.56	2449.89	3.73	-0.51					2.3812		
849	D	6	6	133	135		69.58	2450.74	3.84	-0.70	2.54	22.82	1.22	1.04	2.3812		
849	D	6	6			136	69.61	2452.02	3.58						2.3812		*)
849	D	6	6	137	139		69.63	2452.45		-0.78	3.20	25.40	1.68		2.3812		
849	D	6	6	139	140		69.65	2452.88	3.75	-0.62	3.46	26.28	2.02	1.90	2.3812	6.99	
849	D	6	6	141	143		69.68	2455.05	3.62	-1.08	2.99	24.67	1.22	1.21	2.3812		
849	D	6	6	143	145		69.69	2455.49	3.46	-0.78	3.59	26.69	1.95	2.06	2.3812		
849	D	6	6			146	69.71	2456.38	3.45						2.3812		*)
849	D	6	6	147	149		69.72	2456.82	3.51	-0.90	3.11	25.09	1.49	1.56	2.3812		
849	C	7	1	80	82		69.76	2458.61	3.72	-0.89	2.74	23.66	1.21	1.12	2.3812		
849	C	7	1	82	84		69.78	2459.50	3.71	-0.70	3.35	25.94	1.87	1.78	2.3812	5.41	
849	D	6	7	4	7		69.81	2460.86	3.60	-0.84					2.3812		
849	C	7	1	86	88		69.82	2461.31	3.47	-1.19	3.48	26.37	1.47	1.57	2.3812		
849	D	6	7	8	10		69.83	2461.77	3.55	-0.96	2.92	24.38	1.28	1.32	2.3812		
849	C	7	1	88	90		69.84	2462.22	3.49	-1.04	2.89	24.28	1.18	1.26	2.3812		
849	C	7	1	91	93		69.86	2463.14	3.52	-0.91	3.19	25.37	1.54	1.60	2.3812		
849	C	7	1	93	95		69.90	2464.97	3.45	-0.81	2.84	24.06	1.37	1.48	2.3812		
849	D	6	7	17	19		69.91	2465.43	3.45	-1.21	2.77	23.81	0.92	1.03	2.2083	6.36	
849	C	7	1	96	98		69.92	2465.89	3.41	-1.01	2.71	23.55	1.06	1.20	2.2083		
849	C	7	1	98	100		69.94	2466.81	3.36	-0.9	2.71	23.53	1.17	1.35	2.2083		
849	D	6	7	22	24		69.96	2467.73	3.41	-1.01	3.04	24.85	1.34	1.48	2.2083		
849	C	7	1	103	104		69.98	2468.65	3.58	-0.96	2.72	23.58	1.12	1.13	2.2083		
849	C	7	1	106	108		70.02	2470.50	3.30	-0.97	2.86	24.14	1.22	1.45	2.2083		
849	C	7	1	108	110		70.04	2471.42	3.38	-1.18	2.72	23.61	0.90	1.07	2.2083	3.54	
849	C	7	1	111	113		70.07	2472.80	3.32	-0.98	3.00	24.68	1.33	1.54	2.2083		
849	C	7	1	113	115		70.08	2473.26	3.49	-0.79	2.88	24.23	1.42	1.51	2.2083		
849	C	7	1			116	70.11	2474.65	3.42						2.2083		*)
849	C	7	1	116	118		70.13	2475.56	3.62	-0.88	2.80	23.93	1.27	1.26	2.2083		
849	C	7	1	118	120		70.14	2476.02	3.56	-0.80	3.13	25.18	1.61	1.64	2.2083		
849	C	7	1	120	122		70.15	2476.48	3.61	-0.69	2.77	23.79	1.43	1.42	2.2083		
849	C	7	1	122	124		70.18	2477.85	3.69	-0.69	2.87	24.18	1.51	1.44	2.2083		
849	C	7	1			126	70.21	2479.22	3.72						2.2083		*)
849	C	7	1	126	128		70.22	2479.67	3.70	-0.90	2.63	23.20	1.10	1.03	2.2083		
849	C	7	1	128	130		70.25	2481.03	3.93	-0.62	2.51	22.70	1.28	1.03	2.2083	3.74	
849	C	7	1	131	133		70.27	2481.93	3.96	-0.48	3.20	25.40	1.98	1.71	2.2083		

Site	Hole	Core	Section	Top (cm)	Bottom (cm)	Depth *) (cm)	Depth (mcd)	Age (ka)	$\delta^{18}O_{C.\ wuellerstorfi}$ (‰ VPDB)	$\delta^{18}O_{G.\ ruber}$ (‰ VPDB)	$Mg/Ca_{G.\ ruber}$ (mmol mol^{-1})	SST (°C)	$\delta^{18}O_{seawater}$ (‰ SMOW)	$\delta^{18}O_{sw\text{-}ivc}$ (‰ SMOW)	LSR (cm kyr^{-1})	FFI (%)	
849	C	7	1	133	135		70.29	2482.82	3.85	-0.54	2.74	23.66	1.55	1.37	2.2083		
849	C	7	1			136	70.31	2483.71	3.96						2.2083		*)
849	C	7	1	136	138		70.32	2484.15	4.07	-0.44	2.84	24.07	1.74	1.39	2.2083		
849	C	7	1	138	140		70.34	2485.04	3.91	-0.51	2.59	23.04	1.46	1.23	2.2083		
849	C	7	1	141	143		70.36	2485.91	3.99	-0.51	2.67	23.36	1.52	1.23	2.2083		
849	C	7	1	143	145		70.39	2487.22	4.11	-0.47					2.4341		
849	C	7	1			146	70.41	2488.08	3.89						2.4341	4.21	*)
849	C	7	1	146	148		70.42	2488.51	4.20	-0.37	2.62	23.16	1.62	1.17	2.4341		
849	C	7	1	148	150		70.45	2489.79	4.07	-0.52					2.4341		
849	C	7	2	1	3		70.48	2491.05	4.17	-0.57	2.56	22.91	1.37	0.95	2.4341		
849	C	7	2	3	5		70.50	2491.88	4.00	-0.67	2.49	22.61	1.21	0.91	2.4341	5.42	
849	C	7	2	5	7		70.52	2492.71	3.94	-0.47	2.71	23.55	1.60	1.35	2.4341		
849	C	7	2	7	9		70.53	2493.11	3.94	-0.54	2.76	23.76	1.58	1.33	2.4341		
849	C	7	2	9	11		70.56	2494.33	3.92	-0.59					2.4341		
849	C	7	2	11	13		70.58	2495.13	3.85	-0.61	2.68	23.44	1.43	1.25	2.4341	5.27	
849	C	7	2	13	15		70.60	2495.93	3.63	-0.33	2.76	23.74	1.78	1.76	2.4341		
849	C	7	2	15	17		70.62	2496.72	3.76	-0.70	2.60	23.10	1.28	1.16	2.4341		
849	C	7	2	17	19		70.63	2497.12	3.68	-0.45	2.68	23.41	1.59	1.53	2.4341		
849	C	7	2	19	21		70.66	2498.10			2.73	23.62			2.4341		
849	D	7	1	21	23		70.68	2499.09	3.54	-0.39	2.68	23.42	1.66	1.70	2.4341		
849	D	7	1	23	25		70.69	2499.48	3.58	-0.57					2.4341		
849	D	7	1	26	28		70.72	2500.66	3.80	-0.74	3.24	25.54	1.75	1.60	2.4341	5.46	
849	D	7	1	28	30		70.73	2501.05	3.61	-0.89	2.85	24.12	1.30	1.29	2.4341		
849	D	7	1	31	33		70.75	2501.84	3.52	-0.93	3.05	24.86	1.42	1.48	2.3308		
849	D	7	1	33	35		70.79	2503.42	3.68	-0.93	2.80	23.91	1.22	1.16	2.3308		
849	D	7	1	36	38		70.81	2504.22	3.70	-0.52	3.12	25.15	1.89	1.81	2.3308		
849	D	7	1	38	39		70.83	2505.02			3.55	26.58			2.3308		
849	D	7	1	40	42		70.85	2505.83	3.81	-0.03	2.75	23.73	2.08	1.92	2.3308	4.39	
849	D	7	1	42	44		70.88	2507.06	3.91	-0.62	2.69	23.46	1.44	1.21	2.3308		
849	D	7	1	46	47		70.91	2508.30	3.58	-0.46	2.70	23.51	1.60	1.62	2.3308		
849	D	7	1	47	49		70.93	2509.15	3.64	-0.82	2.70	23.50	1.24	1.21	2.3308		
849	D	7	1	50	52		70.95	2510.00	3.84	-0.80	2.69	23.45	1.25	1.07	2.3308		
849	D	7	1	52	54		70.98	2511.30	4.07	-0.14	2.66	23.34	1.89	1.53	2.3308		
849	D	7	1	56	58		71.01	2512.62	4.16	-0.54	2.42	22.30	1.27	0.85	2.3308		
849	D	7	1	62	64		71.08	2515.79	4.09	0.11	2.64	23.27	2.12	1.76	2.3308	4.36	
849	D	7	1			67	71.12	2517.65	4.22						2.3308		*)
849	D	7	1	67	69		71.13	2518.11	3.86	-0.48	2.50	22.63	1.40	1.21	2.3308		
849	D	7	1	71	73		71.17	2520.00	4.11	-0.11	2.48	22.57	1.76	1.37	2.3308		
849	D	7	1	73	74		71.19	2520.95	3.86	-0.22	2.46	22.44	1.62	1.43	2.3308	3.85	
849	D	7	1	76	78		71.21	2521.90	3.94	-0.51	2.49	22.61	1.37	1.11	2.3308		
849	D	7	1	78	80		71.25	2523.82	4.17	0.10	2.48	22.56	1.97	1.54	2.3308		

Site	Hole	Core	Section	Top (cm)	Bottom (cm)	Depth *) (cm)	Depth (mcd)	Age (ka)	$\delta^{18}O_{C.\ wuellerstorfi}$ (‰ VPDB)	$\delta^{18}O_{G.\ ruber}$ (‰ VPDB)	$Mg/Ca_{G.\ ruber}$ (mmol mol^{-1})	SST (°C)	$\delta^{18}O_{seawater}$ (‰ SMOW)	$\delta^{18}O_{sw\text{-}ivc}$ (‰ SMOW)	LSR (cm kyr^{-1})	FFI (%)	
849	D	7	1	82	84		71.27	2524.78	3.88	-0.40	2.35	21.95	1.34	1.13	2.3308		
849	D	7	1	86	88		71.31	2526.71	3.70	-0.34	2.86	24.14	1.85	1.78	2.2254	4.36	
849	D	7	1	88	90		71.35	2528.63	4.13	-0.61	2.56	22.90	1.33	0.93	2.2254		
849	D	7	1	91	93		71.37	2529.60	4.31	-0.34	2.79	23.86	1.79	1.26	2.2254		
849	D	7	1	93	95		71.39	2530.56	3.99	-0.55	2.68	23.41	1.49	1.20	2.2254		
849	D	7	1	96	98		71.41	2531.52	4.08	-0.87					2.2254	6.89	
849	D	7	1	98	100		71.43	2532.47	4.03	-0.55					2.2254		
849	D	7	1	101	102		71.47	2534.38	4.12	-0.19					2.2254		
849	D	7	1	102	104		71.48	2534.85	4.00	-0.49					2.2254		
849	D	7	1			107	71.52	2536.73	3.89						2.2254		*)
849	D	7	1	107	109		71.53	2537.19			2.48	22.53			2.2254		
849	D	7	1	109	111		71.54	2537.65	3.91	-0.77	2.75	23.70	1.33	1.10	2.2254		
849	D	7	1	117	118		71.62	2541.30	3.73	-0.73					2.2254	6.58	
849	D	7	1	118	120		71.63	2541.74	3.62	-0.44	2.66	23.34	1.59	1.58	2.2254		
849	D	7	1	121	123		71.66	2543.07	3.64	-0.57	3.43	26.20	2.06	2.03	2.2254		
849	D	7	1	123	125		71.68	2543.94	3.48	-0.68	2.72	23.58	1.40	1.49	2.2254		
849	D	7	1			127	71.72	2545.65	3.45						2.2254		*)
849	D	7	1	127	128		71.73	2546.07	3.50	-0.99					2.2254		
849	D	7	1	128	130		71.75	2546.91	3.59	-1.01	3.03	24.80	1.33	1.33	2.2254		
849	D	7	1	131	133		71.77	2547.74	3.51	-1.17	2.75	23.71	0.93	1.00	2.2254		
849	D	7	1	133	135		71.80	2548.96	3.56	-1.02	3.00	24.68	1.28	1.31	2.2254	5.07	
849	D	7	1			136	71.81	2549.36	3.26						2.2254		*)
849	D	7	1	139	140		71.85	2550.95	3.49	-1.11	2.95	24.48	1.16	1.24	2.2254		
849	D	7	1	141	143		71.87	2551.72	3.18	-0.72	2.96	24.55	1.56	1.87	2.2254		
849	D	7	1	143	145		71.89	2552.49	3.30	-1.07	3.29	25.71	1.45	1.68	3.4090		
849	D	7	1	147	149		71.91	2553.24	3.40	-0.94	2.94	24.48	1.33	1.47	3.4090		
849	D	7	2	1	3		71.98	2555.80	3.31	-1.18	3.36	25.95	1.39	1.61	3.4090		
849	D	7	2	3	5		72.00	2556.50	3.32	-1.23	2.77	23.80	0.89	1.10	3.4090		
849	D	7	2			6	72.01	2556.85	3.22						3.4090		*)
849	D	7	2	6	8		72.02	2557.20	3.37	-1.04	3.35	25.92	1.52	1.70	3.4090		
849	D	7	2	8	10		72.04	2557.88	3.38	-1.17	3.31	25.78	1.37	1.53	3.4090	7.68	
849	D	7	2			16	72.11	2560.17	3.43						3.4090		*)
849	D	7	2	17	18		72.12	2560.49	3.61	-1.24					3.4090		
849	D	7	2	18	20		72.13	2560.80	3.49	-0.76					3.4090		
849	D	7	2	21	23		72.18	2562.32	3.64	-0.82	2.78	23.84	1.31	1.28	3.4090		
849	D	7	2	23	25		72.19	2562.62	3.57	-0.98	3.19	25.36	1.47	1.49	3.4090		
849	D	7	2	26	28		72.22	2563.48	3.95	-1.01	3.10	25.05	1.37	1.11	3.4090		
849	D	7	2	28	30		72.23	2563.77	3.82	-0.87	2.60	23.06	1.10	0.94	3.4090		
849	D	7	2	31	33		72.28	2565.14	3.84	-0.99	2.75	23.72	1.12	0.94	3.4090		
849	D	7	2	33	35		72.29	2565.41	3.82	-0.72	2.66	23.33	1.31	1.14	3.4090		
849	D	7	2			36	72.31	2565.95	3.02						3.4090		*)

Site	Hole	Core	Section	Top (cm)	Bottom (cm)	Depth *) (cm)	Depth (mcd)	Age (ka)	$\delta^{18}O_{C.\ wuellerstorfi}$ (‰ VPDB)	$\delta^{18}O_{G.\ ruber}$ (‰ VPDB)	$Mg/Ca_{G.\ ruber}$ (mmol mol^{-1})	SST (°C)	$\delta^{18}O_{seawater}$ (‰ SMOW)	$\delta^{18}O_{sw\text{-}ivc}$ (‰ SMOW)	LSR (cm kyr^{-1})	FFI (%)	
849	D	7	2	36	38		72.32	2566.21	3.14	-0.76	2.84	24.06	1.42	1.76	3.4090		
849	D	7	2	38	40		72.33	2566.47	3.67	-0.58					3.4090	5.46	
849	D	7	2	41	43		72.38	2567.77	3.66	-0.99	2.84	24.09	1.19	1.15	3.4090		
849	D	7	2	43	45		72.39	2568.03	3.73	-1.17	2.63	23.22	0.83	0.74	3.4090		
849	D	7	2			46	72.41	2568.54	3.70						3.4090		*)
849	D	7	2	46	48		72.42	2568.79	3.71	-1.08	2.78	23.83	1.05	0.97	3.4090		
849	D	7	2	48	50		72.43	2569.05	3.73	-0.70					3.4090		
849	D	7	2	51	53		72.45	2569.56	3.76	-0.94	3.22	25.48	1.53	1.41	3.3976		
849	D	7	2	53	55		72.49	2570.58	3.69	-1.04	2.64	23.24	0.97	0.90	3.3976		
849	D	7	2	56	58		72.51	2571.10	3.62	-1.00	3.32	25.81	1.54	1.53	3.3976		
849	D	7	2	62	63		72.58	2572.94	3.78	-1.12	2.71	23.53	0.95	0.81	3.3976		
849	D	7	2	63	65		72.59	2573.21	3.69	-1.04	3.15	25.25	1.39	1.32	3.3976		
849	D	7	2	66	68		72.61	2573.76	3.63	-1.01					3.3976		
849	D	7	2	68	70		72.63	2574.32	3.67	-0.86					3.3976		
849	D	7	2	71	73		72.68	2575.75	3.59	-0.87	3.21	25.45	1.59	1.60	3.3976	4.60	
849	D	7	2	73	75		72.69	2576.05	3.63	-1.24	2.82	24.01	0.93	0.91	3.3976		
849	D	7	2	76	78		72.71	2576.65	3.52	-1.20					3.3976		
849	D	7	2	78	80		72.75	2577.89	3.44	-1.47	3.07	24.96	0.90	1.02	3.3976		
849	D	7	2	81	83		72.78	2578.84	3.31	-1.22	2.94	24.48	1.05	1.27	3.3976		
849	D	7	2	83	85		72.79	2579.17	3.38	-1.06	3.02	24.75	1.26	1.42	3.3976		
849	D	7	2			86	72.81	2579.82	3.39						3.3976		*)
849	D	7	2	87	88		72.83	2580.48	3.26	-1.26	2.91	24.35	0.98	1.23	3.3976		
849	D	7	2	88	90		72.85	2581.15	3.31	-1.38	3.33	25.85	1.17	1.39	3.3976		
849	D	7	2	91	93		72.87	2581.83	3.21	-1.08	2.81	23.94	1.07	1.36	3.3976		
849	D	7	2	93	95		72.89	2582.52	3.29	-1.02	2.95	24.52	1.25	1.48	3.3976	4.80	
849	D	7	2	96	98		72.91	2583.21	3.50	-1.11	3.07	24.96	1.26	1.33	3.3976		
849	D	7	2	98	100		72.95	2584.61	3.39	-1.07	2.79	23.88	1.07	1.23	3.3976		
849	D	7	2	101	103		72.97	2585.31	3.41	-1.15	3.11	25.08	1.24	1.39	3.3976		
849	D	7	2	103	105		72.98	2585.67	3.33	-1.15	2.79	23.87	0.99	1.19	2.6772		
849	D	7	2	106	107		73.01	2586.74	3.40	-0.89					2.6772		
849	D	7	2	107	109		73.03	2587.45	3.36	-0.93	2.94	24.48	1.33	1.51	2.6772		
849	D	7	2	113	115		73.09	2589.61	3.49	-0.90	2.94	24.47	1.36	1.44	2.6772		
849	D	7	2			116	73.11	2590.33	3.49						2.6772		*)
849	D	7	2	116	118		73.12	2590.69	3.21	-0.94					2.6772		
849	D	7	2	118	120		73.14	2591.41	3.55	-1.18	2.76	23.74	0.94	0.97	2.6772		
849	D	7	2	121	123		73.16	2592.13	3.44		2.74	23.67			2.6772	4.51	
849	D	7	2	123	125		73.19	2593.21	3.44	-0.55	3.03	24.81	1.79	1.91	2.6772		
849	D	7	2	126	128		73.21	2593.92	3.32	-0.94	2.84	24.07	1.24	1.45	2.6772		
849	D	7	2	128	130		73.23	2594.63	3.55	-0.66					2.6772		
849	D	7	2	130	132		73.26	2595.68	3.69	-0.70	3.33	25.85	1.85	1.79	2.6772		
849	D	7	2	132	134		73.28	2596.43	3.82	-1.05					2.6772		

Site	Hole	Core	Section	Top (cm)	Bottom (cm)	Depth *) (cm)	Depth (mcd)	Age (ka)	$\delta^{18}O_{C.\ wuellerstorfi}$ (‰ VPDB)	$\delta^{18}O_{G.\ ruber}$ (‰ VPDB)	$Mg/Ca_{G.\ ruber}$ (mmol mol^{-1})	SST (°C)	$\delta^{18}O_{seawater}$ (‰ SMOW)	$\delta^{18}O_{sw\text{-}ivc}$ (‰ SMOW)	LSR (cm kyr^{-1})	FFI (%)	
849	D	7	2			136	73.31	2597.55	3.97						2.6772		*)
849	D	7	2	136	138		73.33	2598.31	3.89	-0.28					2.6772		
849	D	7	2	138	140		73.35	2599.07	3.84	-0.88	2.91	24.34	1.36	1.18	2.6772		
849	D	7	2	141	143		73.37	2599.83	4.03	-0.31	3.47	26.34	2.34	2.02	2.6772		
849	D	7	2	143	145		73.40	2600.98	3.84	-0.89	2.91	24.34	1.35	1.17	2.6772		
849	D	7	2			146	73.41	2601.37	4.03						2.6772		*)
849	D	7	2	146	148		73.43	2602.15	4.04	-0.70					2.6772		
849	D	7	2	148	149		73.44	2602.54	3.86	-0.58					2.6772	5.99	
849	D	7	3	1	3		73.48	2604.13	3.94	-0.23	2.51	22.68	1.66	1.41	2.6772		
849	D	7	3	3	5		73.50	2604.94	4.06	-0.54	2.65	23.29	1.48	1.13	2.6772		
849	D	7	3			6	73.51	2605.35	3.74						2.0412		*)
849	D	7	3	6	8		73.52	2605.76	3.63	-0.31	2.63	23.23	1.69	1.67	2.0412		
849	D	7	3	8	10		73.53	2606.18	3.97	-0.62	2.59	23.05	1.35	1.07	2.0412		
849	D	7	3			16	73.61	2609.60	3.58						2.0412		*)
849	D	7	3	16	18		73.62	2610.04	3.62	-0.78	3.01	24.74	1.54	1.53	2.0412		
849	D	7	3	18	20		73.63	2610.48	3.70	-0.66	2.79	23.88	1.48	1.41	2.0412		
849	D	7	3	21	23		73.68	2612.77	3.62	-0.85	2.99	24.64	1.45	1.43	2.0412		
849	D	7	3	23	25		73.70	2613.71	3.67	-0.26					2.0412	7.13	
849	D	7	3			26	73.71	2614.19	3.58						2.0412		*)
849	D	7	3	26	28		73.72	2614.67	3.73	-0.34					2.0412		
849	D	7	3	28	30		73.73	2615.16	3.50						2.0412		
849	D	7	3	31	33		73.78	2617.66	3.67	-0.88					2.0412		
849	D	7	3	33	35		73.80	2618.69	3.55	-0.72					2.0412		
849	D	7	3	35	36		73.81	2619.20	3.57	-0.44					2.0412		
849	D	7	3	37	38		73.82	2619.72	3.52	-0.71					2.0412		
849	D	7	3	38	40		73.84	2620.77	3.49	-1.06	2.88	24.23	1.16	1.24	2.0412		
849	D	7	3	41	43		73.88	2622.87	3.46	-0.98	2.71	23.56	1.09	1.20	2.0412		
849	D	7	3	43	45		73.89	2623.40	3.41	-0.95	3.15	25.22	1.47	1.62	2.0412		
849	D	7	3			46	73.91	2624.46	3.52						2.0412		*)
849	D	7	3	46	48		73.92	2624.98	3.31	-0.82	3.06	24.91	1.54	1.76	2.0412	4.44	
849	D	7	3	48	50		73.94	2626.04	3.40	-0.85	2.78	23.85	1.28	1.43	2.0412		
849	D	7	3	51	53		73.98	2628.12	3.24	-0.76	3.23	25.53	1.73	2.00	2.4124		
849	D	7	3	53	55		73.99	2628.64	3.28	-0.93	2.91	24.35	1.31	1.55	2.4124		
849	D	7	3			56	74.01	2629.66	3.32						2.4124		*)
849	D	7	3	56	58		74.02	2630.17	3.41	-0.87	3.10	25.06	1.51	1.65	2.4124		
849	D	7	3	63	65		74.09	2633.61	3.44		3.44	26.23			2.4124		
849	D	7	3			66	74.11	2634.55	3.54						2.4124		*)
849	D	7	3	66	68		74.12	2635.01	3.51	-0.90	2.67	23.37	1.13	1.20	2.4124		
849	D	7	3	68	70		74.14	2636.11			3.01	24.74			2.4124		
849	D	7	3	71	73		74.17	2637.20	3.40	-0.44	2.70	23.52	1.63	1.77	2.4124	4.36	
849	D	7	3	73	75		74.19	2638.03	3.59	-0.97					2.4124		

Site	Hole	Core	Section	Top (cm)	Bottom (cm)	Depth *) (cm)	Depth (mcd)	Age (ka)	$\delta^{18}O_{C.\ wuellerstorfi}$ (‰ VPDB)	$\delta^{18}O_{G.\ ruber}$ (‰ VPDB)	$Mg/Ca_{G.\ ruber}$ (mmol mol^{-1})	SST (°C)	$\delta^{18}O_{seawater}$ (‰ SMOW)	$\delta^{18}O_{sw\text{-}ivc}$ (‰ SMOW)	LSR (cm kyr^{-1})	FFI (%)	
849	D	7	3			76	74.21	2638.82	3.62						2.4124		*)
849	D	7	3	76	77		74.22	2639.21	3.66	-1.06	2.71	23.54	1.01	0.97	2.4124		
849	D	7	3	77	79		74.23	2639.59	3.66	-0.91	2.71	23.56	1.16	1.12	2.4124		
849	D	7	3	79	81		74.25	2640.33	3.70	-0.88	2.96	24.53	1.40	1.32	2.4124		
849	D	7	3	81	83		74.27	2641.05	3.79	-0.97	2.99	24.65	1.33	1.19	2.4124		
849	D	7	3	83	85		74.29	2641.76	3.65	-0.91	2.77	23.80	1.22	1.18	2.4124		
849	D	7	3	85	86		74.3	2642.10	3.61	-1.08	2.73	23.65	1.01	1.00	2.4124		
849	D	7	3			86	74.31	2642.44	3.77						2.4124		*)
849	D	7	3	87	89		74.33	2643.11	3.82	-0.95	3.15	25.25	1.48	1.31	2.4124		
849	D	7	3	89	91		74.35	2643.77	3.71	-0.80	3.14	25.20	1.62	1.54	2.4124		
849	D	7	3	91	93		74.37	2644.42	3.79	-1.00	2.77	23.77	1.12	0.97	2.4124		
849	D	7	3	93	95		74.39	2645.06	3.82	-0.65	2.94	24.47	1.61	1.45	2.6705		
849	D	7	3			96	74.41	2645.71	3.70						2.6705		*)
849	D	7	3	96	97		74.42	2646.03	3.76	-0.61	2.84	24.08	1.57	1.45	2.6705		
849	D	7	3	97	99		74.43	2646.35	3.77	-0.96	2.87	24.19	1.24	1.11	2.6705		
849	D	7	3	100	101		74.46	2647.32	3.76	-0.87	2.93	24.43	1.38	1.27	2.6705		
849	D	7	3	101	102		74.47	2647.81		-1.02	2.89	24.28	1.20		2.6705		
849	D	7	3	103	105		74.49	2648.30	3.78		3.08	24.99			2.6705		
849	D	7	3	105	107		74.51	2648.97	3.84	-0.73	2.72	23.57	1.35	1.17	2.6705		
849	D	7	3			106	74.51	2648.97							2.6705		*)
849	D	7	3	107	109		74.53	2649.65	3.47	-0.87	3.17	25.31	1.57	1.66	2.6705	8.82	
849	D	7	3	109	111		74.55	2650.35	3.80	-0.68	2.96	24.52	1.59	1.45	2.6705		
849	D	7	3	111	113		74.57	2651.06	3.53	-0.88	3.14	25.21	1.54	1.59	2.6705		
849	D	7	3	113	115		74.59	2651.80	3.47	-0.80	2.84	24.08	1.38	1.48	2.6705		
849	D	7	3			116	74.61	2652.56	3.17						2.6705		*)
849	D	7	3	117	119		74.63	2653.35	3.25	-0.86	3.05	24.89	1.49	1.75	2.6705		
849	D	7	3	119	121		74.65	2654.15	3.54	-1.18	3.09	25.03	1.20	1.25	2.6705	7.34	
849	D	7	3	122	123		74.68	2655.40	3.32	-1.26	2.70	23.49	0.80	1.00	2.6705		
849	D	7	3	123	125		74.69	2655.82	3.32	-1.11	3.54	26.56	1.59	1.80	2.6705		
849	D	7	3	125	127		74.71	2656.68		-1.09					2.6705		
849	D	7	3			126	74.71	2656.68	3.20						2.6705		*)
849	D	7	3	127	129		74.73	2657.55	3.18	-1.33	2.82	23.99	0.83	1.15	2.6705		
849	D	7	3	129	131		74.75	2658.43	3.34	-1.22	2.73	23.62	0.87	1.06	2.6705		
849	D	7	3	132	133		74.78	2659.78	3.23	-1.03	3.26	25.62	1.48	1.75	2.6705		
849	D	7	3	133	135		74.79	2660.23	3.27	-1.11	2.77	23.80	1.02	1.26	2.6705		
849	D	7	3	135	137		74.81	2661.14		-1.15	3.14	25.20	1.26		2.6705		
849	D	7	3			136	74.81	2661.14	3.27						2.6705		*)
849	D	7	3	137	139		74.83	2662.06	3.14	-1.27	3.42	26.14	1.34	1.68	2.6705		
849	D	7	3	139	141		74.85	2662.98	3.30	-1.31	3.48	26.36	1.35	1.58	2.6705		
849	D	7	3	141	143		74.87	2663.90	3.24	-1.20	2.82	23.98	0.96	1.23	2.6705		
849	D	7	3	143	145		74.89	2664.83	2.95	-1.19	3.34	25.90	1.37	1.86	2.6705	6.82	

Site	Hole	Core	Section	Top (cm)	Bottom (cm)	Depth *) (cm)	Depth (mcd)	Age (ka)	$\delta^{18}O_{C.\ wuellerstorfi}$ (‰ VPDB)	$\delta^{18}O_{G.\ ruber}$ (‰ VPDB)	$Mg/Ca_{G.\ ruber}$ (mmol mol^{-1})	SST (°C)	$\delta^{18}O_{seawater}$ (‰ SMOW)	$\delta^{18}O_{sw\text{-}ivc}$ (‰ SMOW)	LSR (cm kyr^{-1})	FFI (%)	
849	D	7	3	145	146		74.9	2665.29	3.17	-1.15					2.6705		
849	D	7	3			146	74.91	2665.75	3.18						2.6705		*)
849	D	7	3	147	149		74.93	2666.67	3.20	-1.15	3.32	25.81	1.40	1.70	3.3473		
849	D	7	4	1	3		74.97	2668.49	3.03	-1.07	2.43	22.32	0.74	1.17	3.3473		
849	D	7	4	3	5		74.99	2669.39	3.13	-0.91	3.31	25.80	1.63	1.98	3.3473		
849	D	7	4			6	75.01	2670.28	3.22						3.3473		*)
849	D	7	4	6	7		75.02	2670.72	3.25	-1.19	2.67	23.38	0.85	1.11	3.3473		
849	D	7	4	7	9		75.03	2671.15	3.24	-0.97	2.91	24.33	1.26	1.54	3.3473		
849	D	7	4	9	10		75.04	2671.59	3.18	-1.00	2.94	24.46	1.26	1.58	3.3473		
849	D	7	4	11	13		75.07	2672.87	3.19	-1.21	2.89	24.29	1.02	1.33	3.3473		
849	D	7	4	13	15		75.09	2673.70	3.15	-0.95	2.83	24.03	1.22	1.56	3.3473		
849	D	7	4			16	75.11	2674.52	3.37						3.3473		*)
849	D	7	4	16	17		75.12	2674.92	3.15	-1.26					3.3473		
849	D	7	4	17	19		75.13	2675.31	3.31	-1.34	2.82	24.00	0.82	1.04	3.3473		
849	D	7	4	19	20		75.14	2676.08		-0.90	2.61	23.14	1.09		3.3473		
849	D	7	4	21	23		75.17	2676.84	3.37	-1.10	3.39	26.07	1.49	1.66	3.3473		
849	D	7	4	23	25		75.19	2677.56	3.31	-0.91	2.87	24.19	1.30	1.51	3.3473		
849	D	7	4	25	27		75.21	2678.26	3.27	-1.04	3.10	25.04	1.34	1.59	3.3473		
849	D	7	4			26	75.21	2678.26							3.3473		*)
849	D	7	4	27	29		75.23	2678.93	3.31	-0.74	2.75	23.70	1.36	1.58	3.3473		
849	D	7	4	29	30		75.24	2679.26	3.48	-0.94	2.99	24.64	1.36	1.45	3.3473		
849	D	7	4	31	33		75.27	2680.18	3.41	-1.03	2.70	23.50	1.03	1.18	3.3473		
849	D	7	4	33	35		75.29	2680.76	3.53	-1.06	3.31	25.78	1.47	1.53	3.3473		
849	D	7	4			36	75.31	2681.30	3.46						3.3473		*)
849	D	7	4	36	37		75.32	2681.56	3.63	-1.09	3.15	25.25	1.34	1.31	3.3473		
849	D	7	4	37	39		75.33	2681.82	3.46	-0.89	3.12	25.13	1.51	1.61	3.3473		
849	D	7	4	40	41		75.36	2682.54	3.65	-1.01	3.02	24.77	1.32	1.28	3.3473		
849	D	7	4	41	43		75.37	2682.78	3.65	-0.80	2.53	22.78	1.11	1.08	3.3473		
849	D	7	4	43	45		75.39	2683.22	3.73	-0.86	2.65	23.29	1.16	1.06	3.3473	6.01	
849	D	7	4	46	47		75.42	2683.85	3.64	-0.79	2.68	23.44	1.26	1.23	3.3473		
849	D	7	4	47	49		75.43	2684.05	3.77	-0.88	2.86	24.14	1.32	1.19	3.3473		
849	D	7	4	49	50		75.44	2684.25	3.61	-0.93	3.01	24.74	1.39	1.38	3.3473		
849	D	7	4	51	53		75.47	2684.83	3.76	-0.94	2.76	23.74	1.17	1.05	3.3473		
849	D	7	4	53	55		75.49	2685.20	3.81	-0.87	3.00	24.70	1.44	1.28	3.3473		
849	D	7	4			56	75.51	2685.56	3.79						4.1334		*)
849	D	7	4	56	57		75.52	2685.74	3.76	-0.79	2.96	24.54	1.48	1.37	4.1334	6.88	
849	D	7	4	57	59		75.53	2685.91	3.81	-1.01	2.81	23.93	1.14	0.98	4.1334		
849	D	7	4	59	60		75.54	2686.09	3.67	-1.12	2.81	23.97	1.04	0.99	4.1334		
849	D	7	4	61	62		75.56	2686.44	3.74	-0.99	3.13	25.17	1.41	1.31	4.1334		
849	D	7	4	63	65		75.59	2686.97	3.80	-0.61	2.96	24.52	1.67	1.52	4.1334		
849	D	7	4	66	67		75.62	2687.50	3.95	-0.78	2.94	24.47	1.48	1.22	4.1334		

Site	Hole	Core	Section	Top (cm)	Bottom (cm)	Depth *) (cm)	Depth (mcd)	Age (ka)	$\delta^{18}O_{C.\ wuellerstorfi}$ (‰ VPDB)	$\delta^{18}O_{G.\ ruber}$ (‰ VPDB)	$Mg/Ca_{G.\ ruber}$ (mmol mol^{-1})	SST (°C)	$\delta^{18}O_{seawater}$ (‰ SMOW)	$\delta^{18}O_{sw\text{-}ivc}$ (‰ SMOW)	LSR (cm kyr^{-1})	FFI (%)	
849	D	7	4	67	69		75.63	2687.68	3.97	-0.93	3.50	26.42	1.74	1.46	4.1334		
849	D	7	4	69	70		75.64	2687.86	3.99	-0.84	3.28	25.69	1.68	1.38	4.1334		
849	D	7	4	71	73		75.67	2688.42	3.87	-0.61	3.21	25.44	1.85	1.65	4.1334		
849	D	7	4	73	75		75.69	2688.81	3.83		3.37	25.98			4.1334		
849	D	7	4	75	77		75.71	2689.21		-0.72	3.45	26.24	1.91		4.1334		
849	D	7	4			76	75.71	2689.21	3.86						4.1334		*)
849	D	7	4	77	79		75.73	2689.63	3.64	-0.65	3.01	24.74	1.67	1.64	4.1334		
849	D	7	4	79	80		75.74	2689.85	3.89	-0.56					4.1334		
849	D	7	4	81	83		75.77	2690.53	4.00	-0.68	3.35	25.93	1.88	1.58	4.1334		
849	D	7	4	83	85		75.79	2691.01	3.57	-0.89					4.1334		
849	D	7	4			86	75.81	2691.51	3.58						4.1334		*)
849	D	7	4	86	87		75.82	2691.77	3.57	-0.55	2.97	24.57	1.74	1.76	4.1334		
849	D	7	4	87	89		75.83	2692.04	3.57	-0.58	3.29	25.74	1.95	1.97	4.1334		
849	D	7	4	89	91		75.85	2692.60	3.50	-0.75	2.61	23.12	1.23	1.31	4.1334	6.44	
849	D	7	4	92	93		75.88	2693.49	3.51	-0.82	3.39	26.06	1.77	1.85	4.1334		
849	D	7	4	93	95		75.89	2693.80	3.74	-0.60	2.78	23.83	1.53	1.42	4.1334		
849	D	7	4	95	97		75.91	2694.45		-0.84	3.03	24.79	1.49		4.1334		
849	D	7	4			96	75.91	2694.45	3.65						4.1334		*)
849	D	7	4	97	99		75.93	2695.13	3.66	-0.66	2.63	23.20	1.34	1.30	4.1334		
849	D	7	4	99	101		75.95	2695.83	3.56	-0.89	2.69	23.45	1.16	1.20	4.1334		
849	D	7	4	102	103		75.98	2696.59		-0.91					4.1334		
849	D	7	4	103	105		75.99	2697.35	3.67	-0.93	2.76	23.75	1.19	1.13	4.1334		
849	D	7	4	105	107		76.01	2698.16		-0.78	2.77	23.81	1.35		1.8826		
849	D	7	4			106	76.01	2698.16	3.63						1.8826		*)
849	D	7	4	107	109		76.03	2699.01	3.78	-0.38	2.44	22.38	1.45	1.32	1.8826		
849	D	7	4	109	111		76.05	2699.90	3.79	-0.60	2.50	22.64	1.29	1.15	1.8826		
849	D	7	4	111	112		76.06	2700.35	3.66	-0.86	2.84	24.05	1.32	1.28	1.8826		
849	D	7	4	113	114		76.07	2700.82	3.55	-0.78	2.70	23.51	1.29	1.33	1.8826		
849	D	7	4	115	117		76.11	2702.79		-0.78	2.57	22.96	1.17		1.8826		
849	D	7	4			116	76.11	2702.79	3.77						1.8826		*)
849	D	7	4	117	119		76.13	2703.83	3.77	-0.77	2.41	22.25	1.03	0.91	1.8826		
849	D	7	4	119	121		76.15	2704.91	3.91	-0.41	2.82	24.00	1.75	1.52	1.8826	7.11	
849	D	7	4	121	123		76.17	2706.03	3.96		2.75	23.71			1.8826		
849	D	7	4	123	125		76.19	2707.16	3.92	-0.22	2.49	22.60	1.65	1.41	1.8826		
849	D	7	4	125	127		76.21	2708.31		-0.55	2.55	22.85	1.37		1.8826		
849	D	7	4			126	76.21	2708.31	3.81						1.8826		*)
849	D	7	4	127	129		76.23	2709.45	3.71	-0.28	2.49	22.59	1.59	1.51	1.9218		
849	D	7	4	129	131		76.25	2710.58	3.76	-0.45	2.65	23.28	1.56	1.44	1.9218		
849	D	7	4	131	132		76.26	2711.13	3.68	-0.31	2.58	23.01	1.65	1.59	1.9218		
849	D	7	4	133	135		76.29	2712.75	3.69	-0.64	3.42	26.17	1.97	1.90	1.9218		
849	D	7	4	135	137		76.31	2713.78	3.96	-0.71	3.17	25.31	1.73	1.46	1.9218		

Site	Hole	Core	Section	Top (cm)	Bottom (cm)	Depth *) (cm)	Depth (mcd)	Age (ka)	$\delta^{18}O_{C.\ wuellerstorfi}$ (‰ VPDB)	$\delta^{18}O_{G.\ ruber}$ (‰ VPDB)	$Mg/Ca_{G.\ ruber}$ (mmol mol^{-1})	SST (°C)	$\delta^{18}O_{seawater}$ (‰ SMOW)	$\delta^{18}O_{sw\text{-}ivc}$ (‰ SMOW)	LSR (cm kyr^{-1})	FFI (%)	
849	D	7	4	137	139		76.33	2714.75	3.80	-0.22	3.49	26.39	2.45	2.30	1.9218		
849	D	7	4	139	141		76.35	2715.69	3.97	-0.59	2.74	23.66	1.51	1.23	1.9218		
849	D	7	4	142	143		76.38	2717.01	3.81	-0.60	3.26	25.62	1.91	1.74	1.9218		
849	D	7	4	143	145		76.39	2717.43	3.91	-0.31	3.28	25.69	2.20	1.97	1.9218		
849	D	7	4	145	147		76.41	2718.24		-0.34					1.9218		
849	D	7	4			146	76.41	2718.24	3.99						1.9218		*)
849	D	7	4	147	149		76.43	2719.01	3.85	-0.38					1.9218		
849	D	7	4	149	150		76.44	2719.38	3.73	-0.58	2.50	22.63	1.30	1.20	1.9218		
849	D	7	5	1	3		76.47	2720.44	3.71	-0.30					1.9218		
849	D	7	5	3	5		76.49	2721.11	3.78	-0.50	2.38	22.09	1.27	1.13	1.9218		
849	D	7	5			6	76.51	2721.74	3.82						1.9218		*)
849	D	7	5	6	7		76.52	2722.05	3.75						1.9218		
849	D	7	5	7	9		76.53	2722.35	3.74	-0.27	2.98	24.61	2.02	1.92	1.9218		
849	D	7	5	9	11		76.55	2723.04		-0.64					1.9218		
849	D	7	5	12	13		76.58	2723.73	3.54	-0.79					1.9218		
849	D	7	5	13	15		76.59	2723.99	3.85	-0.61	2.67	23.38	1.43	1.24	1.9218		
849	D	7	5	15	16		76.6	2724.25	3.62	-0.84	2.95	24.48	1.43	1.41	1.9218		
849	D	7	5			16	76.61	2724.49	3.73						1.9218		*)
849	D	7	5	17	19		76.63	2724.97	3.81	-0.63	2.56	22.89	1.31	1.15	1.9218		
849	D	7	5	19	20		76.64	2725.20	3.78	-0.39	3.07	24.96	1.98	1.84	1.9218		
849	D	7	5	21	23		76.67	2725.87	3.82	-0.74					1.9218		
849	D	7	5	23	25		76.69	2726.29	3.75	-0.77					1.9218		
849	D	7	5			26	76.71	2726.69	3.77						1.9218		*)
849	D	7	5	25	27		76.71	2726.89		-0.47	3.22	25.49	2.01		1.9218		
849	D	7	5	27	29		76.73	2727.08	3.66	-0.51					1.9218		
849	D	7	5	29	30		76.74	2727.27	3.67	-0.63					1.9218	10.83	
849	D	7	5	31	33		76.77	2727.83	3.66	-0.70	3.07	24.94	1.66	1.62	1.9218		
849	D	7	5	33	35		76.79	2728.19	3.62	-0.72	3.14	25.20	1.70	1.68	1.9218		
849	D	7	5	36	37		76.82	2728.72	3.62	-0.49					1.9218		
849	D	7	5	37	39		76.83	2728.89	3.53	-0.32					1.9218		
849	D	7	5	39	40		76.84	2729.06	3.53	-0.91					1.9218		
849	D	7	5	41	43		76.87	2729.57	3.60	-1.21	2.68	23.43	0.84	0.84	1.9218		
849	D	7	5	43	45		76.89	2729.91	3.44	-1.03	2.75	23.71	1.08	1.20	1.9218		
849	D	7	5	46	47		76.92	2730.41	3.54	-0.99					1.9218		
849	D	7	5	47	49		76.93	2730.58	3.55	-0.61					1.9218		
849	D	7	5	50	51		76.95	2730.92	3.43	-0.40	3.51	26.45	2.28	2.41	1.9218		
849	D	7	5	51	53		76.97	2731.26	3.47	-1.07	2.80	23.93	1.08	1.18	1.9218		
849	D	7	5	53	55		76.99	2731.60	3.45	-0.88	3.34	25.91	1.68	1.80	1.9218		
849	D	7	5	56	57		77.02	2732.10	3.31	-0.80					1.9218	11.56	

Table B.2.2. Site 806 oxygen-isotope composition of seawater adjusted for global ice volume ($\delta^{18}O_{ivc\text{-}sw}$) based on *G. ruber* $\delta^{18}O$- and Mg/Ca-data by Medina-Elizalde and Lea (2010) for ~2.75 to 2.4 Ma. Further this table includes sea-surface temperature (SST), $\delta^{18}O_{ivc\text{-}sw}$ and $\delta^{18}O_{sw}$ gradients between Sites 806 and 849. The age model for Site 806 is presented in Table A.2.2 (Appendix A.2). For methodical details see Chapter 5 and Appendix A.2.

Age (ka)	Site 806 $\delta^{18}O_{sw\text{-}ivc}$ (‰ SMOW)	$\Delta SST_{806\text{-}849}$ (°C)	$\Delta\delta^{18}O_{sw\text{-}ivc,\ 806\text{-}849}$ (‰ SMOW) (method 1)	$\Delta\delta^{18}O_{sw\text{-}ivc,\ 806\text{-}849}$ (‰ SMOW) (method 2)	$\Delta\delta^{18}O_{sw,\ 806\text{-}849}$ (‰ SMOW) (method 3)
2388.20	1.62	3.63	0.34	0.18	-0.66
2390.44	1.57	3.83	0.29	0.30	-0.57
2392.51	1.49	3.83	0.23	0.20	-0.64
2395.54	1.74	4.40	0.48	0.34	-0.43
2398.60	1.40	3.76	0.12	-0.03	-0.81
2401.15	1.30	3.77	0.00	0.09	-0.89
2404.43	1.31	3.67	-0.03	0.12	-0.92
2407.51	1.33	3.48	0.00	-0.09	-1.02
2409.66	1.37	3.40	-0.02	-0.10	-1.07
2412.08	1.80	3.80	0.36	0.31	-0.66
2414.38		3.13			
2415.96	1.85	3.52	0.31	0.16	-0.64
2417.82	1.66	2.92	0.12	-0.19	-0.86
2419.37	1.65	3.42	0.04	-0.22	-0.91
2420.58	1.64	3.75	0.14	-0.23	-0.84
2421.80	1.68	3.62	0.21	-0.16	-0.80
2422.94	1.88	4.16	0.42	0.03	-0.63
2423.72	1.96	4.03	0.57	0.04	-0.59
2424.61	2.05	4.53	0.73	0.00	-0.56
2425.22	1.90	4.19	0.48	-0.16	-0.64
2425.93	2.10	5.05	0.62	0.08	-0.27
2426.54	2.04	5.46	0.55	0.02	-0.18
2426.99	1.96	5.40	0.47	-0.04	-0.18
2427.54	1.76	4.30	0.31	-0.12	-0.33
2428.07	1.79	4.54	0.45	0.08	-0.11
2428.48	1.23	4.09	0.10	-0.32	-0.50
2428.98	1.52	5.38	0.57	0.04	-0.13
2429.55		4.80			
2430.00	1.22	4.37	0.35	-0.12	-0.32
2430.64	1.04	5.15	0.19	-0.11	-0.34
2431.30	0.97	4.92	0.10	-0.11	-0.37
2431.92	0.86	4.59	-0.10	-0.21	-0.50
2432.71	1.12	5.08	0.06	0.03	-0.31
2433.63	1.15	4.85	0.09	0.00	-0.42
2434.41	1.11	4.54	0.04	-0.13	-0.53
2435.53	1.04	4.67	-0.04	-0.20	-0.56

Age (ka)	Site 806 $\delta^{18}O_{sw\text{-}ivc}$ (‰ SMOW)	$\Delta SST_{806\text{-}849}$ (°C)	$\Delta\delta^{18}O_{sw\text{-}ivc,\ 806\text{-}849}$ (‰ SMOW) (method 1)	$\Delta\delta^{18}O_{sw\text{-}ivc,\ 806\text{-}849}$ (‰ SMOW) (method 2)	$\Delta\delta^{18}O_{sw,\ 806\text{-}849}$ (‰ SMOW) (method 3)
2436.78	1.00	4.51	-0.10	-0.14	-0.60
2438.09	0.88	4.18	-0.26	-0.22	-0.81
2439.92	0.80	4.37	-0.42	-0.37	-0.95
2442.09		4.22			
2466.90	1.34	2.85	0.05	-0.16	-0.93
2470.63	1.40	3.36	0.08	0.22	-0.80
2473.26	1.21	3.39			
2476.33		3.47			
2478.96	1.45	3.89			
2481.22		3.56			
2483.18		3.84			
2484.27	1.04	3.95	-0.26	-0.27	-0.69
2486.18	1.09	4.05	-0.14	-0.10	-0.56
2487.66	1.32	4.99	0.14	0.08	-0.43
2489.11	1.30	4.22			
2490.30		4.36			
2491.86	1.53	4.59	0.32	0.18	-0.41
2493.66	1.63	4.93	0.36	0.13	-0.44
2495.63	1.63	4.73	0.24	0.02	-0.59
2497.36	1.44	4.52	-0.01	-0.29	-0.89
2499.71	1.60	4.82	0.07	-0.15	-0.79
2502.19	1.68	4.62	0.14	-0.04	-0.72
2504.80	1.68	4.64	0.18	-0.03	-0.55
2506.91	1.49	4.71	0.09	-0.17	-0.57
2509.67	1.32	5.01	-0.11	-0.13	-0.58
2512.50	1.35	5.21	0.00	-0.14	-0.44
2515.24	1.28	5.30	-0.05	-0.13	-0.40
2518.14	1.05	4.29	-0.28	-0.23	-0.56
2520.41	0.98	3.52	-0.42	-0.25	-0.58
2523.30	1.12	3.70	-0.21	-0.11	-0.47
2526.16	1.14	3.71	-0.16	-0.20	-0.57
2528.97	1.26	4.07	0.00	-0.11	-0.54
2531.12	1.13	3.60	-0.09	-0.20	-0.71
2533.80	1.04	3.69	-0.12	-0.26	-0.82
2536.26	1.11	3.70	-0.10	-0.27	-0.82
2538.61	1.31	4.01	-0.01	-0.18	-0.75
2540.25	1.25	2.91	-0.16	-0.30	-0.91
2542.11	1.31	3.12	-0.16	-0.38	-1.04
2543.87	1.39	2.98	-0.10	-0.32	-1.07
2545.54	1.55	3.62	0.11	-0.01	-0.83
2546.78	1.13	3.40	-0.22	-0.29	-1.17

Age (ka)	Site 806 $\delta^{18}O_{sw\text{-}ivc}$ (‰ SMOW)	$\Delta SST_{806\text{-}849}$ (°C)	$\Delta\delta^{18}O_{sw\text{-}ivc,\ 806\text{-}849}$ (‰ SMOW) (method 1)	$\Delta\delta^{18}O_{sw\text{-}ivc,\ 806\text{-}849}$ (‰ SMOW) (method 2)	$\Delta\delta^{18}O_{sw,\ 806\text{-}849}$ (‰ SMOW) (method 3)
2548.27	1.28	3.54	-0.04	-0.14	-1.19
2549.67	1.63	3.55	0.27	0.07	-0.97
2550.89	1.29	3.01		-0.30	
2552.08		3.94			
2552.95	1.34	3.03	-0.15	-0.20	-1.24
2553.95	1.30	2.90	-0.24	-0.07	-1.15
2554.91	1.12	2.94	-0.40	-0.24	-1.35
2555.81	1.40	2.37	-0.11	0.02	-1.11
2556.62	1.20	2.34	-0.29	-0.19	-1.30
2557.76	1.46	2.85	0.00	-0.02	-1.08
2559.09	1.36	2.45	-0.06	-0.19	-1.16
2560.69	1.33	3.52	-0.02	-0.21	-1.08
2562.18	1.33	3.81	0.02	-0.16	-1.00
2564.28	1.36	3.88	0.12	0.09	-0.86
2566.87	0.91	3.54	-0.28	-0.18	-1.21
2569.68	1.22	3.66	0.04	0.03	-1.05
2571.95	1.23	3.50	0.00	-0.15	-1.16
2574.76	1.28	4.02		-0.10	
2577.46		3.68			
2579.91	1.38	3.59	0.10	0.07	-1.11
2582.39	1.56	3.91	0.24	0.18	-0.94
2584.27	1.34	3.55	0.00	-0.03	-1.11
2586.54	1.51	3.92	0.16	0.15	-0.92
2588.69	1.64	3.73	0.24	0.25	-0.81
2590.94	1.25	3.54	-0.21	-0.22	-1.19
2594.73	1.62	3.47	0.16	-0.03	-0.87
2596.65	1.16	2.83	-0.39	-0.53	-1.22
2598.41	0.89	2.77	-0.74	-0.60	-1.28
2599.91	1.20	3.76	-0.37	-0.24	-0.83
2601.74	1.21	4.14	-0.29	-0.18	-0.75
2603.44	1.15	4.42	-0.38	-0.33	-0.76
2606.20	1.26	3.56	-0.17	-0.12	-0.71
2608.92	1.35	3.89	-0.03	-0.11	-0.86
2611.33	1.33	3.49	-0.03	-0.06	-0.95
2614.83	1.36	3.27	0.01	0.04	-0.89
2618.10	1.61	3.32	0.21	0.22	-0.71
2621.50	1.27	2.85	-0.19	-0.25	-1.18
2624.58	1.52	2.96	0.02	-0.09	-0.98
2626.91	1.29	2.86	-0.23	-0.39	-1.18
2629.72	1.41	3.34	-0.13	-0.21	-1.00
2632.57	1.52	3.56	-0.01	-0.02	-0.79

Age (ka)	Site 806 $\delta^{18}O_{sw\text{-}ivc}$ (‰ SMOW)	$\Delta SST_{806\text{-}849}$ (°C)	$\Delta\delta^{18}O_{sw\text{-}ivc,\ 806\text{-}849}$ (‰ SMOW) (method 1)	$\Delta\delta^{18}O_{sw\text{-}ivc,\ 806\text{-}849}$ (‰ SMOW) (method 2)	$\Delta\delta^{18}O_{sw,\ 806\text{-}849}$ (‰ SMOW) (method 3)
2634.61	1.51	3.55	0.08	0.04	-0.75
2636.92	1.51	4.21	0.16	0.13	-0.65
2638.95	1.29	3.69	0.01	0.07	-0.82
2640.72	1.18	3.15	-0.12	0.11	-0.87
2641.98	1.30	3.10	0.08	0.09	-0.86
2643.33	1.37	2.96	0.10	0.06	-0.86
2644.54	1.43	3.09	0.15	-0.04	-0.85
2645.49	1.08	2.83	-0.21	-0.33	-1.14
2646.28	1.27	2.79	0.00	-0.10	-0.92
2646.83	1.29	2.78			
2647.39		2.33			
2647.86	1.07	2.53	-0.16	-0.16	-0.98
2648.28	1.17	2.99	-0.04	-0.06	-0.85
2648.56	1.19	3.27	-0.04	-0.03	-0.83
2648.87	1.02	2.88	-0.27	-0.21	-1.02
2649.17	1.14	3.09	-0.21	-0.09	-0.92
2649.48	0.73	2.41			
2650.16		2.96			
2650.66	1.02	2.69	-0.48	-0.33	-1.15
2651.42	1.23	3.09	-0.33	-0.25	-1.06
2652.18	1.21	3.08	-0.26	-0.22	-1.15
2653.40	1.45	3.30	-0.03	0.04	-0.95
2654.86	1.56	3.52	0.15	0.18	-0.91
2656.52	1.35	3.39	-0.04	0.05	-1.22
2658.37	1.59	3.12	0.21	0.17	-1.09
2660.38	1.49	2.67	0.02	0.04	-1.17
2662.03	1.50	2.69	0.00	0.05	-1.10
2664.26	1.46	2.53	-0.09	0.05	-1.09
2666.48	1.46	3.66	-0.10	0.05	-1.03
2668.10	1.72	3.38	0.19	0.28	-0.78
2670.08	1.63	3.34	0.13	0.21	-0.80
2671.97	1.69	3.65	0.28	0.39	-0.71
2673.98	1.46	3.04	0.01	0.28	-0.83
2675.54	1.36	2.65	-0.06	0.15	-0.93
2677.54	1.36	2.70	-0.06	0.05	-0.88
2679.50	1.25	2.34	-0.12	-0.04	-0.98
2681.31	1.41	2.72	0.04	0.11	-0.80
2682.76	1.18	2.48	-0.13	0.00	-1.03
2684.55	0.97	2.18	-0.34	-0.20	-1.18
2686.24	1.17	2.45	-0.18	0.02	-0.98
2687.81	1.01	2.18	-0.43	-0.40	-1.09

Age (ka)	Site 806 $\delta^{18}O_{sw\text{-}ivc}$ (‰ SMOW)	$\Delta SST_{806\text{-}849}$ (°C)	$\Delta\delta^{18}O_{sw\text{-}ivc,\ 806\text{-}849}$ (‰ SMOW) (method 1)	$\Delta\delta^{18}O_{sw\text{-}ivc,\ 806\text{-}849}$ (‰ SMOW) (method 2)	$\Delta\delta^{18}O_{sw,\ 806\text{-}849}$ (‰ SMOW) (method 3)
2689.17	1.12	2.00	-0.40	-0.46	-1.05
2689.98	0.99	1.98	-0.61	-0.67	-1.17
2692.46	1.05	2.77	-0.54	-0.51	-1.07
2693.45	1.11	2.73	-0.40	-0.34	-0.94
2694.33	1.19	3.00	-0.22	-0.16	-0.84
2695.38	1.16	3.87	-0.17	-0.11	-0.80
2696.61	1.31	3.75	0.06	0.10	-0.61
2698.01	1.31	3.87	0.09	0.14	-0.58
2699.25	1.19	3.67	0.01	-0.08	-0.75
2700.99	1.32	3.85	0.09	0.02	-0.67
2703.15	1.46	3.96	0.18	0.20	-0.44
2705.69	0.80	2.76	-0.54	-0.35	-1.02
2707.89	1.04	3.05	-0.40	-0.23	-0.86
2710.93	1.27	3.86	-0.30	-0.16	-0.60
2712.17	0.96	3.41	-0.57	-0.66	-0.96
2717.22	0.98	3.18	-0.58	-0.58	-0.98
2720.46	1.26	3.43	-0.32	-0.24	-0.76
2722.91	1.18	3.15	-0.33	-0.23	-0.91
2725.72	1.23	2.62	-0.27	-0.34	-0.99
2728.42	0.92	2.32	-0.68	-0.54	-1.42
2730.63	1.46	2.52	-0.18	-0.02	-1.07
2731.96	1.28		-0.40	-0.33	-1.40

Additional references

Medina-Elizalde, M., Lea, D.W. (2010). Late Pliocene equatorial Pacific. Paleoceanography, 25, PA2208, doi:2210.1029/2009PA001780.

Mix, A.C., Pisias, N.G., Rugh, W., Wilson, J., Morey, A., Hagelberg, T.K. (1995). Benthic foraminifer stable isotope record from Site 849 (0–5 Ma): Local and global climate changes. In Proceedings of the Ocean Drilling Program, Sci. Results, 138, pp. 371–412, Ocean Drill. Program, College Station, Tex.

Shackleton, N.J., Hall, M.A. (1984). Oxygen and carbon isotope stratigraphy of Deep Sea Drilling Project Hole 552A: Plio-Pleistocene Glacial History. In Proceedings of the Deep Sea Drilling Project, Initial Rep., 81, pp. 599–609, Deep Sea Drill. Proj., Washington, D.C.

APPENDIX B.3

DATA TABLES FOR CHAPTER 6

Table B.3.1. Site 849 benthic foraminiferal (*Oridorsalis umbonatus*) stable isotopes ($\delta^{18}O$ and $\delta^{13}C$) and Mg/Ca as a proxy for bottom-water temperature (BWT), the oxygen-isotope composition of seawater ($\delta^{18}O_{seawater}$) and sea-level for ~2.65 to 2.4 Ma. Reported Mg/Ca values are normalized to the ECRM752-1 standard.

Site	Hole	Core	Section	Top (cm)	Bottom (cm)	Depth (mcd)	Age (ka)	$\delta^{18}O_{O.\ umbonatus}$ (‰ VPDB)	$\delta^{13}C_{O.\ umbonatus}$ (‰ VPDB)	$Mg/Ca_{O.\ umbonatus}$ (mmol mol^{-1})	BWT (°C)	$\delta^{18}O_{seawater}$ (‰ SMOW)	sea level (m)
849	D	6	5	102	104	67.78	2387.85			1.43	2.14		
849	D	6	5	106	108	67.83	2389.49	3.70	-1.01	1.26	1.06	0.02	-1.38
849	D	6	5	108	110	67.84	2389.81	3.77	-0.96	1.29	1.24	0.12	-11.29
849	D	6	5	114	116	67.89	2391.45	3.69	-1.13	1.37	1.77	0.17	-15.70
849	D	6	5	116	118	67.91	2392.10	3.80	-0.97	1.21	0.67	0.01	-1.34
849	D	6	5	121	123	67.97	2394.06	3.69	-0.85	1.01	-0.94	-0.50	45.82
849	D	6	5	123	125	67.98	2394.39	3.56	-1.31	1.19	0.55	-0.26	23.54
849	D	6	5	127	129	68.03	2396.02	3.75	-1.04	1.14	0.14	-0.17	15.24
849	D	6	5	129	131	68.05	2396.67	3.63	-1.30				
849	D	6	5	132	134	68.08	2397.65	3.66	-1.15	1.26	1.05	-0.03	2.55
849	D	6	5	134	136	68.10	2398.31	3.66	-0.83	1.28	1.19	0.00	-0.10
849	D	6	5	137	139	68.12	2398.96	3.67	-0.64	1.26	1.02	-0.03	2.54
849	D	6	5	139	141	68.15	2399.94			1.51	2.62		
849	D	6	5	141	143	68.17	2400.60	3.69	-1.18	1.23	0.79	-0.07	6.36
849	D	6	5	143	145	68.19	2401.26	3.40	-1.04	1.45	2.29	0.01	-1.31
849	D	6	6	1	3	68.27	2403.88	3.27	-0.75	1.32	1.43	-0.33	30.00
849	D	6	6	3	5	68.29	2404.54	3.22	-1.45				
849	D	6	6	6	8	68.32	2405.53			1.32	1.42		
849	D	6	6	13	15	68.39	2407.84	3.29	-1.06	1.49	2.52	-0.04	3.26
849	D	6	6	17	19	68.43	2409.17			1.29	1.21		
849	D	6	6	22	24	68.48	2410.83			1.64	3.36		
849	D	6	6	24	26	68.49	2411.16	3.28	-1.19	1.49	2.50	-0.05	4.16
849	D	6	6	26	27	68.51	2411.83			1.53	2.74		
849	D	6	6	28	30	68.53	2412.50			1.49	2.53		
849	D	6	6	31	33	68.57	2413.84	3.53	-1.39	1.32	1.46	-0.06	5.14
849	D	6	6	33	35	68.59	2414.51	3.32	-1.29	1.19	0.50	-0.51	46.82
849	D	6	6	36	37	68.61	2415.18			1.48	2.43		
849	D	6	6	38	40	68.65	2416.53	3.48	-1.10	1.56	2.89	0.24	-22.06

Site	Hole	Core	Section	Top (cm)	Bottom (cm)	Depth (mcd)	Age (ka)	$\delta^{18}O_{O.\ umbonatus}$ (‰ VPDB)	$\delta^{13}C_{O.\ umbonatus}$ (‰ VPDB)	$Mg/Ca_{O.\ umbonatus}$ (mmol mol^{-1})	BWT (°C)	$\delta^{18}O_{seawater}$ (‰ SMOW)	sea level (m)
849	D	6	6	41	43	68.67	2417.21	3.56	-1.50	1.29	1.26	-0.08	7.23
849	D	6	6	43	45	68.69	2417.89	3.30	-1.72	1.44	2.22	-0.10	9.00
849	D	6	6	48	50	68.73	2419.25	3.48	-1.24	1.60	3.12	0.30	-27.47
849	D	6	6	51	53	68.77	2420.61	3.43	-1.15	1.30	1.29	-0.20	18.53
849	D	6	6	53	55	68.78	2420.96	3.41	-1.23	1.39	1.91	-0.07	6.10
849	D	6	6	57	59	68.83	2422.67	3.42	-1.85	1.29	1.24	-0.23	20.51
849	D	6	6	63	65	68.89	2424.75	3.95	-1.53	1.30	1.30	0.33	-29.57
849	D	6	6	66	67	68.91	2425.44			1.77	4.04		
849	D	6	6	68	70	68.95	2426.84	4.06	-1.41	1.21	0.70	0.28	-25.47
849	D	6	6	71	73	68.97	2427.54			1.19	0.50		
849	D	6	6	73	75	68.98	2427.89	4.11	-1.34				
849	D	6	6	81	82	69.07	2431.08	4.17	-1.23	1.12	-0.02	0.21	-19.44
849	D	6	6	89	91	69.15	2433.96	4.16	-1.56	1.12	-0.04	0.20	-18.05
849	D	6	6	91	93	69.17	2434.69	3.98	-1.65	1.34	1.58	0.42	-38.00
849	D	6	6	93	95	69.18	2435.06	4.10	-1.28	1.00	-1.02	-0.11	10.35
849	D	6	6	98	100	69.24	2437.27	4.08	-1.41	1.26	1.00	0.38	-34.49
849	D	6	6	100	102	69.26	2438.02			1.57	2.96		
849	D	6	6	102	104	69.28	2438.77	4.29	-1.87	1.43	2.13	0.87	-78.89
849	D	6	6	105	107	69.30	2439.53	4.15	-0.96	1.22	0.78	0.39	-35.10
849	D	6	6	108	110	69.33	2440.68			1.64	3.37		
849	D	6	6	120	121	69.45	2445.38	3.98	-1.47	1.22	0.78	0.22	-19.89
849	D	6	6	122	124	69.48	2446.59	3.71	-1.27	1.19	0.53	-0.11	9.84
849	D	6	6	124	126	69.49	2447.00	4.03	-1.17	1.13	0.08	0.09	-8.40
849	D	6	6	128	130	69.54	2449.06	3.97	-1.20	1.16	0.29	0.08	-7.58
849	D	6	6	133	135	69.58	2450.74	3.74	-1.30	1.17	0.41	-0.11	10.35
849	D	6	6	137	139	69.63	2452.45	3.61	-1.01	1.33	1.52	0.03	-2.99
849	D	6	6	139	140	69.65	2452.88	3.58	-1.10	1.25	0.99	-0.13	11.86
849	D	6	6	141	143	69.68	2455.05	3.58	-0.91	1.54	2.78	0.32	-28.75
849	D	6	6	143	145	69.69	2455.49	3.59	-0.94	1.29	1.21	-0.07	5.96
849	D	6	6	147	149	69.72	2456.82	3.30	-1.22	1.29	1.21	-0.36	32.29
849	C	7	1	80	82	69.76	2458.61	3.41	-1.13	1.22	0.74	-0.36	32.94
849	C	7	1	82	84	69.78	2459.50	3.43	-1.13				
849	D	6	7	8	10	69.83	2461.77	3.40	-1.11	1.40	1.98	-0.06	5.68
849	C	7	1	88	90	69.84	2462.22			1.62	3.25		
849	C	7	1	91	93	69.86	2463.14	3.33	-1.26	1.63	3.30	0.20	-17.93
849	C	7	1	93	95	69.90	2464.97	3.39	-1.15	1.36	1.68	-0.15	13.52
849	D	6	7	17	19	69.91	2465.43	3.37	-1.23	1.47	2.39	0.01	-1.25
849	C	7	1	96	98	69.92	2465.89	3.33	-1.56	1.12	-0.02	-0.63	57.21
849	C	7	1	98	100	69.94	2466.81	3.21	-1.16	1.68	3.58	0.15	-13.61
849	D	6	7	22	24	69.96	2467.73	3.39	-1.35	1.69	3.60	0.34	-30.84
849	C	7	1	103	104	69.98	2468.65	3.36	-1.28	1.26	1.04	-0.33	30.40

Site	Hole	Core	Section	Top (cm)	Bottom (cm)	Depth (mcd)	Age (ka)	$\delta^{18}O_{O.\ umbonatus}$ (‰ VPDB)	$\delta^{13}C_{O.\ umbonatus}$ (‰ VPDB)	$Mg/Ca_{O.\ umbonatus}$ (mmol mol^{-1})	BWT (°C)	$\delta^{18}O_{seawater}$ (‰ SMOW)	sea level (m)
849	C	7	1	106	108	70.02	2470.50	3.35	-1.49	1.20	0.62	-0.45	41.12
849	C	7	1	108	110	70.04	2471.42			1.33	1.52		
849	C	7	1	111	113	70.07	2472.80	3.61	-1.34	1.44	2.23	0.21	-19.23
849	C	7	1	113	115	70.08	2473.26			1.52	2.68		
849	C	7	1	116	118	70.13	2475.56	3.85	-1.24	1.35	1.62	0.30	-27.12
849	C	7	1	118	120	70.14	2476.02			1.39	1.90		
849	C	7	1	120	122	70.15	2476.48	3.80	-1.31	1.43	2.15	0.38	-34.87
849	C	7	1	122	124	70.18	2477.85	3.55	-1.49	1.47	2.38	0.19	-17.62
849	C	7	1	126	128	70.22	2479.67	3.75	-1.35	1.61	3.18	0.59	-53.30
849	C	7	1	128	130	70.25	2481.03	3.91	-1.20	1.22	0.78	0.15	-13.30
849	C	7	1	131	133	70.27	2481.93	3.98	-1.35	1.18	0.46	0.14	-12.54
849	C	7	1	133	135	70.29	2482.82	4.12	-1.48	1.24	0.87	0.38	-34.51
849	C	7	1	136	138	70.32	2484.15	3.98	-1.28	1.12	0.03	0.04	-3.47
849	C	7	1	138	140	70.34	2485.04	4.09	-1.59	1.26	1.01	0.39	-35.58
849	C	7	1	141	143	70.36	2485.91	4.24	-1.68				
849	C	7	1	143	145	70.39	2487.22			1.26	1.00		
849	C	7	1	146	148	70.42	2488.51			1.35	1.66		
849	C	7	1	148	150	70.45	2489.79	4.03	-1.74	1.33	1.53	0.46	-42.05
849	C	7	2	1	3	70.48	2491.05	3.90	-1.67	1.12	-0.02	-0.06	5.70
849	C	7	2	3	5	70.50	2491.88	3.44	-0.82	1.26	1.02	-0.26	23.60
849	C	7	2	5	7	70.52	2492.71			1.59	3.07		
849	C	7	2	7	9	70.53	2493.11			1.62	3.24		
849	C	7	2	9	11	70.56	2494.33	3.76	-1.43	1.26	1.04	0.07	-6.25
849	C	7	2	11	13	70.58	2495.13	3.75	-1.61	1.24	0.92	0.03	-2.79
849	C	7	2	13	15	70.60	2495.93	3.68	-1.60	1.12	0.02	-0.27	24.50
849	C	7	2	15	17	70.62	2496.72			1.31	1.38		
849	D	7	1	21	23	70.68	2499.09	3.05	-1.45				
849	D	7	1	23	25	70.69	2499.48			1.40	1.96		
849	D	7	1	28	30	70.73	2501.05	3.20	-1.97	1.41	2.05	-0.25	22.47
849	D	7	1	31	33	70.75	2501.84	3.53	-1.96	1.24	0.88	-0.21	18.91
849	D	7	1	33	35	70.79	2503.42	3.33	-2.04	1.10	-0.14	-0.66	60.13
849	D	7	1	36	38	70.81	2504.22	3.24	-2.36	1.39	1.92	-0.23	21.27
849	D	7	1	38	39	70.83	2505.02	3.74	-1.85	1.23	0.82	-0.01	1.16
849	D	7	1	40	42	70.85	2505.83	3.87	-2.07	1.62	3.25		
849	D	7	1	42	44	70.88	2507.06	3.68	-1.97	1.22	0.73	-0.09	8.41
849	D	7	1	46	47	70.91	2508.30			1.10	-0.17		
849	D	7	1	47	49	70.93	2509.15	3.89	-1.75	1.30	1.33	0.27	-24.56
849	D	7	1	50	52	70.95	2510.00	3.99	-2.19	1.00	-1.01	-0.22	19.82
849	D	7	1	52	54	70.98	2511.30	3.89	-2.34	1.65	3.42	0.79	-71.53
849	D	7	1	56	58	71.01	2512.62			1.28	1.14		
849	D	7	1	62	64	71.08	2515.79			1.60	3.15		

Site	Hole	Core	Section	Top (cm)	Bottom (cm)	Depth (mcd)	Age (ka)	$\delta^{18}O_{O.\ umbonatus}$ (‰ VPDB)	$\delta^{13}C_{O.\ umbonatus}$ (‰ VPDB)	$Mg/Ca_{O.\ umbonatus}$ (mmol mol^{-1})	BWT (°C)	$\delta^{18}O_{seawater}$ (‰ SMOW)	sea level (m)
849	D	7	1	67	69	71.13	2518.11	4.40	-1.23	1.32	1.46	0.81	-73.86
849	D	7	1	71	73	71.17	2520.00	3.97	-1.91	1.32	1.45	0.38	-34.58
849	D	7	1	76	78	71.21	2521.90	4.25	-1.41	0.95	-1.40	-0.06	5.05
849	D	7	1	78	80	71.25	2523.82	4.00	-1.67	1.77	4.03		
849	D	7	1	82	84	71.27	2524.78	3.93	-1.88	1.12	0.03	-0.02	1.54
849	D	7	1	91	93	71.37	2529.60	3.57	-2.23	1.51	2.63	0.28	-25.03
849	D	7	1	93	95	71.39	2530.56			1.14	0.15		
849	D	7	1	96	98	71.41	2531.52	3.68	-2.31	1.41	2.01	0.23	-20.52
849	D	7	1	98	100	71.43	2532.47	3.92	-1.64				
849	D	7	1	101	102	71.47	2534.38	3.67	-2.22	1.41	2.02	0.22	-20.19
849	D	7	1	102	104	71.48	2534.85	3.55	-2.42	1.93	4.79	0.79	-72.06
849	D	7	1	107	109	71.53	2537.19	3.51	-2.02	1.22	0.73	-0.27	24.18
849	D	7	1	109	111	71.54	2537.65	3.65	-2.44				
849	D	7	1	117	118	71.62	2541.30	3.80	-1.40	1.35	1.63	0.25	-22.94
849	D	7	1	118	120	71.63	2541.74	3.35	-1.71	1.21	0.66	-0.44	40.33
849	D	7	1	121	123	71.66	2543.07	3.43	-1.75	1.09	-0.27	-0.59	53.99
849	D	7	1	123	125	71.68	2543.94	3.31	-1.85	1.12	0.00	-0.65	58.72
849	D	7	1	127	128	71.73	2546.07	3.26	-1.29	1.20	0.64	-0.54	48.65
849	D	7	1	128	130	71.75	2546.91	3.34	-2.12				
849	D	7	1	131	133	71.77	2547.74	3.42	-1.67	1.27	1.10	-0.26	23.49
849	D	7	1	133	135	71.80	2548.96	3.39	-0.98	1.32	1.44	-0.20	18.57
849	D	7	1	139	140	71.85	2550.95	3.53	-1.48	1.18	0.49	-0.30	27.66
849	D	7	1	141	143	71.87	2551.72	3.06	-1.45				
849	D	7	1	143	145	71.89	2552.49	3.42	-1.32	1.10	-0.19	-0.58	53.13
849	D	7	1	147	149	71.91	2553.24	3.20	-1.68	1.27	1.12	-0.48	43.23
849	D	7	2	1	3	71.98	2555.80	3.02	-1.30	1.43	2.11	-0.41	37.28
849	D	7	2	6	8	72.02	2557.20	2.80	-1.60	1.26	1.05	-0.89	80.80
849	D	7	2	8	10	72.04	2557.88	3.15	-1.47	1.29	1.22	-0.50	45.43
849	D	7	2	17	18	72.12	2560.49	3.11	-0.30	1.48	2.47	-0.23	20.82
849	D	7	2	18	20	72.13	2560.80	2.92	-1.65	1.21	0.66	-0.87	79.43
849	D	7	2	21	23	72.18	2562.32	3.47	-1.46	1.14	0.14	-0.46	41.37
849	D	7	2	23	25	72.19	2562.62	3.21	-1.57	1.13	0.05	-0.74	66.98
849	D	7	2	26	28	72.22	2563.48	3.51	-1.70	1.17	0.39	-0.34	31.35
849	D	7	2	28	30	72.23	2563.77	3.63	-1.11	1.21	0.65	-0.16	14.96
849	D	7	2	31	33	72.28	2565.14	3.61	-1.74	1.23	0.81	-0.15	13.34
849	D	7	2	33	35	72.29	2565.41	3.59	-1.60	1.07	-0.40	-0.47	42.66
849	D	7	2	36	38	72.32	2566.21	3.62	-1.42	1.08	-0.36	-0.43	38.99
849	D	7	2	38	40	72.33	2566.47	3.73	-1.52				
849	D	7	2	41	43	72.38	2567.77	3.51	-1.65	1.12	0.01	-0.45	40.60
849	D	7	2	43	45	72.39	2568.03	3.82	-1.61	1.15	0.27	-0.06	5.80
849	D	7	2	46	48	72.42	2568.79			1.60	3.13		

Site	Hole	Core	Section	Top (cm)	Bottom (cm)	Depth (mcd)	Age (ka)	$\delta^{18}O_{O.\ umbonatus}$ (‰ VPDB)	$\delta^{13}C_{O.\ umbonatus}$ (‰ VPDB)	$Mg/Ca_{O.\ umbonatus}$ (mmol mol^{-1})	BWT (°C)	$\delta^{18}O_{seawater}$ (‰ SMOW)	sea level (m)
849	D	7	2	48	50	72.43	2569.05	3.49	-1.24	1.20	0.62	-0.31	28.25
849	D	7	2	51	53	72.45	2569.56	3.41	-1.35	1.81	4.21	0.51	-46.18
849	D	7	2	53	55	72.49	2570.58	3.78	-1.28	1.24	0.92	0.05	-4.89
849	D	7	2	56	58	72.51	2571.10			1.37	1.77		
849	D	7	2	62	63	72.58	2572.94	3.10	-1.22	1.30	1.31	-0.53	48.12
849	D	7	2	63	65	72.59	2573.21			1.28	1.18		
849	D	7	2	66	68	72.61	2573.76	3.39	-1.32	1.16	0.30	-0.49	44.72
849	D	7	2	68	70	72.63	2574.32	3.30	-1.20	1.35	1.65	-0.25	22.42
849	D	7	2	71	73	72.68	2575.75	3.47	-1.48	1.18	0.45	-0.38	34.13
849	D	7	2	73	75	72.69	2576.05	3.26	-1.46	1.22	0.77	-0.50	45.25
849	D	7	2	76	78	72.71	2576.65			1.36	1.73		
849	D	7	2	78	80	72.75	2577.89	3.39	-1.09	1.22	0.73	-0.38	34.34
849	D	7	2	81	83	72.78	2578.84			1.35	1.63		
849	D	7	2	83	85	72.79	2579.17	3.14	-1.41				
849	D	7	2	87	88	72.83	2580.48			1.68	3.56		
849	D	7	2	88	90	72.85	2581.15	3.28	-1.30				
849	D	7	2	91	93	72.87	2581.83	3.23	-1.61	1.56	2.89	0.00	0.10
849	D	7	2	93	95	72.89	2582.52	3.31	-1.49				
849	D	7	2	96	98	72.91	2583.21	3.26	-1.69	1.38	1.86	-0.23	20.83
849	D	7	2	98	100	72.95	2584.61	3.24	-1.55	1.28	1.19	-0.42	38.09
849	D	7	2	101	103	72.97	2585.31	3.36	-1.49	1.35	1.67	-0.17	15.74
849	D	7	2	103	105	72.98	2585.67	3.36	-1.37	1.43	2.12	-0.07	6.42
849	D	7	2	106	107	73.01	2586.74	3.35	-0.99	1.35	1.66	-0.19	16.84
849	D	7	2	107	109	73.03	2587.45	3.32	-1.48	1.48	2.42	-0.03	2.93
849	D	7	2	113	115	73.09	2589.61			1.24	0.87		
849	D	7	2	116	118	73.12	2590.69	3.29	-1.34	1.29	1.22	-0.36	32.33
849	D	7	2	118	120	73.14	2591.41	3.55	-1.32	1.35	1.64	0.01	-0.49
849	D	7	2	121	123	73.16	2592.13	3.54	-1.39	1.00	-1.02	-0.67	60.67
849	D	7	2	123	125	73.19	2593.21			1.28	1.15		
849	D	7	2	126	128	73.21	2593.92	3.62	-1.70	1.24	0.88	-0.12	10.82
849	D	7	2	128	130	73.23	2594.63	3.28	-1.46				
849	D	7	2	130	132	73.26	2595.68			1.61	3.20		
849	D	7	2	132	134	73.28	2596.43	3.50	-1.66	1.68	3.58	0.44	-40.28
849	D	7	2	141	143	73.37	2599.83	3.96	-1.60	1.16	0.28	0.07	-6.41
849	D	7	2	143	145	73.40	2600.98	4.07	-1.39	1.17	0.36	0.20	-18.57
849	D	7	2	146	148	73.43	2602.15	3.58	-1.79	1.16	0.34	-0.29	26.11
849	D	7	2	148	149	73.44	2602.54	4.08	-1.46	1.19	0.50	0.25	-23.07
849	D	7	3	1	3	73.48	2604.13	3.78	-1.59	1.41	2.03	0.34	-30.65
849	D	7	3	3	5	73.50	2604.94	3.40	-1.31	1.24	0.92	-0.33	29.85
849	D	7	3	6	8	73.52	2605.76	3.54	-1.43	1.45	2.25	0.15	-13.78
849	D	7	3	8	10	73.53	2606.18	3.86	-1.57	1.29	1.27	0.22	-20.02

Site	Hole	Core	Section	Top (cm)	Bottom (cm)	Depth (mcd)	Age (ka)	$\delta^{18}O_{O.\ umbonatus}$ (‰ VPDB)	$\delta^{13}C_{O.\ umbonatus}$ (‰ VPDB)	$Mg/Ca_{O.\ umbonatus}$ (mmol mol^{-1})	BWT (°C)	$\delta^{18}O_{seawater}$ (‰ SMOW)	sea level (m)
849	D	7	3	18	20	73.63	2610.48	3.56	-1.17				
849	D	7	3	21	23	73.68	2612.77	3.38	-1.50				
849	D	7	3	23	25	73.70	2613.71	3.50	-1.37				
849	D	7	3	26	28	73.72	2614.67			1.80	4.18		
849	D	7	3	28	30	73.73	2615.16	3.38	-1.49				
849	D	7	3	31	33	73.78	2617.66	3.30	-0.97	1.58	2.99	0.10	-8.73
849	D	7	3	33	35	73.80	2618.69	3.54	-0.96				
849	D	7	3	35	36	73.81	2619.20			1.90	4.62		
849	D	7	3	41	43	73.88	2622.87	3.15	-0.91	1.04	-0.68	-0.98	89.09
849	D	7	3	43	45	73.89	2623.40	3.10	-1.46	1.50	2.54	-0.22	20.26
849	D	7	3	46	48	73.92	2624.98	2.96	-1.41	1.96	4.90	0.23	-21.07
849	D	7	3	48	50	73.94	2626.04	3.34	-1.28	1.22	0.77	-0.42	38.59
849	D	7	3	51	53	73.98	2628.12	3.16	-1.36	1.36	1.71	-0.37	33.57
849	D	7	3	53	55	73.99	2628.64			1.33	1.51		
849	D	7	3	56	58	74.02	2630.17	3.13	-1.19	1.23	0.84	-0.61	55.85
849	D	7	3	63	65	74.09	2633.61	3.15	-1.85	1.27	1.10	-0.53	48.42
849	D	7	3	68	70	74.14	2636.11	3.06	-2.04	1.70	3.66	0.02	-2.07
849	D	7	3	71	73	74.17	2637.20	3.15	-1.19	1.60	3.13	-0.02	1.58

Table B.3.2. Site U1313 benthic foraminiferal (*Oridorsalis umbonatus*) stable isotopes ($\delta^{18}O$ and $\delta^{13}C$) and Mg/Ca as a proxy for bottom-water temperature (BWT), the oxygen-isotope composition of seawater ($\delta^{18}O_{seawater}$) and sea-level for ~2.65 to 2.4 Ma. Sea-level values are adjusted for changing deep-water masses after Craig and Gordon (1965) (sl_{CG65}) and Lang et al. (2016) (sl_{L16}) – for methodological details see Chapter 6. Reported Mg/Ca values are normalized to the ECRM752-1 standard. Further this table includes benthic foraminiferal (*Cibicidoides wuellerstorfi*) stable isotopes ($\delta^{18}O$ and $\delta^{13}C$) for ~2.56 to 2.50 Ma. $\delta^{18}O$ values of *C. wuellerstorfi* are adjusted for species-specific offset from equilibrium by the addition of +0.64‰ (Shackleton and Hall, 1984).

Site	Hole	Core	Section	Top (cm)	Bottom (cm)	Depth (mcd)	Age (ka)	$\delta^{18}O_{O.\ umbonatus}$ (‰ VPDB)	$\delta^{13}C_{O.\ umbonatus}$ (‰ VPDB)	$Mg/Ca_{O.\ umbonatus}$ (mmol mol^{-1})	BWT (°C)	$\delta^{18}O_{seawater}$ (‰ SMOW)	sea level (sl_{CG65}) (m)	sea level (sl_{L16}) (m)	$\delta^{18}O_{C.\ wuellerstorfi}$ (‰ VPDB)	$\delta^{13}C_{C.\ wuellerstorfi}$ (‰ VPDB)
1313	C	12	3	112	114	114.12	2413.84	3.36	-0.58	1.98	5.02	0.66	-15.99	6.53		
1313	C	12	3	132	134	114.32	2417.78	3.22	-0.77	2.55	7.20	1.06	-12.78	-29.21		
1313	C	12	4	0	2	114.47	2420.74	3.20	-0.82	2.13	5.66	0.66	-4.42	8.15		
1313	C	12	4	8	10	114.57	2422.71	3.36	-1.02	2.32	6.39	1.00	-21.99	-22.64		
1313	C	12	4	16	18	114.66	2424.48	3.41	-0.60	2.27	6.20	1.01	-25.97	-23.22		
1313	C	12	4	24	26	114.74	2426.05	3.54	-0.52	1.88	4.54	0.72	-30.43	-3.43		
1313	C	12	4	28	30	114.78	2426.84	3.54	-0.54	2.04	5.25	0.90	-33.61	-32.73		
1313	C	12	4	32	34	114.82	2427.63			2.36	6.52					

Site	Hole	Core	Section	Top (cm)	Bottom (cm)	Depth (mcd)	Age (ka)	$\delta^{18}O_{O.\ umbonatus}$ (‰ VPDB)	$\delta^{13}C_{O.\ umbonatus}$ (‰ VPDB)	$Mg/Ca_{O.\ umbonatus}$ (mmol mol^{-1})	BWT (°C)	$\delta^{18}O_{seawater}$ (‰ SMOW)	sea level (sl_{CG65}) (m)	sea level (sl_{L16}) (m)	$\delta^{18}O_{C.\ wuellerstorfi}$ (‰ VPDB)	$\delta^{13}C_{C.\ wuellerstorfi}$ (‰ VPDB)
1313	C	12	4	36	38	114.86	2428.42	3.68	-0.63	1.93	4.75	0.91	-43.54	-54.80		
1313	C	12	4	40	42	114.9	2429.21	4.53	-0.80	1.93	4.78	1.77	-121.23	-143.62		
1313	C	12	4	44	46	114.94	2430.00	4.53	-0.67	2.29	6.28	2.15	-128.33	-188.49		
1313	C	12	4	48	50	114.98	2430.79	4.45	-0.80	1.83	4.31	1.57	-111.77	-140.73		
1313	C	12	4	52	54	115.02	2431.58	4.46	-0.95	2.07	5.41	1.86	-118.04	-165.32		
1313	C	12	4	56	58	115.06	2432.37	4.10	-0.79	1.73	3.80	1.10	-78.05	-94.43		
1313	C	12	4	60	62	115.1	2433.16	4.49	-0.90	1.88	4.55	1.67	-116.33	-144.85		
1313	C	12	4	64	66	115.14	2433.94	4.47	-1.12	1.69	3.61	1.42	-110.83	-120.19		
1313	C	12	4	72	74	115.22	2435.52	4.39	-0.92	1.94	4.84	1.64	-108.78	-139.15		
1313	C	12	4	80	82	115.3	2437.10	4.41	-0.98	1.82	4.27	1.53	-108.45	-132.84		
1313	C	12	4	84	86	115.34	2437.88	4.45	-0.74	1.81	4.20	1.54	-111.35	-138.08		
1313	C	12	4	88	90	115.38	2438.67	4.28	-0.71	2.08	5.45	1.69	-101.59	-154.72		
1313	C	12	4	96	98	115.46	2440.25	4.44	-0.71	1.78	4.05	1.50	-110.04	-129.53		
1313	C	12	4	104	106	115.54	2441.82	4.31	-0.83	1.96	4.89	1.58	-102.17	-107.97		
1313	C	12	4	112	114	115.62	2443.40	4.30	-0.93	1.83	4.32	1.42	-97.93	-69.01		
1313	C	12	4	120	122	115.7	2444.98	4.30	-0.90	1.79	4.09	1.37	-97.01	-58.44		
1313	C	12	4	128	130	115.78	2446.56	4.42	-1.10	1.70	3.68	1.39	-106.28	-60.98		
1313	C	12	4	136	138	115.86	2448.12	4.38	-0.95	1.74	3.88	1.39	-103.28	-70.32		
1313	C	12	4	144	146	115.94	2449.67	4.17	-0.83	1.84	4.34	1.30	-86.90	-60.04		
1313	C	12	5	2	4	116.02	2451.21	4.00	-0.45	1.80	4.16	1.09	-70.38	-39.80		
1313	C	12	5	10	12	116.1	2452.76	4.17	-0.58	1.96	4.89	1.44	-89.19	-98.98		
1313	C	12	5	18	20	116.18	2454.20	3.89	-0.96	1.84	4.35	1.02	-60.78	-84.27		
1313	C	12	5	26	28	116.26	2455.55	3.89	-0.69	2.08	5.44	1.30	-66.28	-96.17		
1313	C	12	5	34	36	116.34	2456.90	3.81	-0.72	2.25	6.12	1.38	-61.87	-83.52		
1313	C	12	5	42	44	116.42	2458.25	3.62	-0.49	2.26	6.15	1.20	-44.61	-47.21		
1313	C	12	5	50	52	116.5	2459.60	3.11	-0.75	3.18	9.16	1.45	-12.09	-64.06		
1313	B	12	2	118	120	116.62	2461.62			2.64	7.53					
1313	B	12	2	122	124	116.66	2462.29	3.30	-0.12	2.34	6.47	0.96	-16.87	-19.10		
1313	B	12	2	126	128	116.7	2462.97	3.23	-0.49	2.41	6.74	0.96	-11.72	-18.77		
1313	B	12	2	130	132	116.74	2463.64	3.02	-0.31	2.81	8.06	1.08	1.27	-29.84		
1313	B	12	2	134	136	116.78	2464.32			2.61	7.43					
1313	B	12	2	138	140	116.82	2464.99			2.48	6.96					
1313	B	12	2	142	144	116.86	2465.66	3.07	-0.16	2.60	7.39	0.96	-0.40	-19.39		
1313	B	12	2	146	148	116.9	2466.34	3.19	-0.07	2.31	6.36	0.83	-6.62	-6.82		
1313	B	12	3	0	2	116.94	2467.01	3.18	-0.76	2.56	7.24	1.04	-10.13	-26.25		
1313	B	12	3	4	6	116.98	2467.68	3.23	-0.39	2.51	7.08	1.04	-13.10	-26.30		
1313	B	12	3	10	12	117.04	2468.69	3.18	-0.43	2.70	7.71	1.15	-12.06	-36.72		
1313	B	12	3	14	16	117.08	2469.37			3.00	8.65					
1313	B	12	3	18	20	117.12	2470.04	3.18	-1.00	3.02	8.70	1.40	-16.80	-59.91		
1313	B	12	3	22	24	117.16	2470.72	3.22	-0.58	2.61	7.41	1.12	-14.18	-34.38		
1313	B	12	3	26	28	117.2	2471.39	3.16	-0.93	2.51	7.08	0.98	-7.32	-22.16		

Site	Hole	Core	Section	Top (cm)	Bottom (cm)	Depth (mcd)	Age (ka)	$\delta^{18}O_{O.\ umbonatus}$ (‰ VPDB)	$\delta^{13}C_{O.\ umbonatus}$ (‰ VPDB)	$Mg/Ca_{O.\ umbonatus}$ (mmol mol^{-1})	BWT (°C)	$\delta^{18}O_{seawater}$ (‰ SMOW)	sea level (sl_{CG65}) (m)	sea level (sl_{L16}) (m)	$\delta^{18}O_{C.\ wuellerstorfi}$ (‰ VPDB)	$\delta^{13}C_{C.\ wuellerstorfi}$ (‰ VPDB)
1313	B	12	3	30	32	117.24	2472.07	3.23	-1.00	2.57	7.27	1.10	-14.68	-33.58		
1313	B	12	3	34	36	117.28	2472.74	3.44	-0.51	2.67	7.61	1.39	-35.17	-60.69		
1313	B	12	3	38	40	117.32	2473.42	3.26	-1.43	3.32	9.52	1.69	-27.67	-88.54		
1313	B	12	3	44	46	117.37	2474.26	3.52	-1.14	2.58	7.33	1.40	-41.16	-62.83		
1313	B	12	3	48	50	117.42	2475.10	3.80	-1.08	2.55	7.20	1.64	-65.83	-85.90		
1313	B	12	3	52	54	117.46	2475.77	3.82	-0.11	2.92	8.39	1.96	-73.02	-115.38		
1313	B	12	3	56	58	117.5	2476.45	3.81	-1.00	2.15	5.74	1.29	-59.80	-54.47		
1313	B	12	3	60	62	117.54	2477.12	3.89	-1.29	2.02	5.17	1.23	-65.32	-53.13		
1313	B	12	3	64	66	117.58	2477.80	3.70	-1.21	2.03	5.20	1.05	-48.05	-50.18		
1313	B	12	3	68	70	117.62	2478.47	3.83	-1.53							
1313	B	12	3	72	74	117.66	2479.38	4.02	-1.18	1.66	3.46	0.93	-69.15	-73.66		
1313	B	12	3	76	78	117.7	2480.29	4.40	-1.40	1.91	4.70	1.62	-108.83	-155.11		
1313	B	12	3	80	82	117.74	2481.20	4.31	-1.45	1.57	2.96	1.10	-93.20	-110.80		
1313	B	12	3	84	86	117.78	2482.11	4.50	-1.49	1.57	2.96	1.29	-110.49	-122.62		
1313	B	12	3	88	90	117.82	2483.02	4.60	-1.48	1.66	3.46	1.51	-121.43	-135.74		
1313	B	12	3	96	98	117.9	2484.89	4.54	-1.50	1.72	3.75	1.53	-117.92	-119.22		
1313	B	12	3	104	106	117.98	2486.76	4.60	-1.37	1.82	4.26	1.71	-125.18	-103.56		
1313	B	12	3	112	114	118.06	2488.62	4.46	-1.10	1.64	3.34	1.34	-108.16	-53.46		
1313	B	12	3	120	122	118.14	2490.49	4.26	-1.20	2.06	5.34	1.64	-99.49	-81.04		
1313	B	12	3	128	130	118.22	2492.36			2.31	6.34					
1313	B	12	3	136	138	118.3	2493.99	3.95	-1.06	1.88	4.53	1.13	-67.66	-34.66		
1313	B	12	3	144	146	118.38	2495.62	3.82	-0.47	1.87	4.51	0.99	-55.38	-21.97		
1313	B	12	4	0	2	118.44	2496.79	3.30	-0.86	2.07	5.39	0.70	-12.42	4.99		
1313	B	12	4	2	4	118.46	2497.15	3.62	-0.86	2.15	5.72	1.10	-43.28	-31.89		
1313	B	12	4	8	10	118.52	2498.20	3.24	-0.81	2.17	5.80	0.74	-9.02	1.03	3.59	0.82
1313	B	12	4	10	12	118.54	2498.56	3.45	-0.76							
1313	B	12	4	18	20	118.62	2499.97	3.13	-0.93	2.47	6.95	0.92	-4.17		3.26	0.82
1313	B	12	4	28	30	118.72	2501.73	3.19	-0.99	2.38	6.62	0.89	-7.43	-12.40	3.22	0.78
1313	B	12	4	30	32	118.74	2502.08			2.39	6.65					
1313	B	12	4	32	34	118.76	2502.43			2.22						
1313	B	12	4	34	36	118.78	2502.78			2.29	6.26					
1313	B	12	4	38	40	118.82	2503.49	3.19	-1.07						3.25	0.94
1313	B	12	4	42	44	118.86	2504.19			2.41	6.72	0.30				
1313	B	12	4	48	50	118.92	2505.25								3.43	0.78
1313	B	12	4	50	52	118.94	2505.60			2.61	7.41					
1313	B	12	4	54	56	118.98	2506.31			2.35	6.50					
1313	B	12	4	56	58	119.00	2506.66			2.46	6.90				2.05	0.41
1313	B	12	4	58	60	119.02	2507.01	2.99	-1.10	2.30	6.33		11.44	11.81	3.63	0.74
1313	B	12	4	60	62	119.04	2507.37					0.62			3.50	-0.04
1313	B	12	4	62	64	119.06	2507.72								3.56	0.74
1313	B	12	4	64	66	119.08	2508.07	3.23							3.29	0.68

Site	Hole	Core	Section	Top (cm)	Bottom (cm)	Depth (mcd)	Age (ka)	$\delta^{18}O_{O.\ umbonatus}$ (‰ VPDB)	$\delta^{13}C_{O.\ umbonatus}$ (‰ VPDB)	$Mg/Ca_{O.\ umbonatus}$ (mmol mol^{-1})	BWT (°C)	$\delta^{18}O_{seawater}$ (‰ SMOW)	sea level (sl_{CG65}) (m)	sea level (sl_{L16}) (m)	$\delta^{18}O_{C.\ wuellerstorfi}$ (‰ VPDB)	$\delta^{13}C_{C.\ wuellerstorfi}$ (‰ VPDB)
1313	B	12	4	66	68	119.10	2508.42			2.33	6.42				3.66	0.70
1313	B	12	4	68	70	119.12	2508.78	3.39	-1.30	2.13	5.64	0.84	-21.32	-8.62	3.63	0.76
1313	B	12	4	70	72	119.14	2509.13	2.92		2.50	7.04	0.72	14.90	1.09	3.64	0.69
1313	B	12	4	72	74	119.16	2509.48	3.00		2.19	5.89	0.52	12.49	18.62	3.46	0.24
1313	B	12	4	74	76	119.18	2509.83	3.08		1.80	4.18	0.17	13.62	49.85	3.70	0.42
1313	B	12	4	76	78	119.20	2510.19	3.78	-1.59	1.94	4.81	1.02	-52.94	-29.25	3.56	0.34
1313	B	12	4	78	80	119.22	2510.54	3.44		2.35	6.51	1.11	-29.70	-37.92	3.70	0.36
1313	B	12	4	80	82	119.24	2510.94	3.97	-1.78	1.85	4.41	1.12	-68.73	-39.91		
1313	B	12	4	82	84	119.26	2511.34	4.11	-1.29	1.92	4.71	1.33	-82.86	-60.59	3.93	0.19
1313	B	12	4	84	86	119.28	2511.80	4.14	-1.57	1.76	3.97	1.18	-82.56	-47.64	4.09	0.53
1313	B	12	4	86	88	119.30	2512.27	4.05	-1.45	1.83	4.30	1.17	-75.49	-46.99	4.13	0.38
1313	B	12	4	88	90	119.32	2512.73	3.92	-1.27	1.81	4.20	1.01	-63.00	-33.18	4.27	0.07
1313	B	12	4	90	92	119.34	2513.20	4.11	-1.50	1.94	4.82	1.36	-83.44	-65.23	4.58	0.54
1313	B	12	4	92	94	119.36	2513.66	4.32	-1.32	1.88	4.54	1.50	-101.04	-78.05	4.34	0.16
1313	B	12	4	94	96	119.38	2514.12	4.21	-1.53	1.91	4.67	1.42	-91.35	-71.23	4.33	0.51
1313	B	12	4	96	98	119.40	2514.59	4.32	-1.31	1.79	4.13	1.40	-99.28	-69.66	4.07	0.12
1313	B	12	4	98	100	119.42	2515.05	4.22	-1.44	1.73	3.79	1.22	-89.05	-53.57	4.23	0.42
1313	B	12	4	100	102	119.44	2515.52	4.29	-1.36	1.72	3.77	1.28	-95.25	-59.60	4.30	0.32
1313	B	12	4	102	104	119.46	2515.98	4.30	-1.48	1.90	4.63	1.51	-100.00	-80.25	4.16	-0.15
1313	B	12	4	104	106	119.48	2516.45	4.29	-1.38	1.73	3.82	1.29	-95.02	-60.78	4.31	-0.06
1313	B	12	4	106	108	119.50	2516.91	4.43	-1.43	1.75	3.93	1.46	-108.41	-76.23	4.40	0.05
1313	B	12	4	108	110	119.52	2517.37	4.21	-1.52	1.62	3.25	1.07	-85.49	-43.63	4.39	-0.03
1313	B	12	4	110	112	119.54	2517.84	4.38	-1.43	1.88	4.56	1.57	-107.05	-96.97	4.35	0.10
1313	B	12	4	112	114	119.56	2518.30	4.32	-1.49	2.14	5.68	1.78	-105.85	-124.31	4.26	-0.28
1313	B	12	4	114	116	119.58	2518.77	4.52	-1.84	1.54	2.81	1.27	-111.84	-86.23	4.39	-0.67
1313	B	12	4	116	118	119.60	2519.23	4.35	-1.75	1.81	4.19	1.44	-102.30	-109.89	4.39	-0.40
1313	B	12	4	118	120	119.62	2519.70	4.30	-1.59	1.58	3.04	1.11	-92.54	-87.27	4.46	-0.23
1313	B	12	4	120	122	119.64	2520.16	4.44	-1.40	1.60	3.12	1.26	-105.42	-109.79	4.43	-0.25
1313	B	12	4	122	124	119.66	2520.63	4.23	-1.79	1.58	3.01	1.03	-85.92	-89.78	4.41	-0.39
1313	B	12	4	124	126	119.68	2521.09	4.29	-1.72	1.70	3.65	1.25	-94.51	-102.08	4.40	-0.17
1313	B	12	4	126	128	119.70	2521.55	4.24	-1.53	1.64	3.34	1.12	-88.64	-82.46	4.22	-0.09
1313	B	12	4	128	130	119.72	2522.02	4.28	-1.57	1.75	3.91	1.30	-94.37	-90.48	4.36	-0.45
1313	B	12	4	130	132	119.74	2522.48	4.20	-1.76	1.76	3.96	1.24	-87.48	-76.61	3.97	-0.09
1313	B	12	4	132	134	119.76	2522.95	4.00	-1.25	1.73	3.80	0.99	-68.57	-46.62	4.07	0.10
1313	B	12	4	134	136	119.78	2523.41	4.08	-1.43	1.61	3.21	0.93	-73.34	-32.62	3.94	-0.09
1313	B	12	4	136	138	119.80	2523.88	4.13	-1.51	1.56	2.91	0.90	-76.31	-22.20	4.24	-0.24
1313	B	12	4	138	140	119.82	2524.34	4.21	-1.38	1.62	3.22	1.06	-85.07	-35.13	4.31	0.35
1313	B	12	4	140	142	119.84	2524.81	4.19	-1.63	1.66	3.44	1.10	-84.60	-71.68	4.08	-0.23
1313	B	12	4	142	144	119.86	2525.27	4.19	-1.51	1.67	3.50	1.11	-84.23	-76.82	4.11	0.17
1313	B	12	4	144	146	119.88	2525.73	4.20	-1.52	1.56	2.93	0.98	-82.85	-67.16	4.18	-0.35
1313	B	12	4	146	148	119.90	2526.20	4.09	-1.48	1.71	3.73	1.07	-76.78	-77.74	4.21	-0.09

Site	Hole	Core	Section	Top (cm)	Bottom (cm)	Depth (mcd)	Age (ka)	$\delta^{18}O_{O.\ umbonatus}$ (‰ VPDB)	$\delta^{13}C_{O.\ umbonatus}$ (‰ VPDB)	$Mg/Ca_{O.\ umbonatus}$ (mmol mol^{-1})	BWT (°C)	$\delta^{18}O_{seawater}$ (‰ SMOW)	sea level (sl_{CG65}) (m)	sea level (sl_{L16}) (m)	$\delta^{18}O_{C.\ wuellerstorfi}$ (‰ VPDB)	$\delta^{13}C_{C.\ wuellerstorfi}$ (‰ VPDB)
1313	B	12	4	148	150	119.92	2526.66	4.20	-1.39	1.62	3.24	1.06	-84.39	-78.60	4.45	-0.08
1313	B	12	5	0	2	119.94	2527.13	4.00	-1.52	1.61	3.18	0.84	-66.24	-61.45	4.41	-0.05
1313	B	12	5	2	4	119.96	2527.59	4.12	-1.59	1.52	2.66	0.83	-74.68	-62.56	4.30	-0.17
1313	B	12	5	4	6	119.98	2528.06	4.13	-1.41	1.75	3.90	1.15	-81.24	-93.86	4.11	-0.39
1313	B	12	5	6	8	120.00	2528.52	4.03	-1.66	1.69	3.61	0.97	-70.05	-79.46	4.25	-0.51
1313	B	12	5	8	10	120.02	2528.99	4.22	-1.54	1.46	2.32	0.84	-81.72	-69.79	4.30	-0.30
1313	B	12	5	10	12	120.04	2529.45	4.05	-1.48	1.54	2.80	0.80	-68.76	-67.72	4.30	-0.05
1313	B	12	5	12	14	120.06	2529.91	4.00	-1.41	1.45	2.24	0.61	-61.56	-52.47	4.24	-0.23
1313	B	12	5	14	16	120.08	2530.38	4.20	-1.69	1.60	3.14	1.03	-83.43	-92.82	4.35	-0.14
1313	B	12	5	16	18	120.10	2530.84	4.07	-1.46	1.75	3.94	1.10	-76.07	-102.05	4.23	0.00
1313	B	12	5	18	20	120.12	2531.31	4.16	-1.55	1.60	3.13	0.99	-80.21	-93.60	4.08	0.12
1313	B	12	5	20	22	120.14	2531.77	3.98	-1.56	1.72	3.77	0.97	-66.73	-91.13	4.07	-0.06
1313	B	12	5	22	24	120.16	2532.24	4.15	-1.09	1.73	3.83	1.15	-82.54	-105.67	4.23	0.09
1313	B	12	5	24	26	120.18	2532.70	3.97	-1.22	1.89	4.58	1.16	-69.75	-104.21	4.09	0.45
1313	B	12	5	26	28	120.20	2533.16	4.00	-1.09	1.79	4.12	1.08	-70.54	-94.46	4.10	0.45
1313	B	12	5	28	30	120.22	2533.63	3.97	-1.25	1.86	4.47	1.14	-69.30	-97.25	4.11	0.22
1313	B	12	5	30	32	120.24	2534.09	3.93	-1.01	1.85	4.41	1.08	-65.08	-89.57	3.99	0.62
1313	B	12	5	32	34	120.26	2534.56	3.95	-1.17	2.01	5.12	1.28	-70.06	-105.23	3.91	0.43
1313	B	12	5	34	36	120.28	2535.02	4.01	-1.01	1.64	3.37	0.90	-67.54	-68.48	3.93	0.34
1313	B	12	5	36	38	120.30	2535.49	3.89	-1.04	2.11	5.57	1.33	-66.59	-105.23	3.48	0.43
1313	B	12	5	38	40	120.32	2535.95	3.98	-1.33	2.00	5.08	1.29	-72.29	-99.77	3.86	0.67
1313	B	12	5	40	42	120.34	2536.42	3.93	-1.11	1.94	4.80	1.17	-66.50	-86.48	3.86	0.46
1313	B	12	5	42	44	120.36	2536.88	3.88	-1.32	1.94	4.81	1.13	-62.14	-80.11	3.62	0.29
1313	B	12	5	44	46	120.38	2537.34	3.84	-1.05						2.86	-0.21
1313	B	12	5	46	48	120.40	2537.81	3.89	-1.21							
1313	B	12	5	48	50	120.42	2538.27	3.82	-1.23	1.77	4.03	0.87	-53.44	-44.08	3.91	0.43
1313	B	12	5	50	52	120.44	2538.74	3.72	-1.16	1.92	4.71	0.94	-46.93	-45.25	3.71	0.78
1313	B	12	5	52	54	120.46	2539.17	3.32	-1.35	1.94	4.80	0.57	-11.40	-6.81		
1313	B	12	5	54	56	120.48	2539.59	3.41	-0.96	1.84	4.35	0.54	-17.30	-0.08		
1313	B	12	5	56	58	120.50	2540.02	3.25	-1.08	1.85	4.41	0.40	-3.45	17.30		
1313	B	12	5	58	60	120.52	2540.45	3.25	-1.13	1.99	5.05	0.56	-6.31	7.29		
1313	B	12	5	60	62	120.54	2540.88	3.42	-0.79	1.99	5.02	0.72	-21.51	-3.06	3.57	0.77
1313	B	12	5	62	64	120.56	2541.27	3.11	-1.16	1.94	4.83	0.36	7.95	32.43		
1313	B	12	5	64	66	120.58	2541.67	3.33	-0.76	1.95	4.85	0.58	-12.21	12.28		
1313	B	12	5	66	68	120.60	2542.07	3.10	-0.84	1.88	4.56	0.29	9.31	39.42		
1313	B	12	5	68	70	120.62	2542.47	2.97	-0.93	2.09	5.48	0.38	17.80	31.52		
1313	B	12	5	70	72	120.64	2542.87	3.05	-0.62	1.97	4.96	0.34	12.16	35.58	3.46	0.83
1313	B	12	5	72	74	120.66	2543.27	3.07	-0.92	2.16	5.74	0.56	6.69	16.26		
1313	B	12	5	74	76	120.68	2543.67	2.97	-0.59	1.78	4.05	0.03	24.08	64.76		
1313	B	12	5	76	78	120.70	2544.07	2.78	-0.84	1.99	5.05	0.08	36.85	59.82		
1313	B	12	5	78	80	120.72	2544.47	2.84	-0.80	2.22	6.00	0.38	26.93	32.98		

Site	Hole	Core	Section	Top (cm)	Bottom (cm)	Depth (mcd)	Age (ka)	$\delta^{18}O_{O.\ umbonatus}$ (‰ VPDB)	$\delta^{13}C_{O.\ umbonatus}$ (‰ VPDB)	$Mg/Ca_{O.\ umbonatus}$ (mmol mol^{-1})	BWT (°C)	$\delta^{18}O_{seawater}$ (‰ SMOW)	sea level (sl_{CG65}) (m)	sea level (sl_{L16}) (m)	$\delta^{18}O_{C.\ wuellerstorfi}$ (‰ VPDB)	$\delta^{13}C_{C.\ wuellerstorfi}$ (‰ VPDB)
1313	B	12	5	80	82	120.74	2544.87	3.01	-0.58	2.05	5.32	0.38	14.65	33.34	3.24	1.04
1313	B	12	5	82	84	120.76	2545.26	2.65	-0.71	1.88	4.52	-0.18	50.88	84.13		
1313	B	12	5	84	86	120.78	2545.66	2.92	-0.91	2.18	5.84	0.43	19.83	29.08		
1313	B	12	5	86	88	120.80	2546.06	2.75	-0.65	1.93	4.77	-0.01	40.83	69.48		
1313	B	12	5	88	90	120.82	2546.46	2.76	-0.68	2.01	5.11	0.09	37.72	60.20		
1313	B	12	5	90	92	120.84	2546.86	2.88	-0.81	2.31	6.35	0.51	21.71	21.71	3.26	1.15
1313	B	12	5	92	94	120.86	2547.26	2.63	-0.72	2.11	5.57	0.07	47.50	61.71		
1313	B	12	5	94	96	120.88	2547.66	2.74	-0.76	2.24	6.09	0.31	35.19	39.96		
1313	B	12	5	96	98	120.90	2548.06	2.69	-0.61	2.12	5.58	0.13	42.13	56.14		
1313	B	12	5	98	100	120.92	2548.46	2.76	-0.57	2.03	5.22	0.11	37.63	58.24		
1313	B	12	5	100	102	120.94	2548.85	2.76	-0.77	2.22	6.02	0.31	34.30	40.35	3.09	0.95
1313	B	12	5	108	110	121.02	2550.45	3.12	-0.37	2.26	6.17	0.71	0.36	3.71		
1313	B	12	5	110	112	121.04	2550.85	2.86	-0.49	2.20	5.91	0.39	25.03	32.97	3.08	1.01
1313	B	12	5	116	118	121.10	2552.05	3.13	-0.40	2.20	5.91	0.66	0.54	8.51		
1313	B	12	5	120	122	121.14	2552.84	3.18	-0.43	2.16	5.77	0.67	-3.05	7.51	3.06	0.95
1313	B	12	5	124	126	121.18	2553.64	3.17	-0.28	1.91	4.66	0.38	2.56	33.26		
1313	B	12	5	128	130	121.22	2554.44	3.24	-0.34	1.94	4.83	0.49	-3.89	23.83		
1313	B	12	5	130	132	121.24	2554.84	3.05	-0.17	2.23	6.06	0.61	7.42	12.77		
1313	B	12	5	132	134	121.26	2555.24	3.14	-0.51	2.11	5.54	0.57	1.63	16.33		
1313	B	12	5	138	140	121.32	2556.43	3.38	-0.46	1.95	4.86	0.64	-17.49	9.67		
1313	B	12	5	140	142	121.34	2556.83	3.00	-0.51	1.89	4.60	0.20	18.32	50.13	3.37	0.83
1313	B	12	5	142	144	121.36	2557.21	3.39	-0.44	2.02	5.19	0.73	-19.64	1.48		
1313	B	12	5	144	146	121.38	2557.59	3.23	-0.38	2.45	6.87	0.99	-12.72	-22.14		
1313	B	12	5	148	150	121.42	2558.35	3.15	-0.73	1.94	4.81	0.40	4.04	32.12		
1313	B	12	6	4	6	121.49	2559.65	3.35	-0.35	2.06	5.34	0.73	-16.69	1.67		
1313	B	12	6	14	16	121.59	2561.30	3.54	-0.46	2.02	5.17	0.87	-32.74	-11.35		
1313	B	12	6	22	24	121.66	2562.40	3.82	-1.12	2.01	5.13	1.15	-58.40	-36.25		
1313	B	12	6	30	32	121.74	2563.72	3.56	-0.49	2.00	5.09	0.88	-34.63	-11.76		
1313	B	12	6	34	36	121.78	2564.37	3.62	-0.07	2.16	5.77	1.11	-43.35	-32.87		
1313	B	12	6	38	40	121.82	2565.03	3.77	-0.29	2.24	6.09	1.34	-58.39	-53.59		
1313	B	12	6	42	44	121.86	2565.69			2.15	5.74					
1313	B	12	6	54	56	121.98	2567.67	3.52	-0.33	2.20	5.93	1.05	-34.72	-27.09		
1313	B	12	6	62	64	122.06	2568.99	3.73	-0.23	2.39	6.67	1.44	-56.90	-62.65		
1313	B	12	6	70	72	122.14	2570.31	3.50	-0.16	2.03	5.22	0.85	-29.62	-9.03		
1313	B	12	6	78	80	122.22	2571.62	3.40	-0.62	2.03	5.20	0.75	-20.91	-0.01		
1313	B	12	6	86	88	122.3	2572.94	3.39	-0.53	2.39	6.66	1.10	-26.49	-32.16		
1313	B	12	6	94	96	122.38	2574.25	3.59	-0.35	2.24	6.08	1.16	-41.68	-51.50		
1313	B	12	6	102	104	122.46	2575.57	3.27	-0.33	2.01	5.13	0.60	-8.55	-29.79		
1313	B	12	6	110	112	122.54	2577.12	3.19	-0.24	2.45	6.87	0.95	-8.89	-80.14		
1313	B	12	6	118	120	122.62	2578.67	3.33	-0.28							
1313	C	13	3	2	4	122.82	2583.08	3.16	0.05							

Site	Hole	Core	Section	Top (cm)	Bottom (cm)	Depth (mcd)	Age (ka)	$\delta^{18}O_{O.\ umbonatus}$ (‰ VPDB)	$\delta^{13}C_{O.\ umbonatus}$ (‰ VPDB)	$Mg/Ca_{O.\ umbonatus}$ (mmol mol^{-1})	BWT (°C)	$\delta^{18}O_{seawater}$ (‰ SMOW)	sea level (sl_{CG65}) (m)	sea level (sl_{L16}) (m)	$\delta^{18}O_{C.\ wuellerstorfi}$ (‰ VPDB)	$\delta^{13}C_{C.\ wuellerstorfi}$ (‰ VPDB)
1313	C	13	3	10	12	122.9	2584.90	3.20	-0.34							
1313	C	13	3	16	18	122.97	2586.46	3.14	-0.49							
1313	C	13	3	18	20	123.00	2587.11	3.25	-0.50							
1313	C	13	3	26	28	123.05	2588.40	3.18	-0.26							
1313	C	13	3	32	34	123.11	2589.70	3.26	-0.54							
1313	C	13	3	34	36	123.14	2590.35	3.35	-0.48	2.10	5.51	0.77	-16.96	-1.62		
1313	C	13	3	38	40	123.18	2591.29	3.36	-0.58	1.90	4.62	0.57	-14.60	16.80		
1313	C	13	3	42	44	123.22	2592.24	3.42	-0.95	2.00	5.09	0.73	-21.46	1.44		
1313	C	13	3	46	48	123.26	2593.18	3.66	-0.84	1.90	4.62	0.86	-41.82	-10.39		
1313	C	13	3	50	52	123.3	2594.13	3.69	-0.66	1.90	4.65	0.90	-44.21	-13.39		
1313	C	13	3	54	56	123.34	2595.07	3.78	-1.07	2.24	6.07	1.35	-59.15	-54.11		
1313	C	13	3	58	60	123.38	2596.08	3.68	-1.10	2.19	5.87	1.20	-49.35	-40.58		
1313	C	13	3	62	64	123.42	2597.09	3.90	-1.26	1.79	4.10	0.97	-61.21	-21.38		
1313	C	13	3	66	68	123.46	2598.09	3.87	-1.20	2.44	6.82	1.62	-70.17	-83.15		
1313	C	13	3	70	72	123.5	2599.10	3.76	-1.35	2.69	7.67	1.72	-64.43	-96.57		
1313	C	13	3	74	76	123.54	2600.11	3.64	-1.64							
1313	C	13	3	82	84	123.62	2602.13	3.61	-1.70	2.22	6.00	1.16	-43.25	-69.43		
1313	C	13	3	90	92	123.7	2604.14	4.03	-1.27	1.65	3.40	0.92	-69.46	-22.84		
1313	C	13	3	98	100	123.78	2606.16	4.11	-1.25	1.75	3.94	1.14	-79.61	-40.50		
1313	C	13	3	106	108	123.86	2608.17	3.80	-1.13	1.81	4.19	0.89	-52.05	-23.16		
1313	C	13	3	114	116	123.94	2610.19	3.95	-0.65	1.72	3.74	0.93	-63.94	-27.78		
1313	C	13	3	122	124	124.02	2612.13	3.91	-0.66	1.91	4.69	1.13	-64.93	-41.64		
1313	C	13	3	130	132	124.1	2614.08	3.10	-0.44	1.96	4.90	0.37	8.13	31.74		
1313	C	13	3	138	140	124.18	2615.93	3.69	-0.41	1.64	3.32	0.57	-38.55	16.50		
1313	C	13	3	146	148	124.26	2617.68	3.12	-0.36	1.75	3.94	0.15	10.37	54.26		
1313	C	13	4	4	6	124.34	2619.43	3.49	-0.30	1.84	4.34	0.62	-25.04	11.54		
1313	C	13	4	12	14	124.42	2621.18	3.35	-0.06	1.96	4.91	0.62	-14.26	11.96		
1313	C	13	4	20	22	124.5	2622.92	3.18	-0.15	1.73	3.84	0.19	5.64	51.32		
1313	B	13	1	74	76	124.74	2628.17	2.86	-0.82	2.20	5.92	0.38	25.33	33.19		
1313	B	13	1	94	95	124.94	2632.55	3.06	-0.85	2.29	6.26	0.67	5.44	7.11		
1313	B	13	1	100	102	125	2633.70	3.38	-0.53	2.51	7.06	1.19	-27.42	-40.39		
1313	B	13	1	105	107	125.05	2634.66	3.50	-0.56	1.88	4.53	0.67	-26.16	6.91		
1313	B	13	1	115	117	125.15	2636.57	3.63	-0.58	2.35	6.52	1.30	-47.37	-50.44		
1313	B	13	1	125	127	125.25	2638.49	3.48	-0.63	1.76	3.96	0.52	-22.36	21.14		

Additional references

Craig, H., Gordon, L.I. (1965). Deuterium and oxygen-18 variations in the ocean and the marine atmosphere. In Stable isotopes in oceanographic studies and paleotemperatures, edited by Tongiorgi, E., pp. 9–130, Spoletto, Pisa, Italy.

Lang, D.C., Bailey, I., Wilson, P.A., Chalk, T., Foster, G., Gutjahr, M. (2016). Incursions of southern-sourced water into the deep North Atlantic during late Pliocene glacial intensification. Nat. Geosci., 9, doi:10.1038/NGEO2688.

Shackleton, N.J., Hall, M.A. (1984). Oxygen and carbon isotope stratigraphy of Deep Sea Drilling Project Hole 552A: Plio-Pleistocene Glacial History. In Proceedings of the Deep Sea Drilling Project, Initial Rep., 81, pp. 599–609, Deep Sea Drill. Proj., Washington, D.C.

Eidesstattliche Versicherung gemäß § 8 der Promotionsordnung der Naturwissenschaftlich-Mathematischen Gesamtfakultät der Universität Heidelberg

1. Bei der eingereichten Dissertation zu dem Thema

Late Pliocene to early Pleistocene millennial-scale climate fluctuations and sea-level variability: A view from the tropical Pacific and the North Atlantic

handelt es sich um meine eigenständig erbrachte Leistung.

2. Ich habe nur die angegebenen Quellen und Hilfsmittel benutzt und mich keiner unzulässigen Hilfe Dritter bedient. Insbesondere habe ich wörtlich oder sinngemäß aus anderen Werken übernommene Inhalte als solche kenntlich gemacht.

3. Die Arbeit oder Teile davon habe ich ~~wie folgt~~/bislang nicht[1)] an einer Hochschule des In- oder Auslands als Bestandteil einer Prüfungs- oder Qualifikationsleistung vorgelegt.

Titel der Arbeit: _____

Hochschule und Jahr: _____

Art der Prüfungs- oder Qualifikationsleistung: _____

4. Die Richtigkeit der vorstehenden Erklärungen bestätige ich.

5. Die Bedeutung der eidesstattlichen Versicherung und die strafrechtlichen Folgen einer unrichtigen oder unvollständigen eidesstattlichen Versicherung sind mir bekannt.

Ich versichere an Eides statt, dass ich nach bestem Wissen die reine Wahrheit erklärt und nichts verschwiegen habe.

Ort und Datum _____ Unterschrift _____

[1)] Nicht Zutreffendes streichen. Bei Bejahung sind anzugeben: der Titel der andernorts vorgelegten Arbeit, die Hochschule, das Jahr der Vorlage und die Art der Prüfungs- oder Qualifikationsleistung.

12/2012